The Construction and Analysis of a Whole-Sky Map Using Underground Muons

Graham L. Giller
Lincoln College



A thesis submitted for the degree of
Doctor of Philosophy at the University of
Oxford, Hilary Term, 1994.



The Construction and Analysis of a Whole-Sky Map Using Underground Muons

Graham L. Giller
Lincoln College



A thesis submitted for the degree of
Doctor of Philosophy at the University of
Oxford, Hilary Term, 1994.

ABSTRACT

A sample of 16 million underground muons has been collected between January, 1989, and June, 1993, at a depth of 2090 m.w.e. in the SOUDAN 2 detector. This data-set has been passed through standard event reconstruction programs to give a sample of 14 million muons after run and event cuts. The trajectories of all muons in this data-set have been projected back onto the celestial sphere.

Software has been developed to compute the apparent motions of the Sun and Moon as viewed from the surface of the Earth. The errors on the coordinates computed by these programs are well understood. The programs have been used to search the data-set for evidence of the cosmic ray shadow cast by the stopping of primaries in the Sun and Moon. This procedure was used to test the assumption that the detector alignment is known to $\sim 0.25°$ and that the resolution is $\sim 1°$. The observed distribution of events was found to be consistent with this hypothesis. However the test performed lacked sufficient power to reject strongly the alternative hypothesis, that no shadow had been observed. A 95% lower limit of $0.46°$ was set on the single-muon resolution.

A procedure has been developed to construct and analyse a map of the underground muon flux across the entire celestial sphere. A whole-sky background calculation has been developed and it has been verified that the background computed for the observed data-set is an acceptable description of the distribution of event coordinates. By a monte-carlo procedure, it has been demonstrated that the statistical properties of the analysis method are understood and agree with the distribution computed analytically. It has been shown that there is no evidence for drift or bias in the background computed.

The procedure has been applied to the data-set, asymmetrically divided into two subsets of 10.6 and 3.3 million muons respectively. A search for anomalous muon excess in the larger data-set found the largest deviation to be an excess within $1.9°$ degrees of Active Galactic Nucleus 3C 273. The significance of the excess was estimated to be $\sim 10\%$ and the significance of it's proximity to 3C 273 to be $\sim 2\%$. A 1.7 s.d. excess was found in the identical position in the smaller data set. The number of excess events for both data-sets, scaled by their relative exposures, were consistent at the level of 1 s.d. The overall level of confidence is conservatively estimated to be better than 99%.

On the assumption that this excess does represent a real flux of muons, due to primary cosmic rays from 3C 273, the region in excess was examined in

greater detail. A maximum likelihood fit was used to extract confidence limits for the strength, coordinates, and r.m.s. width of the excess. It was found that association with 3C 273 should be rejected, with a confidence of 95%, unless the r.m.s. source width was permitted to increase from the *a priori* value of 1° to 2.4°. With this modification excess coordinates were estimated to be $\alpha = (188.2^{+2.1}_{-2.8})°$, $\delta = (2.2^{+2.3}_{-2.1})°$.

The background subtracted distributions of a selection of event parameters were examined and found to be consistent with the background expectation. On the assumption that the flux has the same spectral index as the background, the underground muon flux was estimated to be $10.3^{+11.3}_{-9.2} \times 10^{-12}\,\mathrm{cm}^{-2}\mathrm{s}^{-1}$. Such a flux is not consistent with the observed γ-ray flux from 3C 273, and can only be explained by unconventional physics.

ACKNOWLEDGEMENTS

Firstly I must thank my supervisor, Dr. John Cobb, for help, suggestions and criticisms and for the many long discussions we have had over this work. I must also thank Prof. D. Siegmund, of Stanford University, for his help with the statistical analysis. I would also like to thank Profs. Marvin Marshak, Earl Peterson and Don Perkins for their interest and enthusiasm, and Roger Cashmore for hiring me!

In Oxford: I should particularly thank Nick West, who put up with my ever increasing demands on the computer system for disk space, memory, and CPU hours, Wade Allison, who provided lifts to the Rutherford Lab. and searching questions; at the Rutherford Lab.: Geoff Pearce, Peter Litchfield, Dave Cockerill; various Minnesotans including: David DeMuth, Garrick Villaume, Sue Kasahara; Bill Miller and the mine crew.

The people in the office (who put up with my use of five desks and half a filing cabinet) over the last three years: Mark Lancaster, Alex Byrne, David Bailey, and Tim Yip, ZEUS enthusiasts to a man; and the people in the other offices: Paula Collins (a fan), Patrick Luffman (a customer), Peter Morawitz, Mike Lay, Rob Black. And finally, other friends: David Jehan, Martyn Green, Jason Tigg, Eu Jin Chua, and Rebecca Woodgate.

NOTATION

The reader may be unfamiliar with some of the notations used in this thesis. These notations are explained below:

i, The symbol $\sim$ is used to represent the relationship "is distributed as." It is also common in Physics to use this symbol to represent the relationship "of order." Both notations are used, the meaning implied should be immediately obvious from the context.

ii, The symbol $N(\mu, \sigma^2)$ is used to represent the Normal distribution with mean μ and standard deviation σ. $N(0, 1)$ is the *standard* Normal distribution. The symbol Uniform(a, b) is used to represent the uniform distribution with lower bound a and upper bound b.

iii, The symbol Z is conventionally used to represent a random variable drawn from the standard Normal distribution.

iv, Exp x is used to mean "the expected value of x," Var x for "the variance of x," Cov(x, y) for "the covariance of x and y" and Cor(x, y) for "the correlation of x and y."

v, sup Z means "the supremum of the set Z." The supremum of a set need not be a member of the set itself, whereas the maximum, max Z, must. For example: the set of rational numbers less than $\sqrt{2}$ has a supremum, $\sqrt{2}$ itself, but no maximum, as for any rational number $p < \sqrt{2}$ there exists a rational number q such that $p < q < \sqrt{2}$.

CONTENTS

ABSTRACT iii

ACKNOWLEDGEMENTS v

NOTATION vi

1 INTRODUCTION 1
- 1.1 Overview . . . 1
- 1.2 The Soudan 2 Experiment . . . 2
- 1.3 Point Sources High Energy Cosmic Rays . . . 7
- 1.4 Observations of Anomalous Deep Underground Muon Flux . 11

2 PROCESSING AND CHARACTERISTICS OF THE DATA-SET ANALYSED 13
- 2.1 Introduction . . . 13
- 2.2 The Appearance of the Raw Data . . . 13
- 2.3 The Processing Required for Astronomical Analysis . . . 16
- 2.4 Muon Reconstruction by FMR . . . 17
- 2.5 Muon Reconstruction by SEARCH . . . 19
- 2.6 A Comparison of SEARCH and FMR . . . 21
- 2.7 The DMC Data-Set . . . 26
- 2.8 Characteristics of the Data-Set Analysed . . . 29

3 A STUDY OF THE EFFECT OF DETECTOR MISALIGNMENT AND THE COMPUTATION OF SOLAR & LUNAR COORDINATES 35
- 3.1 Introduction . . . 35
- 3.2 The Effect of a Systematic Misalignment of the Detector Axes 35

3.3 Current Status of the Detector Alignment 43
3.4 Drift-Velocity Errors and their Effect on the Accuracy of Reconstruction 44
3.5 Use of the Solar and Lunar Shadows to Verify Alignment . . 45
3.6 The Motions of the Sun and Moon 46
3.7 Computation of the Trajectories of the Sun and the Moon . . 51
3.8 Verification of Program Accuracy by Computation of the Times of Solar and Lunar Eclipses 61

4 SEARCH FOR THE COSMIC RAY SHADOWS CAST BY THE SUN AND THE MOON 67
4.1 Introduction 67
4.2 Variation of the Shadow Depth as a Function of Event Coordinate Rotation 67
4.3 Maximum Likelihood Analysis of the Event Distributions About the Sun and the Moon 73
4.4 Summary and Conclusions 87

5 THE CONSTRUCTION OF A WHOLE SKY MAP OF THE DEEP UNDERGROUND MUON FLUX 89
5.1 Introduction 89
5.2 A Whole Sky Map 90
5.3 Understanding the Diffuse Background Cosmic Ray Flux 91
5.4 A Whole Sky Background Calculation 98
5.5 Demonstration of the Validity of the Method 101
5.6 Specification of the Whole Sky Maps 104
5.7 Independent Bins Analysis 107
5.8 Verification of the Whole Sky Background 111
5.9 Smoothing the Maps 112
5.10 The Whole Sky Monte Carlo 115
5.11 Monte-Carlo Simulation of the Behaviour of a Map Containing a Source 119

6 GENERAL ANALYSIS OF THE WHOLE SKY MAP 129
6.1 Introduction 129
6.2 General Analysis of Map 1 129

6.3 Comparison of the Two Independent Maps 139
6.4 Summary and Conclusions of the General Analysis 141
6.5 Examination of the Combined Maps in the Region of Selected Sources 142

7 FURTHER ANALYSIS OF THE 3C 273/MX–1 REGION 151
7.1 Introduction 151
7.2 Maximum Likelihood Fits to the Combined Data Set 152
7.3 Examination of the Combined Maps in the Region of the MX–1 Antipode 158
7.4 Enhancement of the Signal 159
7.5 Study of Event Variable Distributions for the Enhanced Sample 159
7.6 Fit to the Primary Spectral Index for the Enhanced Sample . 164
7.7 Conclusions from the Analysis of Event Variables 168
7.8 Flux Calculations 169

8 SUMMARY AND CONCLUSIONS 175
8.1 Summary 175
8.2 Conclusions 177
8.3 Comparison with the Results of Other Experiments 180
8.4 Implications of a Muon Signal from 3C 273 182
8.5 Suggestions for Further Work 183

A THE SOUDAN 2 COLLABORATION 185

B ASTRONOMICAL COORDINATES 187
B.1 Spatial Coordinate Systems 187
B.2 Representation of Data on the Sphere (The Aitoff Plot) . . . 190

C STATISTICAL CONSIDERATIONS 193
C.1 The Maximum Likelihood Ratio Test 193
C.2 The Statistics of Correlated Searches 195

D AITOFF PROJECTION MAPS OF THE COMBINED DATA SET 203

BIBLIOGRAPHY 229

CHAPTER 1

INTRODUCTION

This chapter serves as an introduction to this thesis. Its purpose is to describe the structure of the thesis and the context under which the investigation was undertaken. As such the chapter is divided into three parts: in the first, the general structure of the thesis is described; in the second, the operation and nature of the SOUDAN 2 detector are described; and, in the third, the physics motivation behind the work is discussed.

1.1 Overview

In this thesis the construction and analysis of a map (a large 2-d histogram) of the directions (projected onto the celestial sphere) of deep underground muons are described. The goal of the analysis is to identify candidate regions of the sky where an anomalously large flux of deep underground muons, consistent with emission from a point source, is observed and to attempt also to associate such regions with known astrophysical objects. The discovery of a statistically unambiguous excess would require the transport of some quantum from the region of the source to the Earth, where an interaction gives rise to muons in an underground detector, and is of interest to Particle Physics. This is also of Astrophysical interest, as the association of such a signal with a known object would provide insight to the processes occurring at the source. However, the work presented here is mainly concerned with the development and preliminary application of the analytical techniques required for such an investigation and not with the physics consequences of such a discovery — i.e. in the main it is an investigation in statistical astronomy.

The processing required to render the data into a form suitable for the production of a map is described in Chapter 2. The characteristics of the data selected for analysis are also given. The alignment of the SOUDAN 2 detector, an essential parameter for an astronomical investigation, is believed to be known to $\sim 0.25°$. In Chapters 3 and 4, the large data-set available is used to test whether this hypothesis should be rejected.

In Chapter 5 the manner in which a sky-map may be constructed is discussed. The background calculation that must be performed is described in some detail and the principle tested on the data. The manner in which the map may be analysed is studied, and the results of a Monte-Carlo simulation of the adopted procedure are given.

Data reconstructed in the SOUDAN 2 detector represents the world's largest sample of deep underground muons suitable for such analysis. In Chapter 6 the analytical techniques developed are applied to the available data-set and the region of the sky that contains the largest excess is identified. In Chapter 7, a more in detailed investigation of the muon flux from this region of the sky is made.

The results of this investigation are summarized in Chapter 8.

1.2 The Soudan 2 Experiment

The SOUDAN 2 collaboration[1] operates a large fine-grained tracking calorimeter in an underground laboratory located in the Tower-Soudan Iron Mine in Minnesota, USA. (47.81° N, 92.25° W). The detector is installed in an experimental hall 714 m beneath the surface (2090 m.w.e.).

The design of the detector is modular in nature and consists of 224 drift-calorimeter modules stacked in a rectangular array providing a continuous fiducial mass of 960 tons. Each module weighs $\sim$ 4.3 tons and is 2.5 m $\times$1 m $\times$1 m in dimension. The full detector array is 5.4 m high, 8 m across, and 15 m deep.

The design was optimized for *difficult* nucleon decay modes, such as the $SU(5)$ mode $p \rightarrow \nu K^+$, and provides a high-resolution, three-dimensional, reconstruction of events within the detector of a "bubble chamber" quality[2]. In addition, the calorimetric nature of the detector provides further information for event analysis.

The modular nature of the detector allows easy maintenance of the calorimeter, and has allowed data to be read out from the module array during construction of

[1] See Appendix A for a full list of collaborating institutions and physicists.

[2] Event display pictures for some cosmic ray muons are shown in Chapter 2.

the full detector. Although construction is now complete, the detector grew from one *half-wall* (a $1 \times 4 \times 1$ array of modules) to approximately two thirds of the final configuration during the period in which the data analysed here was collected.

The detector is surrounded by an active shield to allow the separation of events contained within the fiducial volume of the detector into those due to the interaction of neutral particles from the deep inelastic scattering of high energy cosmic ray muons in the rock overburden and those due to neutrino and nucleon decay interactions (if they occur) within the detector volume.

A surface array has been added to allow cosmic ray composition studies to be made using coincidences between the surface and underground detectors. A Čerenkov telescope will also be incorporated into this work.

The low background nature of an underground laboratory, and the high quality event reconstruction required for nucleon decay studies, allows the detector to be used for other experimental investigations. These include searches for evidence of:

i, neutrino oscillations by measurement of the flavour ratio of events induced by the neutrinos from atmospheric cosmic ray interactions[41, 73];

ii, magnetic monopoles passing through the detector[5]; *and*

iii, the cosmic ray muon astronomy studies described in this thesis.

1.2.1 The Detector Modules

The design and performance of the SOUDAN 2 calorimeter modules are fully described in Reference [80]. A summary of their operation is given here.

Each detector module is a 4.3 ton *stack* of corrugated steel sheets. The steel provides the fiducial mass for calorimetry and drift tubes, placed in the hexagonal "pockets" between the corrugations, allow particle detection and tracking. Figure 1.1 shows the cross-section of a single drift tube. The metre long tubes are made from the resistive polymer Hytrel and placed in longitudinal pockets in a "sandwich" made from two sheets of Mylar. Twenty one copper electrodes are also bonded to the Mylar, to provide a linear potential gradient from -9 kV in the centre of each tube to 0 V at both tube mouths. This assembly is known as *bandolier*. The bandolier and steel sheets are assembled into a stack which is compressed and put inside a gas-tight cover.

In operation, each module is filled with a mixture of 85% Argon and 15% CO_2. There is also a small proportion of water present. Particle detection is via the

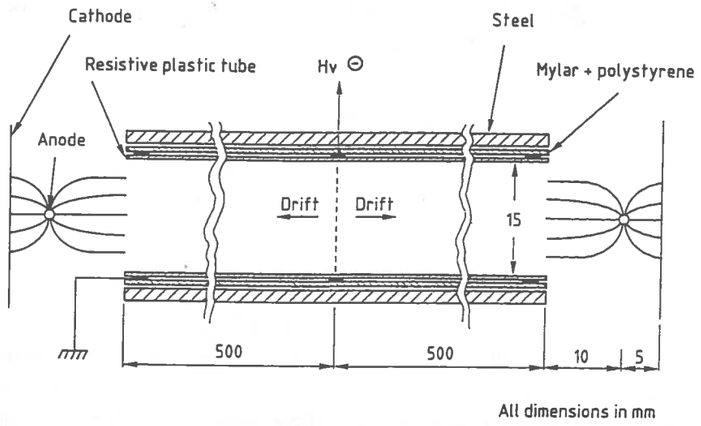


Figure 1.1: The cross-section of a single drift tube.

ionization produced when a charged particle crosses a gas filled tube. The electrons freed drift at a constant velocity of $\sim 0.6\,\mathrm{cm}\ \mu\mathrm{s}^{-1}$ towards the tube mouths where amplification occurs by avalanche in the field around an anode wire held at $+2.2\,\mathrm{kV}$ and strung across the end of the tubes. The current induced by the drift of positive ions, away from the anode wires and towards a cathode pad at the end of each tube, is detected on both the anode wires and strips of cathode pads. These currents are identical in their time-profiles, but have different magnitudes due to the geometry of the electrodes. The *wireplanes* and *cathode boards* are fitted into each module before it is sealed.

The anode wires and cathode strips are crossed to allow the location of the tube that was *hit* in two dimensions (x from the anode number and y from the cathode number). For events which cross a number of adjacent tubes, the third dimension (z) is added from the relative drift times of individual pulses. Figure 1.2 shows a section through a fully assembled module.

1.2.2 The Veto-Shield

The veto-shield that surrounds the main detector is constructed from 1400 modules. Each module consists of eight hexagonal proportional tubes arranged in a 2×4

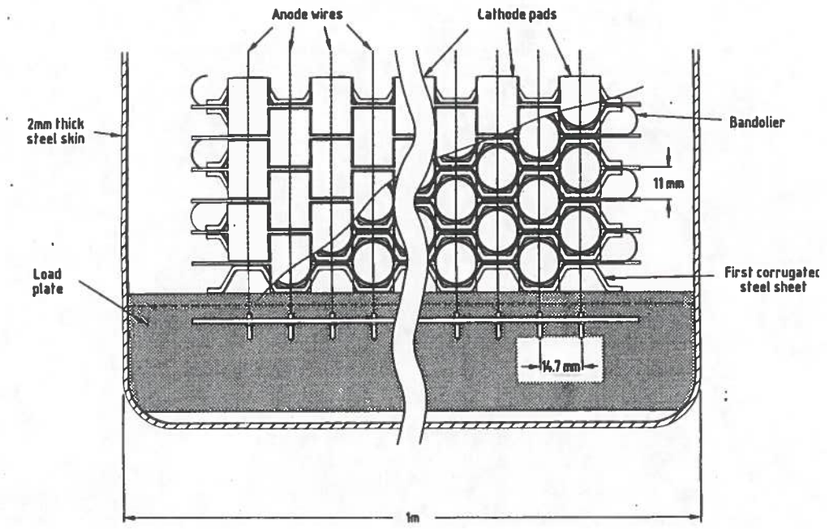


Figure 1.2: The cross-section of the *stack* inside a fully assembled calorimeter module.

geometry. Every $1\ \mu\mathrm{s}$ the combined output of each group of 4 tubes is read into a F.I.F.O. buffer $128\ \mu\mathrm{s}$ deep. When the main detector triggers, the entire buffer is then read out and stored with the information from the main detector. A processor is run to identify coincident two-layer activation of the shield, or CTL's. The shield is not used to trigger the main detector or in the reconstruction of muon tracks.

1.2.3 The Soudan 2 Detector During Assembly

Figure 1.3 is a photograph taken during assembly of the main detector. In the foreground, modules undergoing the final stages of construction and testing can be seen. In the background, surrounding the detector, are the panels of veto-shield modules. On the right-hand side, towards the front, the racks of electronics can be seen. On the bottom of each module are the drift high-voltage cables, and around the edges the anode and cathode cables are brought out through the gas-tight seal.

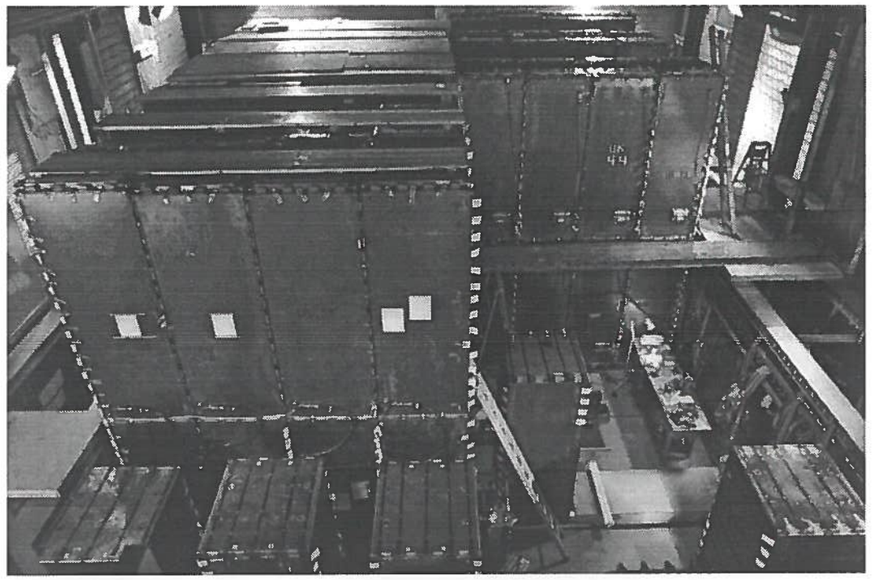


Figure 1.3: A photograph of the SOUDAN 2 detector during assembly.

1.2.4 The Detector Electronics and the Trigger

The signals from the anode wires and cathode strips are pre-amplified and then digitized by an array of 6-bit flash A.D.C.'s. To reduce the number of channels that must be read out from a mostly quiescent detector the output is multiplexed before digitization. This is done by summing the anode and cathode signals in groups of eight. Time division multiplexing is not implemented, so the demultiplexing required must be done by pattern recognition methods. The multiplexing scheme is defined so that if a pulse on an anode channel is uniquely matched to a pulse on a cathode channel then the *half-tube* that was hit is unambiguously determined. The electronics channels are organised into groups known as *physical looms* (before multiplexing) and *logical looms* (after multiplexing). A physical loom corresponds to all the channels (anodes or cathodes) from either the front or back of a half-wall.

The output of the A.D.C.'s are sampled every 200 ns and stored in a F.I.F.O. register 1024 words deep. When the detector is triggered the detector is read out for a further 512 time slices before the data is transferred to the computer performing

D.A.Q. operations. The trigger is then at word 512 in the anode-time and cathode-time projections.

The trigger of the SOUDAN 2 detector is fully described in Reference [13]. It was designed to trigger on nucleon decay/neutrino induced events. The trigger works by looking for groups of positive going pulses, or *edges*, within a given time window on adjacent channels. The trigger parameters (number of edges etc.) and the logical combination required to trigger the detector may be programmed from the D.A.Q. computer. Because the trigger works in this manner, the time at which the trigger occurs is not necessarily equal to the time, T_0, at which the event that caused the trigger occurred. However, this may often be deduced from the circumstances of the event. For events that cross both the fronts and backs of modules T_0 is fixed, as the different drift direction in front and back half-tubes creates track segments that are only consistent at one time.

1.3 Point Sources High Energy Cosmic Rays

The cosmic ray spectrum extends to very high energies. The highest energy claimed to date is $\sim 10^{20}$ eV[88]. Although statistical acceleration mechanisms, such as the "collision" between a charged particle and a magnetized gas cloud, can reach energies of ~ 1 TeV, they are limited by the typical sizes and velocities of interstellar gas clouds and are unable to produce acceleration to the higher end of the cosmic ray spectrum. Acceleration to ~ 10 TeV is possible in the magnetic shocks present in the plasma ejected from a supernova. However, above these energies, large-scale mechanisms seem unable to produce the acceleration required and model making has concentrated on discrete objects such as X-ray binary stars and Active Galactic Nuclei (A.G.N.).

To produce a beam of high energy particles one requires an accelerator. If that beam is also required to produce an intense flux of neutral particles, that may cross Galactic/intra-Galactic space without scattering in the magnetic fields present, one also needs to dump the beam into a target. It is possible to build models of discrete astrophysical objects in which such conditions exist. To illustrate that such models are plausible, a simple model of an A.G.N. is described below. Acceleration in stars such as X-ray binaries has also been considered[40]. One of the mechanisms proposed for Cygnus X–3 is reviewed in Reference [85].

1.3.1 Particle Acceleration in Active Galactic Nuclei

Active Galactic Nuclei (such as quasars, Seyfert galaxies, BL Lacertae type objects etc.) are extremely powerful sources of radiation. Our galactic centre outputs $\sim 10^{39}$ erg s^{-1} whereas the most powerful, high redshift, quasars output $\sim 10^{48}$ erg s^{-1}. Recently emission of low energy[3] γ-rays ($\lesssim 20$ GeV) consistent with point-like emission from a number of A.G.N. has been reported by the EGRET experiment on the Compton Gamma-ray Observatory[38]. The power output of these sources is so great that a gravitationally driven acceleration method is normally considered — gravitation acceleration is the most efficient method known, liberating some 10% of a body's rest mass as it falls onto a compact massive object. If the luminosity of a typical A.G.N. is at the Eddington limit[4], given by $\mathcal{L}_E \simeq 10^{46}(M/M_8)$ erg s^{-1} where $M_8 = 10^8 M_\odot$, this requires a nucleus with a mass of $\sim 100 M_8$ for an A.G.N. with a luminosity of $\sim 10^{48}$ erg s^{-1}. Such a massive body is usually assumed to be a black hole.

To illustrate a model of an A.G.N. in which electrostatic acceleration may occur, after Blandford[18] we shall consider a set of thought experiments (a full treatment of electrodynamics in the region of a spinning black hole is given in Reference [56]). These experiments are illustrated in Figure 1.4.

In Experiment (a) we consider the effect of placing a black hole into a uniform electric field. As space is gathered in around the black hole the electric field lines are drawn with it, so the field lines are distorted as if the event horizon was a conducting surface. The solution of Maxwell's Equations in a Schwartzschild metric confirms this description — the event horizon becomes an equipotential surface.

In Experiment (b) we consider a black hole surrounded by a magnetized plasma accretion disc. The magnetic field lines are *frozen* into the plasma by M.H.D. interactions and so are drawn with the plasma towards the black hole. As plasma crosses the event horizon the field lines frozen with it become causally disconnected. This induces a transient electrical field. If we assume that plasma within the Schwarzschild radius, r, is engulfed causing transient fields for a time given by the light-crossing time, r/c, then the equation $\partial \boldsymbol{B}/\partial t = -\boldsymbol{\nabla} \times \boldsymbol{E}$ can be approximated by $Bc/r \approx BR/\mu_0 r$, where R is the surface resistance of the event horizon.

[3] In this thesis the nomenclature used for the branches of the γ-ray spectrum is not rigidly adhered to. "Low" and "high" energy will be used relative to the approximate scale set by current particle accelerator energies of ~ 0.1 TeV.

[4] The steady state condition for an accreting object at which outward force due to radiation pressure equals the gravitational force on the accreting matter[50].

Therefore, $R \approx \mu_0 c = Z_0$. This turns out to be the correct value.

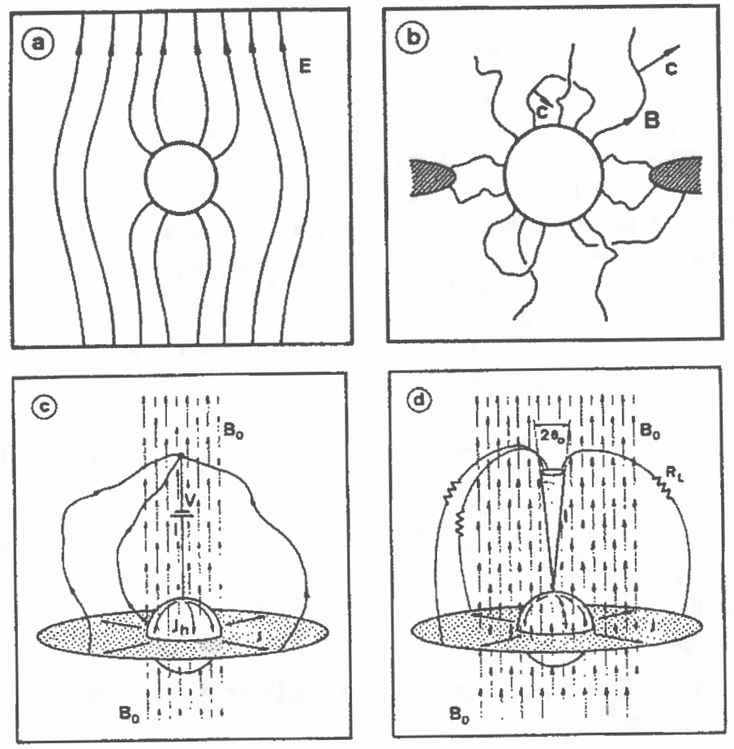


Figure 1.4: Four thought experiments that illustrate the electromagnetic properties of a black hole. Taken from reference [18].

In Experiment (c) a non-rotating black hole embedded in a uniform magnetic field is connected to an e.m.f. (This may be arranged by dropping electrons into the poles and protons in at the equator, for example.) A current will flow on the conducting surface, and as this current is perpendicular to a magnetic field there will be a Lorentz force that causes the hole to spin.

Experiment (d) is then inevitable. We consider a rotating black hole (a Kerr black hole) surrounded by a magnetized plasma accretion disc. This configuration

will generate an e.m.f. by unipolar induction. The e.m.f. will be proportional to the angular momentum of the hole and the magnetic flux threading the hole.

1.3.2 The Model and Real A.G.N.

The model developed above necessarily produces acceleration into a beam aligned with the spin axis of the black hole that is surrounded by an accretion disc. Many A.G.N. are observed to possess a single or a back-to-back pair of highly relativistic jets which emit synchrotron radiation over scales of 10 kpc to 1 Mpc[91]. If the beam in then dumped into dust clouds, or other orbiting material, then this provides a target for the production of γ-rays via the decay of pions. The cloud will also be heated to a high temperature, producing absorbtion or emission lines (depending on the angle from which the object is viewed) in the A.G.N.'s spectrum. An elaboration of the simple model developed here may be used to explain the wide variety of characteristics observed in A.G.N. of different types.

In real A.G.N., with typical masses and flux densities, such an accelerator may generate an e.m.f. of $\sim 10^{20}$ V with an internal resistance of $\sim 30\ \Omega$. The radiative losses from electrons accelerated to such energies, by synchrotron radiation and inverse compton scattering, will be immense, so it is unlikely that a 10^{20} eV electron beam may be directly accelerated. However, it has been suggested that re-acceleration may occur in the termination shock of the jet or that the main beam may be a proton beam rather than an electron beam[18].

1.3.3 The Emission of Quanta other than Photons by A.G.N.

Most astrophysical work on A.G.N. is concerned with their emission of photons across the electromagnetic spectrum. However, as pointed out by many authors, the upper end of the cosmic ray spectrum cannot be explained in terms of a discrete electromagnetic accelerator[5]. The dumping of a hadronic beam into a hadronic target will produced a very large flux of pions and so a high energy neutrino beam will be produced. The conditions in the target may be such that it is impossible for photons to escape[15]. Calculations of the neutrino flux from A.G.N. indicate very

[5] i.e. One in which the principal beam is of quanta for which electromagnetic interactions dominate.

low event rates ($\sim 2 \times 10^4$ km^{-2} year^{-1}[46]), although model making is limited by the (current lack of) observation of such cosmic neutrinos.

For a collision between a beam and a fixed target the centre of momentum energy is $\simeq \sqrt{2mE}$, where m is the target mass and E the beam energy. For a 10^{20} eV beam into a proton target the c.m.s. energy is $\sim 0.4 \times 10^{15}$ eV $= 400$ TeV. This is beyond the reach of current terrestrial accelerators, and so it is possible that such objects are sources of exotic quanta that cannot be produced in terrestrial accelerators.

1.4 Observations of Anomalous Deep Underground Muon Flux

1.4.1 Underground Muons from Cygnus X–3

In the mid 1980s, prompted by a suggestion of Learned[62], underground muon data collected by nucleon decay experiments, which typically have an angular resolution for muons of a few degrees, was searched for evidence of a signal from Cygnus X–3. Cyg X–3 is a powerful X-ray source, and has been observed in many bands of the electromagnetic spectrum. It exhibits a characteristic 4.8 hour period in its emissions and large, aperiodic, flares in radio flux. During such a flare, which typically last for $\sim$ 5–7 days, the radio flux (at $\sim$ 1–10 cm wavelengths) increases by 2–3 orders of magnitude, reaching a peak of[6] $\sim$ 10–20 Jy. During the most intense flares Cyg X–3 is one of the brightest radio sources in the sky. (See Reference [85] for a more detailed discussion of Cyg X–3.)

The SOUDAN 1 and NUSEX experiments independently reported excess fluxes from the direction of Cyg X–3, modulated by the 4.8 hour period of Cyg X–3. SOUDAN 1, at a depth of 1800 m.w.e., reported a flux of $\sim 10^{-11}$ cm^{-2}s^{-1}[58] and NUSEX, at 5000 m.w.e. reported a flux of $\sim 10^{-12}$ cm^{-2}s^{-1}[14]. These results were of marginal *a posteriori* statistical significance ($\sim$ 1%) and searches in other experiments placed limits in conflict with the reported results[7, 16, 65]. In particular, the KAMIOKANDE experiment at 2400 m.w.e., a similar depth to SOUDAN 1, and FRÉJUS, at a similar depth to NUSEX (5000 m.w.e.) found no evidence of any excess. The analysis was continued as data were accumulated. The SOUDAN 1 studies were switched to the larger SOUDAN 2 detector, then under construction at a lower level in the same mine site. The NUSEX collaboration continue to report an

[6] 1 Jansky (Jy) is equal to 10^{-30} W s^{-1} Hz^{-1}.

excess[1].

The SOUDAN 1 group reported a possible correlation of underground muons with the radio flare of October'85[59] and the IMB group reported an excess during the 1983 flare, although neither of these observations were confirmed by KAMIOKANDE[66]. During the January'91 radio flare the muon rate (number of muons per transit) in SOUDAN 2 was examined. An excess with a significance estimated to be $\sim 5 \times 10^{-4}$ was found in the data. The excess was restricted to 2 of the days examined. This was reported[84], defining an *a priori* signal for the other experiments to search for. The results were mixed[76]. The HEGRA surface array found an excess of extensive air showers on both days indicated by SOUDAN 2. The first day was the most significant excess observed in over a year of observation (3.8σ). A very deep underground detector, KGF, reported seeing 4 muons in the two days preceeding the flare, where the expectation was 1 per 25 days. Other surface arrays (CYGNUS and CASA) saw no excess, as did the underground detectors MACRO and IMB.

1.4.2 The Physics Implications of the Reported Muon Flux

If the reported muon signals from Cygnus X–3 are real, then they cannot be explained by conventional physics[85]. The constraints placed by the distance to the source and the apparent phase modulation of the signal require the transport of a stable low mass primary ($\tau \gtrsim 10^7$ s, $m \lesssim 0.5$ GeV) from the source. The lack of disruption of the signal by the Galactic magnetic field (the primary must travel ~ 11 kpc in a field of $\sim 3\,\mu$G) requires a neutral particle. The natural candidate is the photon, but γ-rays are very inefficient at producing muons and the reported flux could not be explained by a conventionally interacting photon.

Although the subject remains controversial, it is still very interesting and remains part of the search for non-standard model physics.

CHAPTER 2

PROCESSING AND CHARACTERISTICS OF THE DATA-SET ANALYSED

2.1 Introduction

In this chapter the appearance of SOUDAN 2 data and the processing required to render SOUDAN 2 data into a form suitable for analysis are described. Two track reconstruction programs, SEARCH and FMR, are run as part of the off-line analysis system at the Tower-Soudan mine site. The action of these programs, and the characteristics of the resulting muon d.s.t., are summarized. Finally, the manner of analyzing the combined d.s.t. is specified.

2.2 The Appearance of the Raw Data

After the main detector triggers, data is read into the VAXcluster at the Tower-Soudan mine where it is queued for off-line processing[1]. The data is read out as a sequence of pulses on the anode and cathode channels of the detector. The multiplexing of the detector electronics folds all the physical looms into the first eight half-walls. Figure 2.1 shows the raw data from a typical event containing a muon. The aim of the processing done at the mine is to reconstruct the physical picture of each event from the logical image read from the detector electronics. This is essential if a physics analysis of the event is to be made.

[1] Processing is managed by SOAP, the Soudan Off-line Analysis Program.

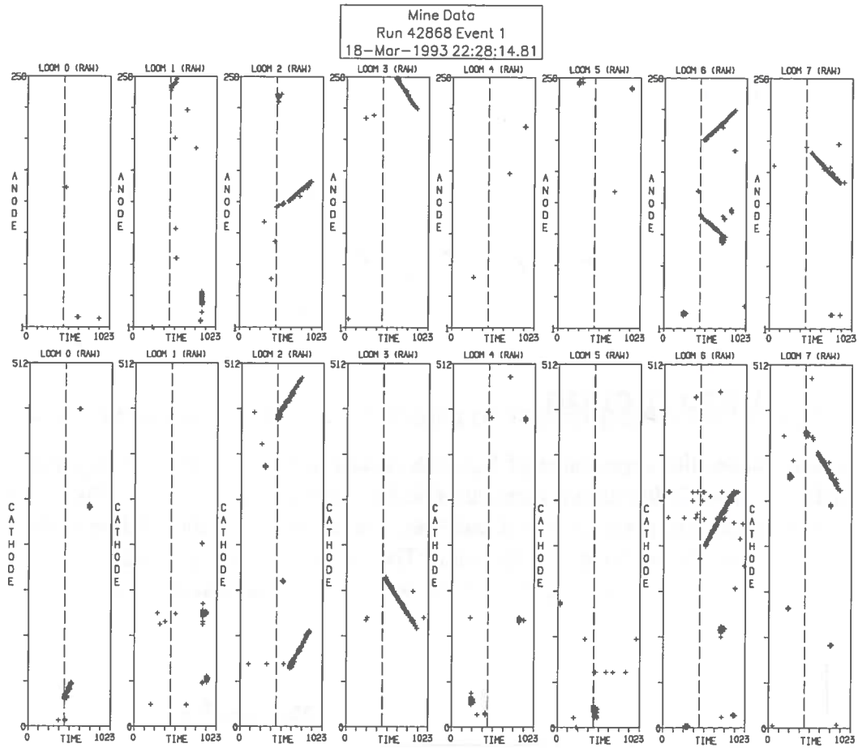


Figure 2.1: The raw anode-time and cathode-time data for a typical event containing a muon. The start of a pulse is marked by a + and plotted as a function of anode/cathode channel number and their location in the roller-RAM (time-tick number). The event T_0 is marked by the broken line. The track slopes differ in sign due to the different drift directions in the front and back of a detector modules.

To reconstruct the event we require other information about the event to replace the information we have lost as a consequence of multiplexing. For example, we might use the information that a muon makes a continuous track through the physical volume of the detector to deduce that the muon in Figure 2.1 passed through the cathode looms in the sequence: {0 2 3 6 7 2} (or its reverse).

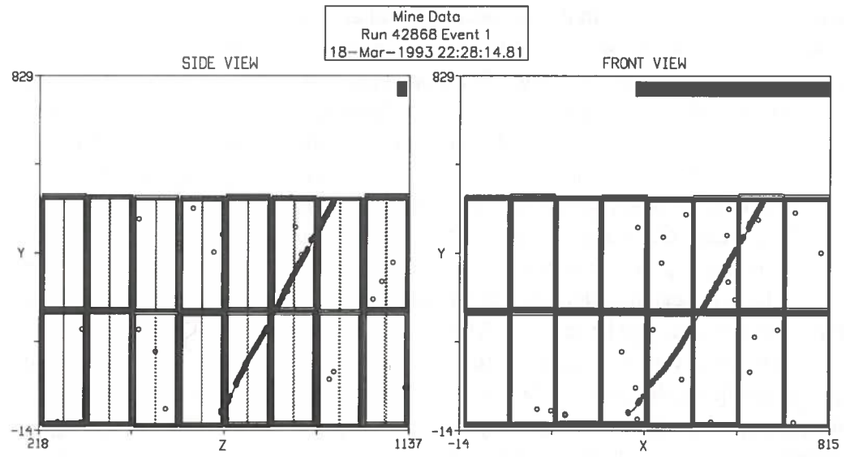


Figure 2.2: The yz and xy projections of the event of Figure 2.1, as reconstructed in the physical detector. Space points (i.e. hits localized in three dimensions) are shown by a ○, or a ● if they lie on a fitted track. In the top right of each picture the veto-shield module that the muon passed through is shown. The heavy rectangles illustrate the edges of the stacked modules.

Figure 2.2 shows two projections of the same event after it has been fully reconstructed. A polynomial curve fit has been made to the muon's trajectory. This is done by a processor, `TRAJEC`, that is not normally part of the off-line analysis, but which may be run while using `STING`[2], as may all of the off-line processors.

[2]The SOUDAN 2 Interactive Graphics program.

2.3 The Processing Required for Astronomical Analysis

The analysis chain required for muon astronomy may be separated into three distinct phases: firstly each event in the detector must be reconstructed to allow the muon's trajectory through the detector to be computed; then this trajectory must be transformed from the coordinate system associated with the detector to one stationary in space; and, finally an astronomical analysis may be performed.

Accurate timing is essential to transforming directions into a coordinate system that does not rotate with the Earth. For a detector with the resolution and exposure of SOUDAN 2, this coordinate system is sufficiently stationary in space to allow astronomical analysis. When the detector triggers, the instant in Central Standard Time at which the trigger occurred is recorded by reading C.S.T. into the D.A.Q. computer from the WWVB receiver. WWVB is a radio station that broadcasts C.S.T. from Ft. Collins, Colorado. If the WWVB time is not available the time from the system clock of the VAX performing D.A.Q. operations is substituted. The VAX's system clock is periodically checked to ensure it is synchronized with WWVB, and adjusted if it is found to be in error. Although there have been periods during which the WWVB clock was not available (mostly restricted to the the earlier data taking runs) a significant discrepancy between the free running VAX clock and WWVB was not present when the WWVB timing was restored[67]. The time of a trigger is converted to Greenwich Mean Sidereal Time using a subroutine, `CSTGMT`, based on a Duffet-Smith algorithm[34].

Two independent track reconstruction programs, `SEARCH` and `FMR` (described below), are run on the raw data read in after a trigger. Summary information, including run and event number, trigger time, and reconstructed track direction, is written to disk for each event and then this data combined into a compact d.s.t. known as a DMC file. One DMC file is written out for each calendar month of detector operation.

To transform data in the *natural* coordinate system of the detector into the equatorial coordinate system stationary in space with respect to the Earth[3], it is necessary to transform from detector coordinates to horizon coordinates (this involves a small rotation about the y-axis of the detector[60, 85]), from horizon coordinates to equatorial coordinates and from equatorial coordinates to celestial

[3]Referred to here as *celestial* coordinates to distinguish it from the coordinate system with the same orientation which co-rotates with the Earth.

coordinates. These transformations are done by subroutines: `TRLCDC`, `TRDCHC`, `TRHCEC`, and `TRECCC`. The latter two are adapted from algorithms given in reference [34]. The coordinate systems are described in Appendix B.

2.4 Muon Reconstruction by `FMR`

Of the two event reconstruction programs run on the raw data, the simplest is `FMR`. The processing done by `FMR`[4] is described fully elsewhere[85, 87]; only a simple overview of the program will be given here. A schematic diagram illustrating the processing required to reconstruct a muon's direction using `FMR` is shown in Figure 2.3 (on Page 18).

The processing is done by two programs. `FMR` itself performs a moment of inertia analysis (subroutine `MINA`) on the data in the logical coordinate space illustrated by Figure 2.1. Each logical loom is divided into boxes and the moments of inertia about the centre of mass of the hits in each box computed. Those boxes which are track-like — i.e. those in which one of the moments is larger than the other — are selected, and all others rejected as noise. This procedure is performed for both the anode-time and cathode-time data and the track-segments which result are matched by comparing the pulse shape (as a function of time) obtained by summing over all hits associated with the segment. Once A-T and C-T pulses are matched, the demultiplexing scheme is used to determine the location of each track segment in an ideal three dimensional detector — i.e. one in which the detector modules are all uniform in dimension and orientation.

Further processing is done by `PRESS`, a separate program which corrects `FMR` track-segments by:

i, correcting the geometry to the real detector geometry when the data was taken;

ii, correcting the drift velocity used by `FMR` to the correct value;

iii, performing a constrained fit on the three two-dimensional projections that may be made from the data; *and*

iv, combining track-segments to make a track for each muon present in the event.

[4]`FMR` is an acronym for Fast Muon Reconstructor.

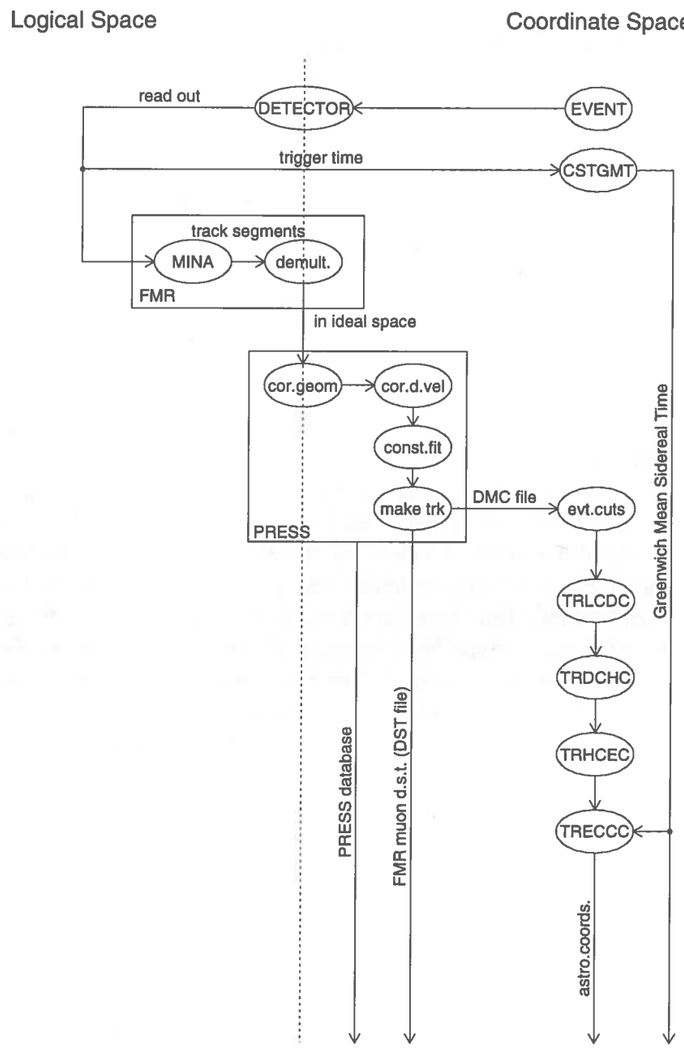


Figure 2.3: A schematic diagram illustrating the processing required to compute the celestial coordinates of a muon track using FMR.

Summary records for all events are written to an FMR muon d.s.t. (called a DST file) and also kept for the DMC file. In multi-muon events, only the track with the longest track-length is kept for the DMC file.

In addition, PRESS maintains a database of status information for each run it has processed. This database is later used to apply cuts which reject runs determined to have low quality. A program called SCRUBBER is run on the PRESS database to flag runs which fail the run-cuts. (These cuts are described in Reference [85] and in Section 2.8.1.)

2.5 Muon Reconstruction by SEARCH

The second event reconstruction program, SEARCH, is more complex than FMR, and uses and entirely different method. Again, only a brief overview will be given here, more details are given elsewhere[53, 54]. Figure 2.4 (on Page 20) shows a schematic diagram of the processing required to reconstruct a muon's direction using SEARCH.

SEARCH processing is done by three main subroutines: SEAR2, SECOML and SEART0. However, the program uses the output of other processors that are run on the data stream by SOAP. The raw data read out from the detector after triggers is packaged into raw pulses, labelled by a channel number and giving the *microstructure* of the pulse — i.e. the output of an A.D.C. as a function of time, by a processor called CREPLR. A processor, SOFTPL, is then run to correct this raw data for:

i, variation in the A.D.C. reference voltage settings;

ii, noise pulses;

iii, cathode strip crosstalk;

iv, long *tails* on pulses to due anode wire avalanche and the electronics response;

v, A.D.C. saturation;

vi, small pulses which have been split due to fluctuations taking some part of the pulse below the compactor threshold; *and*

vii, gain variation among the analogue electronics channels.

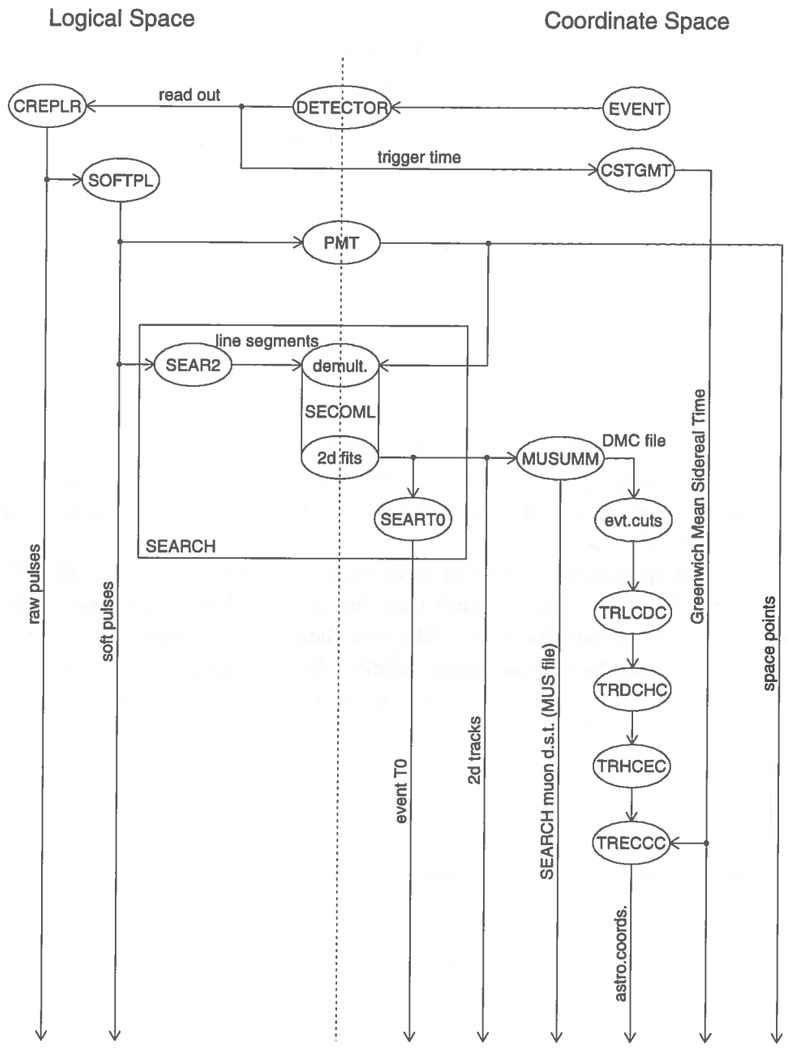


Figure 2.4: A schematic diagram illustrating the processing required to compute the celestial coordinates of a muon track using SEARCH.

The *soft* anode and cathode pulses created by SOFTPL are then matched by a processor called PMT. If a unique identification between an A-T and a C-T pulse may be established then the location of the tube hit that caused this pulse is determined in three dimensions — the drift time being used to supply the third dimension. PMT is never completely successful, but usually a large proportion of the hits on a muon may be matched.

SEAR2 looks for line-segments in single logical looms. It does this by a simple stringing algorithm: pairs of hits on separate channels are joined and the line joining them extrapolated; if another hit lies within a preset distance of the line it is added and the line re-fitted to the three points. This procedure is then repeated until no more hits are added, and until no more pairs of points are found (all possible pairs are considered).

The second processor in SEARCH, SECOML attempts to make tracks by joining line-segments together. Before it may try this, however, it demultiplexes the data and transforms it to the real detector geometry. SECOML follows two strategies to demultiplex the line-segments: if the line-segment contains points that were successfully matched by PMT, and the majority of the points on the line-segment lie in the same physical loom, then the track is assigned to that physical loom; otherwise line-segments are joined in all physical looms permitted by the demultiplexing scheme and those which give the lowest residuals accepted. After demultiplexing there is a unique correspondence between anode line-segments and cathode line-segments which defines the track in three dimensions. Finally, SEART0 is run to estimate the event T_0 (the time-tick at which the event occurred as distinct from the time at which the event triggered the detector).

At this stage the output of SEARCH is pairs of track slopes (called anode and cathode time-lines) in projective detector geometry. An additional subroutine, MUSUMM, was added to create records for a SEARCH muon d.s.t. (called an MUS file). It does this by assuming that all pairs of slopes represent a muon track and discards any unmatched line-segments. As with the FMR output, the record is also kept for the DMC file (in multi-muon events the record with the longest track-length is kept).

2.6 A Comparison of SEARCH and FMR

For most events containing a muon, both SEARCH and FMR will reconstruct a track. As the end user of the data we must decide which program to use. This decision

could be made easily if one program was obviously much better than the other and would be irrelevant if there were no difference between the programs. However this is not the case.

2.6.1 The Di-Muon Resolution

The resolution of the detector-reconstruction chain is usually measured by studying the distribution of the space-angle, ψ, between muon pairs in a multimuon event. Such coincident events are unlikely to have arisen by chance[5] and the angle between the two tracks will be dominated by the resolution of the detector[6]. Figure 2.5 shows an example of a multimuon event.

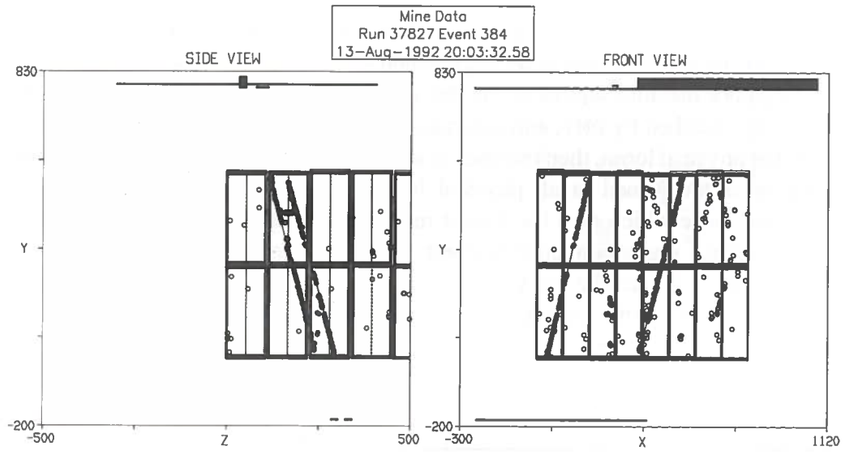


Figure 2.5: The yz and xy projections of di-muon event as reconstructed in the detector. Space points (i.e. hits localized in three dimensions) are shown by a ○, or a ● if they lie on a fitted track. The veto-shield modules that the muon passed through are shown. The heavy rectangles illustrate the edges of the stacked modules.

[5] Although this is a very small background.
[6] Multiple scattering in the rock overburden contributes $\sim 0.3°$[68].

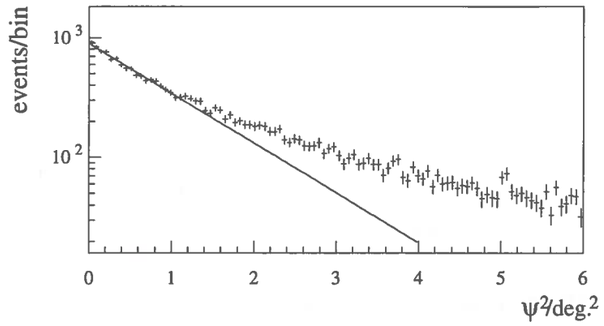


Figure 2.6: The space-angle squared, ψ^2, between muon pairs in events reconstructed by FMR.

The distribution of ψ for di-muons reconstructed by FMR is shown in Figure 2.6 and in Figure 2.7 for those reconstructed by SEARCH. These histograms are not made from the entire data sample available — FMR is less efficient at reconstructing both muons in a di-muon event, so subsets of the data were chosen to given samples of approximately the same size.

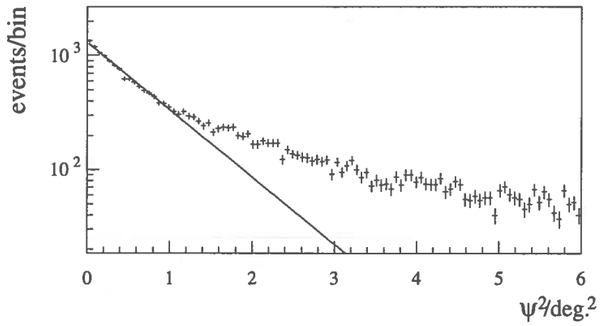


Figure 2.7: The space-angle squared, ψ^2, between muon pairs in events reconstructed by SEARCH.

In the region where $\psi^2 \lesssim (1°)^2$, the data has been fitted to the distribution expected from a Gaussian resolution of r.m.s. σ. i.e.

$$dF(\psi|\sigma) = \frac{1}{2\sigma^2} e^{-\psi^2/4\sigma^2} \psi \, d\psi \qquad (2.1)$$

The exponential includes a factor of $1/4\sigma^2$, and not $1/2\sigma^2$, as it represents the convolution of two independent distributions. From the figures we see that, although a Gaussian is reasonable for small angles, the di-muon space-angle distribution possesses a long tail. After Thomson[85] we allow for this tail by taking the resolution to be Gaussian with a resolution, σ, estimated from the 68th. percentile of the observed distribution. This procedure gives $0.77°$ for SEARCH and $0.88°$ for FMR. Given this difference of just $0.1°$ in the resolution of SEARCH and FMR, there is no clear preference for one program over the other.

2.6.2 Efficiency, Purity and Acceptance

In addition to resolution, the efficiency, purity[7], and acceptance of the two programs are useful figures of merit.

The efficiency and purity are measured by hand-scanning a sample of events that trigger the detector. By this procedure, the efficiency and purity of SEARCH are measured to be 98% and 99% respectively[49, 53]; for FMR they are measured to be 75% and 99%[85].

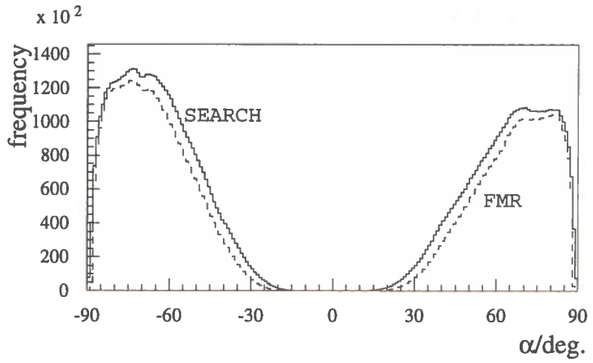


Figure 2.8: The distribution of the projected angle α for muon events reconstructed by SEARCH (solid line) and FMR (broken line).

The angular acceptance is an important quantity for astronomical work. Figures 2.8 and 2.9 show the distribution of events in the projected angles

[7]Where efficiency is defined to be the fraction of events containing a muon that the program is able to reconstruct; and, purity the fraction of reconstructed events that do contain a muon.

$\alpha = \tan^{-1} dy/dz$ and $\beta = \tan^{-1} dx/dz$. From the figures we see that the increased efficiency of SEARCH over FMR is restricted to the region $|\beta| \lesssim 15°$.

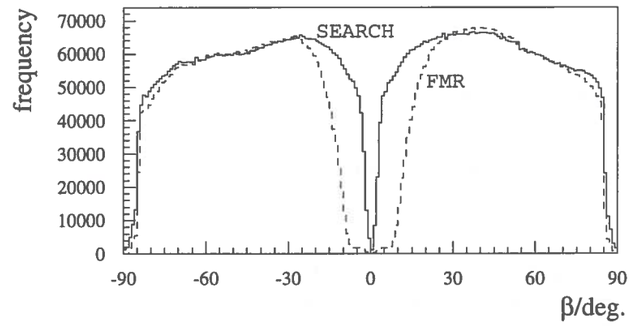


Figure 2.9: The distribution of the projected angle β for muon events reconstructed by SEARCH (solid line) and FMR (broken line).

2.6.3 The Consistency of SEARCH and FMR

As both SEARCH and FMR reconstruct a track for most events containing a muon, it is important to check whether the two programs are consistent. The data-set used in this thesis has been compiled from over four years of detector operation. From the start of data-taking to date, the SOUDAN 2 analysis software has been revised 18 times; in addition the detector database has also been changed many times. There has only ever been one version of FMR run on the data, so FMR provides a stable — if not necessarily the most accurate — picture of each event. The data has been processed under releases 13–16 of SEARCH (the early data was re-processed when release 13 of the software became available), and so the earlier data is likely to be less accurately reconstructed than the later data. In view of this, the test of consistency must take account of time (or, more accurately, run number).

Figure 2.10 shows a running average of the ratio of A-T and C-T slopes (actually $\tan\beta$ and $\tan\alpha$) as a function of run number. The ratio is SEARCH:FMR. The two plots are clearly different, but strongly correlated. They show strong systematic differences of $\sim$ 1–2% in addition to statistical fluctuations. The A-T plot shows a sharp "cliff" at run 35098 which is synchronous with the start of mine production running with release 16 of the software. After this feature, there is no systematic difference between the A-T and C-T ratios. None of the other features can be directly

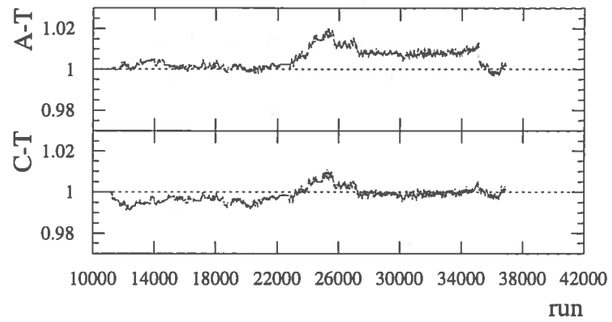


Figure 2.10: Running average slope ratios (SEARCH:FMR) for the data-set running. A point is plotted at the run number for every ten runs processed; each point represents an average over the previous $\sim$ 10000 events that contained both a SEARCH and an FMR muon.

associated with a software change. The correlation between the plots is probably due to errors associated with the drift-velocity. Both slopes are coupled to the drift-velocity by the equation $dz = v\,dt$, where v is the drift-velocity of electrons in a tube and dt is the drift-time of a pulse as measured in the detector electronics.

If the ratio of two slopes is $(1 + \delta)$, where δ is small, then the difference in the slopes is (for example):

$$\alpha' = \tan^{-1}\{(1+\delta)\tan\alpha\} \Rightarrow \alpha' - \alpha \simeq \tfrac{1}{2}\delta \sin 2\alpha \qquad (2.2)$$

where this equation has been derived by making a Taylor expansion about unity. Therefore a 1% error in slope is equivalent to a maximum angular shift of $\sim 0.3°$.

2.7 The DMC Data-Set

2.7.1 A Combined D.S.T.

Both SEARCH and FMR reconstruct muons for most events. Those reconstructions do not agree exactly and the angular acceptances of the programs differ — in particular SEARCH is able to reconstruct events where FMR fails. To accomodate these differences, astronomical analysis is done from the DMC file which summarizes the fits made by both programs for each event. This file is created by further

word	type	program	specification
0	I4		10000 × *run* + *event*
1	I4		b.c.d. trigger time
2	I4		WWVB time/centiseconds from midnight
3	I4	FMR	bits 00–03: estimated number of muons in event
			04–07: number of reconstructed muons in event
			08–15: index number of this muon
			16–23: number of track segments
			24–31: data-set number
4	I4		bits 00–09: track length in units of 2.5 cm
			10–20: summed anode pulse height/track length
			21–31: summed cathode pulse height/track length
5	I2		A-T angle (β) in units of 0.01°
	I2		C-T angle (α) in units of 0.01°
6	I4	SEARCH	bits 00–01: number of unmatched A-T slopes
			02–03: number of unmatched C-T slopes
			04–07: number of matched slopes (muons)
			08–12: index number of this muon
			13: matching flag (always set)
			14–23: no. of line segments modulo 1000
			24: uncontained by fid.vol. hits at start
			25: uncontained by fid.vol. hits at end
			26: start of track points to a crack
			27: end of track points to a crack
			28: start points to in-time shield hit
			29: end points to in-time shield hit
			30: start points to a shield hole
			31: end points to shield hole
7	I4		bits 00–09: track length in units of 2.5 cm
			10–20: summed anode pulse height/track length
			21–31: summed cathode pulse height/track length
8	I2		A-T angle (β) in units of 0.01°
	I2		C-T angle (α) in units of 0.01°
9	I2		A-C angle (γ) in units of 0.01°
	I2		date (yyyyyymmmmmddddd) year−1980
10	byte	FMR	number of tracks
	byte		event cut status (0=passed)
	byte	SEARCH	number of tracks
	byte		event cut status (0=passed)

Table 2.1: Specification of the DMC record.

compressing the information from each program's individual d.s.t., and writing a combined record per event. The record has the structure given in Table 2.1.

2.7.2 Procedure Adopted for Analysis of DMC Events

As the average resolution of SEARCH and FMR are roughly equivalent, but there are systematic differences between the programs which vary as a function of time, the analysis procedure implemented was chosen to rely mostly on FMR data. For all events that pass cuts[8], the FMR reconstruction was chosen if it existed. If it did not, and a SEARCH reconstruction was available for the same event, then SEARCH was used. This procedure relies on the stability of FMR, but exploits the greater efficiency of SEARCH for events on which FMR fails. The regions of (α, β) space where each program contributes data is shown in Figure 2.11.

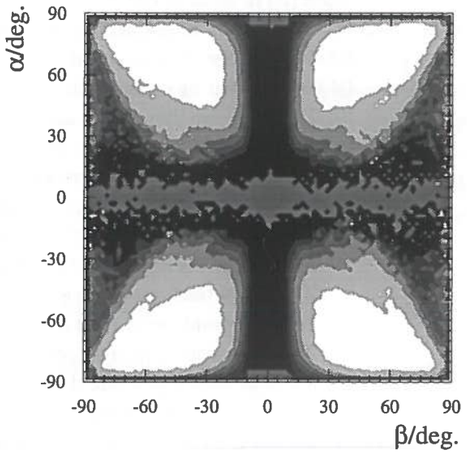


Figure 2.11: The proportion of events contributed by SEARCH and FMR as a function of projected angles (α, β). The contours (changes in shading intensity) are at: 75% FMR, 50%, 25%, 0, 25%, 50%, and 75% SEARCH. The light regions are where the FMR reconstruction is used for the majority of events and the dark regions for SEARCH.

Without an absolute calibration, it is impossible to measure the resolution of DMC events from the data itself. From Figure 2.10, the systematic error between SEARCH

[8]The cuts used are described in Section 2.8.

and FMR is taken to be 2% for the A-T slopes and 1% for the C-T slopes. These are the approximate absolute maxima. Using Equation 2.2 to convert these errors into angular shifts, and combining the angular shifts with the di-muon resolution in quadrature, would give a DMC single-muon resolution of

$$\sigma = \sqrt{(0.6°)^2 + (0.3°)^2 + (0.8°)^2} = 1.04°. \quad (2.3)$$

In this thesis, it is assumed that the DMC resolution is $\sim 1°$, although this value is not taken as precisely determined.

2.8 Characteristics of the Data-Set Analysed

In this section the characteristics of the data-set available for analysis, and the manner in which it is analysed, are described. The data-set is also described in Section 5.6.2.

2.8.1 Run and Event Cuts Applied to the Data-Set

The cuts applied to the data can be separated into two sets: run cuts and event cuts. The run cuts make use of the PRESS database, and were derived in relation to FMR alone — by their nature, however, we are able to apply them to all runs in the DMC data-set. Different event cuts are applied to the SEARCH and FMR reconstructions, and those events that fail flagged during the compilation of the DMC files.

For each run processed by SCRUBBER, the FMR muon rate is compared to two running averages: that of the previous 20 runs and that of the next 20 runs. The run is marked as bad in the PRESS database if the instantaneous rate differs by more than 2 s.d. from both average rates. When reading the DMC file, every time a new run is started the PRESS database entry for that run is checked. If the run was marked as bad then all events from that run are rejected. This procedure may be applied to both FMR and SEARCH data as anomalous detector running conditions — the likely cause of an excessive muon rate — will affect the reconstructed muon rate for both programs in the same way.

In addition to rejecting runs, data quality cuts are also applied to individual events. Similar cuts have been developed for each program[62, 85]. The SEARCH reconstruction of an event is rejected if any of the following are true:

i, the track length is less than 50 cm or over 24 m;

ii, $|dx/dz| < 0.203$ or $|dx/dz| > 11.43$;

iii, $|dy/dz| < 0.121$ or $|dy/dz| > 8.78$;

iv, the summed anode pulse height per unit track length < 30; *or*

v, the summed cathode pulse height per unit track length < 30.

For FMR reconstructions the cuts are the same with the exception of number (iii), which is not applied. These cuts are applied before the data is packed into the DMC record. With some 16 000 000 events before cuts, rounding errors during packing and unpacking of the data cause a very slight softening of the cut in distributions made from the combined d.s.t.

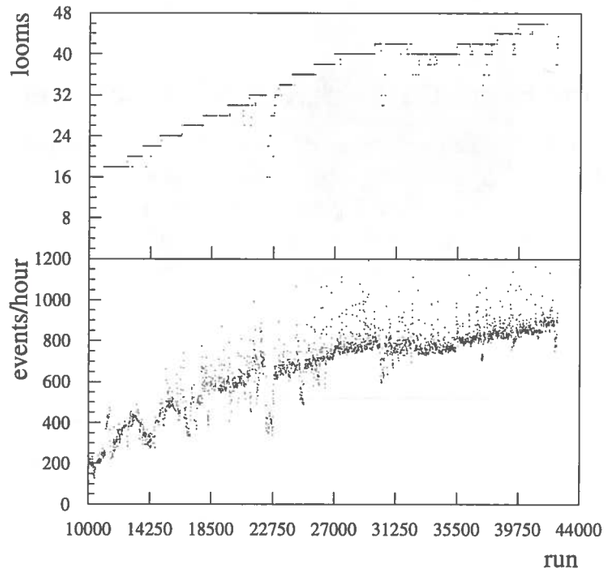


Figure 2.12: The number of active looms (upper plot) and the DMC event rate (lower plot) as a function of run number.

2.8.2 The DMC Data Analysed

The data-set used for analysis in this thesis includes all DMC events that pass the cuts described in Section 2.8.1 for the period January'89 to February'93 inclusive[9]. This data was sub-divided into a large and small data-set, as described in Section 5.6.2. After cuts, there were 10 679 432 events in the larger data-set and 3 258 904 in the smaller.

During this period the SOUDAN 2 detector was under construction in the Tower-Soudan mine. The modular nature of the detector allowed data taking during construction. Figure 2.12 (on Page 30) shows the number of active looms as a function of run number[10] and also the DMC event rate per run. The cosmic-ray background is a constant, so variations in event rate are due to: statistical fluctuations; anomalous detector operating conditions; *and*, changes in the surface area of the detector. The surface area is proportional to the number of active looms, as can be seen from the figure.

2.8.3 Distributions of Event Variable Distributions

In this section distributions of some basic event variables are discussed. The characteristics of the data are also discussed in Chapter 5.

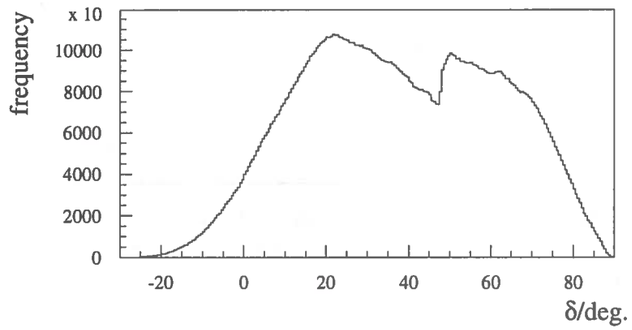


Figure 2.13: The distribution of the event declination, δ, for the entire DMC data-set studied.

[9]Files: `SM198901.DMC`–`SM199302.DMC`.

[10]A data-taking run is ended when a given quantity of data has been read out of the detector — therefore, the number of events/run decreases as the size of the detector increases.

Figure 2.13 shows the distribution of event declination, δ. The majority of the data lies between $-10°$ and $+80°$, with a peak at just over $+20°$. There is a sharp "step" in the data at $\sim 48°$. This is due to the projection of the reconstruction and trigger holes illustrated in Figure 5.1. The number of events goes to zero at low declination due to the attenuation of the muon flux in the rock overburden at increasing slant depths; it goes to zero at high declinations due to the collapse of the solid-angle $\cos\delta d\alpha d\delta$ as $\delta \to 90°$.

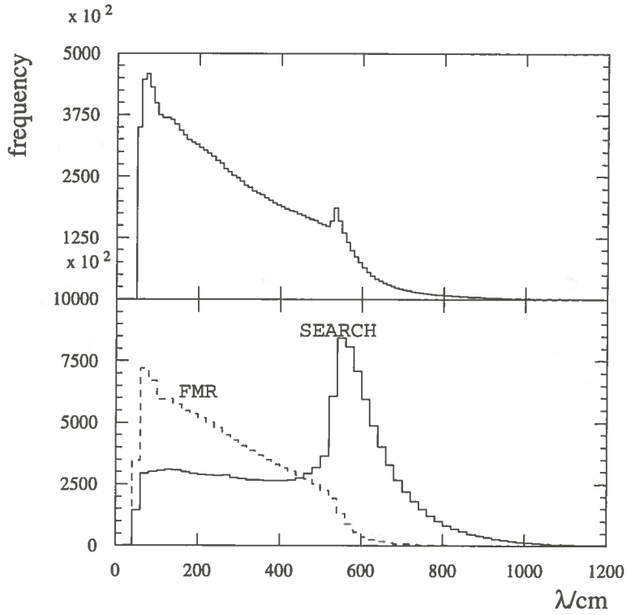


Figure 2.14: The distribution of the reconstructed track-length, λ, for the entire DMC data-set studied (upper plot) and the distribution of track-lengths as reconstructed by SEARCH and FMR (lower plot).

Figure 2.14 shows the distribution of track-lengths, λ. The data shows a distribution that peaks at the lowest track-lengths and steadily decreases as λ increases. There is a narrow peak visible at $\lambda \sim 550\,\text{cm}$. This structure can be attributed to SEARCH and FMR. SEARCH reconstructs track-lengths quite well, and shows a large peak at $\sim 550\,\text{cm}$. The majority of the muon flux is vertical and

the detector is $\sim 500\,\text{cm}$ tall; the peak is displaced from 500 cm by the interaction between the angular distribution of the flux, the phase-space accessible, and the efficiency of the reconstruction programs (it is difficult to reconstruct tracks that lie parallel to the detector axes in projective geometry). The FMR data favours smaller track-lengths — the manner in which FMR track-segments are combined causes track-segments with moments of inertia that disagree with the general direction, perhaps due to noise hits, to be dropped. This tends to result in short tracks.

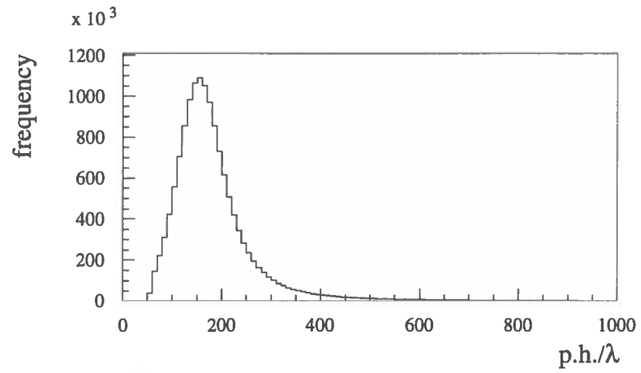


Figure 2.15: The distribution of the pulse-height per unit track length for the entire DMC data-set studied.

Figure 2.15 shows the distribution of the pulse-height per unit track-length, $(\text{a.p.h.} + 0.75 \times \text{c.p.h.})/\lambda$. This combination is chosen because the pulses read out from the anode and cathode channels, due to the same drifted charge, differ in size but have the same time profile. The distribution shows a peak at ~ 150 (arbitrary units) and a long tail which is caused by the detector response and Landau fluctuations of the charge deposited. The distribution is smooth, and shows no anomalous features.

CHAPTER 3

A STUDY OF THE EFFECT OF DETECTOR MISALIGNMENT AND THE COMPUTATION OF SOLAR & LUNAR COORDINATES

3.1 Introduction

In this and the following chapter a study is made of the alignment of the detector, using a search for the Solar and Lunar shadows in the background cosmic ray flux as a calibration signal. The effect of detector misalignment is considered and the accuracy of programs developed to compute the coordinates of the Sun and the Moon is verified. In the following chapter, the programs are used to search for the cosmic ray shadows of the Sun and the Moon in the entire DMC data-set.

3.2 The Effect of a Systematic Misalignment of the Detector Axes

3.2.1 Detector Alignment in Astronomy

If underground muon directions are to be used for an astronomical investigation, we must transform from coordinates moving with the Earth, and orientated with

respect to the detector, to celestial coordinates that have a constant orientation in space. (These coordinate systems are defined in Section B.1 and Reference [12].)

If we are to perform this complex transformation correctly we must know the location and orientation of the detector coordinate system on the surface of the Earth. Such measurements are best performed by the observation of reference stars, however no such reference exists for underground muons so we must rely on surveying and searches for subtle effects in the background muon flux.

3.2.2 The Motion of the Apparent Coordinates of a Source

If the actual detector axes are rotated by angles (ξ, υ, ζ) with respect to the xyz axes that are assumed to hold, the effect in celestial coordinates is to move the apparent coordinates of a source in a elliptical trajectory in the region of the nominal position. Thomson shows that, for small rotations, the shift is given by[83, 85]

$$\begin{aligned} d\alpha(h) &= -\xi \tan\delta \sin h \\ &\quad +\upsilon(\sin\lambda - \cos\lambda \tan\delta \cos h) \\ &\quad +\zeta(\cos\lambda + \sin\lambda \tan\delta \cos h) \\ d\delta(h) &= \xi \cos h - \upsilon \cos\lambda \sin h + \zeta \sin\lambda \sin h \end{aligned} \tag{3.1}$$

where the source has equatorial coordinates (h, δ) and λ is the latitude of the observer (47.8° for SOUDAN 2). Such an error can give rise to a systematic shift in the mean position in addition to the periodic motion about the mean position. It is interesting to note that, as $\lambda \approx 45°$ for SOUDAN 2, the only difference between the effect of rotations of the same sign about the y and z axes is the direction in which this ellipse is traced out.

3.2.3 The Effect on the Point Spread Function of the Detector

If we assume that the events from a source (or blocked by a shadow) arrive at random times, then the apparent p.s.f.[1] of the detector is the convolution of the hour angle distribution, $r(h)$, with the shifted p.s.f. i.e.

$$\text{psf}' = \int \text{psf}\{d\alpha(h), d\delta(h)\}\, r(h)\, dh \tag{3.2}$$

[1]The impulse response of the detector and analysis chain.

It is clearly impossible to evaluate this integral without *a priori* knowledge of the hour angle distribution of the events from the source. However, in the absence of such knowledge there are two sensible cases to consider:

i, the flux has the same hour angle distribution as the background; and,

ii, the flux has no hour angle dependence.

Convolution with the Hour Angle Distribution of the Background

The hour angle distribution of the background flux is a function of both hour angle and declination. Initially three bands of declination were studied: 0°, 30° and 60°. Figure 3.1 shows the hour angle distributions for those three bands. A monte carlo was written to evaluate the integral 3.2 numerically. 10 000 events were generated. For each generated event an hour angle was chosen randomly, using the empirical distributions as a model for the generator. The apparent shift, $d\alpha(h)$ and $d\delta(h)$, was then added to event coordinates generated to model a Gaussian p.s.f. with $\sigma = 1°$.

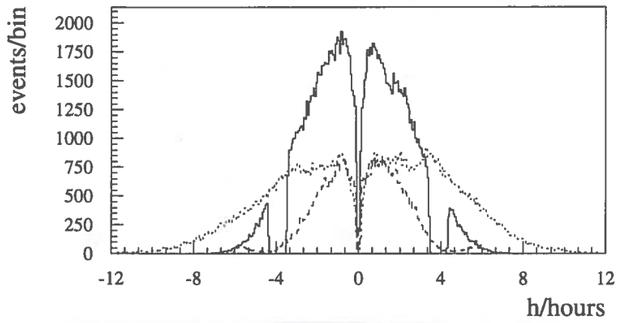


Figure 3.1: The hour angle (h) distribution of the background muon flux at declinations: 0°, broken line; 30° solid line; and, 60°, dotted line.

Figure 3.2 (on Page 38) shows the effect of a large (3°) rotation about the x, y, and z axes of the detector for the three declinations. At the lower declinations, the effect is essentially a systematic shift in the mean source position. This occurs for rotations about all three axes, despite the fact that for rotations about the x axis $\{d\alpha(h), d\delta(h)\}$ has mean zero, and is due to both the systematic shifts of Equation 3.1 and the non-uniformity of $r(h)$ as illustrated by Figure 3.1. At high declinations, the p.s.f. is clearly showing large scale structure. The oscillatory motion of the nominal p.s.f.

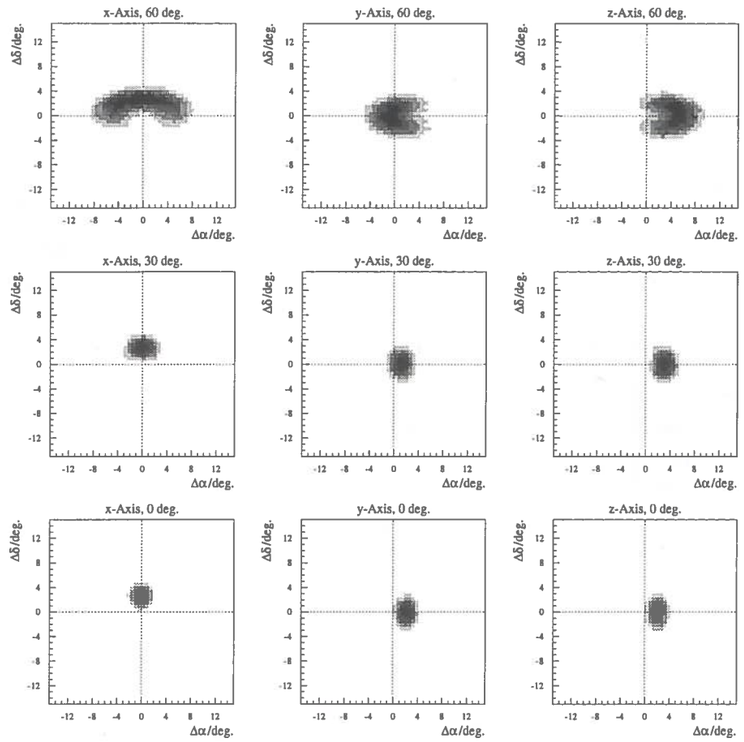


Figure 3.2: The effect on the nominal p.s.f. of a 3° rotation about the x, y, and z-axes of the detector. The source has been assumed to have the hour angle distribution of the background and to have declinations 0°, 30°, and 60°.

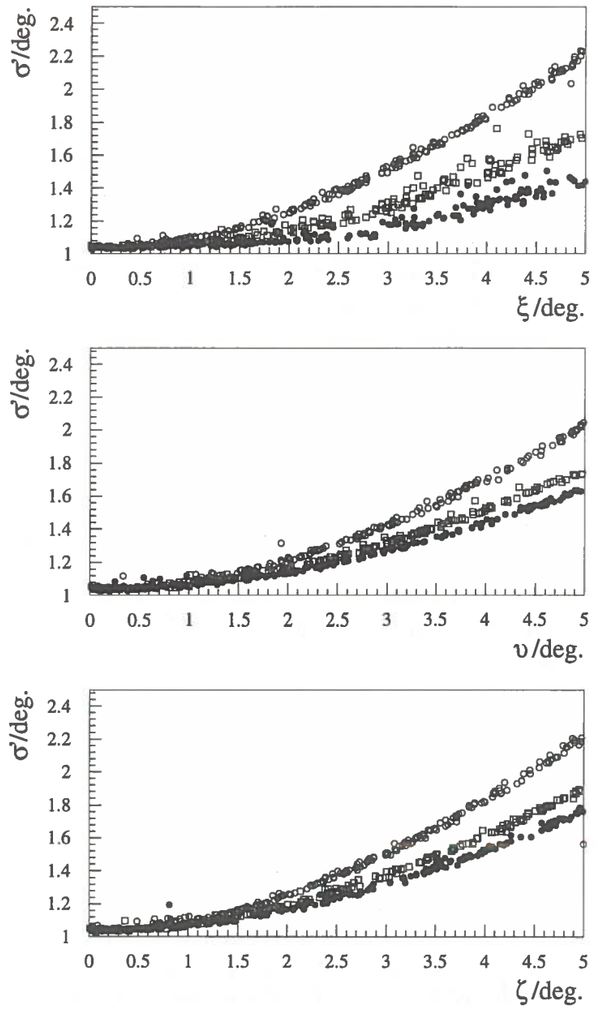


Figure 3.3: The dependence of the r.m.s. of the apparent p.s.f., σ', on the angle on rotation about the x, y and z-axes (ξ, υ and ζ). The source has been assumed to have the hour angle distribution of the background and to have declinations: 0° (•), 30° (▫), and 40° (○).

is accentuated by the distortion ($\propto \sec\delta$) of the coordinate system as we approach the pole.

Fit to the Apparent Point Spread Function

If two Gaussian p.s.f.s are separated by less than $\sim 2\sigma$, where σ is the r.m.s. of the Gaussian, the two sources are unresolved. Similarly, if the r.m.s. displacement of the source position is less than $\sim 2\sigma$ the motion of the mean source position will be unresolved, and the apparent p.s.f. will merely be wider than the nominal p.s.f. (and shifted with respect to it). This phenomenon is illustrated in Figure 3.2.

We therefore attempt to approximate the apparent p.s.f., in this limit, by a displaced Gaussian with a larger width. i.e.

$$\mathrm{psf}'(d\alpha, d\delta|\delta) \approx \frac{1}{2\pi\sigma'^2\cos\delta}\exp -\frac{(d\alpha - d\alpha')^2\cos^2\delta + (d\delta - d\delta')^2}{2\sigma'^2} \qquad (3.3)$$

where σ' and $(d\alpha', d\delta')$ are adjusted to fit the apparent p.s.f. The approximation was studied by fitting Equation 3.3 to the distribution after each iteration of the monte carlo discussed above. Figure 3.3 (on Page 39) shows the functional dependence of σ' on the angles (ξ, υ, ζ).

The fitted value of σ' increases smoothly from 1° as the angle of rotation is increased. This indicates that the approximation is probably reasonable for rotations of up to $\sim$ 3–5° and declinations $\delta \lesssim 40°$. Declinations of 0°, 10°, 20°, 30°, 40° and 50° were considered. The fits at 50° and non-trivial rotation angles (i.e. $\gtrsim 0.5°$) failed with very large values of χ^2, indicating that the model was a very bad match to the data.

Misalignment with a Flat Hour Angle Distribution

The analysis of the previous section was then repeated with $r(h)$ taken to be a constant. This is the distribution we would expect for a very weakly interacting parent particle, such as a neutrino. Figure 3.4 (on Page 41) shows the effect of a large (3°) rotation for events with a flat hour angle distribution.

There is a marked difference between the shapes illustrated in Figure 3.4 and those of Figure 3.2. At low declinations the density of the apparent p.s.f. is that characteristic of the harmonic oscillation $d\delta(h)$, as the $\tan\delta$ dependence in $d\alpha(h)$ reduces this term to a constant. At larger declinations the elliptical motion of the source centre dominates.

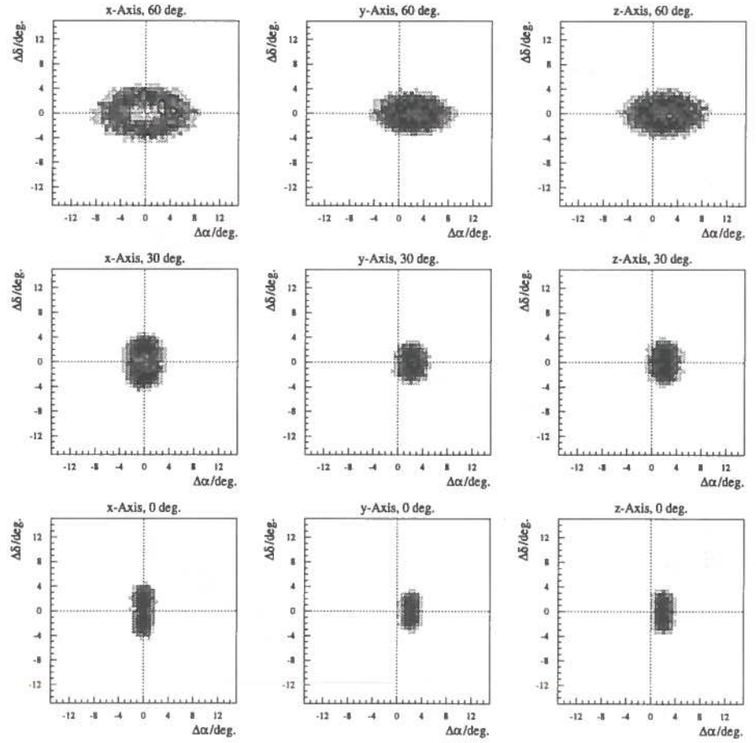


Figure 3.4: The effect on the nominal p.s.f. of a 3° rotation about the x, y, and z-axes of the detector. The source has been assumed to have a flat hour angle distribution and to have declinations 0°, 30°, and 60°.

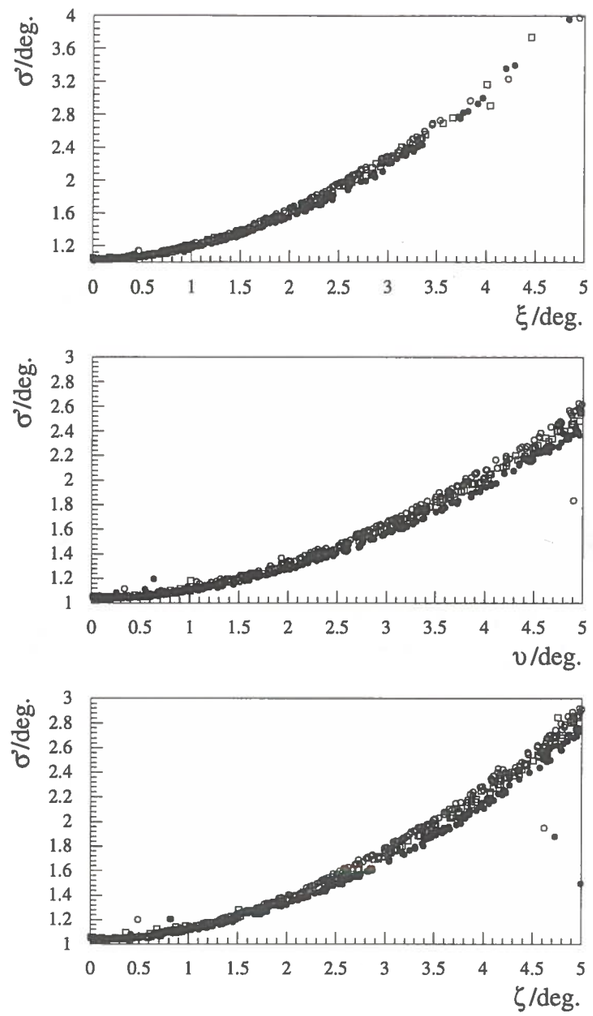


Figure 3.5: The dependence of the r.m.s. of the apparent p.s.f., σ', on the angle on rotation about the x, y and z-axes (ξ, υ and ζ). The source has been assumed to have a flat hour angle distribution and to have declinations: 0° (•), 30° (▫), and 40° (○).

Figure 3.5 (on Page 42) shows the dependence of the fitted resolution, σ', on rotation angle for this hour angle distribution. The obvious difference between Figure 3.3 and Figure 3.5 is that, in the latter, there is little dependence of σ' on the declination of the source. This is probably because the shape of the apparent p.s.f. is dominated by the term $d\delta(h)$, which has mean zero irrespective of the declination. Most fits for $\xi \gtrsim 3.5°$ failed; for these rotations the apparent p.s.f. is annular — a Gaussian is a very bad description of this.

3.3 Current Status of the Detector Alignment

The detector alignment of the SOUDAN 2 detector has been studied previously. However, none of these studies have used an astronomical object for direct calibration. The results of two of the studies made previously are summarized below.

3.3.1 Alignment Using the Rock Overburden

Mark Thomson used the attenuation of the underground muon flux by the rock overburden to study the detector alignment[85]. A map of the surface topology was digitized and used to make a model of the expected muon flux as a function of altitude and azimuth. There were a number of systematic problems with this study:

i, the local rock density is not constant and, due to mining, may fluctuate rapidly; *and*

ii, the surface topology is dominated by an East-West ridge.

There were found to be angular regions where the model of the muon rate disagreed strongly with the observed flux, due to the non-uniform rock density. These regions had to be eliminated from the study. After this was done, the orientation could only be accurately determined for rotations about the y (vertical) axis, due to (ii).

The result of the study was an estimate of the angle, υ, of rotation of the main detector with respect to the North direction. It was found that:

$$\upsilon = (0.4 \pm 1.1)° \text{ West of North.} \tag{3.4}$$

3.3.2 Gyrotheodolite Surveying of the Detector

A gyrotheodolite is a Foucalt gyrocompass rigidly attached to a theodolite. The Foucalt gyrocompass aligns itself perpendicular to the local gravitational field and the direction of motion of the theodolite. Thus, if the theodolite is stationary on the surface of the Earth[2], it will point to true-North (the spin-axis of the planet in space). This device may, therefore, be used to survey the underground detector with respect to true-North.

The surveying[60] was done in two stages: firstly, the orientation of the main detector was surveyed underground; then, the gyrotheodolite was taken above ground and used to measure the coordinates of the Sun (twice) and of stars α UMi and α UMa. (In addition the coordinates of stars α Lyr, α Boo, α Vir, and the planet Jupiter were measured earlier with a gyro. that had unbalanced torques in its suspension fibre and so had a systematic error in its pointing direction.)

The result of this work was that:

i, the "North" axis of the detector coordinate system lies 0.24° West of North; *and*

ii, the software used to perform astronomical transformations is sufficiently accurate for useful work.

3.3.3 The Current Status of the Alignment

The correction obtained in Section 3.3.2 has been included in the transformation software used to project the trajectory of an underground muon back to the celestial sphere. In this thesis it will be assumed that the orientation of the detector is known to an accuracy of ~ 0.1–$0.2°$. The alignment studies described in this thesis must then been viewed in the following context: does the data require us to reject the null hypothesis, H_0, that the detector is correctly aligned?

3.4 Drift-Velocity Errors and their Effect on the Accuracy of Reconstruction

If the incorrect drift-velocity is used when reconstructing track directions there will be a systematic error in the slopes used to project the tracks back to the celestial

[2]Assuming there are no major anomalies in the local gravitational field.

sphere. Thomson shows that if the drift velocity is in error by some fraction, f, then the apparent shift of a source's celestial coordinates will be[83, 85]

$$\begin{aligned} d\alpha(h)/° &= f(0.43 - 0.55\cos h)\sin h \\ d\delta(h)/° &= f(0.22 - 0.07\cos h - 0.27\cos^2 h). \end{aligned} \tag{3.5}$$

His comparison of the directions reconstructed for muons in the main detector with directions computed from *in-time* veto-shield hits showed that the error on the drift-velocity was probably $f \lesssim 1\%$ — and so these effects should be negligible in comparison to the resolution.

3.5 Use of the Solar and Lunar Shadows to Verify Alignment

As noted in Section 3.3, although studies of the alignment of the SOUDAN 2 detector have been made these studies have never included the direct observation of an astronomical object in underground muon data. The observation of the shadow cast in the primary cosmic ray flux by the Solar and Lunar discs (by stopping primaries in the Solar/Lunar mass), first suggested by Clark[24], is a useful test, and is becoming a standard method of calibration for cosmic ray experiments with a large angular acceptance and good angular resolution[55].

The advantages of this test are that:

i, the test is directly sensitive to the single-muon resolution (i.e. the real resolution applicable to underground muon signals); specifically, it is sensitive to systematic errors, such as rotations, that effectively increase the resolution (see Section 3.2.3) but which cannot be observed in the di-muon space-angle;

ii, the test allows the determination of the orientation of the detector;

iii, the test uses the entire data analysis path applicable to searches for underground muon signals;

iv, only conventional physics is involved in the phenomenon.

For a shadow to be visible we require that

i, the magnetic deflection of charged particles; *and*

ii, the deflection between the primary and secondary cosmic rays;

both be sufficiently small that the image of the shadow is not destroyed.

The magnitude of the magnetic deflection angle, due to (i), should be of the same order as the ratio of the gyroradius of the particle to its path length in the field. The gyroradius is given by p[GeV/c] $= 0.3B$[T]r[m] for a uniform field of flux-density B[2]. For a ~ 1 TeV particle in the Earth's magnetic field (around $20\,\mu$T on the surface[51]) the gyroradius is $\sim 170\,000$ km. The atmosphere extends for approximately 20 km above the surface of the Earth, and so the magnetic deflection angle should be of order $20/170\,000 \simeq 0.01°$ for the secondary muons, which is clearly negligible.

The magnetic deflection of the cosmic ray primaries in the interplanetary magnetic fields is much more complicated to evaluate. A measurement of the Solar shadow by the Tibet air-shower array[6] suggests that the effect may be to shift the position of the image in the sky. However, such a phenomenon has not been observed by other groups[55].

The order of magnitude of the deflection between the muon and the parent proton can be safely neglected. The muon has an energy at production of $\gtrsim 1$ TeV; the transverse momentum of the parent pion is ~ 0.3 GeV/c; and that of the muon in the decay of the pion is ~ 0.03 GeV/c[68]. Clearly, the muon-proton angle will be $\lesssim 0.02°$.

As the angular radii of the Sun and Moon are $\theta_0 \approx 0.25°$, and θ_0^2 is an order of magnitude less than σ^2, the shadow cast in the cosmic ray flux will differ only slightly from that cast by a point sink.

3.6 The Motions of the Sun and Moon

3.6.1 The Real Motion of the Sun and Moon

The starting point of any calculation of the motion of the Sun and the Earth through the celestial sphere must be a consideration of their real motion through the Solar System.

The Motion of the Moon through the Solar System

The motion of the Moon about the Earth is exceedingly complicated. Although, from the view point of the Earth, we may naively expect the Moon's motions to be

essentially those of a body in orbit about the Earth the gravitational attraction of the Moon to the Sun exceeds that to the Earth by the factor

$$\frac{M_\odot}{d_\odot^2} \Big/ \frac{M_\oplus}{d_\oplus^2} \simeq 2.15, \tag{3.6}$$

where the mass of the Sun $M_\odot = 1.989 \times 10^{30}$ kg, the mass of the Earth $M_\oplus = 5.987 \times 10^{24}$ kg, the Moon-Sun distance $d_\odot = 1.496 \times 10^{11}$ m and the Earth-Moon distance $d_\oplus = 3.844 \times 10^8$ m[12]. Mean values have been taken for the distances.

It is the fact that this ratio is close to unity that makes the motion of the Moon complicated, as neither the Sun nor the Earth can be neglected to first approximation. The Moon's trajectory through the Solar System is essentially an orbit around the Sun with a mean radius equal to that of the Earth but with this motion heavily perturbed by the Earth. The perturbation introduces an oscillatory motion about the mean orbit and ensures that both bodies have approximately the same anomaly[3] at all times. The orbits of the Earth and the Moon, projected onto the ecliptic plane, are illustrated in Figure 3.6.

The Motion of the Sun through the Solar System

The motion of the Sun through the Solar System is much simpler to model that that of the Moon. As the Solar System contains many members the Sun will not remain at rest at the barycentre[4] but will move about this point.

Considering Jupiter, which is the second heaviest body in the Solar System and an order of magnitude heavier than the third — Saturn, and the Sun alone, Thomson[83] calculates the barycentre to be 7.7×10^8 m from the centre of the Sun. The equatorial radius of the Sun is 6.960×10^8 m[12] and so the barycentre lies just 6% of a Solar radius outside the Sun itself.

The sidereal period of Jupiter is 11.86 years and so, during the 4 years of data taking, there will be a shift in the position of the Sun due to the motion of the barycentre. We expect this shift to be of the same order as the Solar radius, although the effect of the other planets will probably be to reduce this distance.

[3] When describing elliptical motion in a plane the angular coordinate is referred to as the *anomaly*. The *mean anomaly* is the angle swept out by a fictitious body moving in a circular orbit with the same period as the real body and the *true anomaly* is the angle swept out by body during the real motion.

[4] The centre of mass of the system.

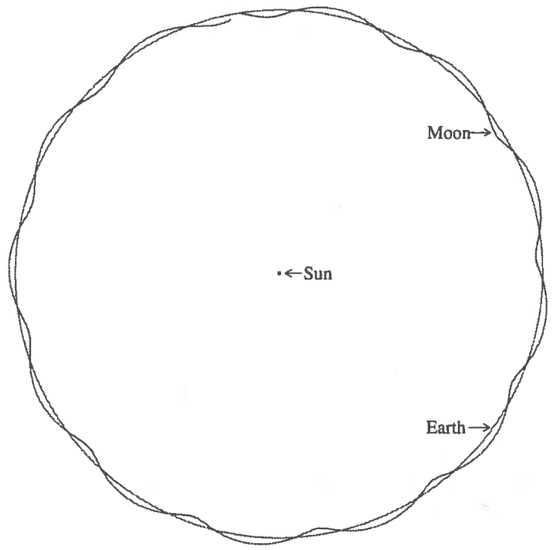


Figure 3.6: The projection onto the plane of the ecliptic of the orbits of the Earth and Moon about the Sun during the calendar year 1992. The eccentricity of the orbit is to scale, but the Earth–Moon distance has been multiplied by a factor of 10 for clarity.

3.6.2 The Apparent Motion of the Sun and Moon

The motion of the Sun and Moon relative to the Earth or, more precisely, relative to a particular point, the observing site, on the surface of the Earth are what we must compute before we can search for the cosmic ray shadows cast by either object. To compute this *apparent* motion from the real motion of the objects through the Solar System we must apply a number of corrections[34].

The first correction is to allow for the flight time of the cosmic ray primaries that just avoid being stopped by the body in question. For the Sun this is $\sim 8^m$ and for the Moon $\sim 1^s$ (the mean Lunar distance is 1.28 light-seconds). Since the Earth is rotating at around $15'$ (of arc) per minute this could give rise to an error of order $2°$ for the Sun. Fortunately, however, the goal of most astronomical (and

all navigational) calculations of the coordinates of the Sun and Moon is to compute where the bodies are observed to be at any given time, not where they physically are. This correction, which is essentially a shift in the time origin, is implicit in the formulae used.

A second correction is to allow for the geocentric parallax that arises when translating coordinates referred to the centre of the Earth to coordinates used at the observing site. This is discussed in Section 3.6.2 below.

Another correction made in optical astronomy, but which is not required here, is to correct for the refraction of an optical photon's path as it passes through the atmosphere. Such a coherent interaction between a highly energetic cosmic ray and the atmosphere is unlikely.

Correction of Geocentric Coordinates to Topocentric Coordinates

Astronomical observations are made in a *topocentric* coordinate system. This system is obtained from the normal geocentric coordinate system, which provides a natural and convenient reference system, by parallel transporting the origin of the coordinate system from the centre of the Earth to the observing site. The effect of such a transformation on remote objects, such as the fixed stars, is negligible however, for a nearby object, it can cause a small (but significant) shift in the apparent position of the body — i.e. it gives rise to parallax.

The order of magnitude of the parallax shift due to this transformation can be estimated by examining the effect when the body is in transit. This is illustrated in Figure 3.7 where: δ is the geocentric declination; ω is the topocentric declination;

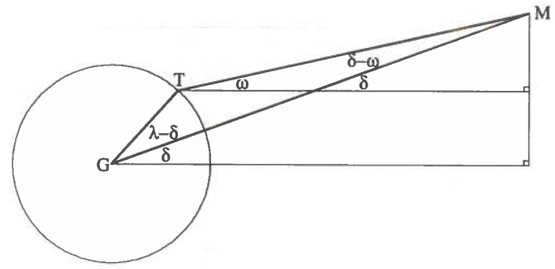


Figure 3.7: The geocentric parallax of a nearby body in transit.

and, λ is the latitude of the observing site. Consider $\triangle GTM$: using the sine and cosine rules we find that

$$\sin^2(\omega - \delta) = \frac{r^2 \sin^2(\lambda - \delta)}{r^2 + R^2 - 2rR\cos(\lambda - \delta)} \tag{3.7}$$

where $r = GT$ and $R = GM$.

This effect will clearly be most significant for the closest body studied — the Moon. Taking $r \sim 6400$ km, $R \sim 4 \times 10^5$ km, $\delta \sim 20°$ and the latitude of the Tower-Soudan mine to be $47.82°$ we have a shift $\omega - \delta \sim 0.4°$, which should be taken into account. For the Sun $R \sim 1.5 \times 10^8$ km so $\omega - \delta \sim 4''$ and the effect can be safely neglected. (This estimate should approximately equal half the *horizontal parallax* of the body (see Section 3.7.1). The Astronomical Almanac gives $\sim 55'$ for the horizontal parallax of the Moon and $\sim 8''$ for the horizontal parallax of the Sun[12], in agreement with the above estimates.)

For the full three-dimensional calculation a considerable simplification results from using vector notation. Since

$$\overrightarrow{GM} = \overrightarrow{GT} + \overrightarrow{TM} \Rightarrow \begin{pmatrix} x \\ y \\ z \end{pmatrix} = R \begin{pmatrix} \cos\delta\cos\alpha \\ \cos\delta\sin\alpha \\ \sin\delta \end{pmatrix} - r \begin{pmatrix} \cos\lambda\cos t \\ \cos\lambda\sin t \\ \sin\lambda \end{pmatrix} \tag{3.8}$$

where (α, δ) are the geocentric coordinates of the body and t is the local sidereal time of the observation. The topocentric coordinates are then given by

$$(\alpha', \delta') = (\tan^{-1} y/x, \sin^{-1} z/\sqrt{x^2 + y^2 + z^2}). \tag{3.9}$$

The Apparent Motion in Topocentric Coordinates

The apparent large scale motion of both the Sun and the Moon, as viewed from the Earth, is an approximately circular orbit about the Earth in a plane inclined at about $23.5°$ (the *obliquity of the ecliptic*) for the Sun and around $25°$ for the Moon. Such motion can be parameterized as

$$(\alpha, \delta) \sim (\omega t, \delta_0 \sin \omega t) \tag{3.10}$$

and is illustrated in Figure 3.8.

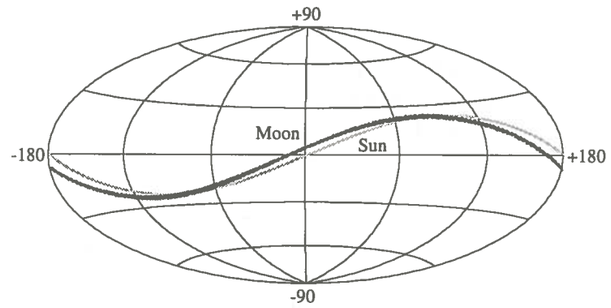


Figure 3.8: The apparent motion of the Sun and Moon in topocentric coordinates during 1992. The coordinates were computed at five equally spaced points for each day of 1992. This includes one Solar cycle and thirteen Lunar cycles. The more complex motion of the Moon is shown by the slight thickening of its trajectory on the sphere.

3.7 Computation of the Trajectories of the Sun and the Moon

The coordinates of the Sun and Moon, as a function of time, are computed using two FORTRAN programs: MOON and SUN1. This section discusses those programs and assesses their reliability by direct comparison with coordinates tabulated in the Astronomical Almanac.

3.7.1 The Program MOON

Quantities Computed by the Program

The trajectory of the Moon is computed as a function of Julian date by the program MOON. The geocentric Right Ascension and declination, and the horizontal parallax[5], must be computed if one wishes to locate the Moon in three dimensions relative to the centre of the Earth. The construction of a *Lunar Theory* sufficiently accurate

[5]The horizontal parallax of the Moon is the angle subtended at the Moon by the equatorial radius of the Earth.

that it may be compared with observations is one of the most difficult problems in celestial mechanics[74]. (Nevertheless, it is possible to compute an ephemeris[6] for the Moon with sufficient accuracy to land on it!)

In the algorithm (taken from Duffet-Smith[34]) a 53 term harmonic series is used to compute the geocentric ecliptic longitude, a 47 term series for the latitude, and 31 for the horizontal parallax.

The Principal Terms

Few of the terms in the harmonic series used arise from one perturbation or phenomenon alone, and so the identification of the physical origin of all the terms is impractical. However, the origin of a few of most significant terms can be identified.

The largest term in the series for the Moon's longitude is

$$6°17'19.5'' \sin M, \tag{3.11}$$

where M the mean anomaly of the Moon, and arises from the first term of the solution to Kepler's equation for elliptical motion, the *equation of centre*. A second term, called the *evection*,

$$1°16'26.45'' \sin(2D - M) \tag{3.12}$$

is introduced by periodic variation of the eccentricity of the Moon's orbit. Here D is the *mean elongation*, which is the angle between the position vector of the Sun and the the position vector of the Moon.

The Error in Determination of Coordinates

To determine the errors in the determination of coordinates by the program, the coordinates (geocentric Right Ascension, declination and horizontal parallax) of the Moon were computed at 0 U.T. on the first fifty days of 1993 (i.e. 0th. January to the 18th. February inclusive) and compared with the coordinates as listed in the Astronomical Almanac for the same times[12]. The almanac quotes Right Ascension to 0.1^s of time[7] ($1.5''$ of arc), declination to $1''$ of arc and horizontal parallax to $0.01''$ of arc. The error discussed below will be defined in the sense: *computed value minus tabulated value*.

[6] A table in which a quantity is tabulated as a function of time.

[7] It is usual to quote Right Ascension in hours, minutes and seconds rather than degrees, minutes and seconds.

The Error in Right Ascension

Figure 3.9 shows a histogram of the scatter of the error in Right Ascension. There is a systematic shift of $\sim -20''$ of arc and a scatter about that shift of $\sim 4''$. To obtain a better estimate of these quantities a Gaussian was fitted to the data. The fit has χ^2/d.o.f. of $6.78/14$ which is good — although the statistic will probably not

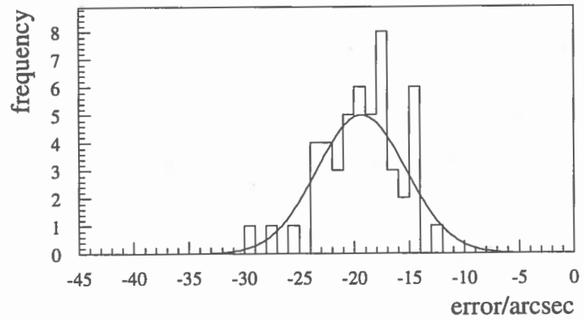


Figure 3.9: The distribution of the error in geocentric Right Ascension of the Moon for the first fifty days of 1993.

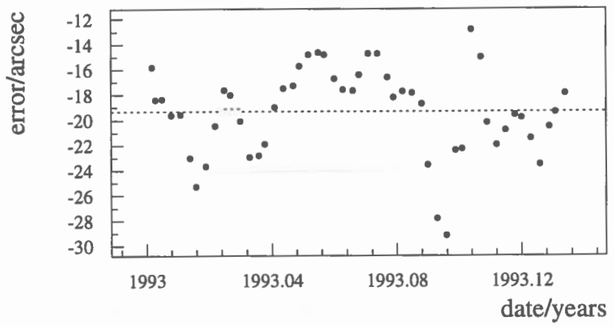


Figure 3.10: The dependence of the error in geocentric Right Ascension on the date for which the coordinates where computed for the first fifty days of 1993. The date is quoted in decimal years. The mean is indicated by the dotted line.

be exactly distributed as χ^2 due to the low statistics of data. The result of the fit is

$$\begin{aligned} \hat{\mu} &= -19.34 \pm 0.87 \\ \hat{\sigma} &= 4.04 \pm 0.89. \end{aligned} \tag{3.13}$$

The dependence of the error on the time for which the coordinates were computed is shown in Figure 3.10. This shows some evidence of a periodic dependence of the error on time. In the earlier data there is also evidence for the second harmonic of this basic period. If this is the case then the estimate of the r.m.s. of the distribution computed by fitting a Gaussian (above) will probably be an overestimate.

The Error in Declination

The error in the declination, shown in Figure 3.11, has a flatter and slightly broader distribution than that of the error in Right Ascension. Again there is a systematic shift, however this time it is smaller than the width of the distribution and positive in sign. No attempt was made to fit the distribution; its sample mean and r.m.s. are

$$\begin{aligned} \text{mean} &= 0.64 \\ \text{r.m.s.} &= 5.35. \end{aligned} \tag{3.14}$$

Figure 3.11: The distribution of the error in geocentric declination of the Moon for the first fifty days of 1993.

The origin of this distribution is immediately obvious from Figure 3.12, which shows the error as a function of time. There is a strong periodic dependence, although there seems to be a glitch at around 1993.1 (5th. February).

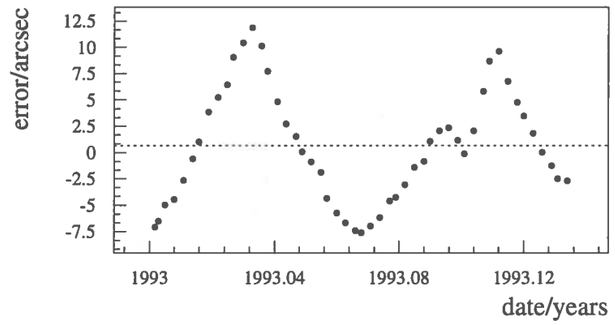


Figure 3.12: The dependence of the error in geocentric declination on the date for which the coordinates where computed for the first fifty days of 1993. The date is quoted in decimal years. The mean is indicated by the dotted line.

The Error in Horizontal Parallax

The error in the horizontal parallax of the Moon is an order of magnitude smaller than the errors in Right Ascension and in declination. There is no evidence for a systematic shift. As in Section 3.7.1 the mean and r.m.s. error were estimated by fitting a Gaussian. The fit is also good (χ^2/d.o.f. $= 8.45/14$), although the same caveat must apply when considering the distribution of the statistic. The result of

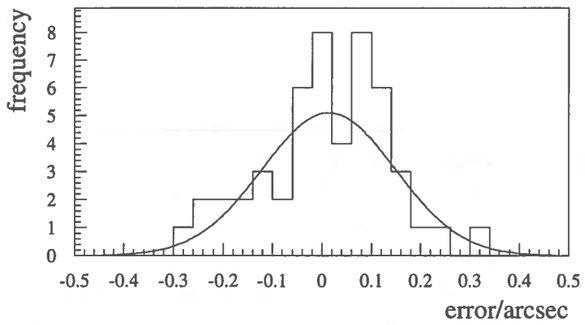


Figure 3.13: The distribution of the error in geocentric horizontal parallax of the Moon for the first fifty days of 1993.

the fit is

$$\begin{aligned} \hat{\mu} &= 0.014 \pm 0.022 \\ \hat{\sigma} &= 0.134 \pm 0.021. \end{aligned} \tag{3.15}$$

It is not obvious from Figure 3.14 that there is a periodicity in the error at the same frequency as that seen in Figure 3.12, although there may be periodicity at the second harmonic of this frequency.

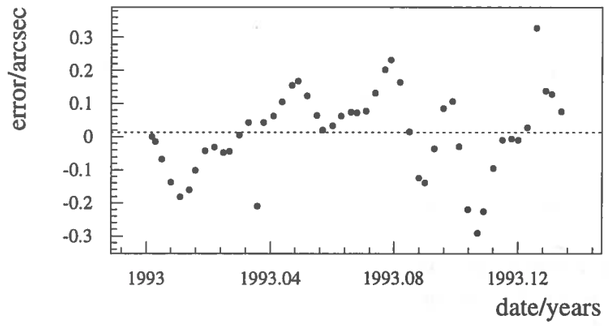


Figure 3.14: The dependence of the error in geocentric horizontal parallax on the date for which the coordinates where computed for the first fifty days of 1993. The date is quoted in decimal years. The mean is indicated by the dotted line.

Overview of the Errors

The agreement of the coordinates as calculated by `MOON` for the first fifty days of 1993 with the coordinates from the Astronomic Almanac is excellent, and far exceeds the accuracy necessary to locate the Moon's shadow in a detector with a resolution of around a degree.

To put these errors in perspective we can consider the size of the region of space that the program places the centre of the Moon in. The horizontal parallax is related to the Earth-Moon distance by

$$r \sin \pi_h = R_\oplus \tag{3.16}$$

where π_h is the parallax, r is the Earth-Moon distance and $R_\oplus$ is the equatorial radius of the Earth[12]. The element of volume due to an error $(d\pi_h, d\alpha, d\delta)$ is

$$d^3\mathbf{r} = R_\oplus^3 \text{cosec}^3 \pi_h \cot \pi_h \cos \delta \, d\pi_h d\alpha d\delta \tag{3.17}$$

Taking the error to be $(0.13'', 4.04'', 5.35')$, $R = 6378$ km, $\delta \sim 20°$ and $\pi_h \sim 57'$ the element of volume is $62\,000\,\text{km}^3$ which is 2×10^{-6} times the volume of the Moon (the Moon's equatorial radius is 1738 km).

The systematic error in Right Ascension of $-19''$ is the angle subtended by 2% of the Moon's radius at the Moon's mean distance. In principle it can be corrected for, however as it is $\sim 0.5\%$ of the resolution this correction has been treated as negligible.

The covariance matrix for the errors is

$$\begin{pmatrix} 0.016 & 0.046 & -0.236 \\ & 19.51 & -7.869 \\ & & 28.65 \end{pmatrix} \tag{3.18}$$

where the columns are in the order (π_h, α, δ) and the units are $(\text{arcsec})^2$.

3.7.2 The Program `SUN1`

Quantities Computed by the Program

The coordinates of the Sun as a function of Julian date are computed by the program `SUN1`. This is a much simpler algorithm than that used by `MOON`. Given the accuracy required, and that the geocentric parallax of the Sun is almost constant at approximately $8''$, this coordinate need not be computed. Therefore just the geocentric Right Ascension and declination of the Sun are computed.

The Algorithm

The algorithm used[62] is much simpler than that used for the Moon. The mean anomaly, M, is computed from the Julian date and this is used to compute the ecliptic longitude of the Sun. Assuming that the obliquity of the ecliptic is constant and that the Solar latitude is zero, this is then converted into celestial coordinates.

The Error in Determination of Coordinates

The errors were determined by computation of the geocentric Right Ascension and declination for the same instances as for the Moon (see Section 3.7.1). The almanac tabulates Right Ascension to 0.01^s of time and declination to $0.1''$ of arc.

The Error in Right Ascension

Figure 3.15 shows the error in Right Ascension as a function of time. There is clear evidence for a systematic shift and a harmonic dependence of the error on time. The data were fitted to

$$a_0 + a_1 \sin 2\pi(t - \tau_1)/T_1 \tag{3.19}$$

by a simple least-squares method. Figure 3.16 shows the distribution of residuals after this fit. The parameters of the fit are determined to be

$$\begin{aligned} a_0 &= 12.185 \text{ arcsec} \\ a_1 &= 6.729 \text{ arcsec} \\ \tau_1 &= 1993.0 \text{ years} \\ T_1 &= 0.8 \text{ years.} \end{aligned} \tag{3.20}$$

The error is clearly dominated by the harmonic term and not random error. The period of 0.8 years is just less than one month.

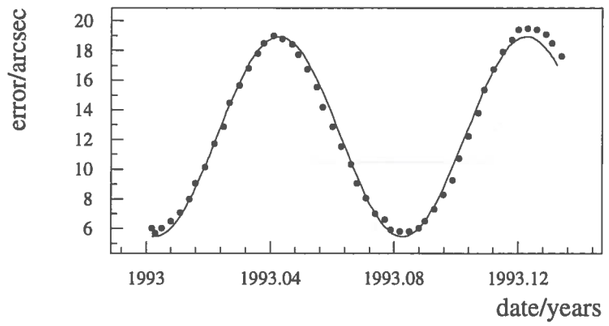


Figure 3.15: The dependence of the error in geocentric Right Ascension on the date for which the coordinates where computed for the first fifty days of 1993. The date is quoted in decimal years.

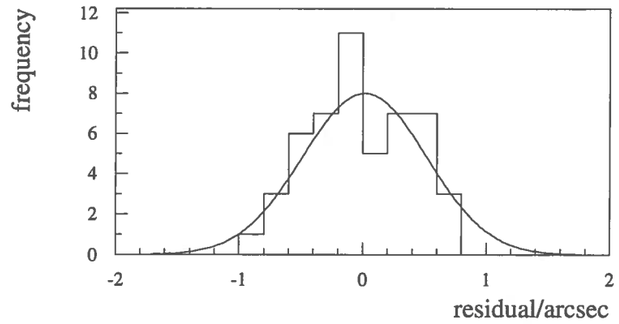


Figure 3.16: The distribution of residuals for the fit of the error in Solar geocentric Right Ascension to a simple harmonic function. The curve is a fitted Gaussian with mean $\hat{\mu} = 0.01$ and r.m.s. $\hat{\sigma} = 0.50$.

The Error in Declination

The error in declination also shows a strong harmonic dependence on time. However, in this case the mean displacement (i.e. the function onto which the periodic motion is superposed) seems to increase with time. This could be due to a real secular error however, as the intercept of the mean displacement appears to be $\sim$ 1993.0 and the expression for the declination of the Sun is itself a truncated

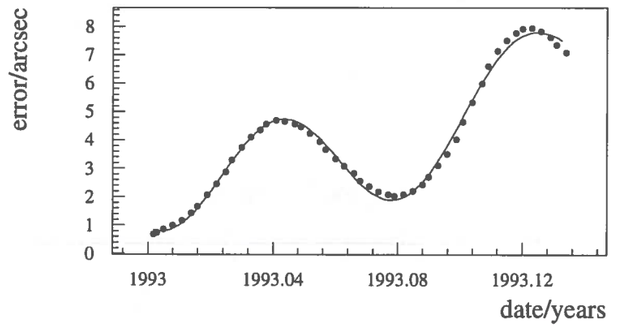


Figure 3.17: The dependence of the error in geocentric declination on the date for which the coordinates where computed for the first fifty days of 1993. The date is quoted in decimal years.

harmonic series, it seems more likely that the mean displacement is itself a longer period oscillation.

This hypothesis was tested by computing the Solar declination for a further fifty days, six months later than the first set. Figure 3.18 shows both data sets and the fitted function. Table 3.1 shows the coefficients computed for a fit to

$$a_0 + a_1 \sin 2\pi(t - \tau_1)/T_1 + a_2 \sin 2\pi(t - \tau_2)/T_2 + a_3 \sin 2\pi(t - \tau_3)/T_3. \quad (3.21)$$

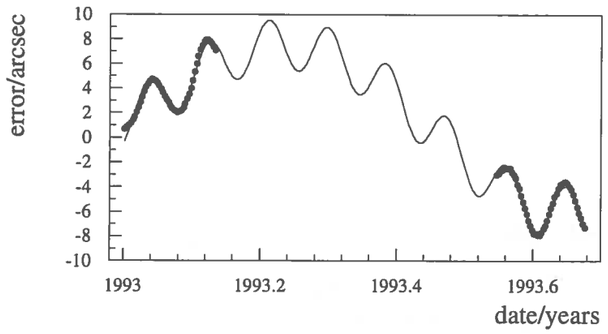


Figure 3.18: The dependence of the error in geocentric declination on the date for which the coordinates where computed for two sets of fifty days during 1993. The date is quoted in decimal years.

n	a_n	τ_n	T_n
0	11.74		
1	2.088	1993.0	0.087
2	7.463	1993.0	0.866
3	−12.391	1995.6	2.953

Table 3.1: Coefficients for the fit of the error in declination to a third order harmonic series.

The distribution of the residuals from this fit is shown in Figure 3.19. As for the Right Ascension, it is clear that the error is dominated by the harmonic term. So that there was reasonable agreement between the data and the fit it was necessary to introduce the long period term, the phase of which is such that its minimum occurs during 1993.

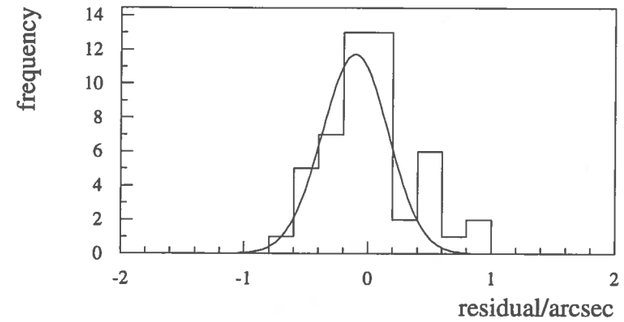


Figure 3.19: The distribution of residuals for the fit of the error in Solar geocentric declination to an harmonic series. The curve is a fitted Gaussian with mean $\hat{\mu} = -0.11$ and r.m.s. $\hat{\sigma} = 0.30$.

Overview of the Errors

Unlike the errors on the coordinates of the Moon, which show a roughly equal mixture of periodic variation and random error (see Section 3.7.1 above), the errors on the coordinates of the Sun are dominated by periodic variation. An accurate *Solar Theory* would require a the use of a large harmonic series for the coordinates, as the Lunar Theory does, whereas the algorithm used has truncated this series after the first few terms. Such truncation would give rise to an error that is mostly due to the first few neglected terms. This seems to be the case for `SUN1`.

3.8 Verification of Program Accuracy by Computation of the Times of Solar and Lunar Eclipses

The analysis of Section 3.7 suggests that the error in the coordinates of the Sun and the Moon are typically less than $\sim 20''$, although if we accept the harmonic series of Section 3.7.2 then the maximum error in declination we should expect is $\sim 35''$ (which occurs during 1992).

For simplicity the analysis concentrated on the coordinates evaluated for a single, arbitrarily chosen, group of dates. Ideally one should take a large and random sample of dates, distributed over the entire period 1989–1993, however such a procedure

is impractical and prone to error (since the "correct" data had to be transcribed by hand from the almanac for analysis).

The computation of the times of Solar and Lunar eclipses allows us to test the underlying systematics of both MOON and SUN1 when used together over the entire period of the data. The times of eclipses, although not truly random[8], are arbitrary and fixed by external physical factors.

3.8.1 Eclipses of the Sun and of the Moon

Eclipses of the Sun occur when the Moon lies between the Sun and the Earth in such a manner that Surface of the Earth intercepts the shadow of the Moon. Eclipses of the Moon occur when the Earth lies between the Sun and the Moon. They do not occur frequently because the plane of the Moon's orbit lies approximately 5° out of the plane of the ecliptic[9] and the bodies must be aligned in three dimensions for an eclipse to occur. Figure 3.20 illustrates this geometry.

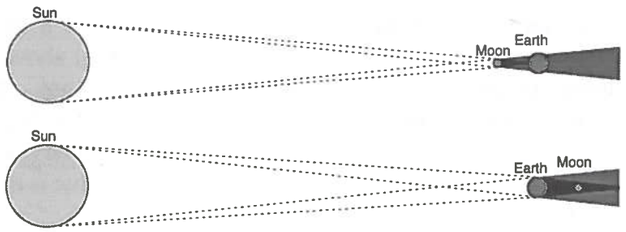


Figure 3.20: A simple illustration of the geometry of the Earth-Sun-Moon system during a Solar (top) and Lunar (bottom) eclipse. Not to scale.

The programs are not sufficiently accurate to compute the locus of the totality on the surface of the Earth. For the 23 eclipses that occur in the period 1989–1993, we shall just compute the time of the geocentric conjunction or opposition (defined as when the Sun and Moon have equal or opposite Right Ascensions) and the coordinates of both bodies at such times.

[8]There is in fact an 18 year and 10–11 day periodicity of the Earth-Moon-Sun system known as the *Saros*. This has been known for around 2500 years. Given an observed 18 year ephemeris the times of phenomena such as eclipses can be predicted with a reasonable accuracy.

[9]The plane of the Earth's orbit about the Sun.

3.8.2 Computation of Eclipse Times and Coordinates for 1989–1993

The Method of Location of Eclipses

For a conjunction or opposition as defined above, the time of an eclipse is the solution of

$$\begin{aligned} \alpha_\odot(t) - \alpha_M(t) &= 0 \text{ for conjunction,} \\ \alpha_\odot(t) - \alpha_M(t) &= 180^\circ \text{ for opposition.} \end{aligned} \tag{3.22}$$

The root of Equation 3.22 was computed using a simple interval bisection algorithm. Once a root was found, the coordinates of the Sun and Moon were computed at that time.

Table of Eclipses for the Period 1989–1993

The Julian date and Solar and Lunar coordinates for the eclipses studied are listed in Table 3.2 (on Page 65).

Comparison with the Almanac

The errors (*computed minus tabulated*) on the time of the geocentric conjunction or opposition and the coordinates of the Sun and Moon are shown in Table 3.3 (on Page 66). The data has the matrix of correlation coefficients given in Equation 3.23. The columns have the same order as the columns of Table 3.3.

$$\begin{pmatrix} 1 & 0.849 & 0.851 & 0.289 & 0.018 \\ & 1 & 1.000 & 0.505 & 0.035 \\ & & 1 & 0.503 & 0.031 \\ & & & 1 & -0.021 \\ & & & & 1 \end{pmatrix} \tag{3.23}$$

As we would expect, the error in the Right Ascension of the Sun and of the Moon are completely correlated, and are very strongly correlated with the error in the Julian date of the eclipse. This is not surprising as there is a direct connection between time and Right Ascension due to the rotation of the Earth. From Table 3.3, we note a systematic decrease in the error in the declination with time. This is illustrated in Figure 3.21, and is probably a periodic rather than secular variation.

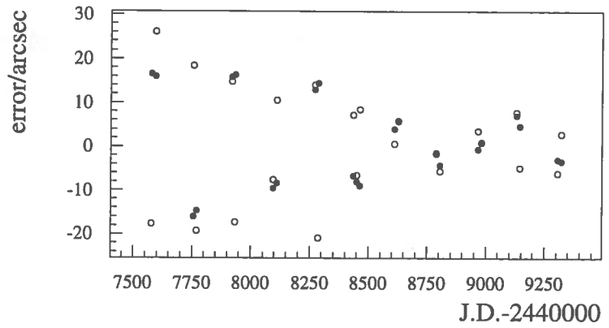


Figure 3.21: The systematic dependence of the error in the declination of the Sun (filled circles) and the Moon (hollow circles) of the Julian date of the conjunction or opposition.

Overall, this confirms the result of Section 3.7 for a much wider range of times: that the error in the coordinates of the Sun and of the Moon are at all times less than $1'$ of arc. There are systematic shifts of order $20''$, and systematic dependence of the errors on time, however these effects can be probably be neglected with reasonable confidence.

Body	Julian Date	R.A.	declination	
		Sun/Moon	Sun	Moon
		1989		
Moon	2447578.13742	$22/10^h15^m52.520^s$	$-10°46'28.60''$	$+11°04'21.20''$
Sun	2447593.29794	$23^h12^m52.752^s$	$-5°03'32.51''$	$-3°47'12.44''$
Moon	2447755.62553	$9/21^h46^m00.798^s$	$+13°27'30.32''$	$-13°37'19.39''$
Sun	2447769.77990	$10^h38^m03.726^s$	$+8°37'43.03''$	$+7°24'01.99''$
		1990		
Sun	2447918.28604	$20^h35^m48.671^s$	$-18°38'04.46''$	$-19°35'42.53''$
Moon	2447932.31393	$21/9^h32^m45.272^s$	$-14°33'51.73''$	$+14°07'56.13''$
Sun	2448094.60885	$8^h04^m47.193^s$	$+20°21'00.70''$	$+21°08'12.44''$
Moon	2448110.11242	$9/21^h05^m23.303^s$	$+16°39'47.89''$	$-16°00'50.39''$
		1991		
Sun	2448272.48854	$19^h49^m09.501^s$	$-21°04'25.58''$	$-21°19'54.65''$
Moon	2448286.77949	$20/8^h49^m14.562^s$	$-17°46'42.84''$	$+16°37'26.86''$
Moon	2448434.61945	$6/18^h21^m44.470^s$	$+23°20'49.48''$	$-24°37'26.26''$
Sun	2448449.29592	$7^h22^m12.791^s$	$+22°05'48.50''$	$+22°05'32.75''$
Moon	2448464.29589	$8/20^h22^m24.052^s$	$+19°25'13.36''$	$-18°02'47.70''$
Moon	2448611.93327	$17/5^h55^m50.389^s$	$-23°26'13.76''$	$+24°25'43.95''$
		1992		
Sun	2448626.46856	$19^h00^m11.859^s$	$-22°43'10.39''$	$-22°20'39.72''$
Moon	2448788.70337	$5/17^h35^m20.235^s$	$+23°19'08.68''$	$-23°54'00.16''$
Sun	2448804.01623	$6^h38^m57.402^s$	$+23°08'17.09''$	$+22°22'19.96''$
Moon	2448966.48870	$17/5^h08^m34.398^s$	$-22°54'48.21''$	$+23°13'09.62''$
Sun	2448980.53136	$18^h10^m44.453^s$	$-23°25'00.08''$	$-22°24'45.87''$
		1993		
Sun	2449129.10678	$3^h53^m32.177^s$	$+20°15'51.72''$	$+21°19'49.89''$
Moon	2449143.04173	$4/16^h50^m12.257^s$	$+22°28'11.84''$	$-22°18'38.71''$
Sun	2449305.41889	$15^h16^m29.895^s$	$-18°09'00.13''$	$-19°12'49.49''$
Moon	2449320.76597	$16/4^h20^m53.887^s$	$-21°29'11.12''$	$+21°07'02.30''$

Table 3.2: The Solar and Lunar eclipses studied to verify the accuracy of the computation of Solar and Lunar coordinates for the years 1989–1993. The Right Ascension and declination are the geocentric coordinates at the time of the geocentric conjunction or opposition. The data were taken from [8, 9, 10, 11, 12].

J.D.	ΔJ.D.	$\Delta\alpha/''$		$\Delta\delta/''$	
		Sun	Moon	Sun	Moon
2447578.13742	$2^m14.86^s$	27.60	27.24	16.42	−17.66
2447593.29794	$2^m12.26^s$	34.02	33.30	15.80	26.07
2447755.62553	$2^m11.27^s$	26.19	26.19	−16.10	18.30
2447769.77990	$2^m22.31^s$	25.47	25.47	−14.63	−19.23
2447918.28604	$2^m12.97^s$	28.48	28.46	15.74	14.75
2447932.31393	$2^m20.42^s$	27.96	27.96	16.23	16.23
2448094.60885	$1^m23.95^s$	6.71	6.71	−9.59	−7.59
2448110.11242	$1^m36.22^s$	4.34	4.34	−8.36	10.57
2448272.48854	$2^m37.39^s$	33.53	33.53	12.93	13.96
2448286.77949	$2^m16.57^s$	29.97	29.97	14.35	−20.84
2448434.61945	$2^m03.88^s$	19.70	19.83	−6.80	7.17
2448449.29592	$1^m48.07^s$	16.58	16.22	−8.16	−6.63
2448464.29589	$2^m00.17^s$	14.70	14.70	−9.03	8.40
2448611.93327	$2^m02.13^s$	19.24	19.14	3.94	0.63
2448626.46856	$2^m02.04^s$	16.88	16.88	5.70	5.78
2448788.70337	$2^m15.78^s$	27.46	27.46	−1.36	−1.60
2448804.01623	$2^m23.15^s$	29.57	29.14	−4.21	−5.62
2448966.48870	$1^m54.72^s$	17.55	17.48	−0.61	3.57
2448980.53136	$1^m50.15^s$	16.13	15.41	0.93	0.87
2449129.10678	$2^m29.13^s$	30.96	30.49	7.03	7.76
2449143.04173	$2^m10.36^s$	30.56	30.56	4.66	−4.89
2449305.41889	$1^m23.69^s$	4.82	5.18	−3.07	6.09
2449320.76597	$1^m38.83^s$	6.02	6.02	−3.41	2.82
mean	$2^m03.93^s$	21.50	21.38	1.23	0.57
s.d.	32.97^s	10.55	10.46	10.36	12.40

Table 3.3: The error between the computed times and coordinates and the data of Table 3.2.

CHAPTER 4

SEARCH FOR THE COSMIC RAY SHADOWS CAST BY THE SUN AND THE MOON

4.1 Introduction

In this chapter the results of searches for the shadow cast in the cosmic ray flux by the Solar and Lunar discs, using the programs discussed in Chapter 3, are presented. The entire DMC data-set available for analysis was used.

4.2 Variation of the Shadow Depth as a Function of Event Coordinate Rotation

The principal alignment errors considered in this section are small rotations (ξ, υ, ζ) about the (x, y, z) axes of the horizon coordinate system. Although only two angles need be considered (since a direction is completely specified relative to some set of axes by just two angles) it is more convenient to use three angles. When the angles are small, the rotation matrices $\{R_i(\theta)\}$ approximately commute. Our aim is to ask whether the data is consistent with the assumption that the detector is correctly aligned. On the assumption that this hypothesis, H_0, is true, the angles (ξ, υ, ζ) are more convenient to deal with than the Euler angles (α, β, γ).

The Data Set Analysed

The data set analysed for the shadow search was the DMC files (i.e. SEARCH and FMR) for the period: 1st. January, 1989, to 28th. February, 1993. The horizon coordinates (a, A) of the muon, and of the Sun or Moon at the time of the trigger (and an identifying flag to label the event as a *Solar muon* or *Lunar muon* — i.e. one near either object), for all muons within 20° of either the Sun or Moon, were extracted from the main data set and written to a separate file. The coordinates of the Moon were expressed in the topocentric system. The normal cuts and event selection criteria for DMC files were used.

There were 274329 events within 20° of the Sun and 376048 within 20° of the Moon. Fewer events were found near the Sun due to the smaller proportion of live-time during which the Sun is *visible* in the detector.[1] Figure 4.1 shows the distribution of trigger times in Central Standard Time.

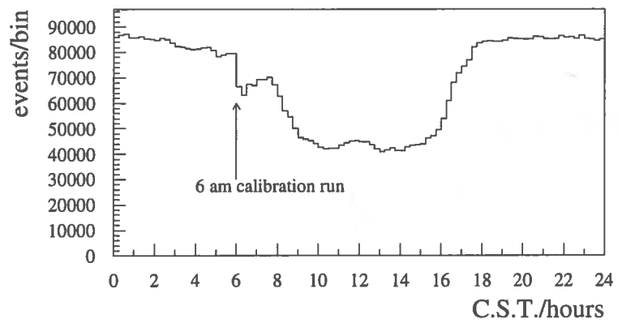


Figure 4.1: The distribution of event trigger times as a function of Central Standard Time.

Analysis Method

To perform the analysis a MINUIT[48] job was written. The program stored the muon (a_μ, A_μ) and object (a_o, A_o) coordinates in an array. For a given set of angles,

[1] During the day, when muons with coordinates near the Sun have the least rock to pass through between production in the atmosphere and the detector underground, maintenance or construction work is frequently done on the detector.

and Gaussian resolution σ, the coordinates of the events were rotated using

$$\begin{pmatrix} x \\ y \\ z \end{pmatrix} = R_z(\zeta)R_y(\upsilon)R_x(\xi) \begin{pmatrix} -\cos a_\mu \sin A_\mu \\ \sin a_\mu \\ \cos a_\mu \cos A_\mu \end{pmatrix}. \tag{4.1}$$

Let the total number of events within cones of half-angle[2] $\psi_c = 1.585\sigma$ and $\sqrt{10}\psi_c$ to the nominal direction of the Sun/Moon be n_c and n_r respectively. For a shadow of angular radius θ_0 we expect n_c to be

$$\bar{n}_c \simeq \psi_c^2 \frac{dn}{d\psi^2} - \theta_0^2 \frac{dn}{d\psi^2}\left(1 - \mathrm{e}^{-\psi_c^2/2\sigma^2}\right) \tag{4.2}$$

This expression represents the expected number of events due to the background *minus* those due to primaries which stop in the Sun or Moon. The background rate $dn/d\psi^2$ is estimated from the number of events within the large cone. i.e. We assume the background is flat in ψ^2.

$$\frac{dn}{d\psi^2} \simeq \frac{n_r}{10\psi_c^2} \tag{4.3}$$

θ_0 was taken to be $\sim 0.26°$ for both the Sun and the Moon. The angular radius of the Sun varies between $15'43.91''$ and $16'15.94$; that of the Moon between $14'42.05''$ and $16'45.14''$[12]. A mean radius of $\sim 0.26°$ is thus an acceptable approximation.

As n_c is typically ~ 3000, the statistic $X^2 = (n_c - \bar{n}_c)^2/\bar{n}_c$ is distributed as χ^2 with one degree of freedom. We can thus study the suitability of coordinate rotations by examining the dependence of X^2 on (ξ, υ, ζ) and use X^2 to define confidence intervals for the parameters in the usual manner[3].

Event Distribution with Current Alignment

The space angle squared distribution, in optimal bins, with the nominal alignment and resolution is shown in Figure 4.2. This illustrates that the investigation will be limited by the statistics available. The deficit in the *on shadow* bin is only one standard deviation deep (3323 events are observed and 3371, from the background, minus 65, due to the shadow, expected) in the optimum cone. The data are consistent

[2] A 1.585σ cone is the optimum (i.e. the one that maximizes the significance of the effect) size for a Gaussian resolution of r.m.s. σ. See Reference [85].

[3] i.e. By looking at the variation of X^2 in the region of $\min X^2$

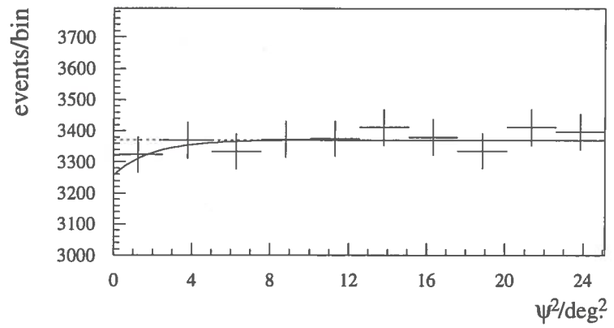


Figure 4.2: The space angle (ψ) squared distribution of events about the nominal shadow centre. The dotted line is the background rate and the solid line the expected distribution for a 1° resolution.

both with the hypothesis that we are observing a shadow and also with the alternative hypothesis: *that no shadow has been observed.*

The data prefer H_0 to the alternative but, as the χ^2 probability for the alternative hypothesis is only 60%, we are not justified in rejecting it. A more powerful test, such as one which takes account of the shape of the event distribution, may give a stronger result, therefore it is worth pursuing this analysis to learn about the parameter space to be explored by that procedure (see Section 4.3).

4.2.1 Effect of Rotation about the Coordinate Axes

Figure 4.3 (on Page 71) shows the variation of X^2 as a function of independent rotations ξ, υ and ζ. Each parameter is scanned through a range of 6°. During this scan the other two angles were fixed to 0°.

The regions of parameter space where $X^2 \gtrsim 4$ cannot be interpreted as indicating a strong preference for having a shadow elsewhere. The result of Section 4.2 shows that the expected shadow depth corresponds to $X^2 \sim 1$, so it is unlikely to have fluctuated to such a large value. We must interpret this as indicating that the assumption that the background is flat is invalid for a cone of size $\sim 1.585\sqrt{10}\sigma$.

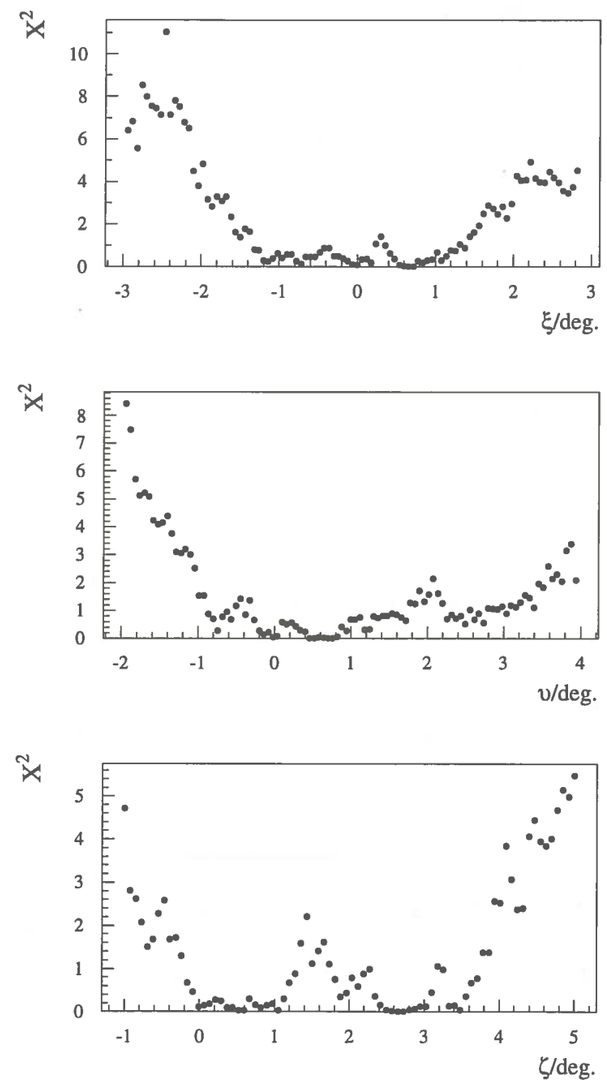


Figure 4.3: The dependence of the standardized error, X^2, on the angle of rotation about the x, y and z-axes (ξ, υ and ζ).

4.2.2 Fit with Resolution and Angles Free

Estimation of a Confidence Interval for σ Given H_0

If we assume the alignment is correct we can then determine a confidence interval for the resolution, σ, by investigation the dependence of X^2 on σ. Figure 4.4 illustrates this for the range: $0.2° < \sigma < 5.2°$. The curve is a fitted polynomial, to allow

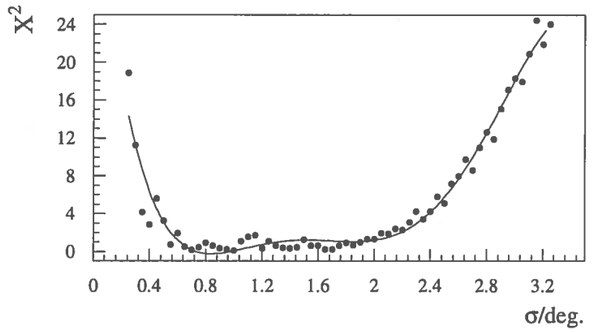


Figure 4.4: The dependence of the standardized error, X^2, on detector resolution, σ, for a Gaussian event distribution about the shadow centre. We assume $(\xi, \upsilon, \zeta) = \mathbf{0}$.

interpolation. The rise in X^2 for large σ is not consistent with the behaviour we would expect for a Gaussian resolution. The shadow should have the distribution

$$\frac{dn}{d\psi^2} \propto 1 - \frac{\theta_0^2}{2\sigma^2} e^{-\psi^2/2\sigma^2}. \tag{4.4}$$

The shadow has a shape with the scale set by σ and a depth with the scale set by θ_0^2/σ^2. For $\sigma \sim$ 2–3° the shadow has no perceptible depth for the number of events discussed here and there can be no error between the data and the background. The rise in X^2 is more likely to be due to the incorrect assumption that the background in the cone of size $1.585\sqrt{10}\sigma$ is flat.

Therefore, we set a one sided confidence interval on σ.

$$\left.\begin{array}{l}\sigma > 0.60° \\ \sigma > 0.46°\end{array}\right\} \text{with confidence} \left\{\begin{array}{l}68\% \\ 95\%\end{array}\right. \tag{4.5}$$

Estimation of (ξ, υ, ζ) and σ

A statistically significant detection of a shadow by this method is only possible if the real single-muon resolution were overestimated by the di-muon space angle distribution. e.g. If σ were 0.5° then the 65 muon deficit in the optimal bin would be removed from a background of $\sim 0.5^2 \times 3371 = 843$ events, with a significance of $\gtrsim 2$ standard deviations.

To allow for this possibility the variation of X^2 as a function of all four parameters was studied. No improvement to the nominal values was found.

4.3 Maximum Likelihood Analysis of the Event Distributions About the Sun and the Moon

The motivation of the search for Solar and Lunar shadows in the cosmic ray flux is to demonstrate the alignment and resolution of the SOUDAN 2 detector. We should therefore consider the possibility that the detector is not completely aligned, or that the resolution is not that indicated by the di-muon space angle distribution.

The effect of misalignment on the apparent p.s.f. of the detector is considered in Section 3.2.3. One possible result of detector misalignment is a systematic shift in the coordinates of the image centre. To allow for this, the shadow search was implemented by fitting a Gaussian shadow of fixed depth, but free to move in *relative* azimuth and altitude, to the observed muon flux.

For this analysis to be possible it assumes that the misalignment is small (less than $\sim$ 5°). This assumption is justified by the earlier alignment studies (see Section 3.3).

4.3.1 Maximum Likelihood Fitting of the Shadow

The fit procedure examined the distribution of muons in a relative topocentric coordinate system. i.e. The angular coordinates were[4]

$$\begin{aligned}\Delta A &= (A_\mu - A_o)\cos a_o \\ \Delta a &= a_\mu - a_o\end{aligned} \tag{4.6}$$

[4]Two other coordinate systems were also defined.

where a_μ is the altitude and A_μ the azimuth of a muon, and where the coordinates of the Sun or Moon (a_o, A_o) had been obtained from the coordinates computed by the programs of Section 3.7. For the Moon topocentric coordinates were used.

Modelling the Background Distribution

The Sun and the Moon are always at low declinations (see Figure 3.8 on Page 51) and so muons near either body are to be found at altitudes of between ~ 0 and $\sim 60°$. The distribution of the Solar/Lunar altitude for the events selected in Section 4.2 is shown in Figure 4.5. The strong dependence on altitude is due to the effect of the rock overburden on the muon flux.

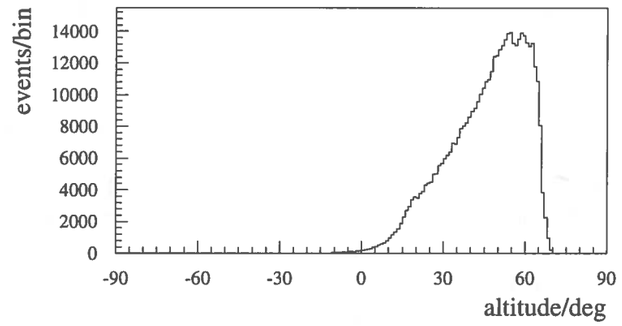


Figure 4.5: The distribution of Solar/Lunar altitude for muons within 20° of the Sun or the Moon.

The distribution of the Solar/Lunar Azimuth is approximately flat, as shown in Figure 4.6. The shape of this figure can be explained as the effect of convolving the 20° window with a flat event distribution over a restricted range of azimuths.

The analysis is performed in a relative coordinate system. The effect of transformation to this system is to smear the systematic dependences of the data. However, although the averaging is not sufficient to flatten the background distribution, it is reasonable to expect that the shape of the background should be smooth (underneath the statistical fluctuations).

Therefore, rather than computing the shape of the background, the data were binned in a large, $0.1° \times 0.1°$, histogram and its shape fitted to a polynomial in the relative coordinates $(\Delta a, \Delta A)$. The fit was done only for the data where $|\Delta a| < 10°$ *and* $|\Delta A| < 10°$, to avoid effects similar to those shown by Figure 4.6. The data

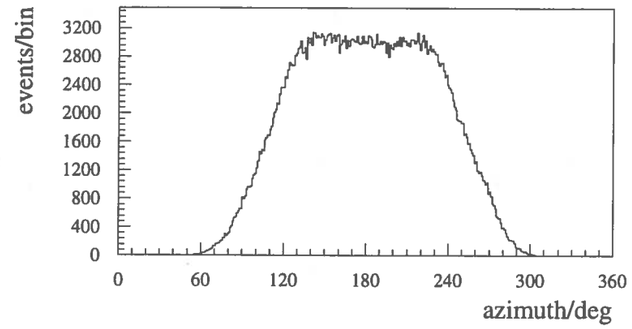


Figure 4.6: The distribution of the Solar/Lunar azimuth for muons within 20° of the Sun or the Moon.

used have the covariance matrix (columns: $\Delta a/°$, $\Delta A/°$)

$$\begin{pmatrix} 32.471 & 0.112 \\ & 33.342 \end{pmatrix} \tag{4.7}$$

and a correlation coefficient of 3.39×10^{-3}. The correlations between Δa and ΔA are clearly negligible, and so the polynomial fitted was of the form

$$B(\Delta a, \Delta A) = B_0(1 + \lambda_1 \Delta a + \frac{1}{2!}\lambda_2 \Delta a^2 + \ldots)(1 + \zeta_1 \Delta A + \frac{1}{2!}\zeta_2 \Delta A^2 + \ldots) \tag{4.8}$$

where $\{\lambda_i\}$ and $\{\zeta_i\}$ are coefficients to be determined.

Fitting the Background Model

The coefficients were determined using the *maximum likelihood ratio* as a test statistic in the manner of the COMPTEL group[19]. Initially all coefficients were put to zero, and the background scale factor, B_0, fitted. Each coefficient was then fitted and if Λ, twice the log of the ratio of the likelihood for the fit with the parameter free to the likelihood for the fit with the parameter fixed[5], for that coefficient was greater than unity the model modified to include a non-zero value for that coefficient. This procedure was then repeated with higher order coefficients until two successive coefficients were not accepted for each coordinate.

[5]This is the test statistic. It indicates the degree of preference for the new model compared to the old one and is distributed as χ^2_1 for this procedure. See Section C.1 for further details.

The projections of the data and the fitted polynomial for the combined Solar and Lunar shadow analysis are are shown in Figures 4.7 and 4.8.

Fitting the Shadow

The shadow depth, D, was computed from the background rate, $dN/d\psi^2$ where ψ is the space angle to the shadow centre. dN was taken to be all events within $5°$ of the nominal shadow centre, so

$$D \simeq dN \times \frac{\theta_0^2}{25}. \tag{4.9}$$

The shape of the histogram can then be fitted to

$$B(\Delta a, \Delta A)B_0 - \frac{D\, d\Omega}{2\pi\sigma^2} \exp - \frac{(\Delta a - \Delta a_0)^2 + (\Delta A - \Delta A_0)^2}{2\sigma^2}, \tag{4.10}$$

where the real shadow centre, $(\Delta a_0, \Delta A_0)$, is to be determined by the fit. For the rest of this section the subscript 0 will be dropped. During the fit B_0 was left free to allow a scaling of the background to compensate for the missing events due to the shadow. σ can be fixed to the nominal value or fitted itself.

The coincidence between the angular radii of the Sun and the Moon allows us to improve the statistics of the analysis by directly combining the data near the Sun and the data near the Moon.

The Principal Axis of the Fit

The analysis in Section 4.3.2 is done in the normal horizon coordinate system. i.e. In the spherical polar coordinate system where a is the angle above the xz plane and A is the angle in that plane. In principle, the detector misalignment about any of the axes xyz can be extracted from such analysis. However, by virtue of the fact that a rotation about the y axis is identical to a translation in A, the analysis is most sensitive to rotations about the y-axis of the coordinate system.

We can maximize the sensitivity to rotations about the other axes by taking new coordinate systems in which x and z are the principal axes. For a unit position vector (x, y, z) we can use

$$\left.\begin{array}{rcl} x &=& -\cos a \sin A \\ y &=& \sin a \\ z &=& \cos a \cos A \end{array}\right\} \text{ to define } (a, A)$$

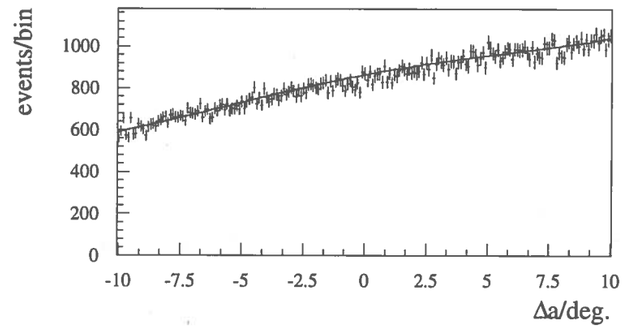


Figure 4.7: The projection onto the Δa axis of the histogram of event coordinates and of the background model B. Both the Sun and Moon events are included. The fit is good, $\chi^2/\text{d.o.f.} = 0.94$ for the projection.

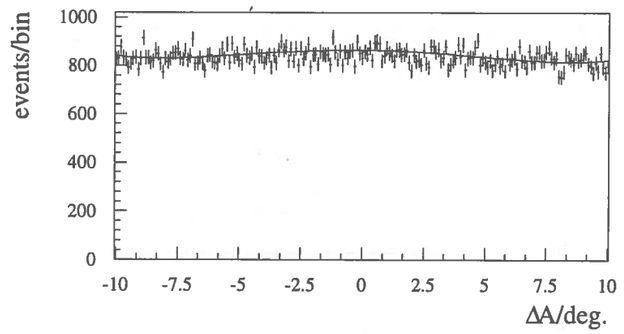


Figure 4.8: The projection onto the ΔA axis of the histogram of event coordinates and of the background model B. Both the Sun and Moon events are included. The fit is reasonable, $\chi^2/\text{d.o.f.} = 1.2$ for the projection.

$$\left.\begin{array}{rcl} x &=& \cos b \cos B \\ y &=& -\cos b \sin B \\ z &=& \sin b \end{array}\right\} \text{ to define } (b, B)$$

$$\left.\begin{array}{rcl} x &=& \sin c \\ y &=& \cos c \cos C \\ z &=& -\cos c \sin C \end{array}\right\} \text{ to define } (c, C). \qquad (4.11)$$

where (a, A) is the normal system discussed above and (b, B) & (c, C) are new complementary systems.

Although in the alternative coordinate systems it is simpler to interpret a systematic shift in terms of a rotation about the principle axis of the respective system, there is no change to the data analysed nor how it is distributed on the sphere — only how the rectangular coordinate system we use is mapped onto the sphere. i.e. Although the *efficiency* for a particular estimator is improved, the overall *power* of the test should not be changed. Therefore we shall assess the significance by taking the weakest of the three results. This should then be a conservative estimate of the significance.

4.3.2 Fit to the Combined Solar and Lunar Shadows in the Horizon Coordinates (a, A)

For the combined data set it was found that the background could be described by a 4th. order polynomial in Δa and ΔA. The coefficients determined are shown in Table 4.1. The likelihood for this model (actually $-\ln L$ where L is the likelihood) was $\mathcal{L} = 85354.45$ (this number only has meaning in comparison to the likelihood for another model). The shadow was estimated to be 90.75 events deep.

n	B_0	λ_n	ζ_n
0	$0.44148 \times 10^{+1}$		
1		0.25907×10^{-1}	-0.11018×10^{-2}
2		-0.21152×10^{-2}	-0.27776×10^{-2}
4		0.11881×10^{-3}	0.24164×10^{-3}

Table 4.1: Coefficients for the fit of the combined Solar and Lunar shadow data to a smooth polynomial.

Fit with the Resolution Fixed

With the resolution fixed to the nominal value of $\sigma = 1.0°$, the fit put the shadow centre at

$$\begin{aligned} \Delta a/° &= -1.62 \pm 1.08 \\ \Delta A/° &= -2.16 \pm 1.31, \end{aligned} \qquad (4.12)$$

where the errors have been estimated by assuming that the likelihood surface is parabolic with covariance matrix given by the Hessian matrix (the inverse of the matrix of second derivatives at the maximum). The likelihood for the model including the shadow was $\mathcal{L} = 85352.70$.

More reliable estimates of the errors (i.e. in terms of a standard 68% or 1 s.d. confidence region on the parameters) can be obtained by examining the shape of the likelihood surface around the maximum. The contour bounding the 68% confidence region is that given in Figure 4.9.

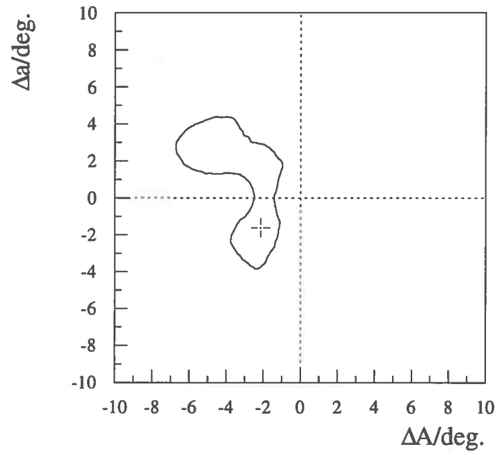


Figure 4.9: The 1 s.d. confidence region for the shadow centre from the combined data set. The best fit position is marked by the cross. This contour is an approximation to the true contour as the parameter B_0 was held fixed at its best estimate $\hat{B}_0$; as the correlation between B_0 and the angular coordinates is very weak ($\rho \sim 10^{-4}$) this is a reasonable approximation.

The space angle squared distribution about the fitted shadow centre, computed by rebinning the $0.1° \times 0.1°$ histogram used for the fitting, is shown in Figure 4.10.

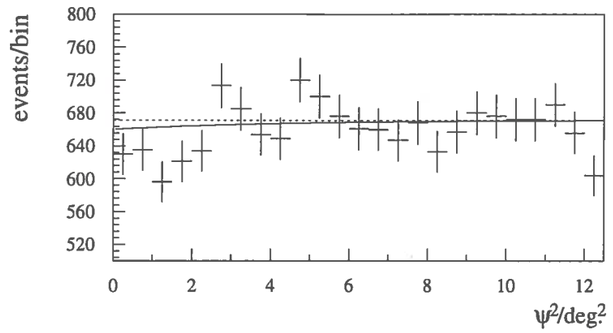


Figure 4.10: The space angle (ψ) squared distribution for events about the fitted shadow centre. The dotted line is the background rate and the solid line the expected distribution for a 90.75 event shadow with a 1° resolution.

Although the fit has clearly located a local minimum of the correct angular size, it is deeper than we would expect and not well described by the expected distribution. (With a 1° degree resolution, the figure shows little visible difference between a flat and "shadow" distribution.) This statement can be made more quantitative by considering the maximum likelihood ratio

$$\begin{aligned} \Lambda &= 2\ln\frac{L(D=0)}{L(D=90.75)} \\ &= 2\times(85354.45-85352.70) \\ &= 3.5. \end{aligned} \tag{4.13}$$

Λ should be distributed as χ^2_2 (see [19, 35]), as there are two additional free parameters (the coordinates of the shadow centre) introduced into the model, so the confidence with which we could reject the hypothesis $D = 0$ (i.e. that we have not actually observed a genuine shadow but rather a fluctuation of the background) is $Pr(\chi^2_2 < 3.5) = 83\%$. This is less than 2 s.d. $\sim 95\%$ confidence.

Fit with the Resolution Free

As noted in Section 2.7.2, we take SOUDAN 2 to have a Gaussian resolution of $\sigma \sim 1°$ as a reasonable working description of the di-muon space angle distribution. It is therefore not unreasonable, when studying a phenomenon directly sensitive to the single muon resolution, to allow σ to be a free parameter in the fit.

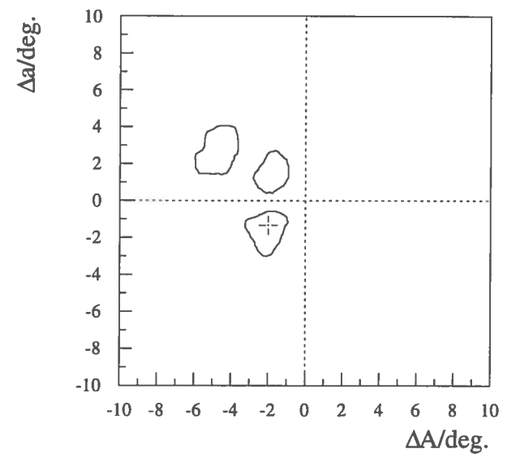


Figure 4.11: The 1 s.d. confidence region for the shadow centre in the (a, A) coordinate system. The best fit position is marked by the cross. This contour is an approximation to the true contour as the parameters B_0 and σ were held fixed at their best estimates $\hat{B}_0$ and $\hat{\sigma}$; these contours should be treated with caution as the correlation between σ and ΔA is large ~ -0.6.

The fit puts the shadow centre at

$$\begin{aligned} \Delta a/° &= -1.32 \pm 1.18 \\ \Delta A/° &= -1.99 \pm 1.99, \end{aligned} \tag{4.14}$$

with resolution

$$\sigma/° = 0.63 \pm 0.43 \tag{4.15}$$

where the errors have also been estimated from the matrix of second derivatives at the maximum. The likelihood for the model including the shadow was $\mathcal{L} = 85351.60$.

The contour bounding the 68% confidence region are the regions given in Figure 4.11. The single region of Figure 4.9 has become three separate regions. The interpretation of this is that we should expect the true value of the parameters to lie within one of the three regions in 68% of a sample of independent data sets, given that the model is correct. The likelihood maximum is clearly not parabolic, as a "good" maximum should be. Figure 4.12 shows how the likelihood varies as a function of σ at the maximum found. It shows a shallow and asymmetric minimum

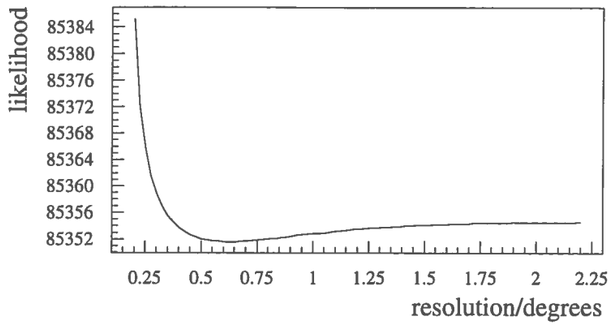


Figure 4.12: The variation of the likelihood (actually $-\ln L$) as the detector resolution, σ, is varied between 0.25° and 2.25°.

of $\mathcal{L}$ (maximum of L). The strong preference for $\sigma \gtrsim 0.25°$ is due to the fact that such a small resolution would place the entire ~ 90 event hole in just a few bins of the fit, corresponding to a significance of many (i.e. $\gg 2$) standard deviations.

The matrix of correlation coefficients is shown in Equation 4.16. The columns are in the order: $(\sigma, B_0, \Delta A, \Delta a)$.

$$\begin{pmatrix} 1 & -0.003 & 0.103 & -0.610 \\ & 1 & 0.000 & 0.505 \\ & & 1 & 0.005 \\ & & & 1 \end{pmatrix} \tag{4.16}$$

The large correlation coefficients $\mathrm{Cor}(\sigma, \Delta a) = -0.61$ and $\mathrm{Cor}(B_0, \Delta a) = 0.51$ suggest we should treat confidence intervals extracted in the manner described above with caution. The procedure probably underestimates the true error.

The space angle squared distribution about the fitted shadow centre, computed by rebinning the $0.1° \times 0.1°$ histogram used for the fitting, is shown in Figure 4.13. The distribution of events about the minimum is clearly in better agreement with the shape expected from a Gaussian hole than that of Figure 4.10. However, Figure 4.13 is not the best way of assessing the significance of the fit. With the resolution free, the maximum likelihood ratio

$$\begin{aligned} \Lambda &= 2 \ln \frac{L(D=0)}{L(D=90.75)} \\ &= 2 \times (85354.45 - 85351.60) \\ &= 5.7 \end{aligned} \tag{4.17}$$

should be distributed as χ^2_3. The confidence with which we could reject the hypothesis $D = 0$ is $Pr(\chi^2_3 < 5.7) = 87\%$. This is better than that for $\sigma = 1°$, however still less than 2 s.d.

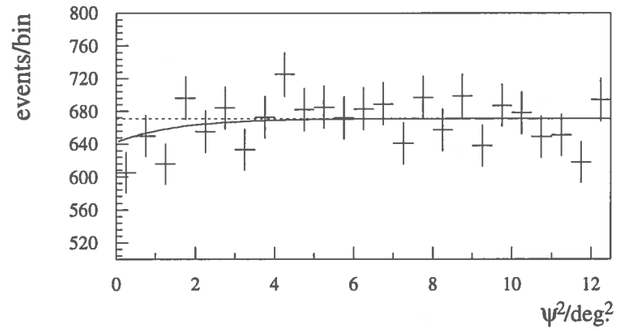


Figure 4.13: The space angle (ψ) squared distribution for events about the fitted shadow centre. The dotted line is the background rate and the solid line the expected distribution for a 90.75 event shadow with a 1° resolution.

4.3.3 Fit to the Combined Solar and Lunar Shadows using the Coordinates (b, B)

Fitting the background in the (b, B) coordinate system was more difficult than in the (a, A) system. The background could be described by a 5th. order polynomial in Δb and ΔB. The coefficients determined are shown in Table 4.2 (on Page 85). The likelihood for this model was $\mathcal{L} = 85796.30$.

Fit with the Resolution Fixed

With the resolution fixed to the nominal value of $\sigma = 1.0°$, the fit put the shadow centre at

$$\begin{aligned} \Delta b/° &= 1.64 \pm 2.06 \\ \Delta B/° &= -1.92 \pm 2.02, \end{aligned} \tag{4.18}$$

where the errors have been estimated from the covariance matrix at the maximum. The likelihood for the model including the shadow was $\mathcal{L} = 85793.56$. The contour

bounding the 68% confidence region is that given in Figure 4.14 (on Page 85). The parameter ΔB is constrained very weakly by the data. The extrema of the contour give a range of $\sim 7°$ for the estimate of ΔB to lie within. The constraint on Δb is better, but still large giving a total range of $\sim 3°$. As the space angle squared distribution about the fitted shadow centre is not flat, it is hard to draw any conclusions from it. The maximum likelihood ratio for this fit is

$$\begin{aligned} \Lambda &= 2 \times (85796.30 - 85793.56) \\ &= 5.48, \end{aligned} \tag{4.19}$$

giving a confidence level of $Pr(\chi^2_2 < 5.48) = 93.5\%$.

Fit with the Resolution Free

With the resolution free it was not possible to make a reliable fit using this procedure. This is probably due to the more complex shape of the background in the $(\Delta b, \Delta B)$ coordinate system.

4.3.4 Fit to the Combined Solar and Lunar Shadows using the Coordinates (c, C)

Fitting the background in the (c, C) coordinate system was also difficult. The background could be described by a 4th. order polynomial in Δc and ΔC. The coefficients determined are shown in Table 4.3 (on Page 86). The likelihood for this model was $\mathcal{L} = 85589.20$.

Fit with the Resolution Fixed

With the resolution fixed to the nominal value of $\sigma = 1.0°$, the fit put the shadow centre at

$$\begin{aligned} \Delta c/° &= -1.86 \pm 1.76 \\ \Delta C/° &= 1.44 \pm 2.44, \end{aligned} \tag{4.20}$$

with the errors estimated in the usual manner. The likelihood for the model including the shadow was $\mathcal{L} = 85586.14$. The contour bounding the 68% confidence region is shown in Figure 4.15 (on Page 86). Better constraints are placed on the shadow centre (i.e. the area bounded by the 68% contour is smaller) here than in either the

n	B_0^b	λ_n^b	ζ_n^b
0	$0.45325 \times 10^{+1}$		
1		0.27869×10^{-1}	0.44917×10^{-2}
2		-0.41869×10^{-2}	-0.13981×10^{-1}
3		-0.17144×10^{-2}	-0.44511×10^{-2}
4		0.26897×10^{-3}	0.61018×10^{-2}
5		0.14367×10^{-2}	-0.28631×10^{-2}

Table 4.2: Coefficients for the fit of the combined Solar and Lunar shadow data to a smooth polynomial in the (b, B) coordinate system.

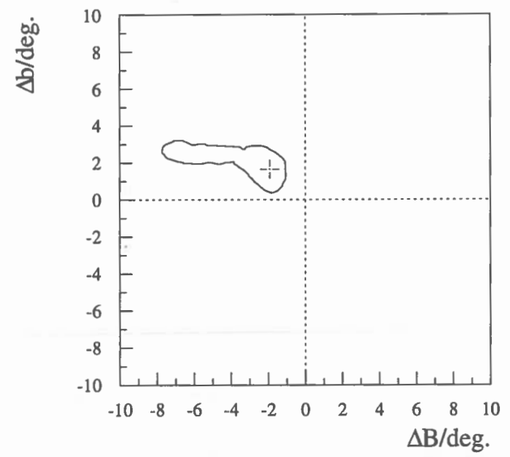


Figure 4.14: The 1 s.d. confidence region for the shadow centre in the (b, B) coordinate system. The best fit position is marked by the cross. This contour is an approximation to the true contouras the parameter B_0 was held fixed at its best estimate $\hat{B}_0$. The correlation coefficients were $\sim 2\%$.

n	B_0^c	λ_n^c	ζ_n^c
0	$0.44433 \times 10^{+1}$		
1		0.40956×10^{-3}	0.26291×10^{-1}
2		-0.23588×10^{-2}	-0.30646×10^{-2}
3		-0.16162×10^{-3}	0.14093×10^{-3}
4		0.28383×10^{-3}	0.18906×10^{-3}

Table 4.3: Coefficients for the fit of the combined Solar and Lunar shadow data to a smooth polynomial in the (c, C) coordinate system.

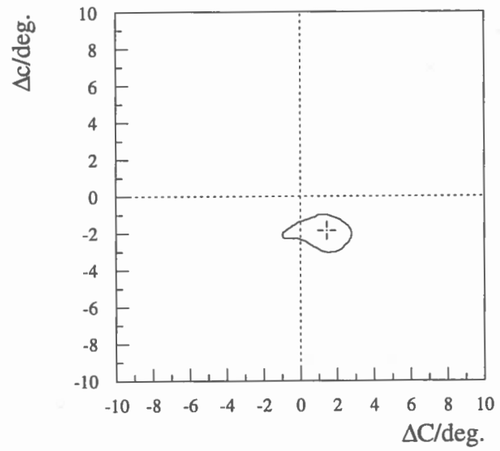


Figure 4.15: The 1 s.d. confidence region for the shadow centre in the (c, C) coordinate system. The best fit position is marked by the cross. This contour is an approximation to the true contour as the parameter B_0 was held fixed at its best estimate $\hat{B}_0$. The correlation coefficients were $\sim 2\%$.

(a, A) or (b, B) coordinate system. As in Section 4.3.3, the distribution of space angle squared about the shadow centre is not flat, so few conclusions can be drawn from it. The maximum likelihood ratio for this fit is

$$\begin{aligned} \Lambda &= 2 \times (85589.20 - 85586.14) \\ &= 6.12, \end{aligned} \tag{4.21}$$

giving a confidence level of $Pr(\chi_2^2 < 6.12) = 95.3\%$, marginally below 2 s.d. or 95.5%.

Fit with the Resolution Free

As in Section 4.3.3, it was not possible to make a reliable fit with the resolution free. Again, this is likely to be due to the complexity of the background shape.

4.4 Summary and Conclusions

The goal of both Sections 4.2 and 4.3 has been to ask whether observation of the shadow cast by the Sun and Moon in the cosmic ray flux requires us to reject the hypothesis that the SOUDAN 2 detector is correctly aligned to $\sim 0.25°$. In the absence of a strong calibration source, the advantage of this method is that it is directly sensitive to both the single muon resolution and the alignment of the detector.

The most efficient way of estimating systematic rotations about the detector axes, from the data, is the analysis of Section 4.2. The most powerful method is to fit the shape of the shadow, on the assumption that the p.s.f. model is correct. Neither analysis provided compelling evidence for the rejection of the null hypothesis and, as Figure 4.2 (on Page 70) illustrates, the data is entirely consistent with H_0. From the fits, and following the procedure of Section 4.3.1, we conservatively estimate the confidence with which we could reject H_0 as 83%. All three fits find a systematic displacement of $\sim$ 1–2°. This is considerably larger than that suggested by other studies [60, 85], although with an error of similar magnitude. It therefore seems unlikely that the fits have converged to the genuine shadow or, if they have, the systematic displacement is determined badly.

The utility of both analyses was reduced by the strong systematic dependence of the background flux on angular coordinates. Our ability to deal with this problem

will be increased with a larger data sample, as will the statistical significance of the shadow.

Around 30% of the total 14 million event sample was accumulated in the final 15% of the time (10.7 million from January'89–June'92; 3.3 million from July'92–February'93). From Equation 4.4, we see that the significance of the shadow (number of s.d.) $\propto \sqrt{n}/\sigma^2$, where n is the number of background events and σ the resolution. If data in the full detector is accumulated at double this rate (i.e. at ~ 0.8 million events/month) there should be a 2 s.d. deficit in the optimum cone by June 97.

A reduction of $\sim 30\%$ in σ is equivalent to doubling the size of the data sample. The di-muon space angle distribution already suggests that, at least for the latest SEARCH data, a resolution of $0.5^\circ \lesssim \sigma \lesssim 1^\circ$ is suitable[61]. This should give a $\gtrsim 2$ s.d. deficit by April'95.

If the fits of Section 4.3, with significance $\lesssim 2$ s.d., have genuinely found the shadow due to the Sun and the Moon, then this more powerful test may give an acceptable level of significance before then.

CHAPTER 5

THE CONSTRUCTION OF A WHOLE SKY MAP OF THE DEEP UNDERGROUND MUON FLUX

5.1 Introduction

In this chapter, the construction and analysis of a whole sky map of the underground muon flux is considered. The motivation of the analysis method is discussed.

The origin of the shape and evolution of the background is treated in some detail. By considering simple examples, it is shown that this shape and evolution can be completely understood as the consequence of the observations made. Using this knowledge, a method for the computation of a whole sky background is developed and implemented.

The technical details of the construction of maps of the muon flux are discussed and a number of map analysis methods are studied. An analysis procedure is chosen and the results of a monte carlo simulation of the entire analysis chain, implementing this procedure under the null hypothesis (that there are no point sources of underground muons), are presented. Finally, a study is made of the behaviour of the analysis procedure when a source has been added to the map.

5.2 A Whole Sky Map

5.2.1 Motivation of the Sky Survey

Most underground detectors can see (in muons) over half the celestial sphere. To date, most searches for point sources of deep underground muons associated with discrete astrophysical objects have concentrated on studying the deviation from the background of the number of events in an on source cone (see References [7, 14, 16, 58, 65, 84, 85]) The cone, of semi-angle ψ, is optimized from *a priori* knowledge of the detector's resolution — usually extracted, as in Chapter 2, from the di-muon space angle distribution — typically of order 1–2°. The solid angle subtended by a cone of semi-angle ψ is $2\pi(1-\cos\psi)$, which is $\sim 10^{-3}(\psi[^\circ])^2$. If a typical survey examines some $\sim$ 10 sources[85] then less than 1% of the sky has been examined.

Given that the observation of a source consistent with the claimed positive observations of Cygnus X–3[14, 58, 84] requires new physics, it is possible that any list of interesting objects compiled from *a priori* knowledge of the physics processes involved omits an object that may be a strong source. Also, some models of Active Galactic Nuclei[15] suggest that the A.G.N. may be so optically dense that only weakly interacting particles may escape; i.e. the A.G.N. responsible for an intense flux of cosmic rays (usually assumed to be neutrinos in this case) may have no counterpart visible in the electromagnetic spectrum.

The above arguments suggest that we should search the entire acceptance of the SOUDAN 2 detector for point sources of underground muons. This can best be accomplished by constructing a map (i.e. a large 2-dimensional histogram) of the muon flux in celestial coordinates. A map of the background expectation is also required.

5.2.2 The Statistical Consequences of Searching

One of the advantages of the analysis method using "on source" cones is that the statistical interpretation of the result is simple and therefore robust. If we examine a number of independent source positions a statistical penalty is paid. However, this penalty is trivial to compute. It is shown in Section 5.7 that the study, in this manner, of the $\sim$ 3000 independent bins, with a size typical of the resolution, that can be packed onto the visible sky is not a particularly powerful method of searching for point sources with *unknown* coordinates.

The statistical penalty for searching the entire map is considerably harder to compute. We can consider the set of $\sim$ 14 million muons as a Poisson field with an expectation of $\bar{n}(\alpha,\delta)$ events per unit solid angle. The total number of events within a cone centered at (α,δ) is the integral over a small region of this field. The behaviour of the standardized deviation, $Z(\alpha,\delta)$, is a realization of a two dimensional stochastic process. As such, the probability $Pr(\sup Z > b)$ can be computed[4, 77] (see Section C.2.3 for further details of this calculation).

5.3 Understanding the Diffuse Background Cosmic Ray Flux

There are no point sources of underground muons that are sufficiently strong to allow detection without a careful background subtraction. To search the visible sky for point sources we therefore require a background map, of the same region of the sky, for subtraction. Although the background is primarily due to secondary muons from showers initiated by cosmic ray protons, and this flux is isotropic, the observed flux is far from flat. Figure 5.1 (on Page 92) shows the distribution of background muon events in equatorial coordinates (h,δ). The background flux of muons is strongly attenuated by the rock overburden, and this gives the distribution its gross shape. Due to discontinuity in shading, the figure shows a "cut off" of the background flux along a line on constant altitude. In reality the flux reduces to zero smoothly. Inhomogeneity in the rock overburden causes local variation of the background, and introduces some asymmetry into the rate. Due to mining, such variations can be discontinuous and pronounced. The distribution also shows sharp notches, due to reconstruction and triggering[1] inefficiencies, along the East-West plane and the North-South plane (meridian circle).

5.3.1 The Origin of the Shape of the Background in Celestial Coordinates

The Background in Real Space

Let the coordinates of the background muons be distributed as $r(h,\delta)$ in equatorial coordinates. The shape of the background in celestial coordinates arises from the

[1] The trigger was optimized for proton decay events[13].

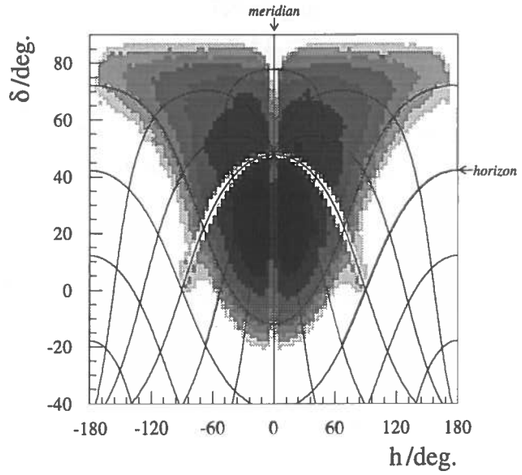


Figure 5.1: The *butterfly* plot: the distribution of background muon events in equatorial coordinates. Also shown are lines of constant altitude and azimuth (30° intervals). The relative muon rate is shown by the variation in intensity from black (maximum) to white (minimum).

transformation of this distribution. The Right Ascension, hour-angle and local sidereal time of the event are linked by Equation B.2. As there is no coupling between declination and the other coordinates, we can consider only one declination without loss of generality. Given that a muon is observed at local sidereal time t, the probability of that muon having Right Ascension α is

$$Pr(\alpha) = r(t - \alpha). \tag{5.1}$$

If we make observations with some distribution, $l(t)$, of times, the expected number of muons, at a given Right Ascension, is therefore

$$n(\alpha) = \int_{-\infty}^{\infty} r(t - \alpha) l(t)\, dt = (r \otimes l)(\alpha) \tag{5.2}$$

where $r(h)$ has been assumed to be a periodic function of time and $\otimes$ represents the convolution operation. If, and only if, $l(t)$ is a constant, irrespective of $r(h)$,

or $r(h)$ a constant irrespective of $l(t)$, then $n(\alpha)$ will be flat. In all other cases, the shape of the background is determined by Equation 5.2.

The Background in Transform Space

The shape and evolution of the background are easier to understand by considering Equation 5.2 in transform space. The convolution is equivalent to a filtering operation

$$n = r \otimes l \Leftrightarrow \nu = \rho \times \lambda, \tag{5.3}$$

where Greek functions are the Fourier transforms of Roman functions.

As $r(h)$ is a periodic function its Fourier transform consists of δ-functions at the harmonics of the fundamental period. Each δ-function is multiplied by the appropriate Fourier series coefficient. Figure 5.2 illustrates a typical hour-angle distribution.

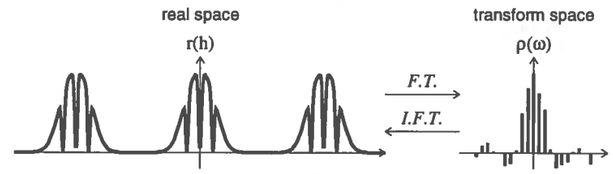


Figure 5.2: The hour-angle distribution in real and transform space.

For simplicity consider a single observation. However, unlike the impulse observation of Equation 5.1, we take the observation to start at time t_0 and last for period T. The transform of this observation is a sinc function with bandwidth $\Delta\omega \propto 1/T$ and phase $\delta_0 = e^{i\omega t_0}$. i.e. The act of observing for a period T is equivalent to operating on the hour angle spectrum with a low pass filter of bandwidth $\Delta\omega$. As a result all frequencies other than D.C. are attenuated and a frequency dependent phase shift is introduced — equivalently, the Right Ascension distribution of the background is the result of smoothing the hour-angle distribution in a manner determined by the observations performed. The effect of this operation is illustrated in Figure 5.3.

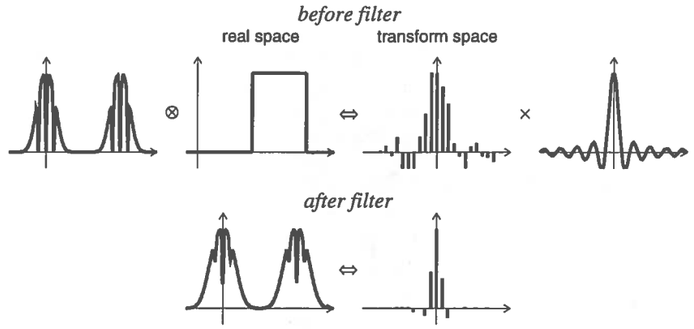


Figure 5.3: The effect of observation on the hour-angle distribution in real and transform space.

5.3.2 The Evolution of the Shape of the Background

The remarks of Section 5.3.1 provide a framework within which the effect of a series of observations can be described. As the Fourier transform is linear, the filter arising from a series of observations is the superposition of the filters that arise when each observation is taken individually.

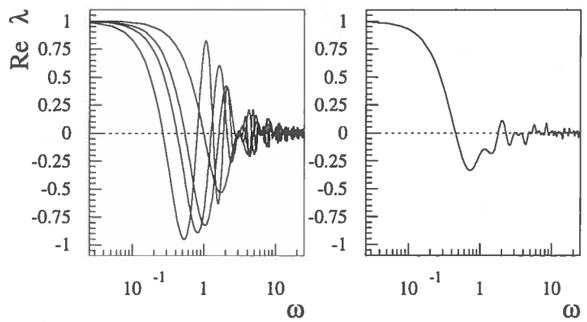


Figure 5.4: *On the L.H.S.*: The real part of filters that result from four independent observations of equal period, but at random times. *On the R.H.S.*: The real part of the combined filter that results from making all four observations.

Additional Observations with the Same Period

If a set of observations are made at times $\{t_n\}$, but all with the same period, T, then the only difference between the transforms of each individual observation is the phase $\delta_n = e^{i\omega t_n}$. These phases will generally differ at all frequencies except D.C.

Figure 5.4 (on Page 94) shows the filter that results from the combination of four observations taken at random times (drawn from the uniform distribution) but with equal periods. The precise behaviour of the filter is dependent on the distribution of the observation times. However, it is reasonable to assert that the effect of making many observations is, *on average*, to attenuate progressively the higher-order harmonics of the hour-angle distribution. The lower-order frequencies are less strongly attenuated, but their phases will be changed as more observations are made.

Additional Observations with Differing Periods

If the observations are made at the same time on differing sidereal days, i.e. such that all the phases are equal, but for differing periods $\{T_n\}$, then the difference between the transforms of the individual observations is the bandwidth $\Delta\omega_i$. The amplitude of the individual filters will generally be less than unity for all frequencies other than D.C.

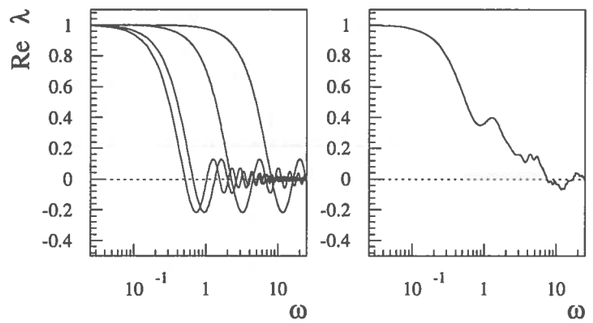


Figure 5.5: *On the L.H.S.*: The real part of filters that result from four independent observations of differing period, but with no relative phase. *On the R.H.S.*: The real part of the combined filter that results from making all four observations.

Figure 5.5 shows the filter that results from the combination of four observations taken for random periods (drawn from the uniform distribution). The trivial effect of the global phase, $e^{i\omega t_0}$, has not been included. *On average*, the effect is also to attenuate the higher frequencies, although the same caveat (this time regarding the distribution of periods) applies.

The General Evolution of the Background

From the above we infer that as more observations are made, at random times and for random periods, the background will become progressively flatter until, after a very large number of observations have been made, it will be acceptable to represent it by a constant. The higher-order harmonics will probably become negligible rather rapidly, but the fundamental should remain significant for much longer.

Figure 5.6 shows the Right Ascension distribution at a typical declination for three *integral* data-sets from 1989. The distributions illustrate the behaviour indicated by the analysis above. The integral distributions for the first twelve months of data were fitted to the harmonic series

$$n(\alpha) = a_0 \{1 + a_1 \sin(\alpha + \varphi_1) + a_2 \sin 2(\alpha + \varphi_2)\} . \qquad (5.4)$$

Data Until	a_0	a_1	$\varphi_1/^\circ$	a_2	$\varphi_2/^\circ$
January	19.2	0.372	318.5	-0.097	91.9
February	62.6	0.352	303.9	-0.024	64.6
March	114.5	0.318	282.6	0.038	132.7
April	180.5	0.313	266.3	-0.026	45.5
May	229.8	0.318	256.6	0.019	100.6
June	296.2	0.299	237.4	0.020	87.1
July	350.9	0.268	224.8	0.014	69.7
August	418.5	0.245	205.7	-0.007	132.2
September	480.3	0.199	189.0	0.008	1.7
October	537.6	0.164	170.4	0.005	333.4
November	606.7	0.116	152.5	-0.005	247.1
December	708.3	0.071	135.4	-0.004	-62.3

Table 5.1: Coefficients for the fit of the Right Ascension distribution to an harmonic series for the first twelve integral data-sets.

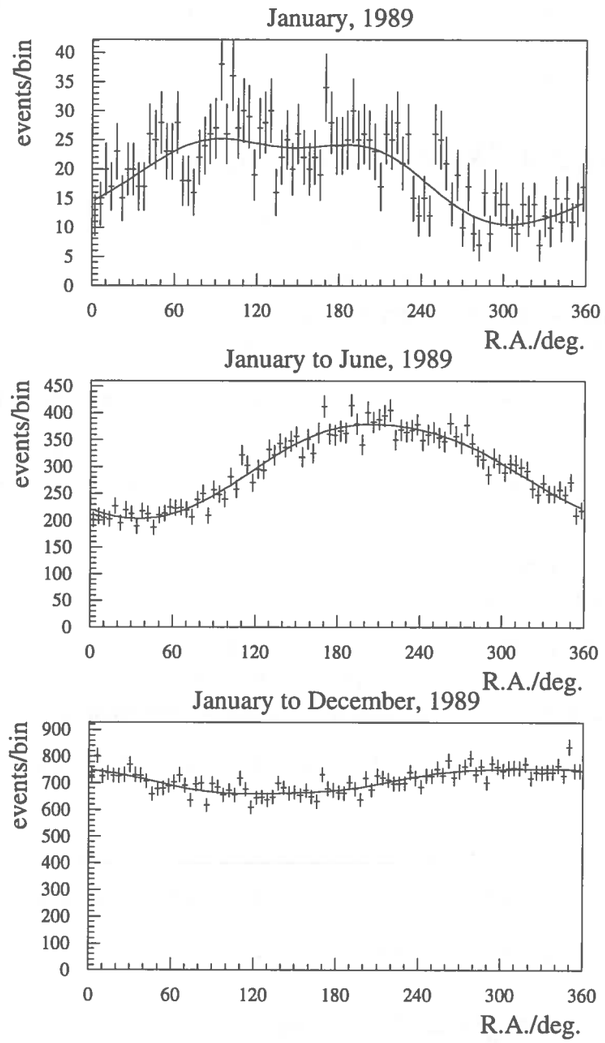


Figure 5.6: The Right Ascension distribution after one, six, and twelve months of data. Data for a 4° band centered on $\delta = 40°$ is plotted. The curves are the result of fitting the first few terms of an harmonic series.

The fitted coefficients are tabulated in Table 5.1. The coefficients of the first harmonic show a clear trend in both amplitude and phase. For the second harmonic the trend in phase is less clear.

5.4 A Whole Sky Background Calculation

As shown in Figure 5.1, the shape of the hour-angle distribution depends strongly on the declination. This means that the phase and amplitude of the harmonics of the background may vary with declination too.

To allow background subtraction at all points on the visible sky we require a background calculation with the following properties:

i, the error on the background estimate should be not be significant when compared to the error on the data;

ii, the calculation must be applied simultaneously to the majority of the visible sky;

iii, the calculation must possess the ability to reproduce the effect of changing detector acceptance *integrated* over the period of observations;

iv, the method must be *bin free* in the sense that the granularity of the estimate is not fixed by the method — in particular the background must resolve points to an order of magnitude less than the detector resolution; *and*

v, as much as possible, the method must be insensitive to the presence of a point source.

It does not need to possess the following properties:

i, the ability to follow the detector acceptance as it changes with time;

ii, the ability to deliver an instantaneous rate.

5.4.1 Other Background Calculations

Previously implemented background calculations[64, 85, 87] have been conditioned by a need to follow the instantaneous muon rates in some approximate manner and to compute the expected number of events in an array of independent optimum cones

at the declination of Cygnus X–3 (one of the cones being centered on Cyg X–3). The computational overhead associated with extending these techniques to cover a very large array of small cones (or rectangular bins), distributed across the visible sky, would be large and these methods were not pursued.

An alternative technique would be to abandon completely all attempts to calculate the expected shape of the background and fit the observed shape to a spherical harmonic expansion. Unfortunately, the acceptance/efficiency notches in the SOUDAN 2 acceptance, as shown by Figure 5.1, produce a very sharp step in the muon rate as a function of declination. A preliminary investigation indicated that the spherical harmonic series required to reproduce this structure would need to include harmonics of fairly high order ($l, |m| \gg 15$). This method was not implemented.

5.4.2 A New Background Calculation

The Basis of the Method

In Section 5.3.1 the hour-angle distribution is generalized to a periodic function of local sidereal time. The requirement that the function was periodic was made for reasons of simplicity, and is not strictly necessary.

If we assume that the distribution *is* truly periodic, a theorem about convolution integrals allows the expression to be evaluated to be simplified considerably. It can be shown that if $a(t)$ is a periodic function, with period T, and $b(t)$ is an aperiodic function then

$$\int_{-\infty}^{\infty} a(s-t)b(s)\,ds = \int_{0}^{T} a(s-t)[b(s)]\,ds \tag{5.5}$$

where $[b(t)]$ is the function $b(t)$ summed over the periods of $a(t)$.

In Equation 5.2, $r(h)$ has been regarded as a p.d.f. and $l(t)$ as the distribution of observations. Thus the integral of r is unity and that of l equal to the number of muons observed. As the shape of l is independent of declination, but the norm of l has the same strong dependence on declination as $r(h, \delta)$, it is convenient to transfer the norm from l to r. Equation 5.2 can then be rewritten as

$$n(\alpha, \delta) = \int_{0}^{24^h} r(t-\alpha, \delta)[l(t)]\,dt \tag{5.6}$$

where $\int n\,d\alpha = \int r\,d\alpha$ and $\int [l]\,dt = 1$.

The method employed in the calculation of the background was based directly on this equation.

Implementation of the Method

The quantity $r(h, \delta)$ is an unknown joint p.d.f. normalized to the observed number of muons. For a very large, D.C., data-set we assume this quantity may be estimated by a histogram of the actual event coordinates. The background is thus estimated by convolution of the observed distribution in equatorial coordinates with the observed local sidereal time distribution. To improve computation time only, this convolution my be implemented via the *Fast Fourier Transform* (F.F.T.) algorithm.

The existence of a source introduces a correlation (i.e. Equation B.2) between the local sidereal time and hour-angle of a muon from the direction of that source. As $[l]$ is taken to be the local sidereal time distribution of the entire data-set (some 10^7 events) and the size of the excess due to a source is unlikely to be more than $\sim$ 4–5 s.d. $\sim$ 200 events in an optimum cone centered on the source, this correlation should not have significant effect on the overall background calculation.

With the background calculation formulated as above, the integral of the background estimate is necessarily constrained to be equal to the total number of events in the data-set. The background predicts, given that number of events and a normal background flux affected by only *local* factors, how those events will be distributed on the sphere.

The Error on the Background

To compute the distribution of the background used about the *true* background is complicated in all but the most trivial cases, and for such cases (the background is flat) anything other than a simple calculation of the background is unnecessary.

As the granularity of the maps to be searched must be an order of magnitude less than the resolution of the detector (i.e. $\sim 0.1°$) we expect the background for a typical bin to be $\sim$ 3–4 events[2]. In this limit, the formula for the propagation of errors is not strictly applicable and the distribution of $n(\alpha)$ can only be computed from knowledge of $r(h)$ and $l(t)$. However, the formula can be used to estimate the order of magnitude of the error.

If $[l_t]$ is computed from a histogram with bin contents m_t then it has variance[2]

$$\mathrm{Var}([l_t]) = \sum_s \left(\frac{\partial [l_t]}{\partial m_s}\right)^2 \mathrm{Var}(m_s)$$

[2]As cone of 1.6° half-angle contains ~3000–4000 events, a bin of $\sim 0.1° \times 0.1°$ will contain $\sim 10^{-3}$ less events.

$$= \sum_{s \neq t} \frac{m_t^2 m_s}{(\sum_r m_r)^4} + \frac{m_t}{(\sum_r m_r)^2}\left(1 - \frac{m_t}{\sum_r m_r}\right)^2. \quad (5.7)$$

For the data-sets analysed, $\sum_r m_r \sim 10^7$ so this quantity can be considered to be determined without error — the error on $[l_t]$ is dominated by the number of events per bin. For a flat distribution with a few 1000 bins in sidereal time,

$$\sqrt{\mathrm{Var}([l_t])}/\mathrm{Exp}([l_t]) \sim 1\%. \quad (5.8)$$

Assuming the error on $[l_t]$ to be negligible, the variance of n_t is

$$\mathrm{Var}(n_t) \approx \sum_s \left(\frac{\partial n_t}{\partial r_s}\right)^2 \mathrm{Var}(r_s). \quad (5.9)$$

If r and l are constant then this is proportional to the variance of $\sum_t r_t = \sum_t n_t$, which illustrates the fact that the background estimate merely results from the appropriate averaging over the band of declination studied. For typical bin size and contents

$$\sqrt{\mathrm{Var}(n_t)}/\mathrm{Exp}(n_t) \sim 1\%. \quad (5.10)$$

5.5 Demonstration of the Validity of the Method

5.5.1 Computation of the Background for a Small Data-Set

Before computing the background for the entire data-set, the procedure was studied on a subset of the data. Events from January'91–April'91 that passed cuts and with a declination within $\pm 1°$ of 40° (approximately the middle of the SOUDAN 2 acceptance) were selected.

The coordinates of these events were used to make 256 bin histograms of hour angle, local sidereal time, and Right Ascension. At this declination approximately 80 optimum cones can be packed into a declination band, so any excess due to a real source would be divided among $\sim$ 3 bins and is unlikely to bias the analysis.

A total of 34036 events were accepted. Figures 5.7, 5.8, and 5.9 (on Page 102) shows the hour-angle distribution, local sidereal time distribution and Right Ascension scan for this data. Figure 5.10 (on Page 103) shows the distribution of the residuals: $(n - \bar{n})/\sqrt{\bar{n}}$. The curve is a Gaussian with mean 0 and r.m.s. 1. For the region $[-2.5, 2.5]$ s.d., the data has $\chi^2 = 8.93$ for 10 d.o.f. which is perfectly acceptable. The shape of the background computed appears to be a reasonable description of the underlying trend.

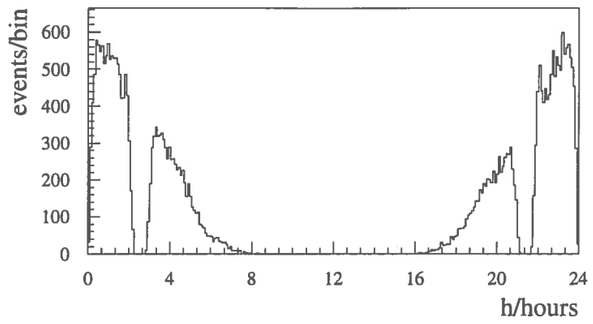


Figure 5.7: The hour-angle distribution for the small data-set.

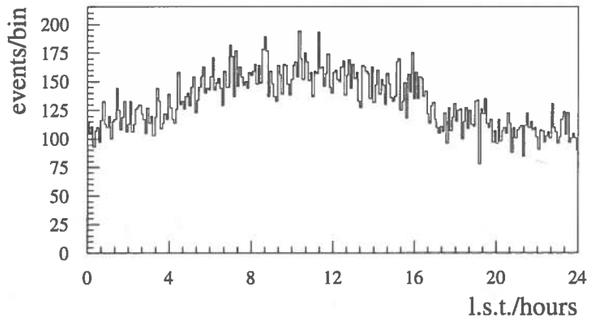


Figure 5.8: The local sidereal time distribution for the small data-set.

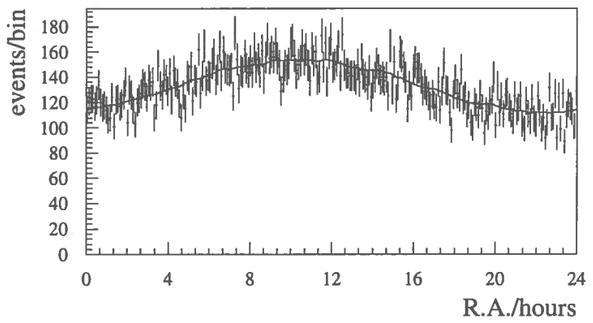


Figure 5.9: The Right Ascension scan for the small data-set. The points with errors are the data and the solid line the background computed.

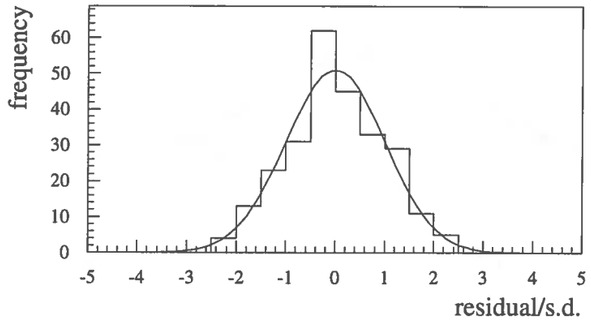


Figure 5.10: The distribution of residuals for the small data-set.

5.5.2 Study of the Fluctuations of the Background

From Figures 5.7 and 5.8 it is clear that the approximation that r_t and $[l_t]$ are constant is not valid. The fluctuations of the background were studied by a monte carlo procedure:

i, the number of events to be generated, n_g, was taken to be a random number drawn from a Poisson distribution with mean 34036;

ii, for each of the n_g events, an hour-angle, h, and local sidereal time, l, were generated according to the observed distributions;

iii, histograms of h, l, were made;

iv, a background was computed from the histograms of h and l;

v, the entire procedure was then repeated 100 times.

Although the p.d.f. $r(h)$ is unknown the observed distribution is the best estimate of the true density. The above procedure should then produce an approximation to the fluctuations of the background about the true background. It is likely to possess some bias, which we shall assume affects only the mean and not the variance to first order.

Figure 5.11 shows the result of this computation. The distribution of $n_i(\alpha) - n_0(\alpha)$, for all Right Ascensions and all i, is approximately a normal distribution. n_0 is the background computed from the actual data and n_i that

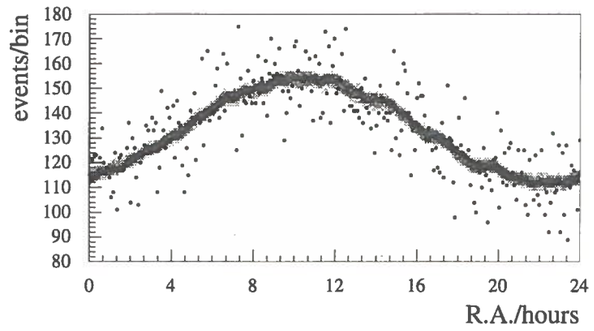


Figure 5.11: The Right Ascension distribution of the data and of the 100 background calculations. The points represent the observed number of events per bin of Right Ascension, and the shaded region the distribution of the estimates of the background.

computed from the ith iteration of the monte carlo. The mean and standard deviation of the distribution were estimated to be

$$\begin{aligned} \hat{\mu} &= -0.01 \pm 0.095 \text{ events} \\ \hat{\sigma} &= 1.74 \pm 0.094 \text{ events.} \end{aligned} \tag{5.11}$$

Although the fit is bad ($\chi^2 = 149$ for 98 d.o.f.), the estimates of the mean and standard deviation agree with the sample mean and standard deviation (-0.05 and 1.72 respectively). The s.d. of the background is $\sim 1\%$ of the mean background (~ 140), in agreement with the approximation of Section 5.4.2. The error on the background is an order of magnitude less than the error on the data and, given that only a small subset of the entire data-set has been used here, it is safe to treat the background calculation as accurate.

5.6 Specification of the Whole Sky Maps

5.6.1 Technical Specification of the Map Files

Four arrays are required to construct and analyse a whole sky map:

i, a 2-d. histogram of the reconstructed event coordinates in equatorial coordinates (the *hour-angle map*);

ii, a 2-d. histogram of the reconstructed event coordinates in celestial coordinates (the *Right Ascension map*);

iii, a 2-d. function with the same resolution of Right Ascension map that specifies the background in celestial coordinates (the *background map*); *and*

iv, a histogram of event trigger times in local sidereal time.

As a pictorial analysis of the data will be developed, 2-dimensional histograms/functions are referred to as *maps* and their bins/finite elements as *pixels*. The complete set of pixels with declination δ will be referred to as the *slice* at declination δ.

In the standard SOUDAN 2 analysis, upward going muons are assumed to be downward going muons[3]. The maximum zenith angle of any reconstructed muon in the detector is therefore 90°. As the SOUDAN 2 detector has latitude 47.8° North, all events have declinations in the range $[-42°, +90°]$.

The granularity of the maps was chosen to be $3600 \times 0.1°$ in hour angle/Right Ascension and $1300 \times 0.1°$ in declination, allowing coverage of all Right Ascensions and all visible declinations to $0.1° \times 0.1°$. The centre of bin (i, j) has coordinates

$$\begin{aligned} \alpha_i/° &= (i-1)/10 + 0.05 \\ \delta_j/° &= (j-1)/10 - 39.95 \end{aligned} \tag{5.12}$$

The histogram of local sidereal time has $3600 \times 24^s = 0.1°$ bins in the range $[0, 24^h]$.

The maps are stored as 1300 record indexed files. Each record is 3601×4 byte words long. The first word is the record number, the remaining 3600 are the values of the pixels from one slice, stored as integers in the sequence $1 \ldots 3600$. Real numbers are multiplied by 10^7 and then stored as integers, giving the 7 digit precision of `REAL*4 D_FLOATING` words on a VAX processor[33]. The l.s.t. histogram is stored as an HBOOK/ZEBRA object[23].

5.6.2 Details of the Production of the Maps

The DMC files for the period January'89 to February'93 were processed for the production of maps. The data was divided asymmetrically into two sets:

i, the *large data-set* using data from January'89 to June'92; *and*

[3]The precision of the detector timing is not sufficient to allow discrimination between upward going and downward going muons.

ii, the *small data-set* using data from July'92 to February'93.

A separate set of maps was made for each data-set. The division into two sets is arbitrary: the first, and larger, set was made with all the data available when the sky map procedure was finalized; the second, smaller, set was made with data accumulated while the preliminary analysis of the first maps was in progress. These two sets will be referred to as Map 1 and Map 2 respectively. A symmetric re-division of the data, after a lengthy initial analysis, would result in an unfairly biased approach.

There were approximately 11×10^6 events processed for the large data-set and 3×10^6 for the small set. This increased rate is due to the continuing installation of detector modules while data taking is in progress. A typical $0.1° \times 0.1°$ pixel from Map 1 contains $\sim$ 3–4 events, the corresponding pixel in Map 2 contains ~ 1 event. Figure 5.12 shows a histogram made from a small region of Right Ascension Map 1.

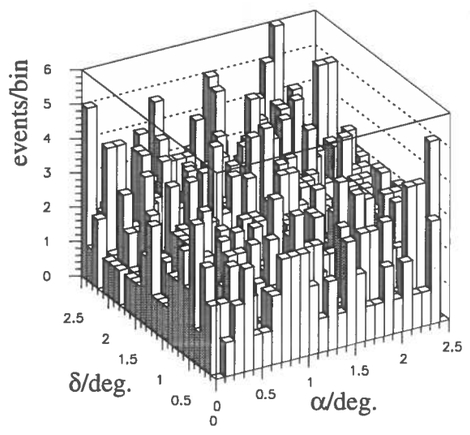


Figure 5.12: A histogram made from a small region of the Right Ascension map made from the large data-set, Map 1.

The standard cuts were applied to the data. These cuts, and the general characteristics of the data, are described in Chapter 2.

5.7 Independent Bins Analysis

The maps as prepared above, and illustrated in Figure 5.12, are not in a form suitable for direct analysis. Because of the small number of events per bin the maps are very noisy. The presence of a source introduces short-range correlations (of size $\sim \sigma$ where σ is the detector resolution) into the data in the region of the map around the source. The raw maps must be reprocessed in a manner that will be sensitive to such correlations. In this Section the simplest possible method, of rebinning the data into bins of a size typical of the detector resolution, is considered.

5.7.1 The Optimum Rectangular Bin

If we rebin the data using an array of close-packed independent rectangular bins the entire visible sky may be covered and the statistical analysis is straightforward. For a source of strength S_{tot} events and coordinates (α_0, δ_0), the proportion of the signal that lies within a bin of dimensions $\Delta\alpha \times \Delta\delta = 2\xi \times 2\upsilon$ *centered on the source* is given by

$$S(\xi, \upsilon|\alpha_0, \delta_0) = \frac{S_{tot}}{2\pi\sigma^2 \sec\delta_0} \int_{\alpha=\alpha_0-\xi}^{\alpha_0+\xi} \int_{\delta=\delta_0-\upsilon}^{\delta_0+\upsilon} e^{-\psi^2/2\sigma^2} d\alpha d\delta, \tag{5.13}$$

where $\psi^2 = (\alpha-\alpha_0)^2 \cos^2\delta_0 + (\delta-\delta_0)^2$. This geometry is illustrated in Figure 5.13. As the Gaussian p.s.f. is separable, this integral can be written in terms of the product of two error functions.

$$S(\xi, \upsilon|\delta_0)/S_{tot} = \text{erf}\frac{\xi\cos\delta_0}{\sigma\sqrt{2}} \text{erf}\frac{\upsilon}{\sigma\sqrt{2}} \tag{5.14}$$

The condition on α_0 has been omitted as the integral is independent of the source's Right Ascension.

If the background rate can be approximated by a constant within the rectangle, then the background expected is $\propto \xi\upsilon\cos\delta_0$. The significance of the deviation that would be measured inside the bin is therefore

$$Z^R(\xi, \upsilon|\delta_0) \propto \frac{\text{erf}\frac{\xi\cos\delta_0}{\sigma\sqrt{2}} \text{erf}\frac{\upsilon}{\sigma\sqrt{2}}}{\sqrt{\xi\upsilon\cos\delta_0}}. \tag{5.15}$$

For positive x, the function $x^{-1/2}\,\text{erf}\,x$ has a single maximum at $x = 0.9899 \approx 1$. Therefore, the optimum rectangle (the one that maximizes Z^R) has dimensions

$$\begin{aligned} \xi &\approx \sqrt{2}\sigma\sec\delta_0 \\ \upsilon &\approx \sqrt{2}\sigma. \end{aligned} \tag{5.16}$$

The dimensions of this bin, and of the optimum cone, are illustrated on Figure 5.13. The proportion of the signal within the optimum rectangle ($\mathrm{erf}^2\, 1 = 0.710$) is almost identical to that within the optimum cone ($1 - e^{-1.256} = 0.715$).

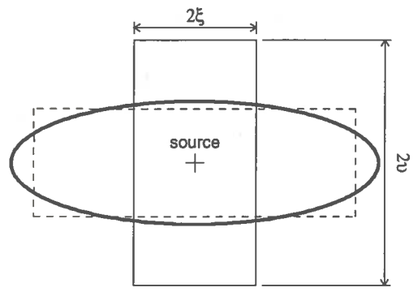


Figure 5.13: A rectangular bin centered on a source with a Gaussian p.s.f. For scale, the heavy ellipse illustrates the geometry of the optimum cone and the broken rectangle that of the optimum rectangular bin.

5.7.2 The Effect of Bin Misalignment

It is unlikely that a source will lie at the centre of any of an array of bins placed arbitrarily on the sky. Consider two bins with the same $2\xi \times 2\upsilon$ geometry but one centered *on source* at (α_0, δ_0) and the other displaced by a small angle to (α_1, δ_1). The proportion of the signal expected in each bin is

$$\begin{aligned} S_0 &= \frac{S_{tot}}{2\pi\sigma^2 \sec\delta_0} \int_{\alpha=-\xi}^{\xi} \int_{\delta=-\upsilon}^{\upsilon} d\alpha d\delta \\ &\times \exp -\frac{1}{2\sigma^2}(\alpha^2 \cos^2\delta_0 + \delta^2) \qquad (5.17) \\ \text{and } S_1 &= \frac{S_{tot}}{2\pi\sigma^2 \sec\delta_0} \int_{\alpha=-\xi}^{\xi} \int_{\delta=-\upsilon}^{\upsilon} d\alpha d\delta \\ &\times \exp -\frac{1}{2\sigma^2}\left\{(\alpha_1 - \alpha_0 + \alpha)^2 \cos^2\delta_0 + (\delta_1 - \delta_0 + \delta)^2\right\} \qquad (5.18) \end{aligned}$$

Equation 5.18 may be written as a power series

$$S_1 = \frac{S_{tot}}{2\pi\sigma^2 \sec\delta_0} \int_{\alpha=-\xi}^{\xi} \int_{\delta=-\upsilon}^{\upsilon} d\alpha d\delta$$

$$\begin{aligned} &\times \exp -\frac{1}{2\sigma^2}\left\{(\alpha^2 \cos^2\delta_0 + \delta^2) + (\alpha_1 - \alpha_0)^2 \cos^2\delta_0 + (\delta_1 - \delta_0)^2\right\} \\ &\times \left[1 - \frac{1}{\sigma^2}\left\{(\alpha_1 - \alpha_0)\alpha \cos^2\delta_0 + (\delta_1 - \delta_0)\delta\right\} + \ldots\right]. \qquad (5.19) \end{aligned}$$

All odd terms in the integral vanish by symmetry, so to first order this is

$$S_1 \simeq S_0 \exp -\frac{1}{2\sigma^2}\left\{(\alpha_1 - \alpha_0)^2 \cos^2\delta_0 + (\delta_1 - \delta_0)^2\right\}. \qquad (5.20)$$

For a close-packed array of bins the maximum misalignment is $\pm(\xi, \upsilon)$. If optimum bins are used then $S_0 > S_1 > \mathrm{e}^{-2}\, S_0$.

5.7.3 Monte Carlo Study of an Independent Bins Analysis

The MACRO group surveyed the sky by studying the distributions of deviations in a close packed array of independent rectangular bins[3]. Equal solid angle bins of $\Delta\alpha \times \Delta \sin\delta = 3° \times 0.04$ where chosen. For this binning $\Delta\alpha$ is constant and $\Delta\delta \propto \sec\delta$ whereas for the optimum rectangle $\Delta\delta$ is constant and $\Delta\alpha \propto \sec\delta$, and so the bins used will be very badly matched to the p.s.f. of the detector at high declinations (given a p.s.f. that is a function of space angle only).

A monte carlo was written to study this analysis method with bins optimized for the SOUDAN 2 resolution. For each iteration a bin centre was chosen randomly in the upper hemisphere and a source's coordinates, relative to that bin centre, chosen to populate the bin uniformly. The proportion of the signal in:

i, an optimum cone centered on the source;

ii, a displaced optimum rectangular bin; *and*

iii, a displaced MACRO rectangular bin

was then computed.

The efficiency of the rectangular bin, ε, is defined to be Z^R/Z^C, where Z^C is the deviation due to the source expected in the on-source cone. From Equation 5.20 we expect to find $\varepsilon \propto \mathrm{e}^{-\psi^2/2\sigma^2}$ where ψ is the space angle between the bin centre. Figure 5.14 shows this relationship from the monte carlo.

For an independent rectangular bins analysis, the χ^2 of the most deviant bin is an analytically simple statistic to study. If $\max\chi^2 > \chi^2_0$ we may reject H_0 with a confidence determined by the number of bins and χ^2_0. If there is a source in the

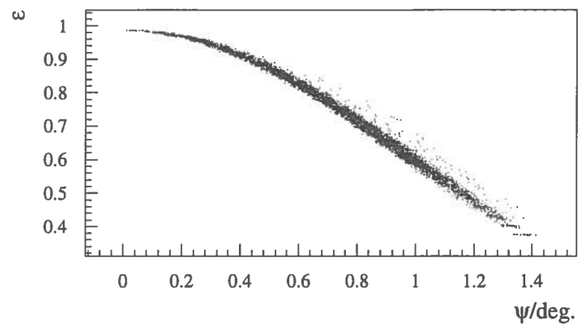


Figure 5.14: Dependence of the efficiency of an optimum rectangle on the space angle between the bin centre and the coordinates of a source.

region of the most deviant bin, and this is the cause of the excess, then the measured $\chi^2 = \varepsilon^2\chi_s^2$, where χ_s^2 is the χ^2 for an on-source bin. The probability of finding the source using an array of bins with an arbitrarily chosen origin, $Pr(\text{detect})$, is therefore equal to $Pr(\varepsilon^2\chi_s^2 > \chi_0^2)$. This distribution was extracted from the monte carlo. Figure 5.15 shows how $Pr(\text{detect})$ varies as a function of χ_s^2/χ_0^2.

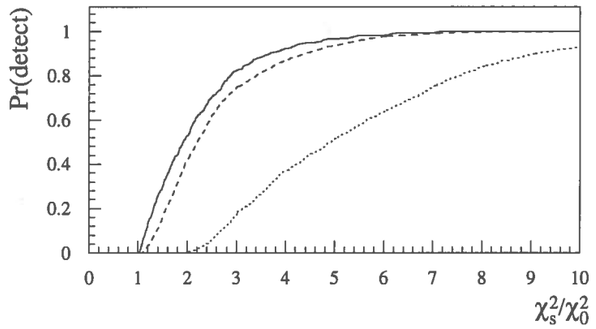


Figure 5.15: The probability of detecting a source with an array of independent close-packed rectangular bins. The solid line is for optimum rectangles at all declinations and MACRO rectangles in $[0, 30°]$. The broken (dotted) line is for MACRO rectangles in $[30°, 60°]$ ($[60°, 90°]$).

5.7.4 Conclusions

Although the use of independent close-packed rectangular bins is susceptible to simple analysis, in practice the power of this method is less than we would naively expect. In particular, the choice of binning suggested by the analytically simple result $d\Omega = d\alpha d(\sin\delta)$ results in a significant loss of power at higher declinations.

Although the MACRO analysis partially corrects for this loss by shifting the array of bins by (ξ, υ), it is better to pursue other methods. These are discussed in Section 5.9.

5.8 Verification of the Whole Sky Background

It is important to verify that the whole sky background computed is a reasonable model of the muon rate across the entire visible sky. This can be done by examining the distribution of deviations $z = (n - \bar{n})/\sqrt{\bar{n}}$ for a set of independent bins sufficiently large that the number of events in each bin, n, is distributed as $N(\bar{n}, \bar{n})$.

Care must be taken that, as the result of this test, we do not reject a valid background model due to the presence of a source or modify the model to eliminate a deviation that is really due to a source. Although it is impossible to compute and test the background using a map that we are certain contains no sources, the work of Section 5.7 shows that it is possible to choose a set of bins that are extremely insensitive to the presence of point sources and yet have an event rate sufficiently high for the normal approximation to be made.

The maps were divided into an array of independent close packed bins with geometry $\Delta\alpha \times \Delta\delta = 0.5° \times 4° \sec\delta$. The maximum efficiency of such a bin is $\text{erf}\, 2^{-3/2}\, \text{erf}\, 2^{3/2} / \text{erf}^2\, 1 = 0.54$ times the efficiency of an optimum bin. This is for a correctly aligned bin at zero declination, the mean is $\lesssim 10\% \times 0.54$ times the optimum for randomly aligned bins and declinations.

For each set of bins with a common declination, where the average expectation exceeded 200/bin, the deviation z was computed. Figure 5.16 shows the distribution of deviations for the 11520 bins that passed this cut. The lowest (bin centre) declination that passed was at $-2°$ and the highest at $+76°$. The curve is a Gaussian with norm 11520, zero mean and unit r.m.s. The χ^2 for the bins with over ~ 10 entries is 65.3 for 60 d.o.f., indicating that the background is an acceptable description of the data.

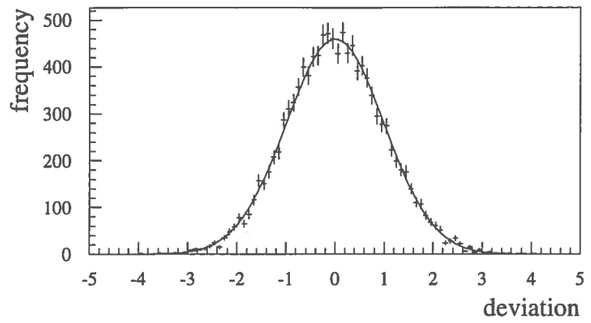


Figure 5.16: The distribution of deviations for 11520 independent close packed bins with a geometry insensitive to point sources.

5.9 Smoothing the Maps

The principal method used to render the raw maps into a form suitable for analysis was to smooth the maps by convolution with a *kernel* chosen using *a priori* knowledge of the p.s.f. The identical procedure must be applied to both the data and background maps.

Two kernels were used:

i, a simple kernel chosen so that the value stored in each pixel of the smoothed map was equal to the number of events seen/expected in an optimum cone centered on that pixel; *and*

ii, a Gaussian kernel with an r.m.s. of 1° — i.e. matched to the *a priori* p.s.f.;

the analysis of both procedures will be followed in parallel.

5.9.1 Optimum Cone Smoothing of the Maps

Optimum cone smoothing was performed for slices 17 to 1283, allowing smoothing with a $1.6°$ cone over the declination range $[-38.35°, 88.25°]$. For each slice the 16 slices on either side were read in and stored in an array. An array of weights was also prepared. If the space angle squared, computed as $\Delta\alpha^2 \cos^2\delta + \Delta\delta^2$, between the each element of the weight array and the central element was less than $2.56(°)^2$ then the weight was set to 1, otherwise it was set to 0. For each of the 3600 bins in

Right Ascension the product of the weights array and the map array was computed, and stored in the appropriate bin of a new, smoothed, map. The arrays wrapped around at $0/360°$. Figure 5.17 is a representation of the process.

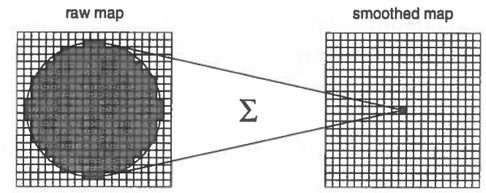


Figure 5.17: A symbolic representation of the process of smoothing a map.

The procedure was implemented in the identical manner for both the Right Ascension maps and the background maps. For the background maps the arithmetic was done as `INTEGER`s, and the pixel values scaled by 10^{-4} for writing to file. This retained the 7 digit precision but allows for the increase of $\sim 10^3$ in pixel value after smoothing.

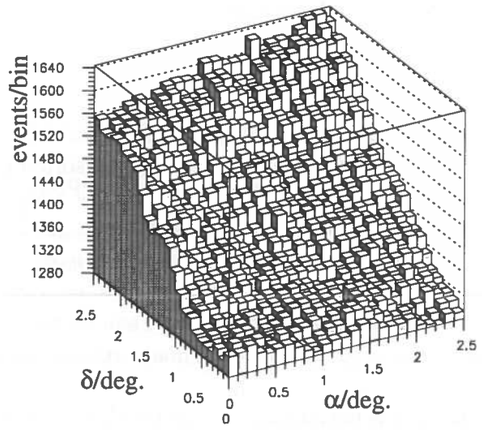


Figure 5.18: A small region of the smoothed map made from the large data set. The same region as in Figure 5.12 (on Page 106) is shown.

Figure 5.18 shows the region of the smoothed Right Ascension map corresponding to the raw map region shown in Figure 5.12. The strong systematic

dependence on the coordinates is now visible.

5.9.2 Gaussian Smoothing of the Maps

The procedure for smoothing with a Gaussian kernel almost identical to that of Section 5.9.1. The weights were taken to be $e^{-\psi^2/2\sigma^2}$, where ψ is the space angle between the weight element and the centre of the array, and the summation is done out to $\pm 3\sigma$. All arithmetic was done in `REAL` rather than `INTEGER` variables and both smoothed Right Ascension map and smoothed background map were stored after scaling by the factor 10^3.

5.9.3 The Deviations Map

Once both the Right Ascension and background maps have been smoothed, it is possible to construct a map of standardized deviations, $Z(\alpha, \delta)$, by subtraction of the background and dividing by the square-root of variance. For the Gaussian kernel this variance must be carefully calculated from the sum of the squares of the weights used. As the number of events/cone is typically ~3000–4000, Z for a given point in the sky, (α, δ), should be distributed as $N(0, 1)$.

5.9.4 Analysis Procedure

A program was written to systematically search for the extrema of Z. As the program searches the map it keeps a list of the most deviant points, sorted by $|Z|$. For the simple kernel, the deviations map prepared is a realization of a Mosaic process[4], and it is characteristic of such a process that the number of turning points (local maxima and minima) in the process is not significantly less than the number of turning points in the underlying field of random variables, so such a search finds *clumps* of local extrema with a size characteristic of the smoothing kernel. A simple search would locate only a few of such clumps (as many extrema are found for each clump).

During the search a point was not added to the current list if it was within 1.6° of a previously found extremum and less deviant than it; if the point was more deviant it was added to the list and all points within 1.6° of that point were removed from the list. i.e. While finding the pixel with the most extreme deviation a list of the clumps was compiled, with the most deviant local extremum taken to represent the size and location of the fluctuation that underlies the clump.

For the Gaussian kernel the number of turning points in the smoothed map is significantly reduced, however the same search program was used.

The distribution of the statistic sup Z, given an underlying Gaussian field may be calculated (see Section C.2). It is assumed that, although the underlying field is Poissonian, this formula is applicable as the covariance function is approximately that of a Gaussian field — the difference between Z_{i+1j} (or Z_{ij+1}) and Z_{ij} is approximately normal as the fluctuations are driven by ~ 100 pixels.

No pixels where the smoothed background estimate is less than 200 events are examined. This is a very conservative cut to ensure normally distributed data and effectively cuts out declinations below $\sim -15°$. At the very highest declinations, where the *size* of a source is $\sim 100°$, the correlation between background estimate and the source is no longer negligible. Therefore, no pixels above $+85°$ are examined.

5.10 The Whole Sky Monte Carlo

A monte carlo was written to simulate the entire analysis procedure. The computation was exceedingly C.P.U. intensive[4] so only a limited study could be made. The simple kernel analysis on the large data-set was simulated.

5.10.1 Implementation of the Whole Sky Monte Carlo

Generation of a Monte Carlo Data Map

A data map was made by generating a Poisson number for each pixel of the background map where the expected number of events was not zero. For a typical map this involves the generation of $\sim 15 \times 10^6$ uniform random numbers, and so the procedure is very sensitive to the quality of the generators used. The `POISSN` routine[21] was rewritten to do some internal arithmetic in `DOUBLE PRECISION` and to generate uniform random numbers using an in-line version of the `RANECU` portable generator[22]. `RANECU` has a sequence length of $\sim 10^{18}$ numbers. The Bayes-Durham Algorithm with an array of length[5] 4099 was implemented[2]. At the end of generation the random number seeds were written to disc, so that the next iteration could begin from the next random number in the sequence.

[4] Each iteration requiring 1 hour of C.P.U. on an *Alpha* machine.

[5] 4099 is a prime number.

The total number of events generated (i.e. the sum over all bins of the monte carlo map) was saved to allow the background map to be normalized to the monte carlo map (their norms will agree on average, but should be identical). As there are $\sim 10^7$ events generated, this correction will typically be $\sim 10^{-4}$.

Further Processing of the Generated Map

Once a monte carlo map had been generated it was processed in an identical manner to the experimental data maps. At the end of each iteration a list of the ten clumps with the most extreme deviations was saved.

5.10.2 Results of the Simulation

A total of 632 iterations were run. Following Siegmund's calculation[77] and Reference [25], we take $\sup Z$ to have the distribution

$$Pr(\sup Z > b) = F(b) = 1 - \exp\left\{-\frac{\Omega}{\Delta\Omega} b^3 \frac{e^{-\frac{1}{2}b^2}}{\sqrt{2\pi}} \nu(b\sqrt{2/\rho r_1})\nu(b\sqrt{2/r_2})\right\} \tag{5.21}$$

ν is Siegmund's function, which is has the limit $\nu(x) \simeq e^{-0.583x}$. $r_1 \times r_2$ is the size (in bins) of a simple *rectangular* kernel. The kernel used is an ellipse with major diameter $\sim \sec\delta$ which, for the purposes of this calculation, we approximate by a *mean rectangle* of 29×56 bins. A parameter, ρ, is introduced as a "fudge factor" to correct for error in this approximation — for a rectangular kernel $\rho \equiv 1$. Ω is the total solid angle searched, and $\Delta\Omega$ the solid angle subtended by the smoothing kernel.

Figure 5.19 shows the observed distribution and fitted p.d.f. $f(b) = dF/db$. The agreement is excellent, $\chi^2 = 39.4$ for 40 d.o.f. ρ is estimated to be 1.92 ± 0.12. There were 417/623 trials in which the most deviant bin (i.e. $\max|Z|$) was positive and 215/623 in which it was negative. This is inconsistent with a common rate independent of sign ($\chi^2 = 64$ for 1 d.o.f.) as we would expect for a genuinely Gaussian process. The asymmetry is probably due to the residual Poissonian nature of the fluctuations, which becomes significant in the tails of the distribution. The observed rates, for a sample of values of the threshold b, are summarized in Table 5.2.

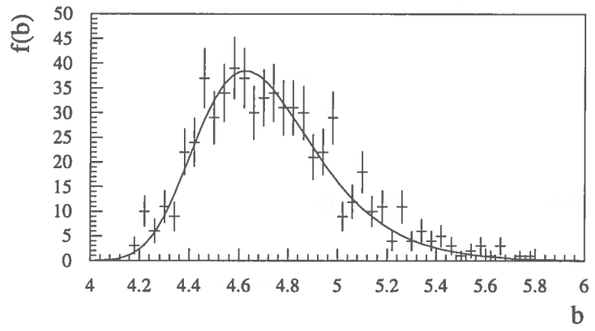


Figure 5.19: The observed and expected distributions of $\max Z$.

b	rate	error
4.7	0.513	0.019
4.8	0.383	0.019
4.9	0.267	0.018
5.0	0.174	0.015
5.1	0.125	0.013
5.2	0.079	0.010
5.3	0.054	0.009
5.4	0.033	0.007
5.5	0.019	0.005
5.6	0.011	0.004
5.7	0.005	0.003

Table 5.2: Table of critical values of $\max Z$, estimated from the monte carlo. Binomial errors are quoted.

5.10.3 Statistical Tests of the Monte Carlo

Given that the monte carlo is a complex simulation of the entire analysis procedure, it is important to verify, where possible, that the monte carlo is behaving in the manner it should. Two types of error are important: bias, when a particular region of the sky is "hot" relative to the norm due to systematic problems with the background calculation; *and* drift, when the probability/trial of finding a given extremum is not constant due to error in the random number generator.

Test of Bias: the Coordinates of Extrema

Figure 5.20 shows the distribution of the 632 extrema on the celestial sphere. If monte carlo is unbiased then α_i should be distributed as Uniform$(0, 360°)$ and δ_i as $\cos\delta$. The Kolmogorov test[52] was used to investigate whether this was true for the actual data. The confidence limits found were 36.2% and 29.6% respectively (combined confidence 34.6%), indicating no significant bias.

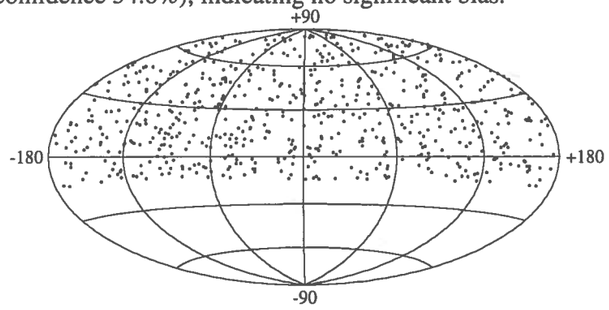


Figure 5.20: The coordinates on the celestial sphere of the global extremum of each of the 632 monte carlo trials. i.e. $(\alpha_i, \delta_i) : Z_i = \max|Z|$.

Test of Drift: the Threshold Crossing Interval

If there is no drift in the simulation then $Pr(\sup Z > b) = p$, for some b, is a constant common to all trials. The probability that there is a interval of t trials between successive occurrences of the event $\max Z > b$ is[6] $p(1-p)^t$. A histogram

[6]This formula implies the somewhat counter-intuitive result that the most likely time we would expect a rare phenomenon to occur is immediately after we start looking for it! The mean, however, is $1/p$ as we would expect.

was made from the observed set of intervals with the threshold set to $b = 5$, and a likelihood fit to the expected distribution made. p was estimated to be 0.175 ± 0.015. (This agrees with the value in Table 5.2.) Figure 5.21 shows the distribution of the 110 intervals.

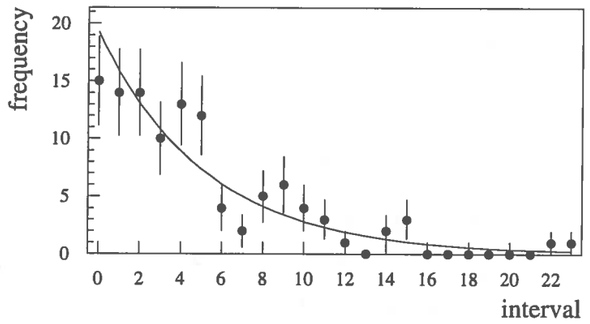


Figure 5.21: The observed and fitted intervals distribution.

A Kolmogorov like test was then used to determine whether there was a significant discrepancy between data and theory. The statistic was taken to be $D_n = \max_i |S_i - F_i|$, where S_i and F_i are the observed and expected cumulative distributions, for $n = 25$ bins. With $\hat{p} = 0.175$ and 110 intervals, the distribution of $D_n\sqrt{n}$ was computed using a monte carlo.

The observed value of $5D_{25}$ was 0.28 and the probability of getting a larger value by chance is estimated to be 86%. Therefore, it seems unlikely that the rate has drifted significantly during the simulation.

5.11 Monte-Carlo Simulation of the Behaviour of a Map Containing a Source

5.11.1 Details of the Simulation Performed

In Section 5.10 the process of surveying a whole sky map is studied under the null hypothesis, H_0: *there are no point sources of underground muons.* In this section the process is examined under the alternative hypothesis, H_n: *there are n point sources of underground muons.* To reduce computation time only one source is postulated, and the analysis is restricted to a $10° \times 10°$ region around this source.

The region chosen[7] is centered on $(190°, 0°)$. The background was taken to be that for the large data-set.

For each of 1000 iterations:

i, The background expectation per bin, typically 2–3, was used to generate a number of background events for bin. A Poisson generator was used. Events were generated for a 1.6° "skirt" surrounding the region under study.

ii, A source was simulated by adding n_{src} events drawn from a Gaussian with width $\sigma = 1°$ and mean position in the centre of the region under study. A Gaussian generator was used to generate pairs of coordinates (α, δ), where $\alpha \sim N(190°, (1°)^2)$ and $\delta \sim N(0, (1°)^2)$, and the bin in which these coordinates lay was incremented by one.

iii, The data was then smoothed in the same manner as the whole sky maps. Smoothing could be performed on the entire $10° \times 10°$ region, with the summations extending into the skirt region.

iv, A deviations map was computed by subtracting the background, and this then searched for $\max Z$.

5.11.2 Six *Empty* Maps

Figure 5.26 (on Page 125) shows six deviations maps that were generated without adding any source events. A colour scale is used to represent the deviation at each pixel: the colour varies linearly from saturated blue (-5 s.d.) through white (-0.35 to $+0.35$ s.d.) to saturated red ($+5$ s.d.). The scale saturates at ± 5 s.d. These maps allow a feel for the typical behaviour of such a Mosaic process to be developed. The eye can pick out *clumps* and *threads* in each field.

5.11.3 Study of the Statistical Misalignment of a 220 Event Source

Initially a 220 event source was added, this corresponds to $\max Z \sim 5$ s.d. Figure 5.27 (on Page 127) shows six maps to which a source was added. A central excess region is clearly visible in all six, although the size, width, and position of the

[7]This choice is based upon the analysis of Chapter 6.

excess shows some scatter. Figure 5.22 shows the distribution of the coordinates of the extremum found (*at peak*) relative to the nominal coordinates of the introduced events (*on source*).

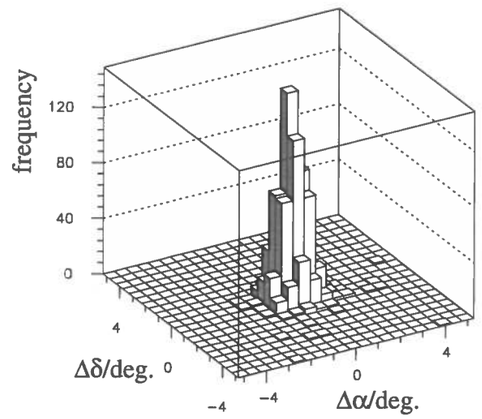


Figure 5.22: The distribution of the peak coordinates about the on source coordinates for a 220 event source.

As this appears to show a Gaussian dependence, the distribution of the space angle between the source and peak, ψ, was fitted to

$$a\psi e^{-\psi^2/2b^2}, \tag{5.22}$$

where a and b are free parameters. This is a convenient parameterization of the form we might expect for a joint Normal distribution. As can be seen from Figure 5.23, the agreement is satisfactory:

$$\begin{aligned} a &= 378 \pm 16 \\ b &= 0.503 \pm 0.003 \\ \chi^2/\text{d.o.f.} &= 1.29. \end{aligned} \tag{5.23}$$

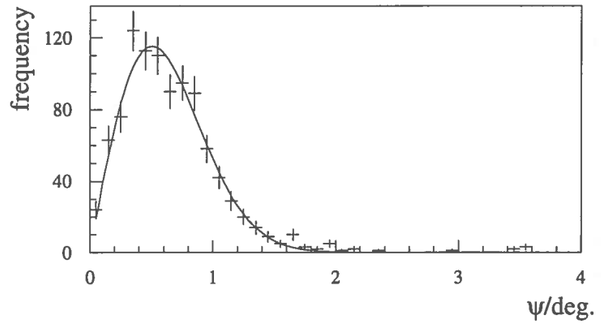


Figure 5.23: The distribution of the space angle between the peak and source for a 200 event source.

5.11.4 Study of Misalignment as a Function of Signal Strength

The analysis of Section 5.11.3 was then repeated for n_{src} =10, 20, 30, 60, 100, 200, 300, 600, 1000 and 2000 events. For each strength, the sample mean and standard deviation of Z was computed at the on-source position and at the peak (maximum) found by searching. Figure 5.24 shows the correlation between these quantities as n_{src} is varied.

For each strength the distribution of space angles, ψ, was fitted to Equation 5.22. This can then be used to compute the probability of finding the source being found (by this procedure) within a given space angle of it's true position. If $\psi_{1-\alpha}$ defines a cone about the true position, such that the probability that the source is not found within the cone is α *per trial*, then

$$\psi_{1-\alpha} = b\sqrt{-2\ln\alpha}. \tag{5.24}$$

Figure 5.25 shows how the radius of the confidence regions varies with n_{src} for those values for which a fit was possible. For $n_{src} \lesssim 100$, there is a background due to maps in which the maximum of Z was not associated with the added source. A cut was made to remove this before fitting.

5.11.5 Conclusions

The monte carlo described shows that analysis procedure adopted is unlikely to find a source at the nominal position (if it is known) — the corollary of this is that the

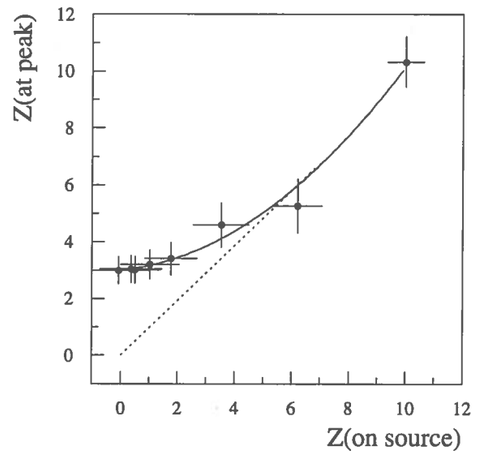


Figure 5.24: The correlation between the deviation, Z, on source and at the peak found. For each strength 1000 iterations were run; the plotted point is the mean and the error bar the standard deviation.

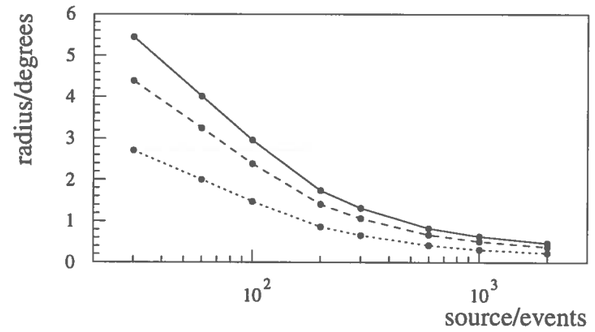


Figure 5.25: The radius of the 68%, 95% and 99% ($\sim$ 1, 2, and 3 s.d.) confidence regions as a function of source strength.

position at which a candidate excess is unlikely to coincide exactly with a known object, event if that object were a real source of deep underground muons. This statistical misalignment is due to fluctuations of both the background and the source events.

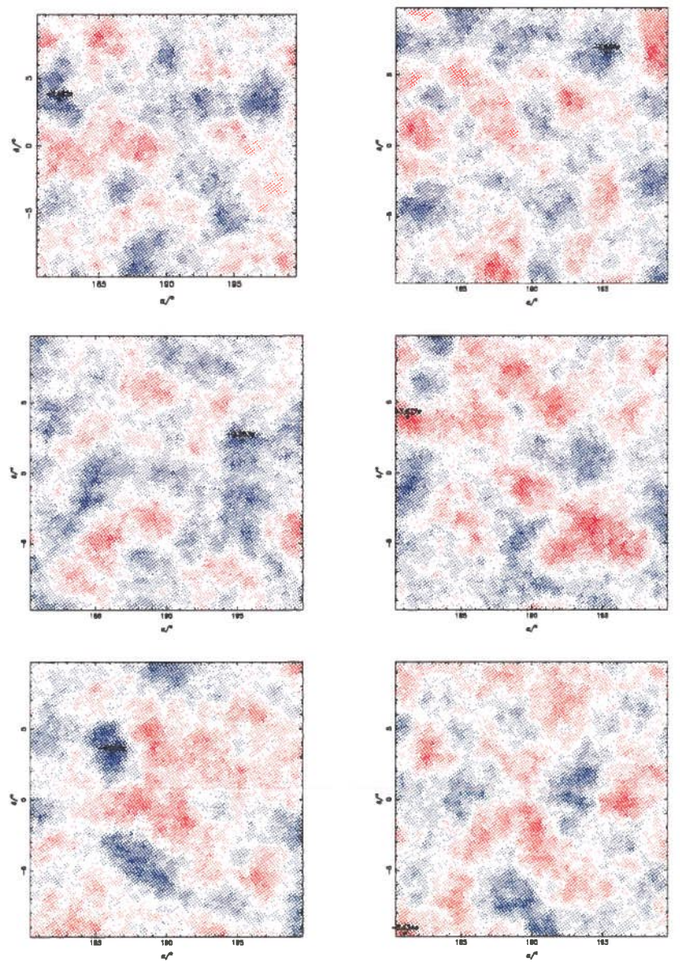


Figure 5.26: Six monte carlo maps for the 20° × 20° region centered on (190°, 0). The scale ranges linearly from −5 s.d. (saturated blue) to +5 s.d. (saturated red). The extremum of each region is marked. No source events were added.

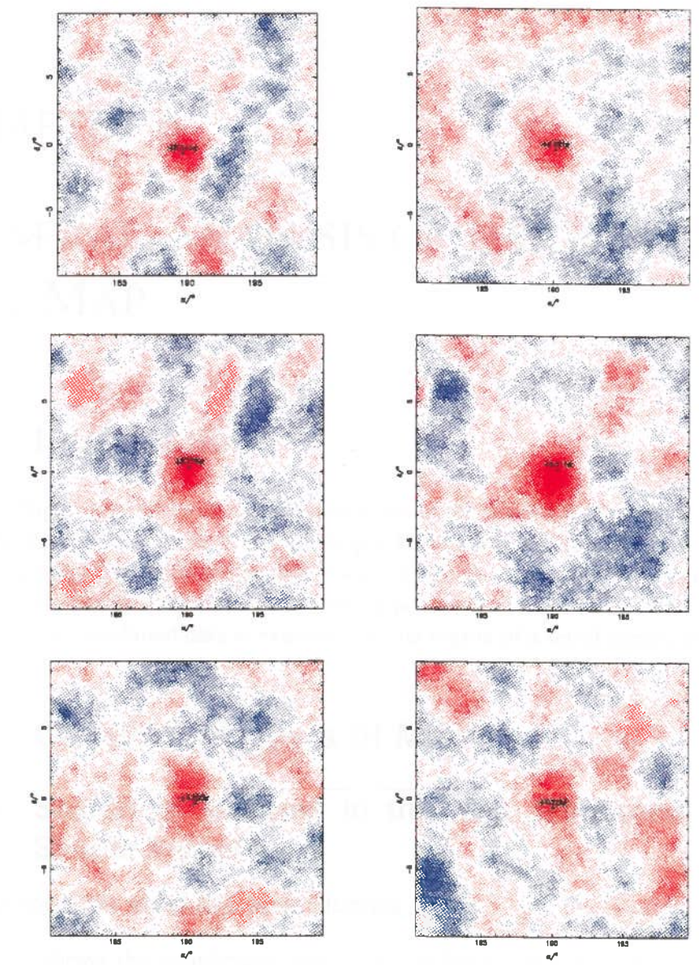


Figure 5.27: Six monte carlo maps for the $20° \times 20°$ region centered on $(190°, 0)$. The scale ranges linearly from -5 s.d. (saturated blue) to $+5$ s.d. (saturated red). The extremum of each region is marked. 200 source events were added at the centre of the map.

Chapter 6

General Analysis of the Whole Sky Map

6.1 Introduction

In this chapter the results of a general analysis of the maps are presented. The maps have been smoothed with both the simple kernel and a Gaussian kernel and the results of these two methods are discussed in parallel. A general analysis is made of Map 1. Map 2 is then studied in a manner dependent upon the result of this analysis. A map of the combined data is examined in the region of a set of candidate sources.

6.2 General Analysis of Map 1

6.2.1 Search of Extrema in the Map Smoothed with a Simple Kernel

List of the Fifty Most Extreme Clumps

Table 6.1 shows the coordinates and deviation for the fifty extrema identified in Map 1 by the search procedure. The coordinates and Z are taken to be those of the most deviant pixel in the clump. For book-keeping purposes, I shall refer to a point with index n as MX–n (for a muon excess) and MD–n (for a muon deficit).

From Section 5.10.2 we see that the most likely value of $\sup Z$ (the mode) is

n	Z	$\alpha/°$	$\delta/°$	n	Z	$\alpha/°$	$\delta/°$
1	5.071	189.25	1.75	26	−4.030	325.65	48.15
2	4.821	50.55	13.65	27	4.027	2.45	30.75
3	−4.510	311.65	60.05	28	−4.020	323.25	−0.55
4	4.457	96.95	46.15	29	4.000	288.65	50.45
5	−4.343	348.75	74.85	30	−3.982	196.65	68.85
6	−4.343	33.75	11.85	31	3.957	138.15	35.15
7	−4.259	48.95	84.05	32	3.942	76.35	47.55
8	4.247	144.85	−13.55	33	3.939	179.35	8.95
9	4.225	83.55	−9.55	34	3.934	120.05	0.35
10	4.220	185.65	26.75	35	3.933	112.45	8.75
11	−4.164	292.35	28.05	36	3.929	95.65	2.95
12	−4.156	231.75	2.65	37	−3.911	112.65	20.05
13	4.155	212.15	37.85	38	3.910	297.15	75.45
14	−4.138	260.75	62.95	39	3.900	146.85	35.35
15	4.122	277.45	66.65	40	3.898	313.05	38.15
16	4.104	175.55	52.35	41	−3.878	348.85	76.66
17	−4.099	185.65	21.45	42	3.862	145.45	−6.75
18	−4.098	157.55	32.55	43	3.852	350.45	−3.45
19	4.097	131.35	75.95	44	3.846	210.65	77.95
20	4.081	139.45	39.35	45	3.829	221.95	12.65
21	−4.078	101.05	15.55	46	−3.818	227.05	40.55
22	4.071	19.75	17.45	47	3.814	193.45	34.45
23	4.066	143.15	4.75	48	3.793	120.65	43.75
24	4.050	208.05	62.25	49	3.786	352.35	62.95
25	−4.042	219.75	−0.15	50	3.775	2.95	15.95

Table 6.1: List of the fifty most deviant clumps in Map 1, as identified by searching the map smoothed with the simple kernel.

~ 4.6. The probability of exceeding this value is just below 50% (see Table 5.2)[1]. The list shows two positive clumps, $Z = 5.1$ at celestial coordinates $(189.25°, 1.75°)$ and $Z = 4.8$ at $(60.55°, 13.65°)$, before the most negative region, $Z = -4.5$ at $(311.65°, 60.05°)$. Since a point source cannot cause a 'hole' in the map (except on the unlikely hypothesis that *all* the muon flux is due to point sources) then an extreme negative region could only be caused by:

i, a statistical fluctuation; *or*

ii, a localized systematic problem with the background calculation.

The analysis of Section 5.10 shows that there is no reason to suspect the latter. Assuming the residual Poissonian bias in the distribution of $\sup Z$ can be neglected, then the probability of the most negative point exceeding $-b$ is equal to $Pr(\sup Z > b)$. This gives a probability of $\sim 81\%$ for this clump; there is no reason to infer that this is due to anything other than a fluctuation.

The two clumps with the largest absolute deviations are also the clumps with the largest positive deviations. They have chance probabilities of 13% and 35% respectively, assuming that their independence (the space angle between the points is 127°) allows the same formula to be used for both points. Neither *a priori* probability is compelling evidence for an anomalous flux at either of the points. However, on this analysis, these points indicate the most likely coordinates of any point source. Based on this analysis alone, there is no justification for treating any of the other positive clumps as candidates.

The distribution of $|Z|$ for these fifty clumps is shown in Figure 6.1. The cutoff at $|Z| \sim 3.5$ is due to the selection of only the top fifty clumps. The distribution shows evidence of the residual Poissonian bias indicated by the monte-carlo of Section 5.10.

Sky Maps in the Region of the Extrema

Figure 6.10 (on Page 147) shows the deviations map for a $20° \times 20°$ region near the three most deviant points (on the left hand side of the figure). The region around MX–1 shows an extended region in excess, with a size of order 5–6°, whereas a more compact excess is found around MX–2 ($\sim 3°$) and MD–3 ($\sim 7° = 3.5° \sec 60°$).

[1] Probabilities are calculated by using the Siegmund formula, Equation 5.21, as fitted to the whole sky monte carlo. See Appendix C for a discussion of this formula.

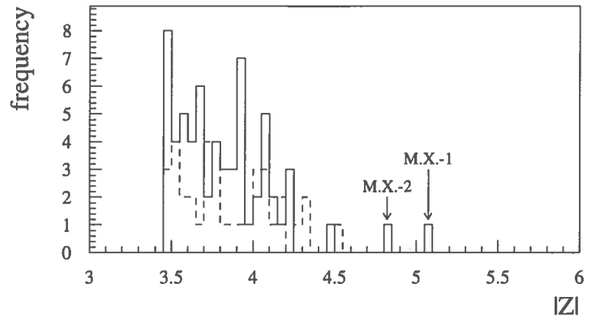


Figure 6.1: The distribution of $|Z|$ for the fifty most deviant clumps found by searching Map 1 after smoothing with a simple kernel. The solid histogram is for the positive clumps, and the broken histogram for the negative clumps.

Test of Association with Known Sources by Positional Coincidence

For each of the 33 positive clumps identified in Table 6.1, the space angle, ψ, to each of a list of possible candidate sources (to avoid duplication, these objects are listed in Table 6.7 on Page 146) was computed. $\min\psi$ was then taken as a statistic to test association of that clump with the nearest source.

Figure 6.2 shows the distribution of $\min\psi$ for a point chosen *at random* within the detector acceptance (i.e. $\delta \in [-15°, 85°]$). 100 000 trials of a simple monte carlo were run to examine this distribution.

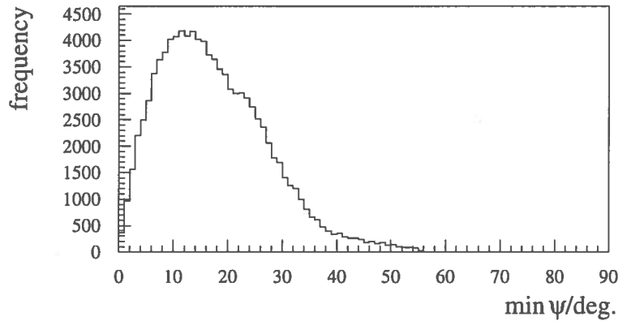


Figure 6.2: The distribution of the space angle between a point chosen at random in the sky and the nearest source (of those listed in Table 6.7).

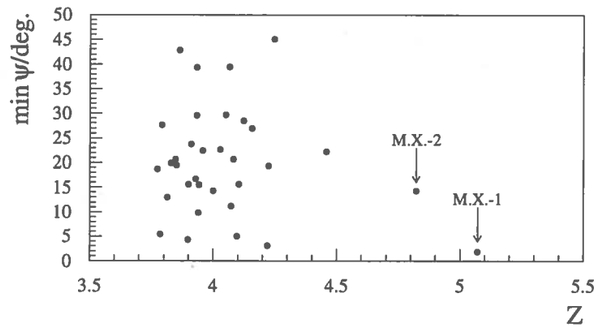


Figure 6.3: The scatter of $\min\psi$ against Z for the 33 positive clumps taken from Table 6.1.

Figure 6.3 shows the distribution of $\min\psi$ against Z for the 33 clumps. Under the null hypothesis, that there are no point sources of underground muons, there should be no correlation between these two variables. From the set selected, the clump with the smallest space angle to a possible source is also the clump that contains the most deviant pixel in the entire sky: MX–1, at $(189.25°, 1.75°)$, is just $1.90°$ degrees away from A.G.N. 3C 273, at $(187.3°, 2.05°)$ J2000.0. A random point was within this distance of any of the listed sources in $1\,189/100\,000$ trials $= 1.2\%$. This is the probability that the clump which contains $\max Z$ lies within $1.90°$ of any of the listed sources — the probability that one or more of the 33 clumps tested lies within that angle of any of the sources is 32%.

The closest source to MX–2 is PKS 0235+164, $14.3°$ away at $(36.05°, 16.62°)$. The nearest source to each of the 33 clumps is shown in Table 6.2.

The Distribution of the Clumps on the Sphere

It is possible that a number of real muon excesses may exist, but that they are not sufficiently large to produce a statistically significant clump in the map. However, such excess may introduce a bias into the distribution of the most deviant clumps on the sphere.

This hypothesis was checked using the Kolmogorov test[52]. The distribution of clump Right Ascensions and declinations were independently checked against their theoretical distributions (see Section 5.10.3). The confidence that the data was not anomalously distributed was 14% for Right Ascension and 52% for declination.

n	Z	$\psi/°$	Name	n	Z	$\psi/°$	Name
1	5.071	1.90	3C 273	32	3.942	15.45	V 0332+53
2	4.821	14.30	PKS 0235+164	33	3.939	9.86	GRO J1220+16
4	4.457	22.16	A 0535+26	34	3.934	39.32	PKS 0528+134
8	4.247	45.00	3C 273	35	3.933	29.62	PKS 0528+134
9	4.225	19.31	PKS 0420-014	36	3.929	16.66	PKS 0528+134
10	4.220	3.16	GRO J1221+23	38	3.910	23.78	GF 2259+586
13	4.155	26.90	GRO J1221+23	39	3.900	15.58	Mrk 421
15	4.122	28.51	4C 38.41	40	3.898	4.36	EXO 2030+37
16	4.104	15.58	Mrk 421	42	3.862	42.79	3C 273
19	4.097	5.02	QSO 0836+710	43	3.852	19.49	QSO 2230+114
20	4.081	20.65	Mrk 421	44	3.846	20.67	QSO 0836+710
22	4.071	11.21	PKS 0202+149	45	3.829	19.94	4C 10.45
23	4.066	39.43	Mrk 421	47	3.814	12.92	GRO J1221+23
24	4.050	29.73	QSO 0836+710	48	3.793	27.59	QSO 0836+710
27	4.027	22.64	3C 454.3	49	3.786	5.42	GF 2259+586
29	4.000	14.26	4C 38.41	50	3.775	18.70	3C 454.3
31	3.957	22.47	Mrk 421				

Table 6.2: The nearest sources for the 33 positive clumps identified when searching Map 1 after smoothing with a simple kernel.

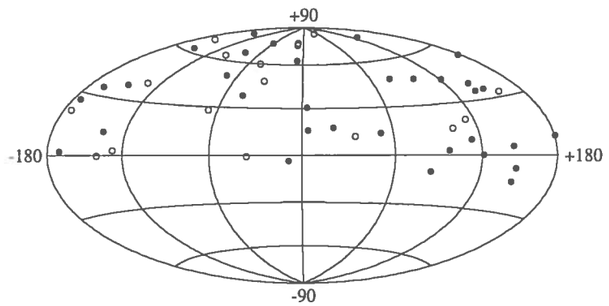


Figure 6.4: The distribution of the 50 most deviant clusters, found by searching Map 1 after smoothing with a simple kernel, on the celestial sphere. Solid circles indicate an excess, and hollow circles a deficit.

The combined confidence is 26%. There is, therefore, no evidence from Map 1 to support this hypothesis. The distribution of clump coordinates is shown in Figure 6.4.

6.2.2 Search of Extrema in the Map Smoothed with a Gaussian Kernel

List of the Fifty Most Extreme Clumps

Table 6.3 shows the coordinates and deviation for the fifty extrema identified by searching Map 1 after it had been smoothed with a Gaussian kernel. As in Section 6.2.1, the most deviant pixel is taken as the coordinates of the clump located.

For this kernel the probability that the most deviant point exceeds some threshold, b, is calculated to be[4, 77]:

$$Pr(\sup Z > b) = 1 - \exp\left\{-\frac{\Omega}{2\sigma^2} b \frac{e^{-\frac{1}{2}b^2}}{(2\pi)^{3/2}}\right\}, \tag{6.1}$$

where Ω is the solid angle searched and σ is the r.m.s. width of the smoothing kernel. For this distribution the most likely value of $\max Z$ is ~ 4.0. The probability of exceeding this value is 66%.

The most deviant point is $Z = 4.4$ at $(189.65°, 2.05°)$, with a probability of 22%. This is clearly due to the same cluster of events that gave rise to the clump MX–1 when smoothed with a simple kernel. The second point is negative, $Z = -4.3$ at $(311.05°, 60.15°)$, and is in the same region of the sky as MD–3. It has a chance probability of 34%. The third most deviant clump is $Z = 4.1$ at $(50.35°, 13.85°)$ with a chance probability of 49%. This is the same region as MX–2. The distribution of $|Z|$ for this kernel is shown in Figure 6.5 (on Page 137).

Sky Maps in the Region of the Extrema

Figure 6.10 (on Page 147) shows the deviations map for a $20° \times 20°$ region near the three most deviant points (on the right hand side of the figure). It is clear that the Gaussian kernel has produced a considerably smoother surface, but that the main features of the image remain the same.

n	Z	$\alpha/°$	$\delta/°$	n	Z	$\alpha/°$	$\delta/°$
1	4.370	189.65	2.05	26	−3.348	337.75	8.75
2	−4.255	311.15	60.15	27	−3.336	195.35	12.75
3	4.126	50.35	13.85	28	3.331	206.85	61.35
4	−4.012	292.05	28.55	29	3.321	179.85	8.75
5	−3.958	231.95	2.55	30	−3.319	219.95	−0.55
6	−3.906	347.95	75.25	31	−3.301	324.45	48.05
7	3.891	96.25	46.45	32	−3.300	157.05	32.15
8	3.796	186.75	27.25	33	3.288	145.55	−7.05
9	3.705	119.85	0.05	34	−3.285	323.15	−0.55
10	3.669	277.05	66.25	35	3.256	145.55	37.85
11	−3.639	185.25	21.35	36	−3.234	13.35	20.15
12	3.626	350.45	−3.35	37	3.225	82.55	−9.45
13	3.588	313.85	37.95	38	−3.205	227.05	40.65
14	−3.588	260.45	63.45	39	−3.203	183.45	30.65
15	3.569	147.35	35.55	40	3.198	182.45	3.75
16	3.558	212.65	37.45	41	3.192	186.95	−3.95
17	3.540	130.95	76.15	42	3.186	333.15	31.55
18	−3.534	100.75	15.95	43	−3.185	198.35	68.35
19	3.528	139.65	39.45	44	3.184	222.45	12.55
20	3.519	176.35	52.55	45	3.181	353.15	63.25
21	3.495	296.65	75.05	46	3.176	289.45	49.75
22	3.453	51.95	−6.85	47	−3.171	339.55	20.85
23	3.440	19.75	17.25	48	3.166	2.85	16.65
24	−3.417	45.35	83.55	49	−3.165	12.95	49.65
25	−3.391	34.05	12.65	50	3.154	38.75	11.35

Table 6.3: List of the fifty most deviant clumps in Map 1, as identified by searching the map smoothed with a Gaussian kernel.

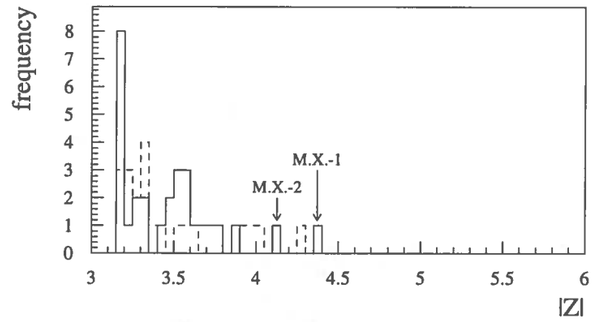


Figure 6.5: The distribution of $|Z|$ for the fifty most deviant clumps found by searching Map 1 after smoothing with a Gaussian Kernel. The solid histogram is for the positive clumps, and the broken histogram for the negative clumps.

Test of Association by Positional Coincidence

The space angle to the nearest listed source was also computed for the 29 positive regions identified in Table 6.3. Figure 6.6 shows the distribution of $\min \psi$ against Z for these 30 regions.

The space angle between MX–1 and 3C 273 has shifted slightly to 2.26°. A random point was within this distance of any of the listed sources in $1\,670/100\,000 = 1.7\%$ of the monte carlo trials. MX–2 is marginally closer to PKS 0235+164.

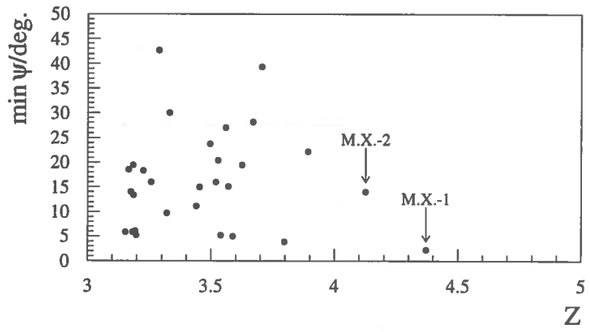


Figure 6.6: The scatter of $\min \psi$ against Z for the 29 positive clumps taken from Table 6.3.

n	Z	$\psi/°$	Name	n	Z	$\psi/°$	Name
1	4.370	2.26	3C 273	23	3.440	11.18	PKS 0202+149
3	4.126	14.07	PKS 0235+164	28	3.331	30.06	QSO 0836+710
7	3.891	22.18	A 0535+26	29	3.321	9.73	GRO J1220+16
8	3.796	3.84	GRO J1221+23	33	3.288	42.75	3C 273
9	3.705	39.25	PKS 0528+134	35	3.256	16.08	Mrk 421
10	3.669	28.11	4C 38.41	37	3.225	18.37	PKS 0420-014
12	3.626	19.42	QSO 2230+114	40	3.198	5.20	3C 273
13	3.588	4.97	EXO 2030+37	41	3.192	6.09	3C 273
15	3.569	15.14	Mrk 421	42	3.186	13.40	SS Cyg
16	3.558	27.10	GRO J1221+23	44	3.184	19.45	4C 10.45
17	3.540	5.21	QSO 0836+710	45	3.181	5.88	GF 2259+586
19	3.528	20.49	Mrk 421	46	3.176	14.00	4C 38.41
20	3.519	16.00	Mrk 421	48	3.166	18.57	3C 454.3
21	3.495	23.79	GF 2259+586	50	3.154	5.88	PKS 0235+164
22	3.453	15.03	PKS 0420-014				

Table 6.4: The nearest sources for the 29 positive clumps identified when searching Map 1 after smoothing with a Gaussian kernel.

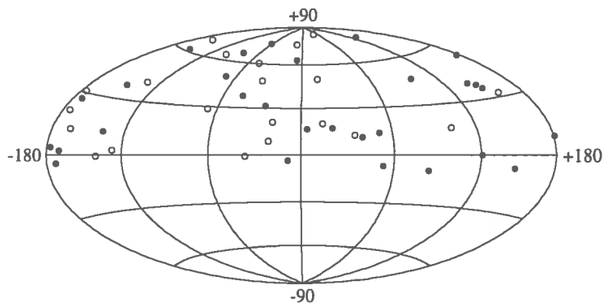


Figure 6.7: The distribution of the 50 most deviant clusters, found by searching Map 1 after smoothing with a Gaussian kernel, on the celestial sphere. Solid circles indicate an excess, and hollow circles a deficit.

The Distribution of the Clumps on the Sphere

Figure 6.7 shows the distribution of the clumps on the sphere. The Kolmogorov probabilities for the distribution of clump Right Ascension and declination were 61% and 99% respectively, giving an overall confidence that the data was not anomalously distributed of 91%.

6.3 Comparison of the Two Independent Maps

6.3.1 *A Priori* Tests on Map 2

If the most deviant pixels of Map 1 do result from an excess of deep underground muons in the region of that part of the sky, and not a statistical fluctuation, then we may expect the *same pixel* in Map 2 to be in excess. For fixed (α, δ), $Z(\alpha, \delta)$ is distributed as $N(0, 1)$ under the null hypothesis, and so we may define an *a priori* test: to examine the deviation in Map 2 in the same pixel as that which is in excess in Map 1. Tables 6.5 and 6.6 show the result of this test for the three most deviant points identified.

Clump	n_1	$\bar{n}_1$	Z_1	n_2	$\bar{n}_2$	Z_2	$Pr(Z > Z_2)$
MX–1	1751	1551.26	5.071	466	430.33	1.719	4.3%
MX–2	3181	2921.40	4.821	969	991.47	−0.714	76.2%
MD–3	5686	6036.40	−4.510	1804	1815.89	−0.279	61.0%

Table 6.5: Result of the *a priori* test for MX–1, MX–2, and MD–3. The pixel identified after smoothing with the simple kernel was used.

Clump	n_1	$\bar{n}_1$	Z_1	n_2	$\bar{n}_2$	Z_2	$Pr(Z > Z_2)$
MX–1	1355.1	1245.4	4.370	365.7	343.7	1.665	4.8%
MD–3	4498.8	4706.4	−4.255	1403.7	1414.7	−0.413	66.0%
MX–2	2451.8	2310.8	4.126	764.0	784.1	−1.008	84.3%

Table 6.6: Result of the *a priori* test for MX–1, MX–2, and MD–3. The pixel identified after smoothing with the Gaussian kernel was used.

There is a deficit in Map 2 at MX–2 and at MD–3 and for both clumps the deficit is consistent with the null hypothesis. At MX–1 there is a 1.7 s.d. excess, consistent

with the null hypothesis at the level of 4%. If this excess is due to a true flux of muons then number of excess events observed in Map 2 must be consistent with that observed in Map 1, scaled by the exposure. Such a test is easiest to make for the simple kernel, as $n - \bar{n}$ is equal to the number of excess events in a 1.6° cone under this procedure.

Assuming the 1% error on the background is negligible, the excess number of events at MX–1 is 200 ± 40. The modular nature of the SOUDAN 2 detector, and the fact that the detector has been under construction while the data was taken, makes it difficult to accurately measure the relative exposure of the two data sets. However, this may be estimated from the ratio of the total event numbers. i.e. The excess in Map 2 should be approximately $3.25/10.6 \times (200 \pm 40) = 61 \pm 12$; it is 36 ± 21, which is consistent at the level of 1 s.d.

6.3.2 Comparison of the Maps in the Region of MX–1

Visual Inspection of the Maps

Figure 6.11 shows the MX–1 region in Map 1 (in greater detail than Figure 6.10) and the same region in Map 2. The coordinates of A.G.N. 3C 273 and 3C 279 are marked. In both images a region of size $\sim 5°$ is in excess. Given the *a priori* knowledge of the detector resolution, and the work of Section 5.11, we should find a peak arising from a 200 event source with the coordinates of 3C 273 within 1.9° of the true position in 95% of trials. Thus the association of MX–1, which is displaced 2.0° from 3C 273, with this A.G.N. is rejected with a confidence of 95%.

However, the most striking feature of this region of Map 2 is a $Z = +4$ peak some $\sim 3°$ away from 3C 273. If the search procedure of Section 6.2 is applied to Map 2, smoothed with the simple kernel, this peak is identified as the 18th. most deviant at $(189.35°, 4.95°)$. The space angle between this peak and MX–1 is 3.2°. Using Equation 5.21, the probability of finding a peak at least this large within this distance of an arbitrary point is computed to be 1.68%. For the Gaussian kernel these numbers are: $Z = 3.9$ at $(189.55°, 5.15°)$, the second most deviant peak in Map 2. Using Equation 6.1, the probability of finding a peak this large within 3.1° of an arbitrary point is 0.2%.

The Association of the Map 2 Peak with the Map 1 Peak

From the analysis of Map 1, the most likely point for an excess of deep underground muons is estimated to be the coordinates of MX–1. At the very same pixel in Map 2 there is an excess with an *a priori* probability of $\sim$ 4–5%. Nearby there is a peak that is quite unlikely to have arisen by chance (less than 2%). The work of Section 5.11 demonstrates that it is possible for a low statistics peak to be displaced from it's nominal position. If we assume that MX–1 is due a real point source, we must therefore ask whether this peak could be due to the same source as that giving rise to MX–1.

Given our *a priori* knowledge of the detector resolution, and a best estimate of the signal strength as 200 events, the 95% confidence region around the true position of the source is 1.9° in radius. For the scaled 61 event source expected in Map 2 (see Section 6.3.1) this confidence region has radius $\sim 3°$. Assuming that these radii may be combined in quadrature the displacement between the peaks is consistent at the level of 2 s.d. (c.r. radius 3.6°, space angle 3.2°).

6.4 Summary and Conclusions of the General Analysis

A general analysis of the map prepared from the large data set has found no evidence for excess of underground muons at a reasonable level of confidence (say 3 s.d. or 99.7%). Taking this data alone, the most likely position for a source is that at the coordinates of the clump labelled MX–1.

A closer inspection of this region has revealed a number of interesting features. The same pixel continues to be in excess in a second, completely independent, data set. The combined probability[2] of this, under the null hypothesis, is $\sim$ 3%. Furthermore, inspection of Map 2 reveals a second peak that has only a $\sim$ 2% chance of being found so close to the coordinates of the peak in Map 1. Both these peaks are quite close to A.G.N. 3C 273 with, given the list of candidate sources, an association probability of $\sim$ 1%. Although none of this is consistent with our *a priori* knowledge of the single muon resolution, it is, nevertheless, interesting and warrants further study. Such analysis will be pursued in Chapter 7.

[2]Using the formula $\alpha_1\alpha_2(1 - \ln \alpha_1\alpha_2)$. This is the probability that $p_1p_2 < \alpha_1\alpha_2$ for two independent tests of individual significance α_1 and α_2, see Reference [35].

6.5 Examination of the Combined Maps in the Region of Selected Sources

In this section the results of a simpler analysis of the combined maps, i.e. the maps made by summing Map 1 and Map 2 on a pixel-by-pixel basis, are presented. The observed and expected muon numbers were measured by examining the appropriate pixel (the closest to the nominal object location) in the appropriate map. This was done for both the simple and Gaussian kernels.

6.5.1 Analysis Method

For the simple kernel $n - \bar{n}$ represents the actual excess of events. The maximum number of signal events, s, that may be accommodated by the observations, at confidence level $1 - \alpha$, can be found by solving Equation 6.2 (see Reference [2]).

$$\begin{aligned} 1-\alpha &= 1 - Pr(\leq n|\bar{n}+s)/Pr(\leq n|\bar{n}) \\ &= 1 - \left\{1 + \text{erf}\frac{n-(\bar{n}+s)}{\sqrt{2(\bar{n}+s)}}\right\} \Big/ \left\{1 + \text{erf}\frac{n-\bar{n}}{\sqrt{2\bar{n}}}\right\}. \end{aligned} \tag{6.2}$$

The normal approximation to the Poisson distribution has been used to write the expression in terms of the error function. This equation was then solved numerically, using the observed values of n and $\bar{n}$.

This number of excess events is converted into a flux by the procedure of Thomson[85]: the background flux in a $1.6°$ cone, at the minimum slant depth accessible to the source, is computed from the Miyake formula[63] for the *vertical* muon intensity; on the assumption that the anomalous flux has the same depth dependence as the background, this is then scaled by $s/\bar{n}$ to obtain the flux limit. i.e.

$$\begin{aligned} \phi &= \frac{174}{d\sec\theta + 400}(d\sec\theta + 10)^{-1.53}\text{e}^{-0.0008(d\sec\theta+10)} \\ &\times\ 2\pi(1-\cos\psi)\frac{s}{\bar{n}}\sec\theta\ \text{cm}^{-2}\text{s}^{-1}. \end{aligned} \tag{6.3}$$

The depth, d, is measured in m.w.e.; θ is the maximum zenith angle of the source and ψ is the semi-angle of the cone. The additional factor of $\sec\theta$ arises from the increased muon content of a shower away from the vertical[40].

6.5.2 List of Sources to be Examined

A list of sources to examine for evidence of anomalous flux was compiled from References [27, 39]. This includes both Galactic and extra-Galactic objects. The sources are discussed very briefly below.

The Crab Nebula

The Crab Nebula has been observed in high-energy gamma rays (over 1 TeV) by the Whipple Čerenkov telescope[89]. It is a supernova remnant of the type known as a *Plerion*[3]. The source is currently detected by the Whipple group with a significance of 45.5 s.d.[71] — the γ-ray flux above 0.4 TeV is measured to be 7×10^{-11} cm^{-2}s^{-1}.

Cygnus X–3, Hercules X–1

Cyg X–3 and Her X–1 are X-ray binaries. They are frequently discussed as candidates for astrophysical high-energy accelerators (see [40] for example). The current status of Cyg X–3 as a candidate source of deep underground muons is reviewed in Chapter 1. Her X–1 is an eclipsing pulsar.

4U 0115+63, V 0332+53, A 0535+26, EXO 2030+36, GF 2259+586

These sources are all X-ray binary systems, 2259+586 is a supernova remnant. See [12, 37, 57].

PSR 1937+21, PSR 1953+29, PSR 1957+20

These three objects are millisecond pulsars, which are believed to consist of an old pulsar *spun up* by accretion from a companion object. 1957+20 is observed to be an eclipsing binary system[57].

SS Cygnae

SS Cyg is a cataclysmic variable star observed to have U Gem type outbursts[4][57].

[3] A young S.N.R. that appears to completely fill the volume it occupies, rather than being a "shell." See Reference [57].

[4] An increase of 2–5 magnitudes lasting for a few days and occurring as quasi-regular intervals of a few weeks to a few months.

Egret A.G.N. γ-ray Sources

The EGRET group has published a preliminary catalogue of Active Galactic Nuclei observed in γ-rays in the range 100 MeV to 20 GeV[39]. The objects from this list that lie within the SOUDAN 2 acceptance are: PKS 0202+149, PKS 0235+164, PKS 0420−014, PKS 0528+134, QSO 0716+714, QSO 0836+710, Mrk 421, 3C 273, 3C 279, 4C 38.41, 3C 454.3, 4C 10.45, QSO 2230+114.

Mrk 421, a BL Lacertae type A.G.N., has been observed by the Whipple group[70] in TeV photons. 3C 273 was the first extra-Galactic γ-ray source to be associated with a known object[82]. It is one of the most powerful quasars in the sky.

In addition, a small number of unidentified sources have been discovered[29]. Of these GRO J0430+29, GRO J1220+16, and GRO J1221+23 have been included.

6.5.3 Results

The results of this analysis are summarized in Table 6.7 (on Page 146). The deviations in an optimum cone, Z^C, and when the data are smoothed with a Gaussian, Z^G, are listed for all the above sources.

Under the null hypothesis, $(Z^C)^2$ and $(Z^G)^2$ should be distributed as χ^2 with 1 degree of freedom. These distributions are shown in Figure 6.8 for the simple kernel and Figure 6.9 for the Gaussian.

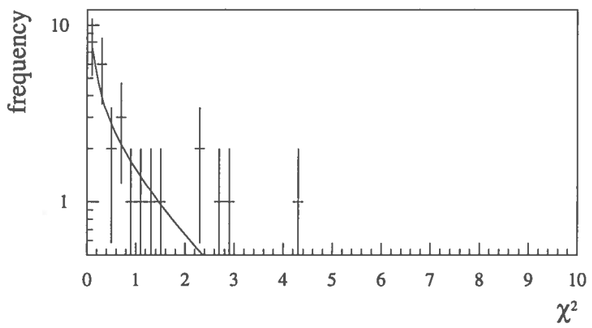


Figure 6.8: The distribution of $\chi^2 = (Z^C)^2$ for the 28 points examined. The curve is the theoretical distribution for 1 degree of freedom.

In both figures, the most deviant point is that for 3C 273 although, given the result of the general analysis which shows the entire region surrounding MX–1

in excess, this should not be treated as a new result. For the Gaussian kernel, χ^2(3C 273) is well separated from the rest of the distribution. For the entire set of sources, the mean deviation is positive. The variance of the mean deviation is 1/28. For the simple kernel $\overline{Z^C} = 0.19 \pm 0.19$ and for the Gaussian $\overline{Z^G} = 0.31 \pm 0.19$, so this is not significant by itself.

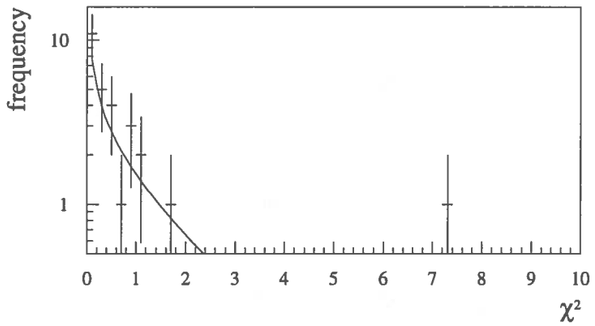


Figure 6.9: The distribution of $\chi^2 = (Z^G)^2$ for the 28 points examined. The curve is the theoretical distribution for 1 degree of freedom.

6.5.4 Conclusions

This analysis has put underground muon flux limits on 27 possible sources after 40 months exposure of the SOUDAN 2 detector. The most deviant of the 28 points examined is that at the coordinates of quasar 3C 273, with a 2.1 s.d. excess in a 1.6° cone and 2.7 s.d. when Gaussian smoothing is used. If there is a real excess, distributed as a 1° Gaussian, at the coordinates of 3C 273 then Gaussian smoothing should be a more powerful test than examining the excess in an optimum cone, leading to a more deviant result as is observed. However, in the general analysis of Map 1 the Gaussian kernel produces a less significant deviation than the simple kernel.

Care must be taken in assessing the significance of this result as the general analysis had already indicated that this region would be in excess. The muon excess in this region of the sky is discussed in further detail in Chapter 7.

Object	$\alpha/°$	$\delta/°$	n	$\bar{n}$	Z^C	Z^G	d/mwe	ϕ/ϕ_0	S/Jy
0115+63	19.45	63.65	8589	8564.58	0.264	0.027	2172	5.47	
0332+53	53.65	53.15	6891	6847.39	0.527	0.665	2099	7.43	
Crab Neb.	83.45	22.05	5016	5012.97	0.043	0.481	2321	5.40	200[1]
0535+26	84.55	26.35	4969	4935.35	0.479	0.695	2246	7.00	
Her X–1	254.35	35.35	4942	5050.32	−1.524	−0.718	2141	4.23	360[2]
1937+21	294.75	21.55	4990	5072.23	−1.155	−0.291	2331	3.60	26[3]
1953+29	298.35	29.05	4989	5109.01	−1.679	−0.911	2207	3.66	0.4[4]
1957+20	299.75	20.75	5064	4991.85	1.021	0.566	2347	7.20	
2030+37	307.65	37.45	4951	5035.88	−1.196	−0.847	2125	4.78	
Cyg X–3	308.15	40.95	4981	4928.98	0.741	0.947	2105	9.33	20[5]
SS Cyg	325.05	43.35	4901	4852.20	0.701	1.205	2096	9.40	
2259+586	345.15	58.85	7667	7581.49	0.982	0.898	2129	7.83	
0202+149	31.25	15.25	4186	4236.84	−0.781	−0.598	2480	3.61	2.5
0235+164	36.05	16.65	4600	4498.90	1.507	1.059	2443	7.71	2.8
0420−014	65.95	−1.35	1440	1454.56	−0.382	−0.163	3197	2.80	1.5
J0430+29	67.55	29.25	5109	5045.62	0.892	0.589	2205	8.39	
0528+134	82.65	13.55	3819	3850.92	−0.514	−0.633	2529	3.84	3.9
0716+714	110.45	71.35	9698	9716.04	−0.183	−0.123	2280	3.80	1.1
0836+710	130.15	70.95	9845	9683.07	1.646	1.303	2273	6.90	2.6
Mrk 421	166.05	38.25	4983	4945.08	0.539	0.575	2120	8.54	<1
J1220+16	185.65	16.75	4533	4518.44	0.217	0.366	2440	5.12	
J1221+23	185.45	23.65	5049	5108.55	−0.833	0.200	2291	4.19	
3C 273	187.25	2.05	2123	2029.95	2.065	2.715	2996	6.51	44.6
3C 279	193.95	−5.75	951	945.83	0.168	0.180	3520	2.82	13.4
4C 10.45	242.15	10.45	3467	3430.48	0.624	0.443	2630	5.22	1.5
4C 38.41	278.45	38.15	5033	5003.42	0.418	0.384	2120	8.15	4.0
2230+114	338.15	11.75	3678	3643.88	0.565	−0.440	2586	5.26	3.7
3C 454.3	343.45	16.15	4429	4426.26	0.041	0.399	2456	4.78	17.2

Table 6.7: List of objects examined for evidence of an associated muon flux. Fluxes are 95% confidence limits. n.b. $\phi_0 = 10^{-12}\,\mathrm{cm}^{-2}\mathrm{s}^{-1}$; for the 3C 273 flux see Chapter 7; Z^C is the deviation in an on-source cone; Z^G the deviation for on-source Gaussian smoothing; the division separates the Galactic and extra-Galactic objects. S is the radio flux at 5 GHz; [1]at 250 GHz; [2]at 8 GHz; [3]in **mJy** at 1 GHz; [4]in **mJy** at 1.5 GHz; [5]approximate flux at 3 GHz during a flare, quiescent flux < 1 Jy.

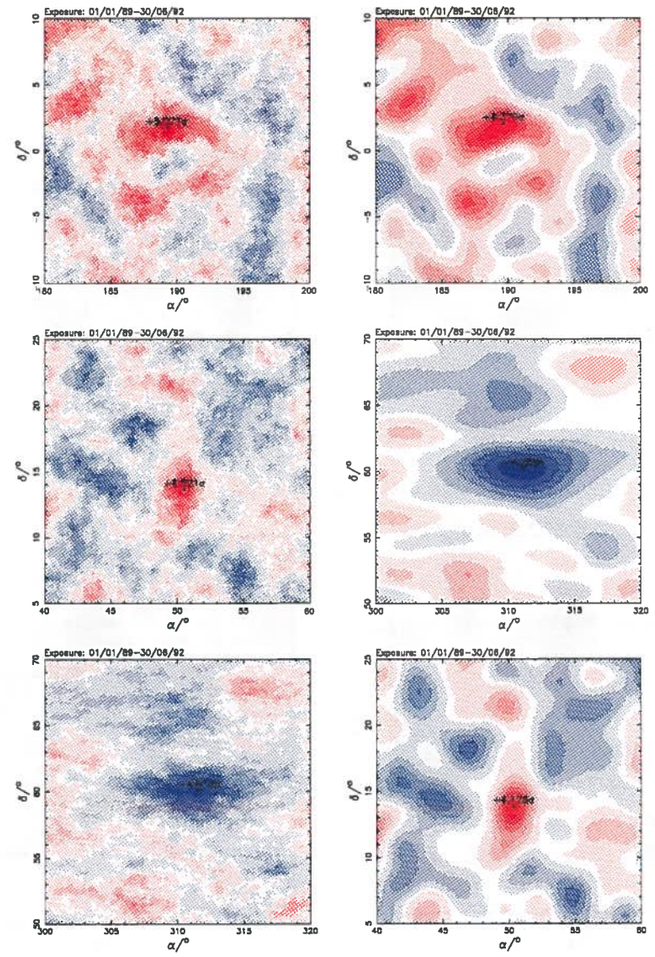
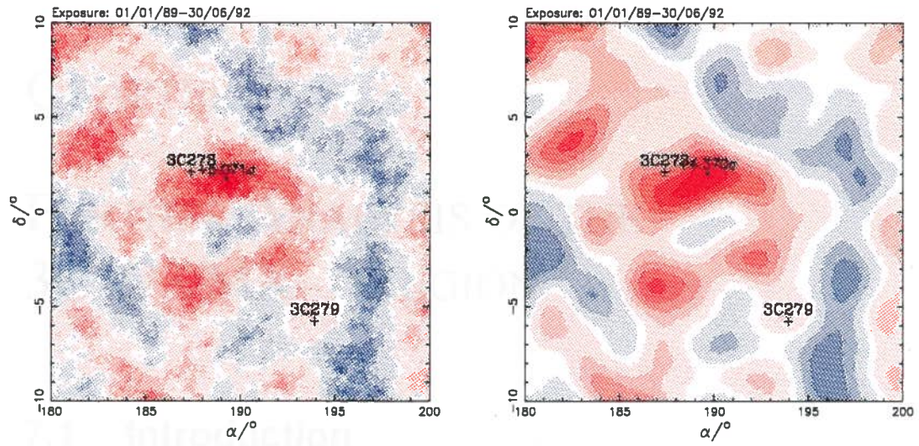


Figure 6.10: $20° \times 20°$ regions surrounding the three most extreme points from Map 1 (simple kernel on the l.h.s., Gaussian kernel on the r.h.s.). The scale ranges linearly from -5 s.d. (saturated blue) to $+5$ s.d. (saturated red). The extremum of each region is marked.

Map 1 (Large Data Set)



Map 2 (Small Data Set)

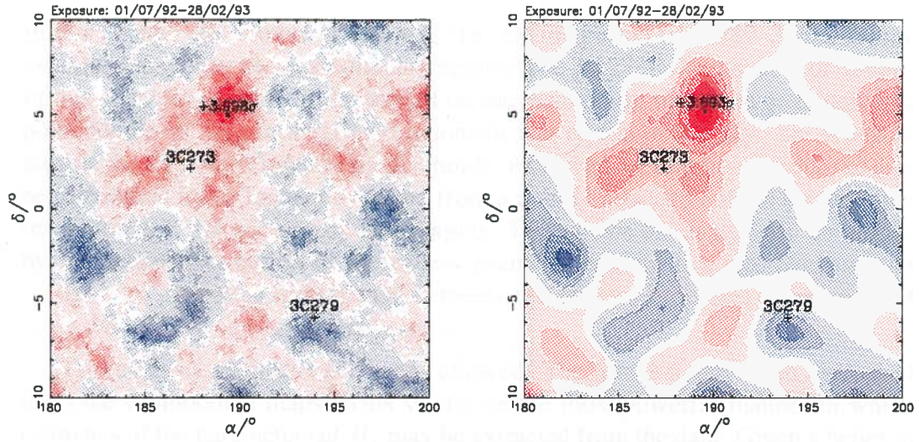


Figure 6.11: $20° \times 20°$ regions surrounding MX–1 for both Map 1 and Map 2 (simple kernel on the l.h.s., Gaussian kernel on the r.h.s.). The scale ranges linearly from -5 s.d. (saturated blue) to $+5$ s.d. (saturated red). The extremum of each region is marked.

CHAPTER 7

FURTHER ANALYSIS OF THE 3C 273/MX–1 REGION

7.1 Introduction

In this chapter the combined data sets (i.e. for the period 01/01/89–30/06/93) are examined in greater detail around the region of the 3C 273/MX–1 excess of muons. In this chapter the data will be treated on the assumption that there genuinely is a point source of deep underground muons in that region of the sky. i.e. We shall assume the alternative hypothesis, H_1, holds. However, the requirement that the data be distributed in the manner expected from *a priori* knowledge of the single muon resolution will not necessarily be imposed. This allows the analysis to be guided by the actual distribution of the excess events — which, if a real phenomenon exists, may indicate a discrepancy between the physics processes occurring and those which have been assumed to occur.

Two analysis methods have been followed. The first is a maximum likelihood fit to the unsmoothed maps. This should be the most powerful manner in which estimates of the parameters of H_1 may be extracted from the data. Given a belief in H_1, the maximum likelihood method allows these estimates to be expressed as multi-dimensional confidence intervals — properly taking into account the correlations between the parameters of the model. The second method is to select a subset of the data that maximizes the deviation observed and to study the characteristics of that set of events.

7.2 Maximum Likelihood Fits to the Combined Data Set

7.2.1 The Maximum Likelihood Fit Program

The maximum likelihood fit was implemented as a MINUIT[48] job. The analysis was restricted to a $60° \times 60°$ region of the sky, centered on $(180°, -10°)$. Data and background histograms were prepared from the unsmoothed maps, with the same $0.1° \times 0.1°$ resolution. The likelihood computed was the product of the Poisson probabilities (actually computed as a sum of logarithms) for a model of the data distribution comprising the background *plus* a Gaussian peak with signal strength, S, coordinates, (α_0, δ_0), and resolution, σ, taken to be parameters. A background scale factor was also fitted. i.e. The fit was performed in the same manner as those described in Chapter 3. As the likelihood is an even function of σ, this parameter was required to lie in the positive range $[0, 10°]$. The fit was free to find a deficit (negative S) or to move the source entirely out of the region for which the likelihood was computed.

7.2.2 Fit to the Background Alone

Initially the fit was made to the background alone. i.e. The source strength was fixed at zero events. The background scale factor, B, was estimated to be 1.0008 ± 0.0013. Although the sum of the background over the entire map is required to equal the total number of events selected, this need not necessarily apply for a smaller region of the sky. For the $60° \times 60°$ region studied 593704 events were read when 593213.7 were expected — an excess of ~ 500 events. If the background alone is fitted we expect the norm to be increased by a factor of $593704/593213.7 \approx 1.0008$.

The likelihood, $\mathcal{L}$, (actually $-\ln L$ where L is the likelihood) at this maximum was -124981. This value has no absolute meaning. However, under the null hypothesis, we should expect maximum likelihood ratio, Λ, to be about $\mathrm{Exp}\,\chi^2_n$ (which is n) if the data is then fitted to a model with n additional (i.e. unnecessary) parameters[19]. Λ cannot be used a statistic as this region has been selected as the result of the analysis of Chapter 6, but may be taken as a crude indicator of the quality of the fit.

7.2.3 Fit with the Resolution Fixed

At first, the fit was made with the resolution fixed to $\sigma = 1°$. The fit estimated the parameters to be

$$\begin{aligned} S &= 263^{+129}_{-125} \text{ events} \\ \alpha_0 &= (189.5^{+0.8}_{-1.2})° \\ \delta_0 &= (1.90^{+0.8}_{-0.9})° \end{aligned} \tag{7.1}$$

with correlation coefficients

$$\begin{pmatrix} 1 & -0.026 & 0.017 \\ & 1 & 0.045 \\ & & 1 \end{pmatrix}. \tag{7.2}$$

(The columns are in the order: S, α_0, δ_0.) The quoted errors are the extrema of the 68% confidence contours. The 68.3%, 95.5% and 99.7% confidence regions (i.e. 1, 2, and 3 s.d.) for the best fit coordinates are shown in Figure 7.1. The full effect

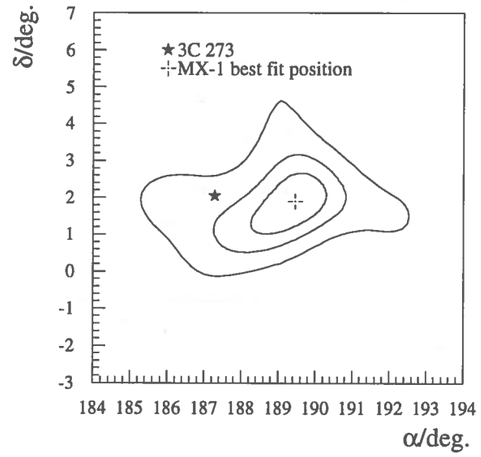


Figure 7.1: The 1, 2, and 3 s.d. confidence regions and the best fit position for a Gaussian excess with r.m.s. 1°. Also marked are the coordinates of 3C 273.

of correlation between the fit parameters has been taken into account while making these contours. 3C 273 lies just outside the 2 s.d. contour: given H_1 and a 1°

resolution, we can reject association with 3C 273 with a confidence of 95.5%. The variation of the likelihood as a function of signal strength is shown in Figure 7.2. The variation is smooth and approximately parabolic.

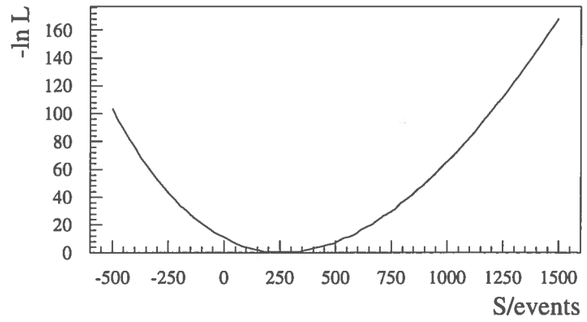


Figure 7.2: The variation of $\mathcal{L} = -\ln L$ as a function of signal strength, S. A constant has been added so that the global minimum of $\mathcal{L}$ occurs at $\mathcal{L} = 0$.

The likelihood at the maximum is $\mathcal{L} = -124991.5$, so $\Lambda = 21 = 7 \times 3$. Clearly the fit has a definite preference for H_1 over H_0. The likelihood surface is very smooth, and the fit program converged without difficulty.

7.2.4 Fit with the Resolution Free

The above analysis has required that the data be described by the *a priori* resolution. Using the maximum likelihood procedure we may ask whether the excess really is best described by a 1° resolution — if it is then a fit with the resolution free should return $\sigma \approx 1°$.

Such fit converged without much difficulty. However, the correlation between S and σ caused the error analysis routine `MINOS`[48] to encounter some non-smooth regions as it explored the likelihood surface. The best estimates of the parameters are

$$\begin{aligned} S &= 657^{+721}_{-587} \text{ events} \\ \alpha_0 &= (188.2^{+2.1}_{-2.8})° \\ \delta_0 &= (2.19^{+2.3}_{-2.1})° \\ \sigma &= (2.41 \pm 2.1)° \end{aligned} \tag{7.3}$$

with correlation coefficients

$$\begin{pmatrix} 1 & -0.542 & 0.199 & 0.878 \\ & 1 & -0.224 & -0.599 \\ & & 1 & 0.162 \\ & & & 1 \end{pmatrix}. \tag{7.4}$$

(The columns are in the order: S, α_0, δ_0, σ.) The errors are larger and more asymmetric when σ is free. Although the fit converges to $\sigma \neq 1°$, the error is sufficiently wide to accomodate 1°. The likelihood for this fit was $\mathcal{L} = -124992.1$ giving $\Lambda = 22.2 = 5.6 \times 4$ — a definite preference for H_1 over H_0.

The estimate of S appears to be only just over 1 s.d. from zero. However, care must be taken in the interpretation of these errors. The asymmetry shows that the likelihood surface is not parabolic and so it is extremely unlikely that twice the quoted error has the probability content of a 2 s.d. confidence interval.

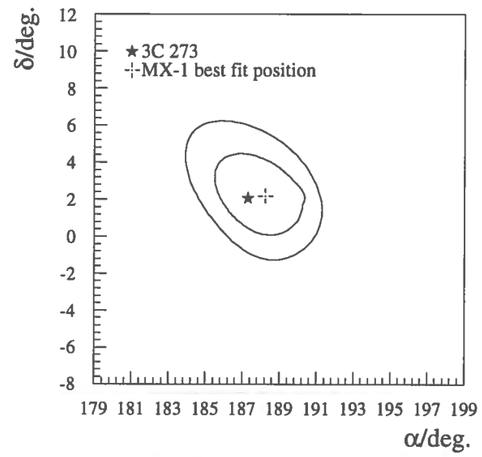


Figure 7.3: The 1, 2 s.d. confidence regions and the best fit position for a Gaussian excess with r.m.s. free. Also marked are the coordinates of 3C 273.

Figure 7.3 shows the 68.3% and 95.5% confidence regions for (α_0, δ_0), and the best fit position, with correlation between all free parameters correctly taken into account. The source coordinates are located with much less precision than in Section 7.2.3 — 3C 273 lies comfortably within the 68% confidence region. However, the fit puts a very poor constraint on σ so this may just be a reduction in

overall precision due to the introduction of an additional free parameter to the fit. The best fit position has moved closer to 3C 273: from a space angle of 2.22° with $\sigma = 1°$ to 0.93° with σ free. The approximate confidence regions for σ and S are shown in Figure 7.4. In the region $\sigma \sim 1°$ and $S \sim 0$ the likelihood surface is quite steep indicating that, although $\hat{\sigma}$ and $\hat{S}$ are not well determined, there is a strong preference against solutions with small σ or near-zero S.

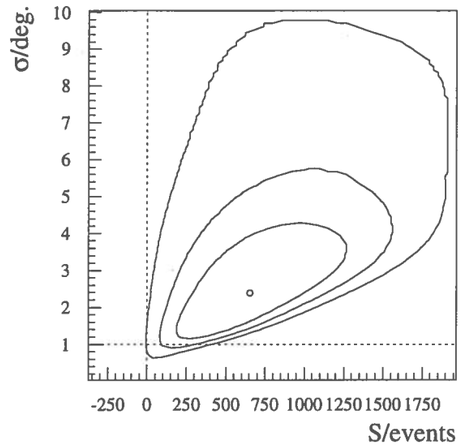


Figure 7.4: The approximate 1, 2 and 3 s.d. confidence regions, and the best fit position, for the resolution, σ, and signal strength, S. These contours are approximations to the true contours as the source coordinates, (α_0, δ_0), were fixed to their best estimate, $(\hat{\alpha}_0, \hat{\delta}_0)$.

7.2.5 Fit at the Coordinates of 3C 273

The result of fitting with the resolution free suggests that, providing we are willing to drop the requirement that $\sigma = 1°$, association of the excess with 3C 273 is possible. It is therefore interesting to estimate σ and S given a source with coordinates fixed to the location of 3C 273.

The result of fitting at $(187.28°, 2.05°)$ is

$$S = 734^{+460}_{-375} \text{ events}$$
$$\sigma = (2.78^{+1.26}_{-1.03})°$$

$$\text{Cor}(S, \sigma) = 0.657. \quad (7.5)$$

The likelihood was $\mathcal{L} = -124991.5$ giving $\Lambda = 21 = 10.5 \times 2$. Figure 7.5 shows the 68% confidence region for the best fit parameters.

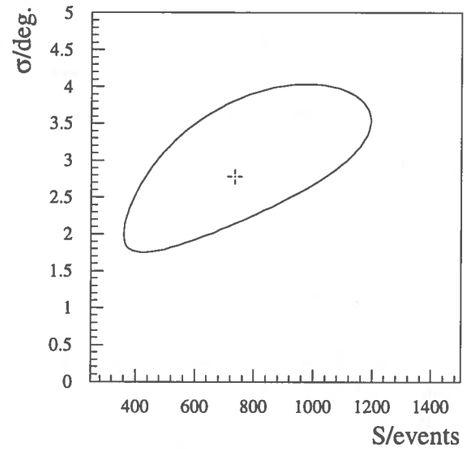


Figure 7.5: The 68% confidence region for the resolution, σ, and strength, S, of a Gaussian excess at the coordinates of A.G.N. 3C 273: $(187.28°, 2.05°)$ J2000.0.

7.2.6 Conclusions from the Fits

If $\sigma = 1°$ then, given H_1, the likelihood fit forces us to reject association with 3C 273 with a confidence of 95.5%. However, as noted in Chapter 6 and shown in Figure 6.11, the the region in excess is larger that that we would expect for a 1° Gaussian. This observation is confirmed by fitting an excess with the resolution free. The data itself is *wider* than 1° and the best estimate of the position moves closer to 3C 273 when the fit is allowed to take account of this. If our *a priori* assumption about the width of the source is incorrect it is possible that this may have forced the fit away from 3C 273. If the source is required to be 3C 273, the fitted resolution is inconsistent with a width of 1°.

7.3 Examination of the Combined Maps in the Region of the MX–1 Antipode

In the analysis chain described in Chapter 2 it is assumed that all muons in SOUDAN 2 are downward going tracks[1]. The error due to this assumption, for ordinary cosmic ray muons, is very small. However, if the excess events at MX–1 were due to a weakly interacting primary, for example a neutrino, then events should also be detected while 3C 273 is below the horizon. These events would have their trajectories inverted by the above assumption and be binned at the MX–1 antipode. This point has coordinates $(9.25°, -1.75°)$.

Figure 7.13 (on Page 173) shows the combined maps in the region of MX–1 and of its antipode. Although the antipode is in excess, the deviation is small ($Z = 1.23$ for the simple kernel and $Z = 0.70$ for the Gaussian) and there are no notable features. If the primary were a neutrino, because the exposure of MX–1 and it's antipode are approximately equal and the interaction cross-section is very small, we should expect a similar excess of ~ 230 events in a 1.6° cone. However, as the background is a strong function of declination, this excess should be on a background of 1422 events rather than 1982 events and so the deviation expected should be $\sim Z = 6$. This hypothesis is clearly ruled out.

Given the non-observation of significant flux at the MX–1 antipode we can place an (approximate) upper limit on the attenuation length of the primary in the rock. If ϕ' is the flux at the antipode and ϕ the flux at MX–1, then

$$\phi' = \left\langle e^{-x/\lambda} \right\rangle \phi \tag{7.6}$$

where λ is the attenuation length and the averaging is done with respect to the path length, x.

If we assume that difference in exposure between the two points can be neglected to first order then $\phi'/\phi \approx s'/s$ where s' and s are the number of excess events at each point. Taking the 95% upper limit for s' (computed using Equation 6.2) and assuming that the averaging can also be neglected, then

$$\lambda \approx \frac{-2R_\oplus}{\ln s'/s}. \tag{7.7}$$

For MX–1: $n = 2217$, $\bar{n} = 1981.6 \Rightarrow s = 200$; for the antipode: $n = 1469$, $\bar{n} = 1422.9 \Rightarrow s' = 113$. Therefore $\lambda \lesssim 63 \times 10^6$ m.w.e.

[1]The SOUDAN 2 detector timing is not sufficient to discriminate between upward going and downward going muons by time of flight.

7.4 Enhancement of the Signal

In the following sections the properties of the actual excess events will be examined by studying background subtracted distributions of event parameters (such as zenith angle, etc.). Two data sets will be studied:

i, the events in a cone centered on the best fit position of Section 7.2.3; *and*

ii, the events in a cone centered on 3C 273.

In both cases a background sample is taken from the close packed array of independent cones that may be constructed at the sample declination. The background distributions are taken to be the sum of the independent cones, normalized to the background expectation computed from the unsmoothed maps.

To allow for the wider distribution indicated by the analysis of Section 7.2.4, the semi-angle of the cone was chosen to be that which maximizes the standardized deviation $Z(\sigma)$ for the given coordinates (α, δ). This procedure was adopted because the confidence interval for $\hat{\sigma}$ is so wide. Z was maximized in a cone of semi-angle 2.5° for 3C 273 and 1.8° for the best fit MX–1 coordinates. These are equivalent to Gaussian resolutions of 1.6° and 1.2° respectively. The excess in these cones was 320 and 258 events respectively.

7.5 Study of Event Variable Distributions for the Enhanced Sample

In this section, the distributions of a subset of event variables in the on-source cone are compared to the expected distribution. This is done by subtracting the distribution taken from off-source cones (normalized as in Section 7.4) from that in the on-source cone. If there is no difference between the on-source and off-source samples then this residual distribution should have the same shape as the off-source distribution.

The event variables examined were: zenith-angle, θ; track-length, λ; the summed pulse height per unit track length, $(\text{a.p.h.} + 0.75 \times \text{c.p.h.})/\lambda$; and the event multiplicity, μ. These variables were chosen because they may be sensitive to physics differences between the excess events and the background sample.

7.5.1 Distributions for the MX–1 Cone

The background subtracted distributions, for the MX–1 cone, are shown in Figure 7.6. Also plotted is the off-source distribution, normalized to the number of excess events. There are no obvious discrepancies between the distributions from on-source and off-source cones. For histogram bins where the number of events in the on-source cone exceeded 10 a χ^2 statistic was computed. (The plotted errors are not accurate for the other bins, in the tails of the distributions.) These results are summarized in Table 7.1. (Tables 7.1, 7.2, 7.3 and 7.4 are on Page 163).

The distribution of track-length, λ, shows periodicity, with peaks at every 70 cm. This is due to FMR which reconstructs tracks in separate looms before combining them to make single tracks. The maximum track length that may be made in a single loom by events from a single cone is $\lambda_{max} = 50 \sec \theta_{max}$ cm. θ_{max} is the zenith angle of the cone when it is in transit. For MX–1, this gives $\lambda_{max} \sim 70$ cm. The periodicity illustrates a systematic problem with track-length as estimated by FMR.

The number of events with a given multiplicity are listed in Table 7.3. The expected number of events for multiplicity μ, $\bar{n}_\mu$(on), was estimated by normalizing the off-source distribution, n_μ(off), to the total background expectation computed from the maps. The greatest discrepancy between the observed and expected number of events is for single muon events, and there is little evidence for an abnormally high multiplicity in the on-source sample. There are three events with ten muons reconstructed in the on-source sample, whereas only four such events were found in the off-source cones, and one 15-muon event with no 15-muon events in the off-source cones. However, this discrepancy of a few events, far into the tail of the distribution, is not very significant (the errors on the background are quite large).

7.5.2 Distributions for the 3C 273 Cone

The same histograms have been made for the larger cone centered on A.G.N. 3C 273. The distributions of the three event variables are shown in Figure 7.7 (on Page 162). Again, the excess events are not distributed in an obviously anomalous manner. The χ^2 for each variable is shown in Table 7.2. The number of events with a given multiplicity are listed in Table 7.4. The excess is mostly single-muon events. As in Table 7.3, there are a few high-multiplicity events ($\mu = 10$, 13, 14) where few were expected. As the MX–1 and 3C 273 cones overlap — approximately $\frac{1}{3}$ of the smaller cone lies inside the larger — these may be the same events.

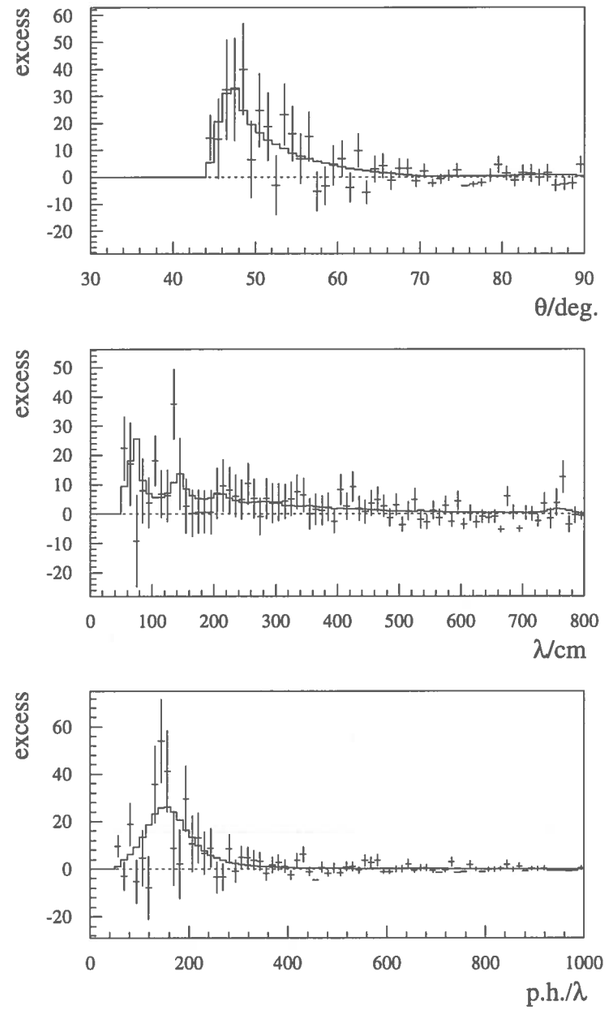


Figure 7.6: The background subtracted distributions of the event variables (θ, λ and p.h./λ) for the MX–1 cone. The points are the excess and the histogram the background normalized to equal the number of excess events.

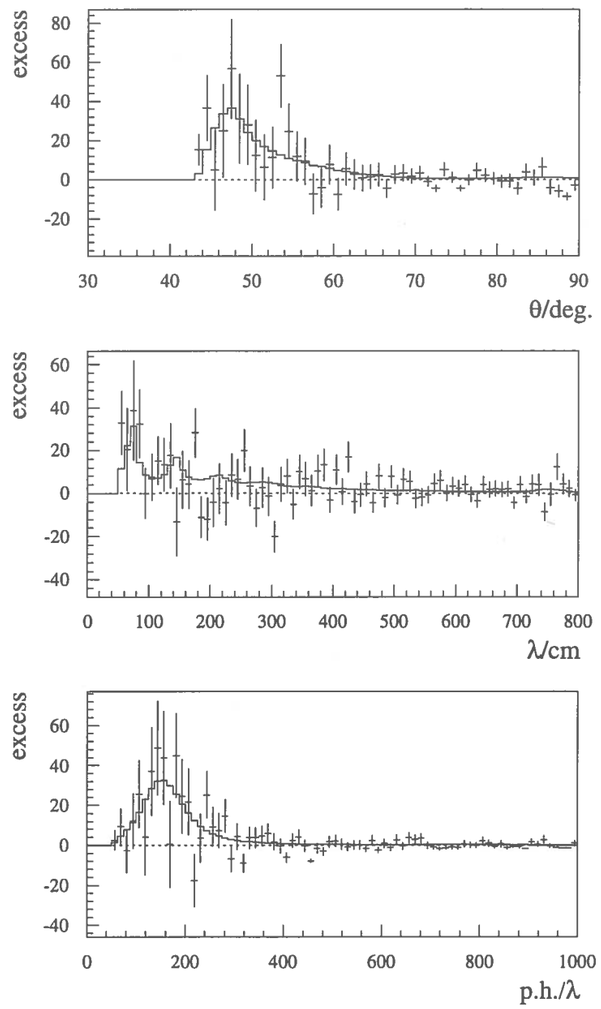


Figure 7.7: The background subtracted distributions of the event variables (θ, λ and p.h./λ) for the 3C 273 cone. The points are the excess and the histogram the background normalized to equal the number of excess events.

variable	χ^2	d.o.f.
θ	11.7	15
λ	26.3	45
p.h./λ	16.6	14

Table 7.1: Table of χ^2's for the MX–1 cone.

variable	χ^2	d.o.f.
θ	17.0	15
λ	58.3	45
p.h./λ	13.5	14

Table 7.2: Table of χ^2's for the 3C 273 cone.

μ	n_μ(on)	n_μ(off)	$\bar{n}_\mu$(on)	μ	n_μ(on)	n_μ(off)	$\bar{n}_\mu$(on)
1	2722	24493	2470	9	0	7	0.713
2	83	793	79.9	10	3	4	0.408
3	22	199	20.3	11	0	3	0.306
4	6	79	7.96	12	0	1	0.102
5	4	38	3.87	13	0	0	< 0.102
6	0	24	2.45	14	0	1	0.102
7	2	15	1.53	15	1	0	< 0.102
8	1	10	1.02				

Table 7.3: The distribution of observed and expected event multiplicities for the event sample taken in a 1.8° cone centered on the MX–1 best fit position.

μ	n_μ(on)	n_μ(off)	$\bar{n}_\mu$(on)	μ	n_μ(on)	n_μ(off)	$\bar{n}_\mu$(on)
1	5197	22288	4860	9	2	6	1.31
2	151	712	155	10	1	4	0.873
3	35	181	39.5	11	0	3	0.654
4	13	73	15.9	12	0	1	0.218
5	5	34	7.42	13	1	0	< 0.218
6	2	22	4.80	14	1	1	0.218
7	3	14	3.05	15	0	0	< 0.218
8	2	9	1.96				

Table 7.4: The distribution of observed and expected event multiplicities for the event sample taken in a 2.5° cone centered on A.G.N. 3C 273.

7.6 Fit to the Primary Spectral Index for the Enhanced Sample

Although the zenith angle distributions of Section 7.5 indicate that there is no significant difference between the spectral index of the excess flux and that of the background, it is nevertheless interesting to tackle this problem from another direction — by directly fitting the primary spectral index.

7.6.1 The Spectral Index

It is assumed in this section that the energy spectrum of the primary particles may be described by a simple power law. i.e.

$$\frac{dN_p}{dE_p} \propto E_p^{-\gamma} \tag{7.8}$$

If the primary is a short-lived particle, i.e. one which decays *promptly*, then the differential spectrum of the muons resulting from this decay should have a similar form:

$$\frac{d^2N_\mu}{dE_\mu d\cos\theta} \propto E_\mu^{-\gamma}. \tag{7.9}$$

However, if the primary is a long-lived particle (e.g. a pion) then the muon will have differential spectrum:

$$\frac{d^2N_\mu}{dE_\mu d\cos\theta} \propto E_\mu^{-(\gamma+1)} \sec\theta, \tag{7.10}$$

where θ is the zenith-angle of the muon.

The normal cosmic ray flux (high-energy protons) has a differential spectral index of $\gamma \approx 2.7$ and gives muons from the decay of secondary pions after some delay — a spectrum similar to Equation 7.10 is appropriate[40].

7.6.2 Method

The spectral index was estimated by the method of Thomson[85]. A model of the rock overburden, made from a U.S. Geological Survey map of the surface topology[83], is used to compute the shape of the expected background muon flux as a function of hour-angle for a given declination. The shape of the actual observed

flux at this declination is then used to estimate the relative efficiency, as a function of hour-angle, of the detector/analysis chain. This efficiency function, and the overburden model, can then be used to construct an expected distribution shape for any spectral index. A likelihood function (a function of spectral index) may then be supplied to standard minimizing programs and used to choose the spectral index that gives the best fit to the data.

The fit program was verified by fitting the spectral index for all the events in the 1.8° cone centered on MX–1. As the excess is less than 10% of the background, this should be dominated by the ordinary background flux. The result should be the value input to the procedure: a primary differential spectral index of $\gamma = 2.7$. Figure 7.8 shows the variation of the likelihood as a function of γ. A 68% confidence

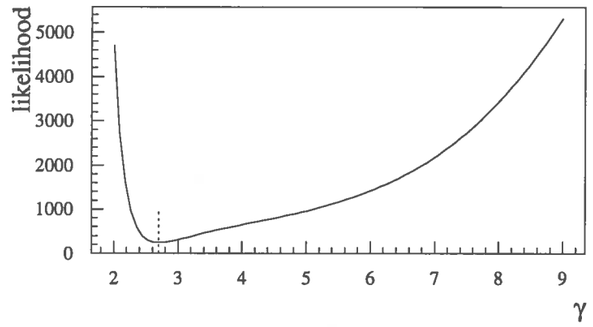


Figure 7.8: The variation of the likelihood, $\mathcal{L}$, as a function of the primary's differential spectral index, γ, for all events within a 1.8° cone of MX–1. The true spectral index is indicated by a broken line.

interval was placed on γ:

$$\gamma = 2.70 \pm 0.02. \tag{7.11}$$

The program has clearly fitted the correct spectral index. The errors indicate a limit to the accuracy of the procedure.

7.6.3 Estimate of the Spectral Index for the MX–1 Cone

The spectral index, for the background subtracted hour angle distribution of events taken from the MX–1 cone, was fitted for both delayed, γ_d, and prompt, γ_p, muons alone. A fit was then made in which the proportion of prompt muons, p, was also a free parameter. The proportion of delayed muons was $(1 - p)$.

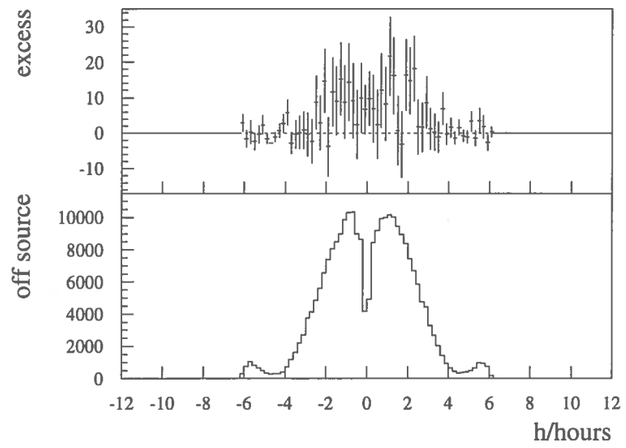


Figure 7.9: The background subtracted on-source and total off-source hour-angle distributions for the MX–1 cones.

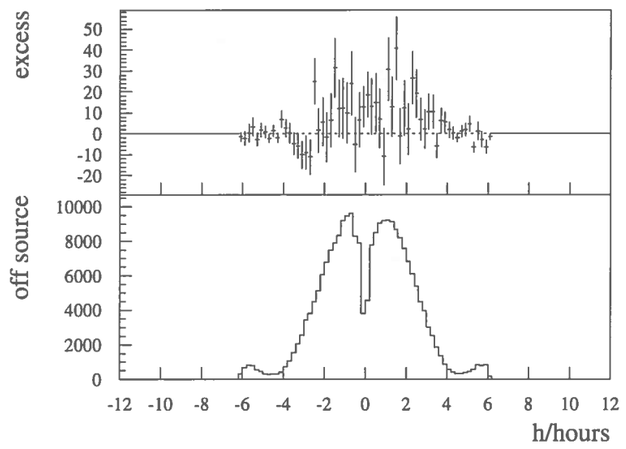


Figure 7.10: The background subtracted on-source and total off-source hour-angle distributions for the 3C 273 cones.

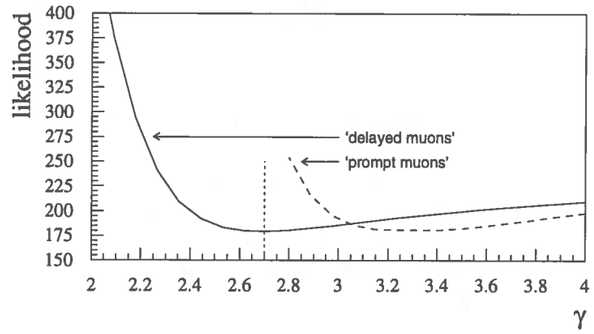


Figure 7.11: The variation of the likelihood, $\mathcal{L}$, as a function of primary's differential spectral index, γ, for events within a 1.8° cone of MX–1 with the background subtracted. The true spectral index of the cosmic ray background is indicated by a vertical line.

The observed hour-angle distributions are shown in Figure 7.9. Figure 7.11 shows the variation of the likelihood with γ. The best estimates were:

$$\begin{aligned} \gamma_d &= 2.69^{+0.06}_{-0.07} \\ \gamma_p &= 3.39 \pm 0.06. \end{aligned} \tag{7.12}$$

The fit preferred $p = 0$ ($\hat{p} = 4 \times 10^{-9}$). There is, therefore, no evidence that the excess in this cone is due to primaries with a spectral index different from that of the normal cosmic ray background.

7.6.4 Estimate of the Spectral Index for the 3C 273 Cone

The above procedure was repeated for the larger cone centered on 3C 273. The observed hour-angle distribution is shown in Figure 7.10 In this case also, there was no evidence for a spectral index different to the background. The best estimates were:

$$\begin{aligned} \gamma_d &= 2.73^{+0.05}_{-0.06} \\ \gamma_p &= 3.42 \pm 0.05 \\ p &= 1.3 \times 10^{-6} \end{aligned} \tag{7.13}$$

7.7 Conclusions from the Analysis of Event Variables

The Distribution of Zenith Angles and Spectral Index Fits

An anomalous spectral index (i.e. not $\gamma = 2.7$) or the production of muons via a decay chain other than $pN \to \pi\pi\ldots \to \mu\mu\ldots$, for example prompt muons that result from charm decays, would lead to the excess having a zenith angle distribution different to the norm. The observed zenith angle distribution, and the spectral index fits, show no evidence for this.

The Distribution of Track Lengths

If the excess muons were stopping in the detector volume, or the primary decay vertex was contained within the detector volume, then the excess events would have an anomalous distribution of track lengths. In addition, this might arise if the track reconstruction programs were not working correctly for the excess events. The data show no evidence for these phenomena.

The Distribution of Pulse Height per Unit Track Length

The distribution of p.h./λ is wide, due to both Landau fluctuations and the detector/electronics response, and so is only likely to be sensitive to gross discrepancies in the ionization deposited along tracks. Such discrepancy could be caused by:

- Large electromagnetic showers on the tracks. This would give rise to many, long, saturated, pulses in the detector modules the track passes through and would also result in atypically bad track reconstruction. The probability of such showers occurring increases with muon energy and so would indicate an excess of unusually energetic events.
- Penetrating particles ionizing at a different rate to muons. This could be due to either the presence of exotic objects, e.g. μ^{++}, or unresolved muon bundles (see below), e.g. $(\mu^+\mu^+\mu^-)$.
- Anomalously charged matter such as free quarks or very heavy particles such as quark nuggets[46].

- Muons with a velocity, β, away from the relativistic region of the Bethe-Bloch curve, which could be due to production via non-standard decay chains.

There is no evidence for any of the above.

The Distribution of Event Multiplicity

It has been suggested[72] that the cross-section for the non-perturbative production of many ($\sim 1/\alpha_W \approx 30$) weak gauge bosons may be very large ($\lesssim 10\,\mu$b) for parton-parton c.m.s. energies of order 10 TeV. The shower from a cosmic ray interaction in this region would possess high muon multiplicities and result in "tight" muon bundles underground. However, there is no evidence that the excess events possess an anomalous multiplicity.

7.8 Flux Calculations

7.8.1 γ-ray Observations of 3C 273

Radio source 3C 273 was originally identified as a source of γ-rays by the satellite experiment COS–B. The γ-ray flux was measured in two energy ranges: $(1.2\pm0.4)\times10^{-6}$ cm^{-2}s^{-1} in 50–150 MeV and $(0.3\pm0.4)\times10^{-6}$ cm^{-2}s^{-1} in 150–500 MeV[82]. These measurements give a flux above 50 MeV of 1.6×10^{-6} cm^{-2}s^{-1} with a differential spectral index of -2.3.

More recently, the EGRET experiment measured γ-ray emission from 3C 273 over the range 20 MeV–30 GeV. The flux was measured to be $(0.30 \pm 0.05) \times 10^{-6}$ cm^{-2}s^{-1} above 100 MeV with a differential spectral index of -2.4 ± 0.1[39].

The Whipple group has also searched for TeV-γ initiated showers from the direction of 3C 273. They do not find a significant excess of showers, and quote a confidence limit of 5.1×10^{-12} cm^{-2}s^{-1}. It is interesting to note that the Whipple measurements are of a 1.6 s.d. excess[71], although extrapolating the EGRET flux to TeV energies shows that the γ-ray flux may be too low for Whipple to have observed a signal.

7.8.2 Underground Muon Flux Calculations

The results of Section 7.2 can be used to calculate the anomalous flux of underground muons in the region of 3C 273/MX–1 under a number of hypotheses. In addition, a

confidence limit may be computed from the results of Table 6.7. As in Section 6.5.1, the absolute efficiency, exposure and spectral index are corrected for by scaling the background flux at the minimum depth by $s/\bar{n}$. The total background, $\bar{n}$, is calculated by integrating the background weighted by the p.s.f.

§	note	$\phi/10^{-12}\,\mathrm{cm}^{-2}\mathrm{s}^{-1}$
7.2.3	$\sigma = 1°$ Gaussian	$9.96^{+4.88}_{-4.73}$
7.2.4	σ & (α_0, δ_0) free	$10.3^{+11.3}_{-9.16}$
7.2.5	σ free at 3C 273	$10.0^{+6.27}_{-5.11}$
6.5	1.6° on-source cone	$< 6.51(95\%)$

Table 7.5: Underground muon flux calculations, and limit, for the 3C 273/MX–1 region.

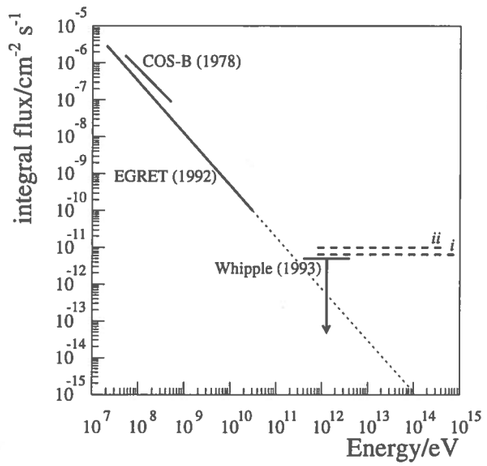


Figure 7.12: 3C 273 muon and γ-ray fluxes. The limit of Section 6.5 is shown by line (*i*) and the fits of Section 7.2 by line (*ii*). The EGRET γ-ray flux has been extrapolated to higher energies.

The muon flux has been calculated for the three fits of Section 7.2 and a confidence limit for the 1.6° cone of Section 6.5. These results are summarized in Table 7.5 and are plotted on Figure 7.12. With no model of the physical process involved, the energy at which the above fluxes should be plotted is unknown. They

are therefore drawn as lines starting from the minimum surface energy a muon must possess to reach the SOUDAN 2 detector: 0.8 TeV. As $\phi_\mu > \phi_\gamma$ it seems unlikely that muon flux from 3C 273 could be due to a conventional interaction involving γ-ray primaries. Muon pair-production in γ-ray induced showers is suppressed by $\approx m_e^2/m_\mu^2$ relative to electron pair-production. This term is from the fermion propagator.

Assuming that the anomalous muon flux is is due high-energy primary cosmic rays from 3C 273, it is possible to calculate roughly the luminosity into the *muon channel*. If each muon arises from a primary of energy $\sim P[\mathrm{TeV}] = 1.6P$ erg then the energy-flux is

$$E_p\phi_\mu \approx 16 \times 10^{-12} P\,\mathrm{erg\,cm^{-2}s^{-1}}\,. \tag{7.14}$$

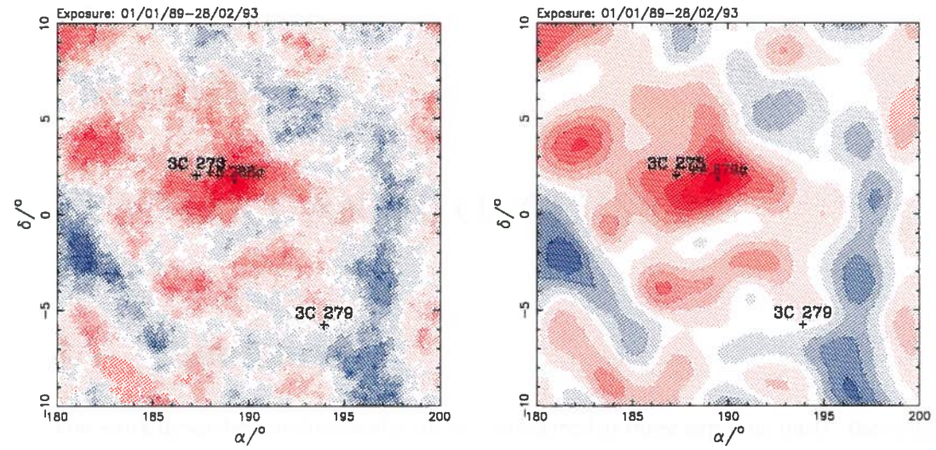
3C 273 has a red-shift of $z = 0.158$. If Hubble's constant, H_0, is $75\,\mathrm{km\,s^{-1}Mpc^{-1}}$ then the distance to 3C 273 is $4z\,\mathrm{Gpc} = 0.6\,\mathrm{Gpc}$. Therefore, the total rate at which 3C 273 radiates into this channel is approximately

$$4 \times 10^{45} Pf\,\mathrm{erg\,s^{-1}} \tag{7.15}$$

where f is the beaming fraction[2]. The primary energy has been corrected for the red-shift. The EGRET group calculate the luminosity of 3C 273 in γ-rays to be $8 \times 10^{45} f\,\mathrm{erg\,s^{-1}}$[38]. The X-ray luminosity is measured to be $1 \times 10^{46} f\,\mathrm{erg\,s^{-1}}$ in the range 2–10 keV[92]. Although such a naive calculation cannot be expected to be accurate to more than an order-of-magnitude, for $P \approx 5$–10 the measured flux gives a luminosity into the muon channel similar to the luminosity into high-energy electromagnetic radiation.

[2]Many A.G.N. are observed to emit highly-relativistic beams. It is normally assumed that the high-energy flux is actually emitted from the beam, and so the actual luminosity is some unknown fraction, f, of the luminosity computed assuming isotropic emission. f is usually assumed to be of order 1–0.1%.

MX–1 Region



MX–1 Antipode Region

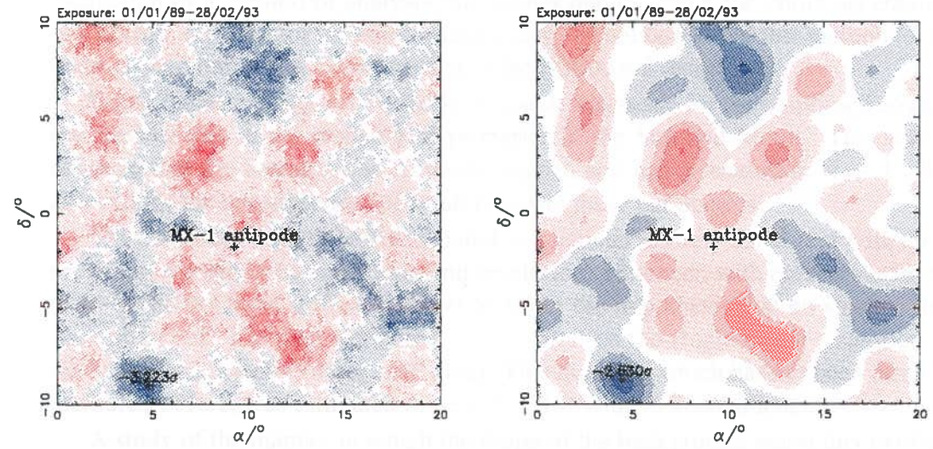


Figure 7.13: $20° \times 20°$ regions surrounding MX–1 and its antipode for the combined maps (simple kernel on the l.h.s., Gaussian kernel on the r.h.s.). The scale ranges linearly from -5 s.d. (saturated blue) to $+5$ s.d. (saturated red). The extremum of each region is marked.

CHAPTER 8

SUMMARY AND CONCLUSIONS

8.1 Summary

The work described in this thesis can be considered as three separate parts: the search for the cosmic ray shadow cast by the Solar and Lunar discs; the development and evaluation of a method of analysis that allows one to search the entire acceptance of a cosmic ray detector for point sources; and, the application of this method to the underground muon data reconstructed in the SOUDAN 2 detector.

Using the entire data-set available, a search was made for the combined cosmic ray shadow due to the stopping of primaries in the Sun and Moon. This search assumed that the detector was correctly aligned and had a resolution of $\sim 1°$, but allowed for the consequences of small errors in these parameters.

The data were found to be distributed in a manner entirely consistent with the *a priori* knowledge of the alignment and resolution. However, with current statistics, this test did not have sufficient power to reject the hypothesis that no shadow had been observed. The data were used to set a limit on the single-muon resolution of the SOUDAN 2 detector (using DMC data). This quantity, which has not been directly measured before, was estimated to be $\sigma > 0.46°$ with 95% confidence.

A study of the manner in which the shape of the background muon flux evolves led to the deduction that the convolution of the observed hour-angle distribution with the observed l.s.t. distribution would provide an estimate of the background that had an acceptably low error and could be applied simply to the entire SOUDAN 2 acceptance. The validity of this method was demonstrated for a restricted data-set.

Two maps of the muon density were prepared from the DMC data and

a background calculated for these data-sets. The accuracy of the whole-sky background calculation was explicitly verified. The data and background maps were then smoothed, to allow searching, and a deviations map created. This deviations map is a realization of a 2-d stochastic process.

The adopted analysis procedure was simulated under the null hypothesis (that there are no point sources of underground muons) by a Monte Carlo procedure and found to agree with a formula computed by Siegmund. The behaviour of the procedure in the presence of a real source was also simulated. It was found that the procedure was able to successfully detect the presence of a source but that, if the source was weak, there was a statistical scatter between the true coordinates of the source and the coordinates at which the method located it.

The method was applied to the entire data-set available, asymmetrically divided into two periods. No unambiguous evidence for a point source was found in either map. However, the most deviant point in the first map was found to be close to A.G.N. 3C 273. This region was also found to be in excess in the second map.

The combined maps were also examined in the region of a set of X-ray binary stars and A.G.N.. No significant excess, other than that already found near 3C 273, was found in the region of any of these objects. A 95% confidence upper-limit, on the assumption that the signal has the same spectral index as the background, was placed on the muon flux from each of the objects.

The data in the region of 3C 273 were examined in greater detail. Maximum likelihood fits were used to estimate the source position, strength and width. The data were found to prefer a width greater than the *a priori* estimate, and could only be associated with 3C 273 if this modification to the hypothesis was permitted. A sample of events from a cone placed around the excess was compared with a background sample from an array of close packed cones at the same declination. The primary spectral index was fitted and the distribution of event parameters compared. No other differences between the data and background could be detected. On the assumption that the source was real, with the same spectral index as the background, the primary cosmic ray flux was estimated to be $(10.0^{+6.27}_{-5.11}) \times 10^{-12}\,\mathrm{cm}^{-2}\mathrm{s}^{-1}$.

8.2 Conclusions

This thesis has demonstrated that it is possible to make a map of the entire sky visible in underground muons[1], to calculate a background distribution for the whole sky, even though the exposure of the detector is not uniform in sidereal time, and to process the resulting data in a manner that is approximately bin-free (as the size of the bins used is an order of magnitude less than the relevant physical dimension — the resolution of the detector) and requires no *a priori* assumptions regarding the location of a source. It has been demonstrated that statistics of the method are fully understood and that the method is superior to the naive approach of dividing the sky into an array of independent bins.

This method has then been applied to the data-set collected in the SOUDAN 2 detector, in an attempt to learn more about the currently unresolved issue of deep underground muons correlated with the location, or activity, of individual astrophysical objects. There were three possible results of this investigation:

i, it might have been shown that there is unambiguous evidence for point sources of underground muons, which would have had profound physical and astrophysical consequences;

ii, it might have been shown that there is unambiguous evidence against such point sources, and the modifications to the standard model proposed to account for previously claimed signals ruled out; *or*

iii, it might have produced an ambiguous result which would allow neither conclusion (i) nor conclusion (ii) to be reached.

Conclusion (iii) is the result of the investigation described in this thesis. Two analysis techniques were adopted: one in which the whole-sky maps produced would be searched in a general manner; and, one in which the maps would be examined only at specific locations. These are clearly not independent tests, for if one of the preselected objects were a strong source giving rise to underground muons then it must, necessarily, also be found by the search procedure. However, under the null hypothesis, the point in the sky at which the most significant deviation occurs, (α_0, δ_0), is entirely random and independent of the deviation at that point, $Z(\alpha_0, \delta_0)$. Therefore, the test of the size of the maximum deviation and the test of the position of the maximum are independent. In addition, the size of the deviation at

[1] Or any other cosmic ray particle.

the identical pixel in a map prepared from independent data is clearly an independent test. The size of largest deviation, in the independent data, within the local area of (α_0, δ_0) is also independent of the original test.

In Chapter 6 a number of tests were performed on the maps prepared from the data. This analysis is compromised because the data has been examined in many ways. However, if the results of these different tests can be combined into a single number, then an estimate of the overall significance may be made.

The tests were performed on the deviations maps produced by smoothing both with a simple and with a Gaussian kernel. The results of these two smoothing procedures are clearly not independent. Table 8.1 lists all the tests performed that we may consider in computing the confidence with which we can reject the null hypothesis. Some of these tests are independent of each other, while others are

n	Kernel	Description	$\alpha_n/\%$
1	Simple	Whole-sky search of Map 1	13.3
2		Examination of Map 1 point in Map 2	4.3
3		Local search of Map 2	1.7
4		Deviation in combined maps for selected sources	1.9
5		Association of Map 1 point with selected sources	1.2
6	Gaussian	Whole-sky search of Map 1	22
7		Examination of Map 1 point in Map 2	4.8
8		Local search of Map 2	0.2
9		Deviation in combined maps for selected sources	0.3
10		Association of Map 1 point with selected sources	1.7

Table 8.1: List of all tests relevant to the rejection of the null hypothesis. α_n is the significance of test n.

not. The interdependencies of the tests are illustrated in the matrix of Table 8.2. From the matrix we see that tests 1, 2 and 5 are independent and that 1, 3 and 5 are independent. This is also true for 6, 7 and 10 and for 6, 8 and 10.

To compute the combined significance of N independent tests[2], with individual significances $\{\alpha_i\}$, we transform to Fisher's variable

$$\eta = -2 \ln \prod_{i=1}^{N} \alpha_i \tag{8.1}$$

[2]Providing that the tests are independent, it does not matter whether the statistics involved were computed from the same data sample or from completely separate data samples.

n	1	2	3	4	5	6	7	8	9	10
1	NI	I	I	NI	I	NI	IC	IC	NI	IC
2		NI	NI	NI	I	IC	NI	NI	NI	IC
3			NI	NI	I	IC	NI	NI	NI	IC
4				NI	I	NI	NI	NI	NI	IC
5					NI	IC	IC	IC	IC	NI
6						NI	I	I	NI	I
7							NI	NI	NI	I
8								NI	NI	I
9									NI	I
10										NI

Table 8.2: Interdependency matrix for the tests of Table 8.1. I = independent; NI = not independent; IC = independent, but combination confusing.

which is distributed as χ^2 with $2N$ degrees of freedom[36]. The significances of the four combinations are shown in Table 8.3. As the four probabilities listed are not those of independent events, we shall follow the conservative procedure of taking the least significant combination. This is the combination 6+7+10 and so, for the muon excess observed in the region of A.G.N. 3C 273, the probability that it arose by chance is less than 0.8%. This makes the result interesting, but is not sufficient to be taken as indicating the existence of the phenomenon beyond reasonable doubt.

Combination	η	$Pr(\chi^2_6 > \eta)/\%$
1+2+5	19.2	0.38
1+3+5	21.1	0.18
6+7+10	17.3	0.82
6+8+10	23.6	0.06

Table 8.3: The significances of the four combinations of independent tests.

8.3 Comparison with the Results of Other Experiments

8.3.1 Searches for Point Sources of Neutrinos

It is likely that sources of high energy photons, produced via $pN \rightarrow \pi^0 \ldots \rightarrow \gamma\gamma \ldots$, are also sources of high energy neutrinos, from the decay of charged pions produced in the initial hadronic interaction. In addition, models of A.G.N.'s have been built in which a neutrino flux is produced via the decay of the Δ-resonances[81] (i.e. in the channel $p\gamma \rightarrow \Delta^+ \rightarrow n\pi^+$). Such treatments often discuss 3C 273 as a candidate, due to both its proximity and very high luminosity across a large part of the electromagnetic spectrum.

A number of searches for horizontal or upward going muons, from the charged-current interaction of high energy neutrinos, in nucleon decay detectors have been made. No evidence for such point sources has been found in the data of the I.M.B., Kamioka and K.G.F. experiments, from which limits of $\phi_\mu < 1.5\text{–}6 \times 10^{-14}\ \mathrm{cm^{-2}s^{-1}}$ may be set[43]. Assuming a spectral index of $\gamma = 2.1$ these limits may be converted into a neutrino flux limit of $\phi_{\nu_\mu} < 3.2\text{–}16 \times 10^{-6}\ \mathrm{cm^{-2}s^{-1}}$. However, as the muon excess MX–1 does not show the large antipodal excess we would expect for a neutrino signal, this flux cannot be compared with that computed in Section 7.8.

8.3.2 Searches for Point Sources of High Energy γ-rays

As discussed in Section 7.8.1, the Whipple group have searched for TeV-γ initiated showers from the direction of 3C 273 and set an upper limit of $5.1 \times 10^{-12}\ \mathrm{cm^{-2}s^{-1}}$. The Whipple telescope has spent more time looking at 3C 273 than any object other than the Crab pulsar, Cygnus X–3 and PSR 0355+54. As γ initiated showers are typically very muon poor and the muon flux computed for MX–1 is approximately twice the γ-ray limit, the muon flux observed cannot be the consequence of conventional showers. In the Whipple analysis cuts are applied to enhance the significance of an excess of conventional showers[89]; if an excess of unconventional showers were present then, presumably, this technique may decrease the significance of such an excess.

8.3.3 Searches for Point Sources of Underground Muons

Only the MACRO experiment has recently reported the result of a systematic search for an underground muon signal[3]. The experiment is deeper than SOUDAN 2, their data sample is $\lesssim 10\%$ of the SOUDAN 2 sample and the analysis method was a study of the deviations in an array of close-packed bins. It has been demonstrated that this method looses a great deal of power when the search is for a source with *a priori* unknown coordinates (see Chapter 5).

To compute a flux limit, MACRO assume the muon flux has no depth dependence. This assumption is clearly unrealistic and makes it difficult to compare the MACRO limit with the MX–1 flux. No direct examination of the 3C 273 region was made, but it is possible to infer a limit[43] of $\approx 16 \times 10^{-12}\ \mathrm{cm^{-2}s^{-1}}$ from the published whole-sky map. This limit is not in conflict with the flux computed here.

8.3.4 Comparison with Reported Underground Muon Flux from the Direction of Cygnus X–3

Both the SOUDAN 1 and NUSEX experiments reported excess underground muon flux from the direction of Cygnus X–3[14, 58]. Although this analysis has found no evidence for such excess from Cygnus X–3 (see Chapter 6), it is interesting to note that both experiments reported an angular distribution of events wider than the angular distribution expected from the *a priori* resolution. The only manner in which the events making up the MX–1 excess were found to differ from the background was that their angular distribution was wider than the $\sim (\sqrt{2})^\circ$ we should expect for a fluctuation or for a real 1° wide signal. The fitted width of $\hat{\sigma} = 2.4^\circ$ requires a true signal width of $\sim 2.2^\circ$ $(= \sqrt{(2.4^\circ)^2 - (1.0^\circ)^2})$.

It could be argued that, under the null hypothesis and as an artifact of the analysis method, a given fluctuation will always lead to a more "significant" result when the kernel scale is allowed to increase. A derivation of the distribution of $\sup Z$ in these circumstances has only recently been made[78] and this work shows that the above is not the case. The result may be understood from the following heuristic argument: the result of smoothing a random field with a kernel of scale σ, in 2-dimensions, is to produce a stochastic process that is realized as a set of "clumps." Each clump has a Normal probability of exceeding a given threshold, b. The effective number of trials is given by $\approx A / \langle C_b \rangle$, where C_b is the clump size and A the search area. For very large A, σ is the only scale in the problem and we expect that $C_b \propto \sigma^2$, so the number of trials, and hence the probability of the most deviant clump exceeding

b, increases rapidly as σ is decreased *not* as it is increased.

Ruddick introduced a massive secondary particle, that decayed to muons, to explain the angular distribution of the SOUDAN 1 and NUSEX results[75]. If the muon excess is real, the data would appear to support this hypothesis, although it is true that the angular resolution of the detector, σ, is not a very well determined parameter which may be underestimated examining by the di-muon space angle distribution.

8.4 Implications of a Muon Signal from 3C 273

From the results of Chapter 7 we see that the characteristics of the excess muon flux in the MX–1 region do not appear to differ strongly from the background. As a consequence of this few constraints can be placed on the nature of the possible signal from 3C 273.

It is possible to rule out all known neutral hadrons as a candidate primary due to the great distance to 3C 273. For a particle with free lifetime τ and mass m, the energy, E, with which the particle must be emitted from an object at the red-shift of 3C 273 is given by $E = (10^{16}\,\mathrm{s})m/\tau$.

Particle	m/ MeV	τ/ s	E/ eV	$\sqrt{s}$/ eV
π^0	140	8.4×10^{-17}	1.6×10^{40}	3.8×10^{18}
K_L	500	5.2×10^{-8}	9.6×10^{33}	3.0×10^{15}
D^0	1900	4.2×10^{-13}	4.4×10^{37}	2.0×10^{17}
B^0	5300	1.3×10^{-12}	4.1×10^{37}	2.0×10^{17}
n	940	890	1.1×10^{22}	3.2 GeV
Λ	1100	2.6×10^{-10}	4.3×10^{34}	6.4×10^{15}
Σ^0	1200	7.4×10^{-20}	1.6×10^{44}	3.0×10^{20}
Ξ^0	1300	2.9×10^{-10}	4.5×10^{34}	6.6×10^{15}
Ξ_c^0	2500	8.2×10^{-14}	3.0×10^{38}	5.4×10^{17}
glueball[1]	700	10^{-22}	10^{41}	10^{19}

Table 8.4: Table of the red-shifted beam energies and microwave background c.m.s. energies for some neutral, ground state, hadrons. The data are taken from reference [2]; [1]from the lattice calculation of reference [20].

This energy is tabulated in Table 8.4 for some ground-state hadrons. Also tabulated is the c.m.s. energy, $\sqrt{s}$, for collision of the particle with 2.7 K background

photons. No account has been taken of the cosmological evolution of the background temperature or photon density, the effect of which would be to increase both the c.m.s. energy and the reaction rate. All the tabulated particles must be accelerated to unreasonably large energies in order that they may travel from 3C 273 to the Earth without decaying in flight, and the computed flux at any of these energies would lead to an unacceptable quasar luminosity. It might be possible to push A.G.N. acceleration models sufficiently to accomodate the neutron energy although, even if this were possible, the c.m.s. energy for interaction with the microwave background photons is sufficient to excite N-baryon resonances in high angular momentum channels, leading to destruction of the neutron (i.e. 3C 273 is beyond the $\sim$ 100 Mpc limit, for particles of that energy, due to the Greisen-Zatsepin cutoff[30, 44, 93]).

If we require that the luminosity[3] into the muon channel is of a similar order of magnitude to the γ-ray luminosity of 3C 273 then the ratio m/τ, for the primary, must be $\lesssim 6 \times 10^{-4}$ eV/s. Either a new long-lived, low-mass, neutral particle or a muon-efficient photon would satisfy these requirements. Recent studies of photoproduction with almost-real photons at HERA would appear to rule out the latter. The ZEUS experiment measure a cross-section of $154 \pm 16 \pm 32\,\mu$b at γp c.m.s. energies of 100–295 GeV[32] corresponding to photon beam energies of 5–45 TeV for a stationary proton target. This cross-section is of a similar order of magnitude to that at low energies and shows no evidence for a "strongly interacting" photon.

8.5 Suggestions for Further Work

If there are point sources of underground muons then SOUDAN 2 will probably find them. The consequences of such a discovery would be immense and this thesis has shown that there are acceptable grounds for continuing the search for point sources. The data from March'93 to date, and for future running, should be accumulated and a third set of maps made when a statistically reasonable sample is available (say some 10 million muons).

The significance of the result discussed here is marginal. The greatest contribution to the significance is from the tests of Section 6.3.1 which, given the result of Section 5.11, are not the most powerful tests that could have been

[3]See Chapter 7 for an approximate calculation of this quantity.

performed. The tests of Section 6.3.2 are more appropriate for a signal with unknown scale, and are just as well defined under the null hypothesis. The inability to utilize these results, under the conservative prescription adopted in Section 8.2, has resulted in the loss of an order of magnitude in significance. The test that is to be performed on this new data-set should therefore be the examination of the deviations map in the region of the excess observed in this data-set, i.e. centered on the MX–1 fit position and with a radius specified by the mean radius of the 99% confidence region for the fit ($\sim 4°$), for evidence of a muon excess.

If the source is real then it seems likely that the response of the detector/analysis chain is not a 1° Gaussian, and in this case both kernels are mismatched. As there was little difference between the total probabilities computed for each kernel there is apparently little statistical penalty associated with the parallel analysis. However, the result of using a Gaussian kernel is to produce a considerably smoother deviations map, and the analytical simplicity that results from this is worth exploiting, so it is probably better to concentrate on the Gaussian kernel in future studies.

The power of any test performed is increased considerably if the detector resolution can be reduced. Although there is a limit set by the multiple scattering of muons in the rock, there is still room for improvement. The reconstruction programs have difficulties associated with the multiplexing of the detector and with the presentation of data in projective geometry. It might be worth investigating whether a fully 3-dimensional reconstruction could be implemented. As the data is, after readout, in a 2-dimensional representation the approach would have to be to define a track in 3-dimensions and then multiplex this track into logical space before computing the residual to each hit. To minimize the problems due to pattern recognition, which contributes the greater part of the error in the reconstruction, a method using robust statistics could be tried as an alternative to least-squares.

This thesis, and previous investigations, have come to the conclusion that, although there is no unambiguous evidence for point sources of underground muons, it may be worth continuing the work a little longer. Clearly, if studies continue to find the absence of irrefutable evidence, then will come a time when the work should be abandoned. I do not believe that this time has arrived yet.

APPENDIX A

THE SOUDAN 2 COLLABORATION

W.W.M. Allison[3], G.J. Alner[4], I. Ambats[1], D.S. Ayres[1], L.J. Balka[1], G.D. Barr[3], W.L. Barrett[6], D. Benjamin[5], P.M. Border[2], C.B. Brooks[3], J.H. Cobb[3], D.J.A. Cockerill[4], K. Coover[1], H. Courant[2], B.B. Dahlin[2], U. DasGupta[2], J.W. Dawson[1], D.M. DeMuth[2], V.W. Edwards[4], B. Ewen[5], T.H. Fields[1], C. Garcia-Garcia[4], H. Gallagher[2], R.H. Giles[3], G.L. Giller[3], M.C. Goodman[1], R.N. Gray[2], S. Heppelmann[2], N. Hill[1], J.H. Hoftiezer[1], D.J. Jankowski[1], K. Johns[2], T. Joyce[2], T. Kafka[5], S.M. S. Kasahara[2], J. Kochocki[5], W. Leeson[5], P.J. Litchfield[4], N.P. Longley[2], F.V. Lopez[1], M.J. Lowe[2],[h], W.A. Mann[5], M.L. Marshak[2], E.N. May[1], D. Maxam[2], L. McMaster[5], R. Milburn[5], W.H. Miller[2], C.P. Minor[2], A. Napier[5], R. Nickson[4], W. Oliver[5], G.F. Pearce[4], D.H. Perkins[3], E.A. Peterson[2], L.E. Price[1], D.M. Roback[2], D.B. Rosen[2], K. Ruddick[2], B. Saitta[5], D.J. Schmid[2], J. Schlereth[1], J. Schneps[5], P.D. Shield[3], M.A. Shupe[2], A. Stassinakis[3], N. Sundaralingam[5], M.A. Thomson[3], J.L. Thron[1], L.M. Tupper[3], G. Villaume[2], E.W.G. Wallis[4], L. Weems[2], S.J. Werkema[2], N. West[3] , U.M. Wielgosz[3], C.A. Woods[4] and S. Yarker[4].

[1]*Argonne National Laboratory, Argonne, IL 60439, U.S.A.*
[2]*University of Minnesota, Minneapolis, MN 55455, U.S.A.*
[3]*Department of Physics, University of Oxford, Oxford, OX1 3RH, U.K.*
[4]*Rutherford Appleton Laboratory, Chilton, Didcot, OX11 0QX, U.K.*
[5]*Tufts University, Medford, MA 02155, U.S.A.*
[6]*Western Washington University, Bellingham, WA 98225, U.S.A.*

APPENDIX B

ASTRONOMICAL COORDINATES

This Appendix describes the various coordinate systems used in astronomy. Reference [12] should be consulted for formal definitions.

B.1 Spatial Coordinate Systems

Ideal Detector Coordinates

In the ideal detector coordinate system the y-axis is the vertical, the z-axis points to true north, and the x-axis points west. Thus the same set of axes are used as for horizon coordinates. The origin is the lower south-west corner of the detector. The direction of a track is expressed in terms of the projected angles:

$$\left.\begin{array}{rcl}\tan\alpha & = & dy/dz \\ \tan\beta & = & dx/dz\end{array}\right\} \alpha,\beta \in [-\tfrac{1}{2}\pi, \tfrac{1}{2}\pi]. \qquad \text{(B.1)}$$

The actual detector axes lie slightly to the west of North. (0.26°, see [60].)

Horizon Coordinates

In horizon coordinates the x-axis points west, the y-axis is the local vertical, and the z axis points to true north. The *altitude*, $a \in [-\frac{1}{2}\pi, \frac{1}{2}\pi]$, is the angle above the xz plane. The *azimuth*, $A \in [0, 2\pi]$, is the angle in the plane, measured positive eastwards. The origin is the observers location on the Earth's surface. Figure B.1 illustrates the definition of the angles. It is usual to express the coordinates of an

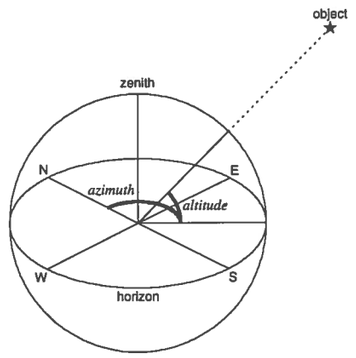


Figure B.1: The horizon coordinate system.

astronomical object relative to the observer in this system. The *zenith angle* is the angle away from the pole, thus: $\theta = \frac{1}{2}\pi - a$.

Equatorial Coordinates

The equatorial coordinate system is the intermediate stage in the transformation from the observer's local coordinates to celestial coordinates. The coordinate system rotates with the Earth, but the origin is located at the centre of the Earth and the axes are expressed relative to the plane of the Earth's equator. The angle in the plane is the *hour angle*, $h \in [0, 2\pi]$, defined as angular distance westwards between the meridian circle (the great circle passing through the celestial poles and the local zenith) and the hour circle (the great circle passing through the celestial poles and the object). The hour angle is thus equal to the time since the object passed the meridian, and it is common to reckon h in hours. The angle above the plane is the *declination*, $\delta \in [-\frac{1}{2}\pi, \frac{1}{2}\pi]$. Figure B.2 illustrates these angles.

Celestial Coordinates

The celestial coordinate system is a coordinate system stationary with respect to the fixed stars. The origin is the centre of the Earth and the angles defined with respect to the plane of the equator. Thus this system is obtained from equatorial coordinates by subtracting the rotation of the Earth.

The angle in the plane is the *Right Ascension*, $\alpha \in [0, 2\pi]$, measured positive eastwards from a reference point to the hour circle of the object. The Right

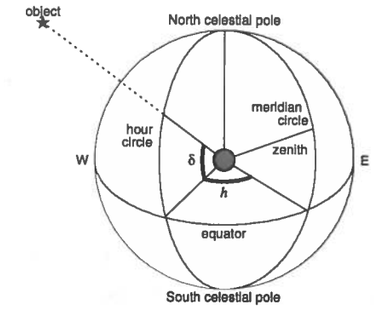


Figure B.2: The equatorial coordinate system.

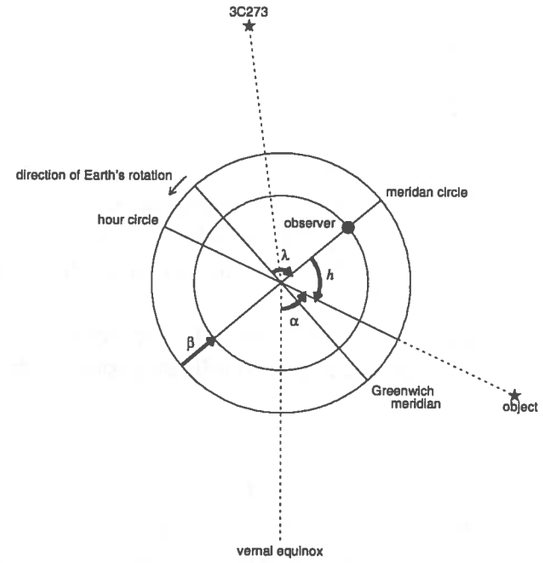


Figure B.3: The relationship between equatorial and celestial coordinates. λ and β are the west longitude and latitude of the observer; h is the hour angle and α the Rigth Ascension of the object.

Ascension and hour angle are linked by

$$\alpha = l - h \tag{B.2}$$

where the local sidereal time, l, is a measure of the rotation of the Earth with repect to the stars. This is illustrated in Figure B.3.

Historically the reference point was taken to be the *vernal equinox* (the ascending node of the ecliptic on the equatorial plane) also called the *Rising of Aries*, however the reference is now taken to be be the Right Ascension of quasar 3C 273.

The direction of the vernal equinox is not constant, but changes slowly with time due to the interaction between the Sun, Moon and the equatorial bulge of the Earth. Right Ascensions are tabulated with respect to a standard equinox (J2000.0) and should then be corrected to the *equinox of date*. This correction is small (typically $\sim 50''$/year [34]). For J2000.0, the Right Ascension of 3C 273 is $12^h29^m6.69971^s$.

The angle above the plane is the declination, identical to the angle defined above.

B.2 Representation of Data on the Sphere (The Aitoff Plot)

Astronomy often involves the representation of data, be it flux, polarisation, frequency etc. as a function of the observing coordinates. Since these coordinates are usually the angles in a spherical polar coordinate system the data can only be represented without distortion actually on the surface of a sphere. However, this is not really practical.

In most of the analytical work in this thesis I have treated the dependence on celestial coordinates as a locally Euclidean coordinate system with a metric

$$ds^2 = \cos^2\delta\, d\alpha^2 + d\delta^2. \tag{B.3}$$

With this formalism the element of length, ds, represents the space angle between two points and the element of area, $\cos\delta\, d\alpha\, d\delta$, the solid angle subtended by a region. This formalism also helps to remind us that writing $d\Omega$ as $d\alpha\, d\sin\delta$ is often less useful than we would initially expect (see Section 5.7).

However, the use of a metric leads us to plot the data as if (α, δ) was a normal rectangular coordinate system. Although locally this causes no problems it brings complications when we attempt to compare images near the poles to images near

the equator since equal areas of the plotting surface no longer represent equal solid angles.

To overcome this difficulty it is usual to plot data that covers a large proportion of the sphere in the *Aitoff projection*. This is a transformation that distorts both angular coordinates (α, δ) into rectangular coordinates (x, y) while preserving areas. x lies in the interval $[-2, 2]$ and y in $[-1, 1]$. The transformation is

$$\begin{aligned} x &= \frac{2\cos\delta \sin\frac{1}{2}\alpha}{\rho} \\ y &= \frac{\sin\delta}{\rho} \\ \text{where } \rho &= \sqrt{1 + \cos\delta\cos\tfrac{1}{2}\alpha}. \end{aligned} \tag{B.4}$$

Figure B.4 shows the projection of the sphere. Wherever this "egg" occurs in this thesis, unless otherwise specified, it should be assumed that it represents data in celestial coordinates. Right Ascension is read from $-180°$ on the L.H.S. to $+180°$ on the R.H.S. Similarly the poles ($\delta = \pm 90°$) are at the top and bottom respectively. The divisions are at $0°$, $\pm 60°$ and $\pm 120°$ in R.A. and $0°$, $\pm 30°$ and $\pm 60°$ in declination.

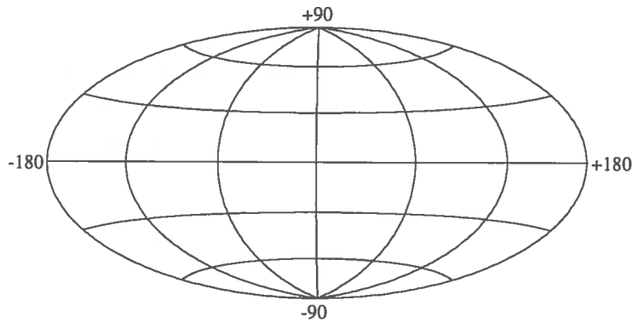


Figure B.4: The Aitoff sphere.

APPENDIX C

STATISTICAL CONSIDERATIONS

In this appendix two statistical issues, relevant to the analysis methods used in this thesis, are discussed. The are the use of the maximum likelihood ratio as a test statistic and the statistical properties of correlated searches on binned data.

C.1 The Maximum Likelihood Ratio Test

In astronomy one frequently wishes to extract the location and strength of a source from a data-set which comprises the arrival directions of quanta that trigger the detector. In high energy astronomy the trigger rate of the experiment is often low, and so the density of particles in the coordinate space considered is also quite low. The use of a χ^2 statistic to fit the source coordinates and strength, in such conditions, may only be possible by binning the data so coarsely that all directional precision is lost, and so is undesirable. In these conditions it is usual practice use a maximum likelihood method to fit the data. Under this procedure, unlike least-squares in which the χ^2 at the best fit position may be used as a statistic to judge the quality of the fit, the maximized likelihood has no absolute meaning and cannot be used as a statistic.

To avoid this problem, and allow the maximum likelihood method to be used for both parameter estimation and hypothesis testing in high energy astronomy, the COS-B group introduced the use of the maximum likelihood ratio as a test statistic[69]. A theorem of Wilks[90] establishes that, if H_0 is a composite hypothesis with p

parameters that describes the data, then the maximum likelihood ratio

$$\Lambda = 2 \ln \frac{\max L(q)}{\max L(r)}, \tag{C.1}$$

where $L(q)$ is the likelihood computed when $p - q$ of the parameters are fixed at their true values and $L(r)$ the likelihood when $p - r$ are fixed at their true values (and $q > r$), is distributed asymptotically as χ^2 for $q - r$ degrees of freedom. Note that this is the ratio of the maximum likelihoods and *not* the maximum of the ratio of likelihoods.

Knowing the p.s.f. (the instrumental response to a point source), the COS-B group fitted the proportion, X, of the γ-ray signal due to a source, with the remaining fraction required to be due to the background, using a maximum likelihood method. The likelihood was also computed with $X = 0$. The goal was to establish whether any of the galaxies examined were point sources of γ-rays. If this is not the case then the fit corresponds to $L(1)$ and the likelihood computed with $X = 0$ corresponds to $L(0)$ — i.e. the likelihood when the free parameter is held at its true value. Therefore, Λ should be distributed as χ^2_1. Although a plot is not included in Reference [69], the tabulated data ($\lambda = \frac{1}{2}\Lambda$ is tabulated) is distributed in this manner.

The COMPTEL group extended this analysis method by implementing the following algorithm: we consider a set of hypotheses, $\{H_n\}$, in which H_0 states that the data is distributed in the manner we would expect for the background; H_1 is equivalent to H_0 plus one point source, of unknown location and strength; H_2 is H_1 with another source; etc. H_i is a sub-hypothesis of $H_j \, \forall \, j > i$. H_n contains $3n + 1$ free parameters: the coordinates and strength of each source and the proportion of the background to be included. For H_n we bin the data in the observing space and compute the expected number of events in each bin from the background plus the proportion of each source that intersects that bin. This allows the likelihood to be computed as the product of Poisson probabilities. The procedure followed is then[19]:

i, state the most simple hypothesis, initially H_0, and fix the parameters of the most general hypothesis, H_n, leaving r free (so that H_n is equivalent to H_0);

ii, state a more complex hypothesis, initially H_1, and fix the parameters of H_n leaving q free (so that H_n is equivalent to H_1);

iii, maximize the likelihood, L, under both hypotheses and compute $\Lambda = 2 \ln \hat{L}(H_n|q)/\hat{L}(H_n|r)$;

iv, if $\Lambda > \Lambda_c$ then reject the simple hypothesis in favour of the more complex hypthesis with confidence $Pr(\chi^2_{q-r} < \Lambda_c)$; in this case $q - r = 3$; *and*

v, repeat until the number of sources required by the data is known.

This procedure requires that the the form of the p.s.f. and a model of the background are known. However, it is possible to parameterize both these quantities and allow them to be fitted under all hypotheses. Once the model required by the data is fixed, confidence regions for the parameters may be extracted by the usual method of tracing out the hyper-contour defined by $\ln L = \ln \hat{L} - \frac{1}{2} d\chi^2$ to give a region of probability content $Pr(\chi^2_q < d\chi^2)$. To take full account of all correlations between the variables, this should be done by a method such as that used by the program `MINOS`[48].

Given a set of bins with expectations $\{\bar{n}_i\}$ and contents $\{n_i\}$ it is sufficient to minimize the function

$$\mathcal{L} = -\ln L = \sum_i (\bar{n}_i - n_i \ln \bar{n}_i) \tag{C.2}$$

as all other terms cancel in the ratio Λ.

C.2 The Statistics of Correlated Searches

The purpose of the following sections is to discuss the behaviour of the smoothing process, applied to the data in the manner described in Chapter 5, to illustrate how this behaviour can be understood in terms of a simple heuristic description of the process, and to define some terms. The following discussion is based on that given in Reference [4]; a more rigorous derivation of the formulae quoted is beyond the scope of this thesis.

C.2.1 The Poisson Clumping Heuristic and an Analogy with Noise Trigger Rates

Some Definitions

We consider a random field, X_t, which we assume is Gaussian. i.e. That $X_t \sim N(0,1) \, \forall \, t$ and $\mathrm{Cov}(X_t, X_s) = \delta_{ts}$. The coordinates at which this field

is defined are taken to be a discrete grid, i.e. $t \in \{t_i\}$. We shall assume here that we may ignore the effect of discretisation to first order.

A stochastic process, Z_t, is said to be a *Gaussian* process if its behaviour is determined solely by the *mean function* and *covariance function*:

$$\text{i.e. } m(t) = \text{Exp}\, Z_t \text{ and } R(s,t) = \text{Cov}(Z_s, Z_t). \tag{C.3}$$

For a stationary process, we put $m(t) = 0$. The conditional distributions may then by specified simply: given $Z_s = z$, the distribution of Z_t is Normal with mean $zR(s,t)/R(s,s)$ and variance $R(t,t) - R^2(s,t)/R(s,s)$. The process possesses a translational invariance, i.e. $R(s,t) = R(s-t,0)$, so we need only define $R(t) = R(t,0)$ which is standardized Var $Z_t = 1$.

If Z_t is obtained by the convolution of X_t with some kernel, K_s,

$$Z_t = \sum_s K_s X_{t-s} \tag{C.4}$$

then the covariance function is given by:

$$\begin{aligned} R(s,t) &= \text{Exp}\, Z_s Z_t - \text{Exp}\, Z_s \,\text{Exp}\, Z_t \\ &= \text{Exp} \sum_{uv} K_u X_{s-u} K_v X_{t-v} \\ &= \sum_{uv} K_u K_v \,\text{Exp}\, X_{s-u} X_{t-v}. \end{aligned} \tag{C.5}$$

Now, Exp $X_i X_j = \delta_{ij}$, so

$$R(s,t) = \sum_u K_{u-s} K_{u-t} = \sum_u K_u K_{u-(s-t)}. \tag{C.6}$$

i.e. The covariance function is equal to the convolution of the kernel with itself. If the covariance function satsifies $R(t) \simeq 1 - \frac{1}{2}\theta t^2$, for small t, then the process is said to be *smooth*. If K is a simple kernel, $K_t = 1 \,\forall\, t \le r; K_t = 0$ otherwise, then Z_t is not smooth; but for a Gaussian kernel, $K_t = \mathrm{e}^{-t^2/2\sigma^2}$, then the process is smooth and $\theta = 1/2\sigma^2$.

If the process is smooth we may define a velocity, V_t, by

$$V_t = \lim_{\delta \to 0} \frac{Z_{t+\delta} - Z_t}{\delta}. \tag{C.7}$$

Clearly Exp $V_t = 0$. Also,

$$\begin{aligned} \text{Exp}\, Z_t V_t &= \lim_{\delta \to 0} \frac{\text{Exp}\, Z_{t-\delta} Z_t - \text{Exp}\, Z_t^2}{\delta} \\ &= \lim_{\delta \to 0} \frac{R(t+\delta, t) - R(t,t)}{\delta} = 0 \end{aligned} \tag{C.8}$$

and

$$\begin{aligned} \text{Exp}\, V_t^2 &= \lim_{\delta \to 0} \text{Exp} \left(\frac{Z_{t+\delta} - Z_t}{\delta} \right)^2 \\ &= \lim_{\delta \to 0} \text{Exp}\, \frac{Z_{t+\delta}^2 + Z_t^2 - 2 Z_{t+\delta} Z_t}{\delta^2} \\ &= \lim_{\delta \to 0} \frac{R(t+\delta, t+\delta) + R(t,t) - 2R(t+\delta, t)}{\delta^2} = \theta. \end{aligned} \tag{C.9}$$

Therefore V_t is distributed as $N(0,\theta)$ and is independent of Z_t. The conditional distributions for V_t may also be found:

$$\begin{aligned} \text{Exp}(V_t | Z_s = b) &= \lim_{\delta \to 0} \frac{\text{Exp}(Z_{t+\delta} - Z_t | Z_s = b)}{\delta} \\ &= \lim_{\delta \to 0} \frac{b\theta}{2\delta} \left\{ (t+\delta-s)^2 - (t-s)^2 \right\} \\ &= -b\theta(t-s) \end{aligned} \tag{C.10}$$

and

$$\begin{aligned} \text{Exp}(V_t V_s | Z_s = b) &= \lim_{\delta \to 0} \frac{\text{Exp}(Z_{t+\delta} Z_{s+\delta} + Z_t Z_t - Z_{t+\delta} Z_s - Z_t Z_{s+\delta} | Z_s = b)}{\delta^2} \\ &= \lim_{\delta \to 0} \frac{R(t+\delta, s+\delta) + R(t,s) - R(t+\delta, s) - R(t, s+\delta)}{\delta^2} \\ &= \lim_{\delta \to 0} \frac{\frac{1}{2}\theta(t-s+\delta)^2 + \frac{1}{2}\theta(t-s-\delta)^2 - \theta(t-s)^2}{\delta^2} \\ &= \theta. \end{aligned} \tag{C.11}$$

The Poisson Clumping Heuristic

The deviations maps computed from the data (see Chapter 5) are a realization of the process, Z_t, in two dimensions. Although the underlying field, X_t, is not

Gaussian but Poissonian with an expectation of 3–4, the covariance function is approximately that of Gaussian process as the fluctuations $Z_{t+\delta} - Z_t$ are Poissonian with an expectation of several hundred.

The heuristic states that fluctuations in X_t manifest themselves as "clumps" in Z_t. Searching the map identifies $\max Z_t$ so we wish to compute the distribution[1] $Pr(\sup_{t\in A} Z_t > b)$, where A is the searched area. The peak of each clump is taken to have a Normal distribution and size C_b. The heuristic then states that the clumps with a peak exceeding b occur at a rate $\lambda_b = Pr(Z_t > b)/\operatorname{Exp} C_b$, so that

$$Pr(\sup_{t\in A} Z_t > b) \approx 1 - \exp\left\{-A\frac{Pr(Z_t > b)}{\operatorname{Exp} C_b}\right\}. \tag{C.12}$$

Analogy with Noise Trigger Rates

For the 1-dimensional it is possible to exploit the fact that the space, t, is well ordered to compute the distribution of Z_t for a generalized kernel, K. This calculation is usually presented in the context of noise theory as, if K_t is the impulse response of an electronic system and X_t is bandwidth limited white noise, then Z_t is the response of the system to noise and the rate at which Z_t crosses a threshold, b, is of interest.

The calculation is straight-forward so only the result will be quoted here. For a derivation see Reference [42]. It is found that the noise trigger rate is given by

$$\text{N.T.R.} = \tfrac{1}{2}\rho_z e^{-b^2/2\sigma^2}, \tag{C.13}$$

where ρ_z is the zero-crossing rate and σ the r.m.s. noise signal. The zero-crossing rate is

$$\rho_z = \sqrt{\int \omega^2 |k(\omega)|^2 d\omega \Big/ \int |k(\omega)|^2 d\omega}\,. \tag{C.14}$$

$k(\omega)$ is the Fourier transform of the impulse-response. Therefore ρ_z is the r.m.s. frequency passed by the system, weighted by the power spectrum. Such a result is clearly reasonable and provides the correct value of the clump rate in 1-dimension. In higher dimensions, this method of calculation is not suitable but the analogy will help us to understand the results derived.

[1] The supremum of a set need not be a member of the set itself, whereas the maximum must. In this case the distinction is slight, but I shall use sup as that is the practice in the literature.

C.2.2 Correlated Searches with a Gaussian Kernel

Let Z_t be a smooth Gaussian process. If $Z_0 = z$ then, from Equations C.10 and C.11,

$$\begin{aligned} \operatorname{Exp}(V_t - V_0 | Z_0 = z) &\simeq -\theta z t \\ \operatorname{Var}(V_t - V_0 | Z_0 = z) &= \mathcal{O}(t^2), \end{aligned} \tag{C.15}$$

for small t. The variance is negligible to first order, so the behaviour of Z_t in the region between $Z_0 = z$ and $Z_{\pm s} = b$ (for small s) is almost deterministic. Given V_0, we may integrate to obtain

$$Z_t = z + V_0 t - \tfrac{1}{2}\theta z t^2 + \mathcal{O}(t^2). \tag{C.16}$$

i.e. The local motion of Z_t follows a parabola. Generalising to d dimensions

$$Z_t \simeq z + v \cdot t - \tfrac{1}{2} z t^T \theta t, \tag{C.17}$$

where θ is a $d \times d$ matrix. If $Z_0 = z$ is a local maximum, and b is some threshold ($z > b > 0$), then the clump size is the projected area of the paraboloid defined by $Z_t > b$:

$$\operatorname{Exp}(C_b | z) \simeq \frac{2\pi^{\frac{1}{2}d}}{d\Gamma(\frac{1}{2}d)} |\theta|^{-\frac{1}{2}} \left\{\frac{2(z-b)}{z}\right\}^{\frac{1}{2}d} = m(z|b). \tag{C.18}$$

This expression is the product of the volume of the unit sphere in d-dimensions and a term from solving $z - \frac{1}{2} z t^T \theta t = b$. For a Gaussian kernel in 2-dimensions, with covariance matrix $\sigma^2 \mathcal{I}$, this is $\pi(z-b)/\sigma^2 z$.

The clump rate, λ_b, may now be extracted by a method known as "conditioning on semi-local maxima." We define a density such that the probability of a local maximum in $[z, z+dz; dA]$ is $L(z)\, dz dA$. The rate at which clumps with maxima $z > b$ occur is given by

$$\lambda_b = \int_b^\infty L(z)\, dz \tag{C.19}$$

and the probability that a Z_t exceeds b is

$$Pr(Z_t > b) \simeq \int_b^\infty L(z) m(z|b)\, dz. \tag{C.20}$$

Let $\phi(x)$ be the standard Normal density. As $Z_t \sim N(0,1)$, and using the approximation[2] $\phi(x)/x \simeq \frac{1}{2}(1 - \operatorname{erf} x/\sqrt{2})$, we anticipate a solution of the

[2] This extremely useful approximation is good to better than 20% for $x > 2$ and is very good for large x. It is an overestimate.

form $L(z) \approx g(z)\phi(z)$ where $g(z)$ is a polynomial. We write $z - b = u$ and $L(b+u) \approx g(b)\phi(b)\mathrm{e}^{-bu}$, assuming that g varies slowly relative to ϕ, so

$$\phi(b)/b \approx \frac{2\pi^{\frac{1}{2}d}}{d\Gamma(\frac{1}{2}d)} \left(\frac{2^d}{b^d|\theta|}\right)^{\frac{1}{2}} g(b)\phi(b) \int_0^\infty u^{\frac{1}{2}d}\mathrm{e}^{-bu}\, du. \tag{C.21}$$

Therefore $g(b) \approx (2\pi)^{-d/2}|\theta|^{1/2}b^2$ and, using Equation C.19,

$$\lambda_b = \left\{\frac{|\theta|}{(2\pi)^d}\right\}^{\frac{1}{2}} b^{d-1}\phi(b). \tag{C.22}$$

The full result for the Gaussian kernel in 2-dimensions is then

$$Pr(\sup_{t\in A} Z_t > b) = 1 - \exp\left\{-\frac{A}{2\sigma^2} b \frac{\mathrm{e}^{-\frac{1}{2}b^2}}{(2\pi)^{3/2}}\right\}. \tag{C.23}$$

C.2.3 Correlated Searches with a Simple Kernel

The above analysis is not exact, yet the result is a good approximation to the real behaviour of the process, Z_t. Unfortunately, such a method cannot be applied to the case of smoothing with a simple kernel. The reason for this can be explained by considering Equation C.13. For a simple kernel, in 1-dimension, the response spectrum $k(\omega) \sim (\sin\omega)/\omega$. With this spectrum, the r.m.s. frequency, ρ_z, diverges. The method "conditioning on semi-local maxima" involves counting the rate at which maxima of Z_t occur in the random plane t. The divergence of ρ_z is equivalent to stating that the number of maxima in a finite area is infinite. This is because Z_t is not a smooth process.

The divergence of ρ_z may be controlled by introducing a cutoff frequency, ω_c, which is done by using bins of finite size. In other words, we cannot treat the problem of smoothing with a simple kernel unless we also treat the discretization of the space t. Before smoothing, but with a cutoff, the r.m.s. frequency is clearly $\propto \omega_c$. After smoothing this is also the case — i.e. taking ρ_z as a measure of the smoothness of the data, Z_t is not smoother than X_t. In the language of time-series analysis: the rate at which turning points occur is not affected by the procedure. This may be seen directly by examining the maps discussed in Chapters 6 and 7.

More sophisticated techniques must be used to derive the distribution of $\sup_{t\in A} Z_t$ for the simple kernel[77], and the analysis is too complicated to discuss here. Nevertheless, many of the concepts of the previous analysis are retained. The fluctuations in X_t still manifest themselves as clumps in Z_t, which occur at a rate λ_b. We may make two naive estimates of the clump size:

i, Exp C_b is just 1 bin, so $\lambda_b A \lesssim m\phi(b)/b$ where m is the total number of bins; *and*

ii, Exp C_b is the kernel size of r bins, so $\lambda_b A \gtrsim (m/r)\phi(b)/b$.

m is the total number of places at which we have placed the kernel and m/r is the total number of independent places where we might have placed the kernel. The true result must lie between these two estimates.

For a "square" space of $m_1 \times m_2 \times \ldots \times m_d$ bins, and a simple kernel of size $r_1 \times r_2 \times \ldots \times r_d$ bins, the expected number of clumps above threshold b is

$$\lambda_b A = b^{2d-1}\phi(b) \prod_i \frac{m_i}{r_i} \nu(b\sqrt{2/r_i}). \tag{C.24}$$

$\nu(x)$ is Siegmund's function:

$$\nu(x) = \frac{2}{x^2} \exp\left\{-\sum_{n=0}^{\infty} \frac{1}{n}\left(1 - \operatorname{erf} x\sqrt{n/8}\right)\right\}. \tag{C.25}$$

For $x < 2$ this may be approximated by $\mathrm{e}^{-0.583x}$ and for large x by $2/x^2$. This calculation assumes edge effects may be neglected; $\nu(x)$ corrects for the effect of discretization. It is important to note that this rate is a factor of b^{2d} higher than the naive, but many would argue very reasonable, guess of (ii).

APPENDIX D

AITOFF PROJECTION MAPS OF THE COMBINED DATA SET

This appendix contains the map of the whole visible sky discussed in this thesis. The map is divided into twelve sections and is drawn in the Aitoff projection to preserve solid angles. Figure D.1 shows where each section lies on the celestial sphere. To help illustrate the distortion of shapes due to the Aitoff projection, each of the candidate objects listed in Table 6.7 is marked with the projection of a $1.6°$ cone centred on it's nominal coordinates. The data has been smoothed with a simple kernel and the standard deviation at each pixel is illustrated by the intensity and colour with which the pixel is marked. The scale ranges linearly from $Z = -5$ (fully blue) to $Z = +5$ (fully red) and then saturates for more deviant points. Pixels where the absolute deviation was less than 0.35 or the background expectation was less than 200 are not plotted. In each section the most deviant point (positive or negative) is marked. The combined data set was used in making this map.

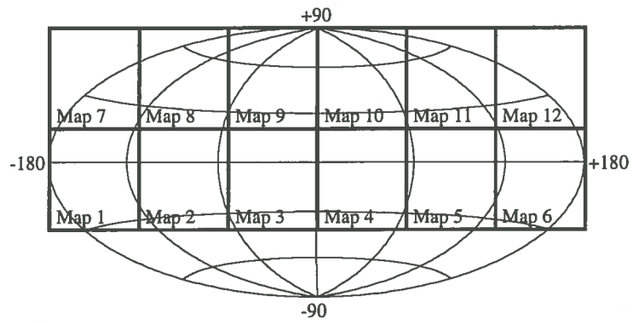
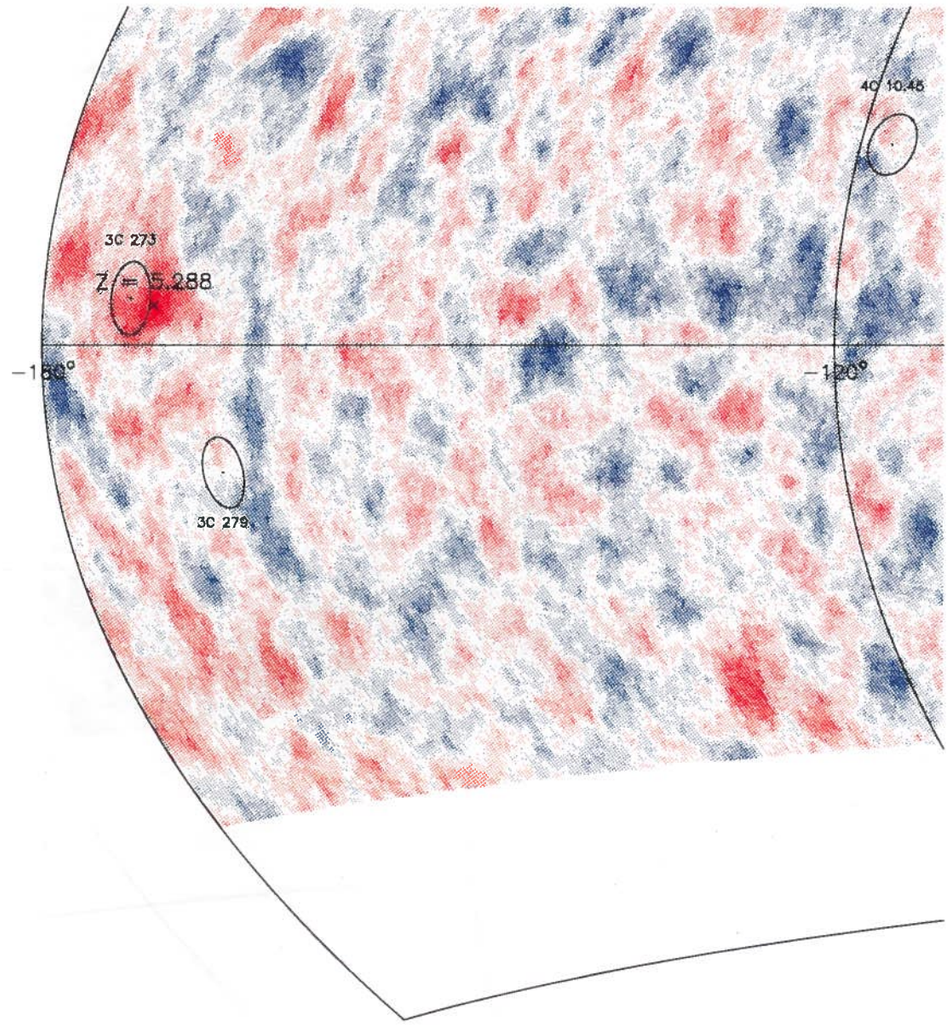


Figure D.1: Key to the location of twelve map sections on the celestial sphere.

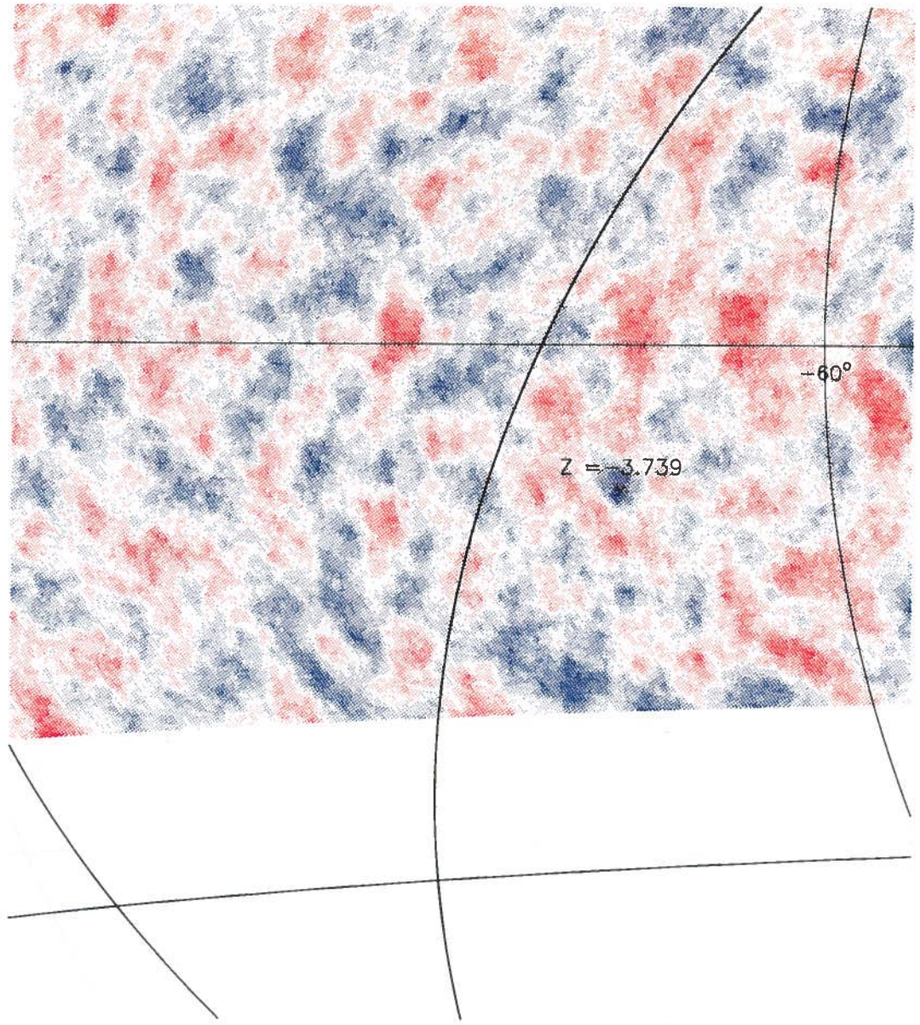
Celestial Coordinates, J2000.0



Exposure: 01/01/89–28/02/93

Aitoff Map No. 1

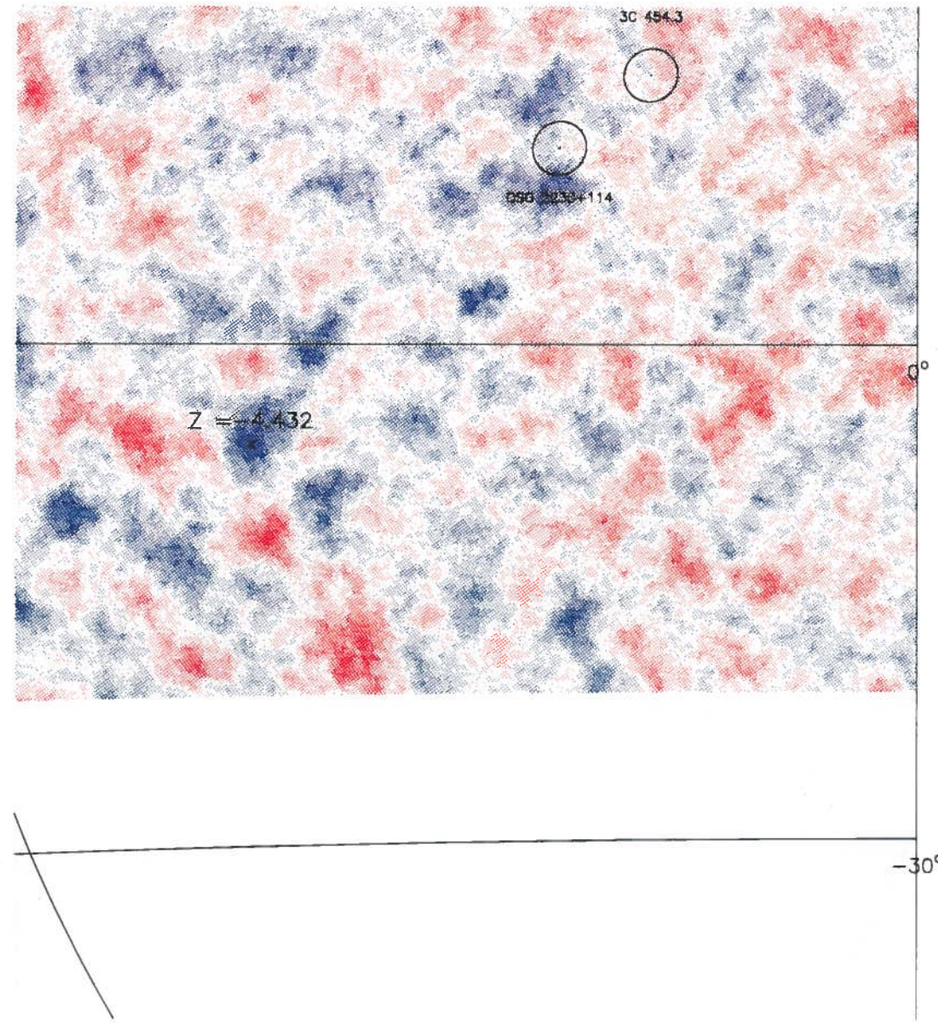
Celestial Coordinates, J2000.0



Exposure: 01/01/89–28/02/93

Aitoff Map No. 2

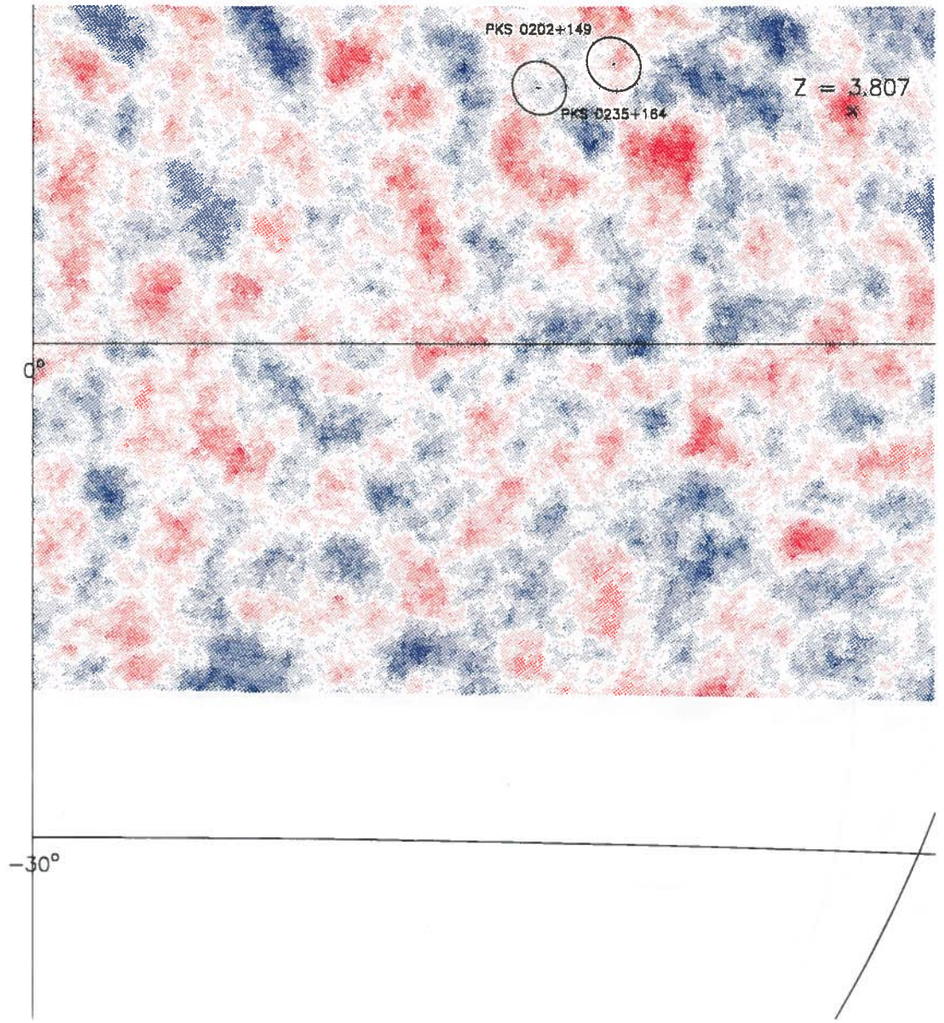
Celestial Coordinates, J2000.0



Exposure: 01/01/89–28/02/93

Aitoff Map No. 3

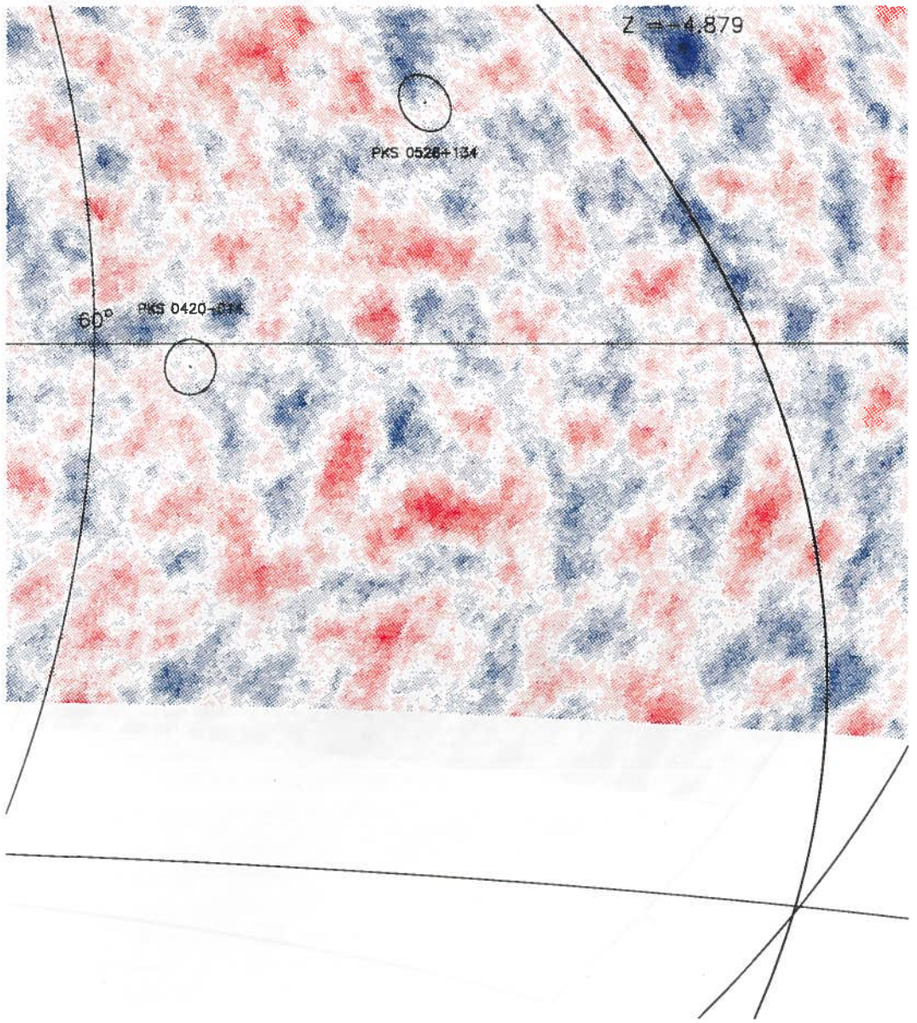
Celestial Coordinates, J2000.0



Exposure: 01/01/89–28/02/93

Aitoff Map No. 4

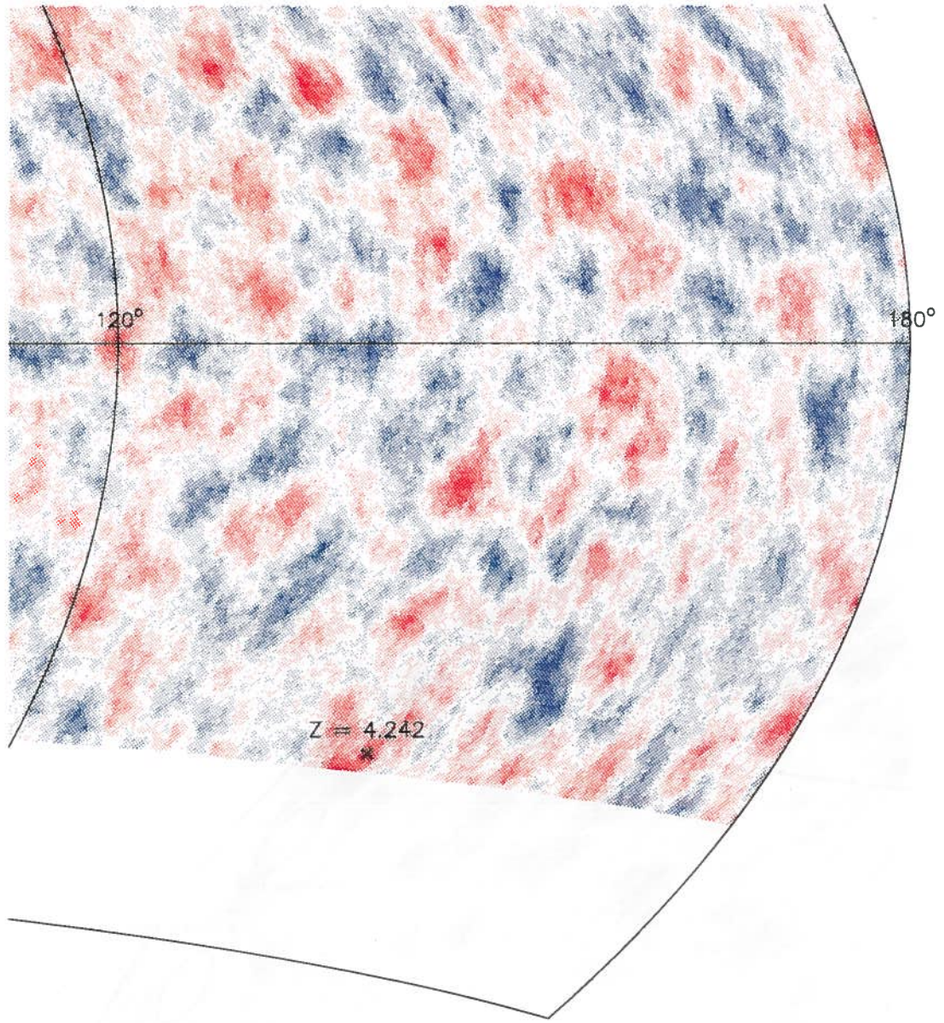
Celestial Coordinates, J2000.0



Exposure: 01/01/89–28/02/93

Aitoff Map No. 5

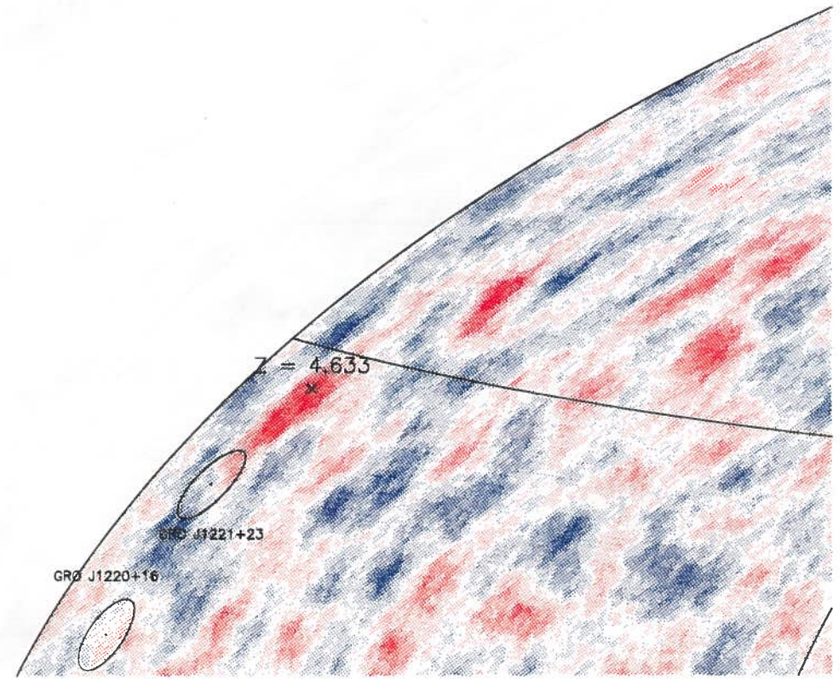
Celestial Coordinates, J2000.0



Exposure: 01/01/89–28/02/93

Aitoff Map No. 6

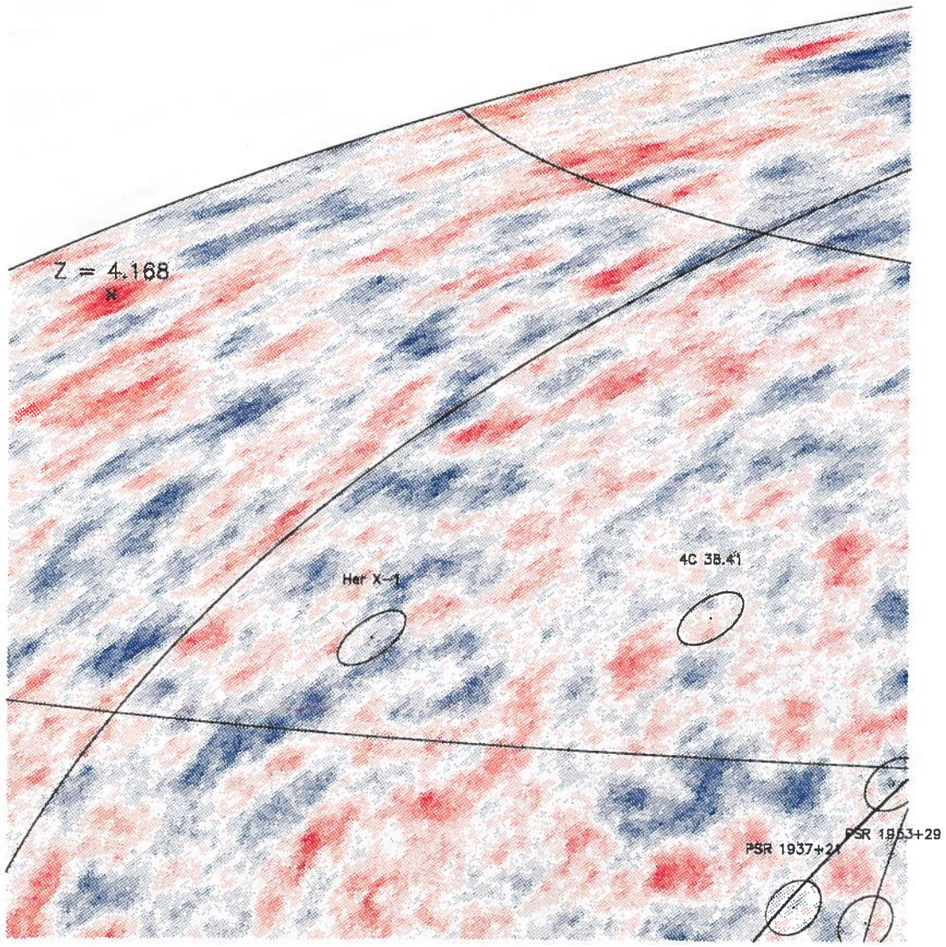
Celestial Coordinates, J2000.0



Exposure: 01/01/89–28/02/93

Aitoff Map No. 7

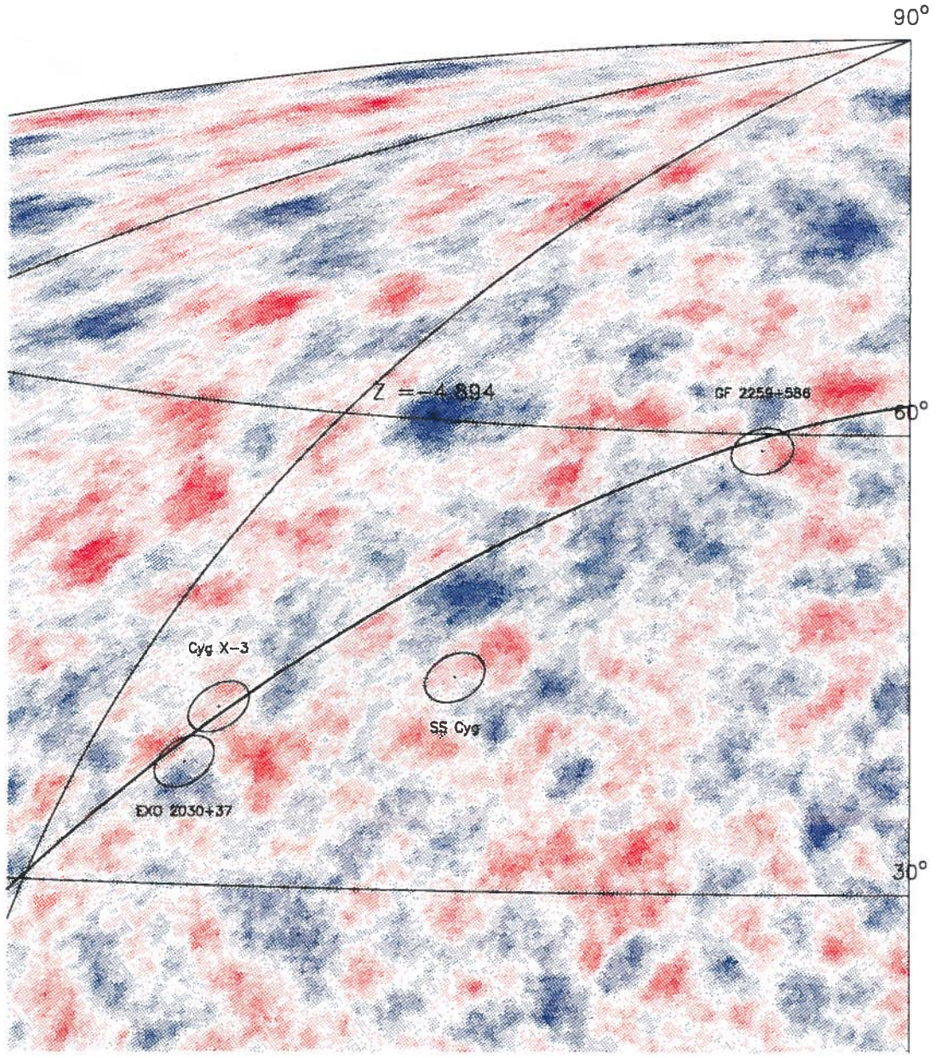
Celestial Coordinates, J2000.0



Exposure: 01/01/89–28/02/93

Aitoff Map No. 8

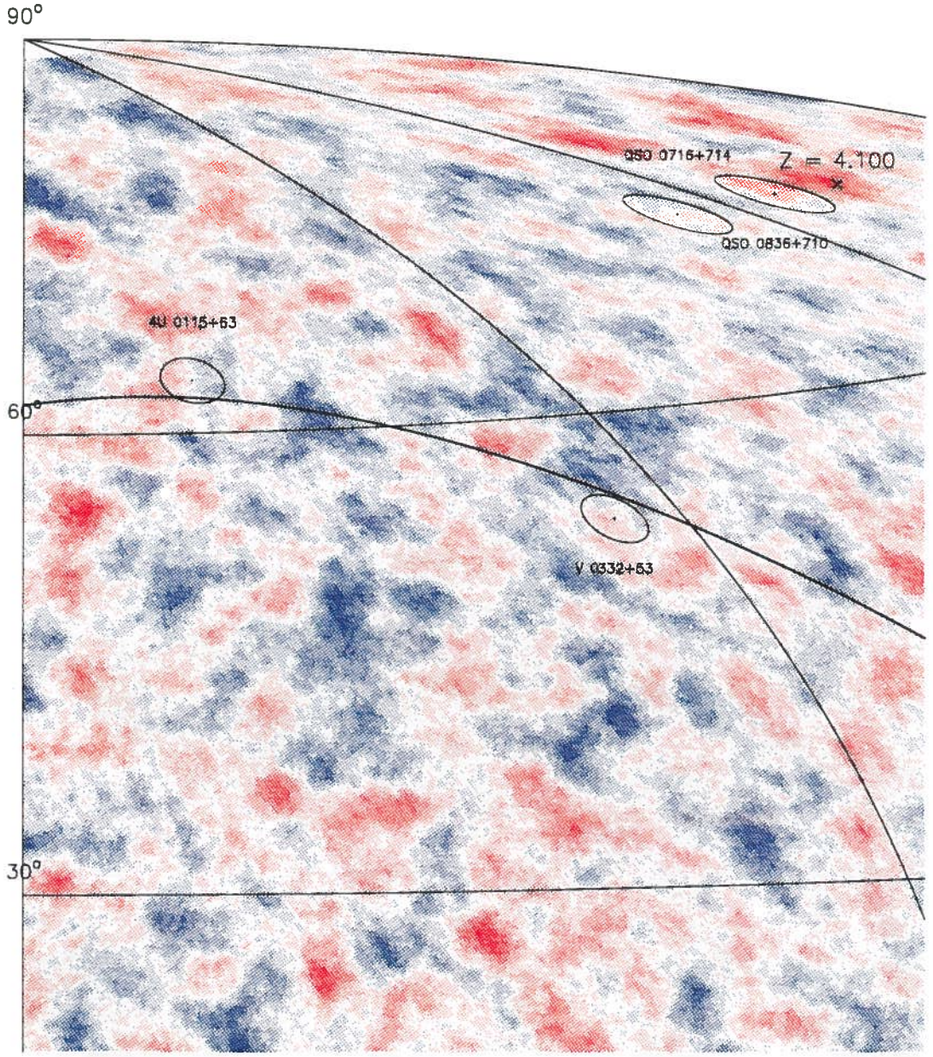
Celestial Coordinates, J2000.0



Exposure: 01/01/89–28/02/93

Aitoff Map No. 9

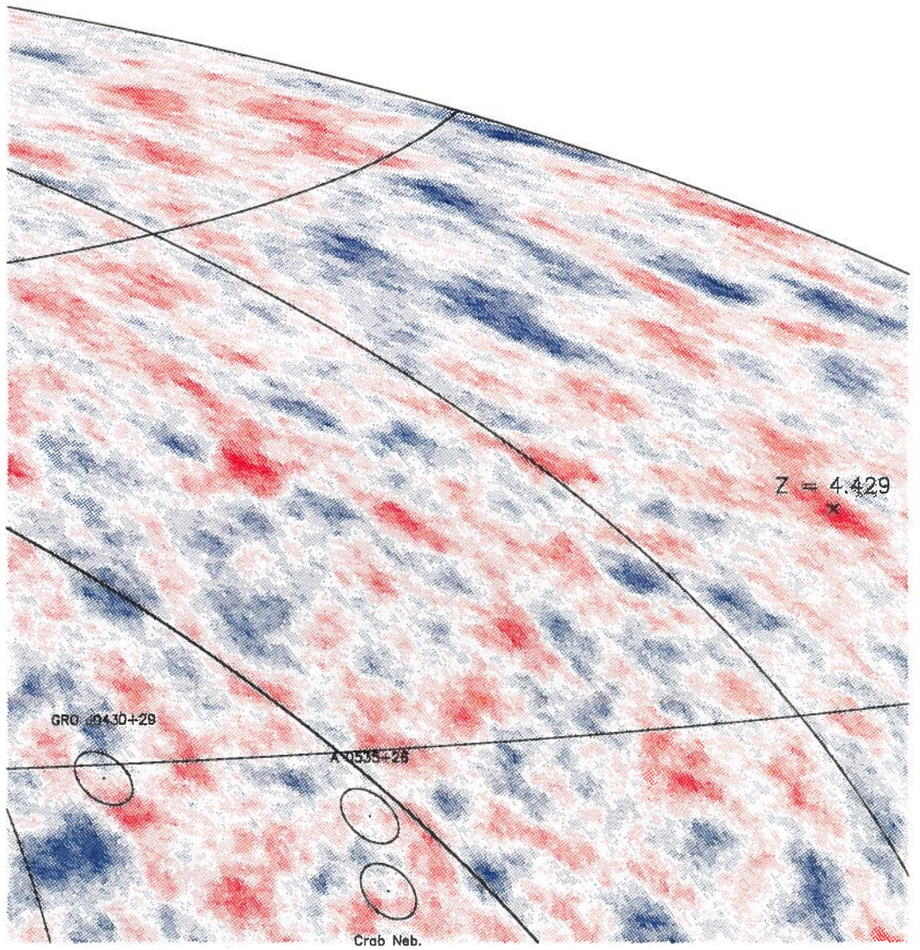
Celestial Coordinates, J2000.0



Exposure: 01/01/89–28/02/93

Aitoff Map No. 10

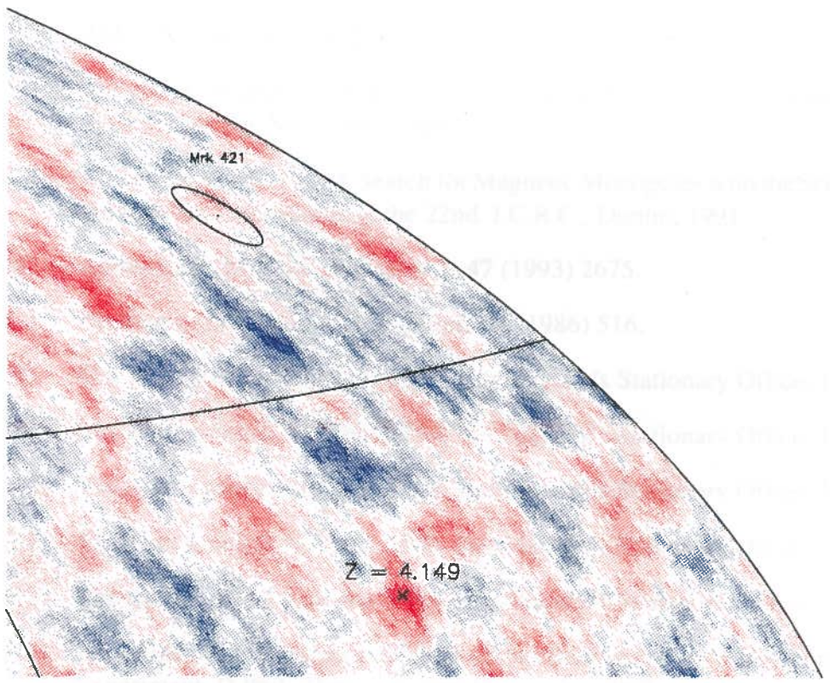
Celestial Coordinates, J2000.0



Exposure: 01/01/89–28/02/93

Aitoff Map No. 11

Celestial Coordinates, J2000.0



Exposure: 01/01/89–28/02/93

Aitoff Map No. 12

BIBLIOGRAPHY

[1] Aglietta, M., *et al.*, in Proceedings of the 21st. International Cosmic Ray Conference, Adelaide, 1989.

[2] Aguilar-Benitez, M., *et al.*(The Particle Data Group), Particle Properties Data Booklet, from Review of Particle Properties, Phys.Rev.D **45** (1992) Part 2.

[3] Ahlen, S. *et al.*, Ap.J. **412** (1993) 301–311.

[4] Aldous, D., Probability Approximations via the Poisson Clumping Heuristic, Springer-Verlag, New York, 1989.

[5] Allison, W.W.M. *et al.*, A Search for Magnetic Monopoles with the SOUDAN 2 Detector, in Proceedings of the 22nd. I.C.R.C., Dublin, 1991.

[6] Amenomori, M. *et al.*, Phys.Rev.D **47** (1993) 2675.

[7] Andreyev, Y.M., *et al.*, JETP Letters **44** (1986) 516.

[8] The Astronomical Almanac **1989**, Her Majesty's Stationary Office, 1988.

[9] The Astronomical Almanac **1990**, Her Majesty's Stationary Office, 1989.

[10] The Astronomical Almanac **1991**, Her Majesty's Stationary Office, 1990.

[11] The Astronomical Almanac **1992**, Her Majesty's Stationary Office, 1991.

[12] The Astronomical Almanac **1993**, Her Majesty's Stationary Office, 1992.

[13] Barr, G.D., The Separation of Signals and Background in a Nucleon Decay Experiment, D.Phil. Thesis, Oxford University, 1987.

[14] Battistoni, G., *et al.*, Phys.Lett.B **155** (1985) 465.

[15] Berezinskiĭ, V.S., Bulanov, S.V., Dogiel, V.A., Ginzburg, V.L. (editor), and Ptuskin, V.S., Astrophysics of Cosmic Rays, North-Holland, 1990.

[16] Berger, Ch., *et al.*, Phys.Lett.B **174** (1986) 118.

[17] Bionta, R.M., *et al.*, Phys.Rev.D **42** (1990) 2967.

[18] Blandford, R.D., Physical Processes in Active Galactic Nuclei, in Active Galactic Nuclei, Saas-Fee Advanced Course 20 (Lecture Notes 1990), Springer-Verlag, 1990.

[19] de Boer, H. *et al.*, Maximum Likelihood Method Applied to COMPTEL Source Recognition and Analysis, Data Analysis in Astronomy IV, Ed. Di Gesù *et al.*, Plenum Press, 1992.
See also [79]

[20] Bordes, J., Gimènez, V., and Peñarrocha, J.A., Phys.Lett.B **223** (1989) 251.

[21] CERN Application Software Group, V110 Short Write Up, CERN Computer Centre, 1993.

[22] CERN Application Software Group, V114 Short Write Up, CERN Computer Centre, 1993.

[23] CERN Application Software Group, HBOOK Reference Manual, Y250 Long Write Up, CERN Computer Centre, 1993.

[24] Clark, G.W., Phys.Rev. **108** (1957) 450.

[25] Cobb, J.H., and Giller, G.L., On the Statistics of Peak Searches, PDK–562 (1993).

[26] Cobb, J.H., and Thomson, M.A., SOUDAN 2 Background Calculations, PDK Note (1991).

[27] Cobb, J.H., private communication.

[28] Cockerill, D.J.A., The Soudan 2 Detector, 4th Topical Seminar on Experimental Apparatus for High Energy Particle Physics and Astrophysics. San Miniato, 1990.

[29] COMPTON Gamma Ray Observatory Science Report 102 (*Email* Message), G.R.O. Science Support Center, 1992.

[30] Cronin, J.W., Nucl.Phys.B. (Proc.Suppl.) **28B** (1992) 213.

[31] Dawson, J.W. *et al.*, Soudan 2 data acquisition and trigger electronics. 1985 IEEE Nuclear Science Symposium, San Francisco, CA.

[32] Derrick, M., *et al.*, Phys.Lett.B **297** (1992) 404–416.

[33] The Digital Equipment Corporation, `VAX-11 FORTRAN` User's Guide, 1982.

[34] Duffet-Smith, P., Astronomy with your Personal Computer, Cambridge University Press, 1985.

[35] Eadie, W.T., Drijard, D., James, F.E., Roos, M., and Sadoulet, B., Statistical Methods in Experimental Physics, North Holland Publishing Company, 1971.

[36] Fisher, R.A., Statistical Methods for Research Workers, Oliver and Boyd, 1958.

[37] The European Space Agency, The EXOSAT Observation Log, Astrophysics Division, Space Science Dept., 1986.

[38] Fichtel, C.E., *et al.*, High Energy Gamma-Ray Emission from Active Galactic Nuclei Observed by the Energetic Gamma-Ray Telescope Experiment (EGRET) in Energetic Gamma Ray Experiment Telescope Contributions to the COMPTON Observatory Symposium, NASA preprint 93–14 (1993), to be published in American Institute of Physics Conference Proceedings.

[39] Fichtel, C.E., *et al.*, Preliminary EGRET Source Catalogue, in Energetic Gamma Ray Experiment Telescope Contributions to the COMPTON Observatory Symposium, NASA preprint 93–14 (1993), to be published in American Institute of Physics Conference Proceedings.

[40] Gaisser, T.K., Cosmic Rays and Particle Physics, Cambridge University Press, 1990.

[41] Giller, G.L., First Results from the Analysis of Atmospheric Neutrinos in SOUDAN 2, Paper contributed to the Int.Conf. on Nuclear and Particle Physics, Glasgow, 1993.

[42] Gillespie, A.B., Signal, Noise and Resolution in Nuclear Counter Amplifiers, Pergammon Press, 1953.

[43] Goodman, M.C., Some Information about 3C 273, PDK–559 (1993).

[44] Greisen, K, Phys.Rev.Lett **16** (1966) 748–750.

[45] Halzen, F., Nucl.Phys.A **461** (1987) 181C–196C.

[46] Halzen, F., Physics Capabilities of Underground Detectors, in Proceedings of the Workshop on Long-Baseline Neutrino Oscillation, Fermilab, 1991.

[47] Hirshfield, A., and Sinnott, R.W., Sky Catalogue 2000.0, Cambridge University Press, 1985.

[48] James, F., and Roos, M., `MINUIT` — Function Minimization and Error Analysis, D506 Long Write up, CERN Computer Centre.
James, F., Interpretation of the Errors on Parameters as Given by `MINUIT`, D506 Supplement, CERN Computer Centre.

[49] Kasahara, S.M.S., private communication.

[50] Katz, J.I., High Energy Astrophysics, Addison-Wesley Publishing Company, 1987.

[51] Kaye & Laby, Tables of Physical and Chemical Constants (15th. Edn., Ed. Bailey, A.E.), Longman Scientific & Technical, 1986.

[52] Kendal, M.G., and Stuart, A., The Advanced Theory of Statistics, vol. 2: Inference and Relationship, Charles Griffin and Co. Ltd., 1973.

[53] Litchfield, P.J., private communication.

[54] Litchfield, P.J., `SEARCH` Processor User Guide, SOUDAN 2 program documentation.

[55] Lorenz, E., Nucl.Phys.B (Proc.Suppl.) **33A,B** (1993) 93.

[56] MacDonald, D., and Thorne, K.S., MNRAS **198** (1982) 345–382.

[57] Maran, S.P., (Ed.), The Astronomy and Astrophysics Encylopedia, Van Nostrand Reinhold, 1992.

[58] Marshak, M.L, *et al.*, Phys.Rev.Lett. **54** (1985) 2079.

[59] Marshak, M.L., *et al.*, in Proceedings of the 23rd. International Conference on High Energy Physics, Berkely, 1986.

[60] Marshak, M.L., and Courant, H., Determining the Absolute Orientation of the SOUDAN 2 Detector, PDK–527 (1993).

[61] Marshak, M.L., Status Report on the Reconstruction of Single Muon Tracks, PDK–528 (1993).

[62] Marshak, M.L., private communication.

[63] Miyake, S., Rappaporteur Talk, Proceedings of the 13th. International Cosmic Ray Conference, Denver, Vol. 5, 1973.

[64] Lowe, M.J., Astronomical Point Sources of Underground Muons, Ph.D. Thesis, University of Minnesota (Minneapolis), 1991.

[65] Oyama, Y., *et al.*, Phys.Rev.Lett. **56** (1986) 991.

[66] Oyama, Y., *et al.*, Phys.Rev.D **36** (1987) 3537.

[67] Peterson, E.A., private communication.

[68] Perkins, D.H., Testing SOUDAN 2 Angular Resolution for Muons through Moon Shadowing, PDK note.

[69] Pollock, A.M.T., *et al.*, Astron.Astrophys. **94** (1981) 116–120.

[70] Punch, M. *et al.*, Nature **358** (1992) 477.

[71] Reynolds, P.T., *et al.*, Ap.J. **404** (1993) 206–218.

[72] Ringwald, A., Multi-W(Z) Production in High-Energy Collisions?, Lecture given at the 4th. Hellenic School on Elementary Particle Physics, Corfu, 1992.

[73] Roback, D.M., Measurement of the Atmospheric Neutrino Flavour Ratio with the SOUDAN 2 Detector, Ph.D. Thesis, University of Minnesota (Minneapolis), 1992.

[74] Roy, A.E., Orbital Motion, Adam Hilger, 1978.

[75] Ruddick, K., Phys.Rev.Lett **57** (1986) 531–534.
See also Phys.Rev.Lett **57** (1986) 2872–2873.

[76] Ruddick, K., Nucl.Phys.B (Proc.Suppl.) **28A** (1992) 382–384.

[77] Siegmund, D.O., private communication.

[78] Siegmund, D.O., and Worsley, K.J., Testing for a Signal with Unknown Location and Scale in a Stationary Gaussian Random Field, Technical Report No. 13, Dept. of Statistics, Stanford University, 1993.

[79] Schönfelder, V., *et al.*, Instrument Description and Performance of the Imaging Gamma-Ray Telescope COMPTEL abord NASA's COMPTON Gamma-Ray Observatory, COMPTEL Preprint No. 2, 1993.

[80] The Soudan 2 Collaboration, in preparation.
See also [28, 31, 86].

[81] Stecker, F.W., and Done, C., Phys.Rev.Lett. **66** (1991) 2697–2700.

[82] Swanenburg, B.N., *et al.*, Nature **275** (1978) 298.

[83] Thomson, M.A., Muon Astronomy at SOUDAN 2, PDK–407 (1989).

[84] Thomson, M.A. *et al.*, Phys.Lett.B **269** (1991) 220.

[85] Thomson, M.A., An Experimental Study of the Possible Association of Deep Underground Muons with Astronomical Point Sources, D.Phil. Thesis, Oxford University, 1991.

[86] Thron, J.L., NIM **283** (1989) 642.

[87] Tupper (nee Kirby-Gallagher), L.M., A Study of Underground Muons in the SOUDAN 2 Detector, D.Phil. Thesis, Oxford University, 1990.

[88] Watson, A.A., The Search for the Origin of the Highest Energy Cosmic Rays, Paper presented at the Int.Conf. on Nuclear and Particle Physics, Glasgow, 1993.

[89] Weekes, T.C. *et al.*, Ap.J. **342** (1989) 379.

[90] Wilks, S.S., Ann.Math.Stat. **9** (1938) 60.

[91] Woltjer, L., Phenomenology of Active Galactic Nuclei, in Active Galactic Nuclei, Saas-Fee Advanced Course 20 (Lecture Notes 1990), Springer-Verlag, 1990.

[92] Worral, D.M. *et al.*, Ap.J. **232** (1979) 683.

[93] Zatsepin, G.T., and Kuzmin, V.A., JETP Lett. **4** (1966) 78.

Note: References to "PDK–n" are to SOUDAN 2 *internal notes.*